Pathway complexity in π-conjugated materials

Pathway complexity in π-conjugated materials

PROEFSCHRIFT

ter verkrijging van de graad van doctor aan de Technische Universiteit Eindhoven, op gezag van de rector magnificus prof.dr.ir. C.J. van Duijn, voor een commissie aangewezen door het College voor Promoties, in het openbaar te verdedigen op vrijdag 24 januari 2014 om 16:00 uur

door

Pieter Aart Korevaar

geboren te Graafstroom

Dit proefschrift is goedgekeurd door de promotoren en de samenstelling van de promotiecommissie is als volgt:

voorzitter:	prof.dr.ir. J.C. Schouten
1e promotor:	prof.dr. E.W. Meijer
copromotor(en):	dr.ir. T.F.A. de Greef
leden:	prof.dr. D. Frenkel (University of Cambridge)
	prof.dr. F. Würthner (Universität Würzburg)
	prof.dr.ir. R.A.J. Janssen
	dr.ir. P. Jonkheijm (UT)
adviseur(s):	dr. S.J. George (Jawaharlal Nehru Centre for Advanced Scientific Research)

Cover design: Peter Korevaar / ICMS Animation Studio

Printed by: Gildeprint Drukkerijen – The Netherlands

A catalogue record is available from the Eindhoven University of Technology Library
ISBN: 978-90-386-3538-5

This work has been financially supported by the European Research Council (FP7/2007-2013) Grant Agreement and the Ministry of Education, Culture and Science (Gravity Program 024.001.035).

Table of contents

1

Polymorphism in the aggregation of π-conjugated materials

Abstract: To arrive at functional organic materials with optimal molecular organization, control over the aggregation process is a prerequisite. Often however, multiple pathways are involved that compete for the same molecular building block, a phenomenon known as pathway complexity. As a result, the material – made from small molecules or polymers – can get entrapped in a metastable pathway while a more stable, but slower formed morphology is aimed for. *Vice versa*, the equilibrium state can be obtained easily but another, less stable morphology is desired as it has more interesting properties. In both cases, the solution processing, starting from molecularly dissolved material, should be optimized to select the desired aggregation pathway. This introduction chapter aims to outline the importance of mechanistic insights derived from self-assembly of one-dimensional fibres in diluted solutions to unravel and control aggregation pathways involved in the processing of π-conjugated materials.

Part of this work has been published as:

"Pathway Complexity in π-Conjugated Materials" P. A. Korevaar, T. F. A. de Greef, E. W. Meijer, *Chem. Mater.* **2013**, DOI: 10.1021/cm4021172.

1.1 Introduction

Control over the nanoscale organization of π-conjugated molecules is regarded as one of the key parameters in the performance of organic electronic devices.[1–7] To obtain the best characteristics, such as high charge-carrier mobility for field effect transistors (FET) or efficient electron-hole separation in bulk heterojunction (BHJ) solar cells, every atom has to be placed at the optimal position in three-dimensional space. The design of individual molecules – either small molecules or polymers – is often straightforward as both theories to predict the electronic properties of the molecular building blocks and synthetic methodologies to obtain them in pure form have reached an exceptional level of sophistication. However, control on the next length scale, beyond the molecular formula, is much more complicated. Finding self-assembly pathways which yield optimal molecular organization is still an endeavour that mainly relies on a trial-and-error approach (Fig 1.1).[1]

The common strategy in the processing of π-conjugated materials is to start with conditions where the molecules or polymers are completely, *i.e.* "molecularly" dissolved. This can be achieved by the addition of a good solvent like chloroform in combination with elevated temperatures. Next, the onset of aggregation is induced by changing the solvent conditions, for instance by spin coating or adding a solvent in which the molecules are less soluble (*i.e.* poor solvent). However, the outcome of the aggregation process is often dependent on the processing methodology, meaning that different preparation protocols attenuate different aggregation pathways and consequently result in different nanoscale morphologies. Obviously, since the performance of functional devices depends on the morphology, unravelling clear relations between processing methodology and pathway selection is of great interest for this field of research. It is therefore not surprising to see a large number of articles[8–21] and reviews[22, 23] recently addressing the need to control self-assembly pathways of π-conjugated molecules.

The influence of aggregation pathways on the molecular organization of functional π-conjugated materials emphasizes the importance of mechanistic insights into molecular self-assembly. In the field of chemical self-assembly, the aggregation of small molecules – including π-conjugated monomers – into one-dimensional fibres is studied in detail. In this introduction chapter we point out that mechanistic insights into aggregation pathways of π-conjugated molecules, as obtained via studies on their molecular self-assembly, can be highly valuable to understand and optimize the processing of π-conjugated functional materials.

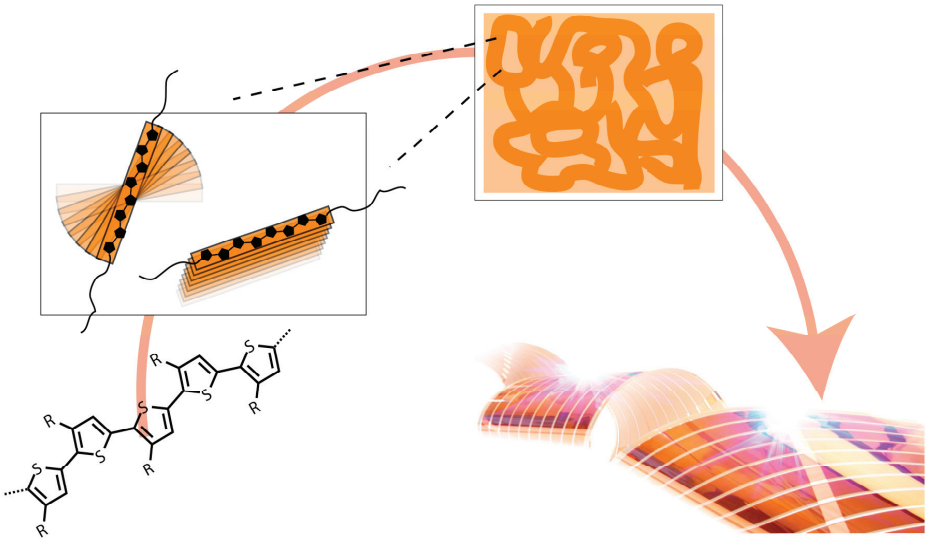

Figure 1.1 | Control over the morphology formed by aggregates of π-conjugated molecules within organic devices is one of the key parameters controlling their performance. Hence, understanding the aggregation pathways that the molecules (or polymers) can follow during the formation of these aggregates is of great interest for the optimization of these materials. Image from ref. 24.

1.2 Kinetic pathways towards metastable morphologies

Metastable morphologies that are formed in the initial aggregation stages of π-conjugated molecules can have major effects on the subsequent self-assembly process. Often, these spurious, metastable structures act as a trap for the molecular building blocks, and due to this entrapment the formation of the desired morphology is retarded or even made impossible at reasonable time-scales. In other cases, however, the metastable structure has superior properties compared to equilibrium aggregates, and hence the preparation protocol should be optimized to favour the metastable pathway while making sure that the nanostructures do not re-equilibrate back to other, lower energy morphologies. In this paragraph, we discuss the influence of kinetic pathways, both for the aggregation of π-conjugated materials as well as the molecular assembly of one-dimensional fibres in diluted solution.

1.2.1 Metastability in π-conjugated materials

To probe the molecular organization of π-conjugated polymers or oligomers, the material can be functionalized with chiral side chains and studied with circular dichroism (CD) spectroscopy. The stereocentres serve as a spectroscopic label, since the magnitude and sign of CD spectra are very sensitive to optical transitions, either within the twisted π-conjugated backbone or in helical aggregates formed by multiple polymer chains. One of the first examples of a chiral π-conjugated polymer that displays different CD spectra when different preparation protocols are applied, is *S*-chiral polythiophene **1** (Fig 1.2), as reported by Bouman

et al.[25] Spin coated films of **1** on glass reveal a bisignated, negative Cotton effect at room temperature, that is erased upon heating the polymer up to 160 °C. Subsequent cooling results in the reappearance of a helical morphology. However, the sign of the Cotton effect depends on the cooling rate applied: whereas slow cooling yields a negative Cotton effect, quenching the sample in at 0 °C yields a completely opposite Cotton effect (Fig 1.2). Only heating the material and cooling slowly results in a reestablishment of the negative Cotton effect. This suggests that fast cooling results in a direct conversion towards metastable aggregates with opposite handedness compared to the thermodynamically stable form that is obtained upon slow cooling.

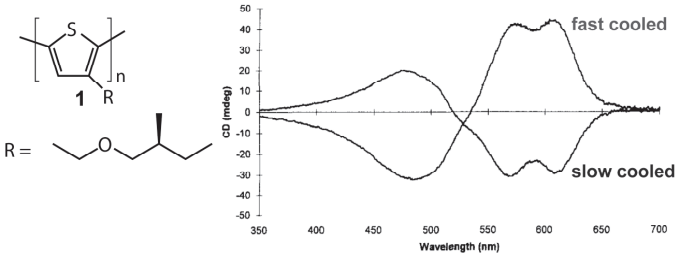

Figure 1.2 | Opposite Cotton effects of chiral polythiophene **1** in thin films reveal multiple aggregation pathways upon fast and slow cooling. Image from ref. 25.

Another illustrative example of kinetically entrapped morphologies that can be obtained by manipulating the preparation method is reported by Swager and co-workers in their studies on the aggregation of poly(*p*-phenylene vinylene), PPV.[26, 27] CD studies on *S*-chiral PPV **2** in pure chloroform yield no Cotton effect, indicating that no helical aggregates are present in this solvent. However, addition of acetonitrile (MeCN) results in a strong bisignate Cotton effect, indicating exciton coupling between adjacent PPV backbone chains within the aggregates formed. Remarkably, if less than 50% MeCN is added, a positive Cotton effect is obtained, whereas adding more than 50% MeCN yields a negative Cotton effect. Furthermore, the positive Cotton effect can also be obtained if the polymer is dissolved in 1,2-dichloroethane (DCE). Spin coating the aggregate-free solution of PPV from pure chloroform results in a film without any chiral organization, as indicated by the absence of a Cotton effect. However, after annealing the film at 45 °C in the presence of chloroform vapour, a negative Cotton effect is obtained. This indicates that the initially disordered polymer chains reorganize into a chiral morphology that is thermodynamically more stable. Also when PPV is spin coated from DCE, the structures initially present in solution are preserved in the bulk state, as evident from the positive Cotton effect of thin films. However, in this case thermal annealing in the presence of either DCE vapour, chloroform vapour or an inert nitrogen atmosphere does not affect the helicity of the aggregates. These results, as schematically represented in Figure 1.3, make clear that by spin coating from different solvents, different pathways can be selected towards morphologies with opposite helicities. Even though in the film only one type can be the most stable state, both pathways result in stable structures that do not interconvert at reasonable time scales.

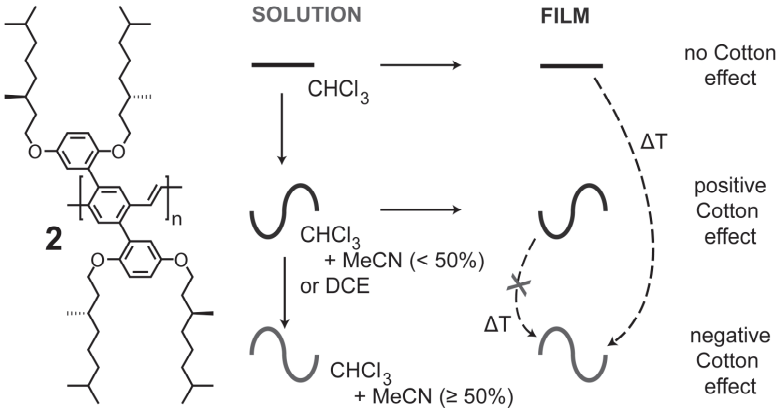

Figure 1.3 | Schematic representation of the diversity of Cotton effects obtained for *S*-chiral poly(*p*-phenylene vinylene) **2** under different conditions in solution and film.[26, 27]

Whereas π-conjugated polymers in most cases fail to crystallize completely and result in a material that contains both crystalline and amorphous domains, small molecules crystallize much easier and often completely. However, in many crystallization processes multiple molecular organizations can be realized, resulting in different crystal structures called polymorphs. In a recent example reported by Stupp and co-workers, control over the different polymorphs is obtained by taking advantage of the differences in growth kinetics between multiple aggregation pathways.[28] The molecule of interest, quarterthiophene **3** (Fig 1.4), is molecularly dissolved in the hydrogen-bond accepting solvent tetrahydrofuran (THF), whereas aggregation occurs in toluene. To obtain a solvent that dissolves **3** and can induce its aggregation by slow evaporation or addition of more toluene, a mixture of dioxane, THF and toluene in a 2:1:1 ratio is applied. Drop casting **3** (2.5 wt%) from the solvent mixture on a Teflon sheet results in the formation of a network of fibres (Fig 1.4b). If however the evaporation is retarded by the presence of toluene vapour, the same experiment yields rhombohedra structures (Fig 1.4c), the second polymorph. Moreover, a third pathway towards hexagonal prisms (Fig 1.4d) can be selected by evaporating a more concentrated solution (5 wt%) in the presence of toluene vapour. However, in both cases fibres are formed next to the rhombohedra and hexagonal prisms, respectively. The fact that fast evaporation yields exclusively fibres suggests that these fibres are formed first and thereafter – if the solvent does not evaporate too fast – convert into a more stable polymorph. Hence, to obtain the exclusive growth of these polymorphs, the aggregation process is slowed down via diffusion of the poor solvent toluene into molecularly dissolved **3**. To retard this diffusion, a membrane is applied as a diffusion barrier, and the viscosity of the toluene phase is increased by dissolving poly(methyl methacrylate). The viscous toluene phase is placed on one side of the vertically oriented membrane, and a 5 wt% solution of **3** in 2:1:1 dioxane/THF/toluene on the other side. After diffusion of both solutions into each other and evaporating the solvent, hexagonal prisms are obtained, whereas the same experiment with a 2.5 wt% solution yields rhombohedra. Next to the differences between these polymorphs that appear on the

micrometre scale (Fig 1.4), two-dimensional grazing incidence small angle X-ray scattering (2D-GISAXS) revealed significant differences in the molecular organization. Another striking difference between these pathways is the position of the aggregates. Whereas the rhombohedra are found mostly at the bottom of the dried membrane, the hexagonal prisms are all anchored perpendicular to the surface of membrane. The involvement of the surface in the growth of the hexagonal prisms suggests a heterogeneous nucleation pathway for this polymorph, whereas rhombohedra are formed via homogeneous nucleation.

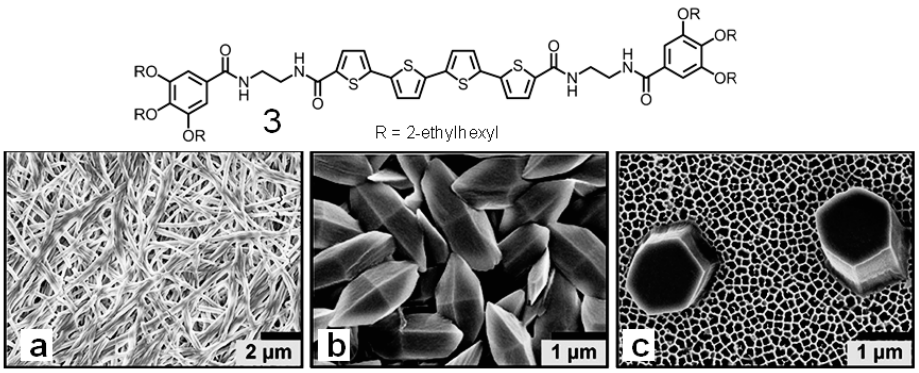

Figure 1.4 | Scanning electron microscopy (SEM) images of the fibre (a), rhombohedra (b) and hexagonal prism (c) morphologies that are obtained for quarterthiophene **3** upon different preparation methods. Image from ref. 28.

An elegant methodology to attenuate different self-assembly pathways resulting in a metastable polymorph was reported recently by Bao and co-workers in their studies on the crystallization of pentacene derivative **4** (Fig 1.5) into an organic semiconducting material.[29] A special solution-shearing process is applied in which a shearing plate drags a solution of **4** in toluene across a heated substrate (Fig 1.5a). The morphology of the thin film is dependent on the shearing speed. Slow shearing (0.4–2.8 mm/s) results in crystal rods oriented along the shearing direction (Fig 1.5c). For higher shearing rates, the morphology changes from comet-shaped, transcrystalline structures (4 mm/s) to a completely isotropic, spherulitic film (8 mm/s), indicating that the orientation along the shearing direction disappears (Fig 1.5d). Apart from these differences in morphology on the sub-millimetre scale, the shearing rate also influences the molecular packing. Grazing incidence X-ray diffraction (GIXD) experiments reveal that the shortest π-π distance obtained in a film prepared with a shearing rate of 8 mm/s equals 3.08 Å, whereas π-π distances of 3.33 Å are obtained for films prepared upon evaporation (*i.e.* no shearing) and in the bulk crystal. Due to this reduction in π-π distance, the charge carrier mobility increases significantly. Thin films prepared with a shearing rate of 2.6 mm/s show an optimum average mobility of 2.1 $cm^2V^{-1}s^{-1}$ along the shearing direction (Fig 1.5b). Although faster shearing rates yield a reduced π-π distance as well, the advantageous effect of this reduction is counteracted by the loss of crystal orientation along the shearing direction. The thin films do not degrade in time and are thermally stable up to 160 °C.

However, exposing the film to toluene vapour yields a relaxation of the decreased π-π distance back to the bulk crystal morphology and a concomitant decrease in charge carrier mobility. This indicates that the solution-shearing process directs the aggregation process into a metastable morphology. As the processing methodology starts from a thin liquid film that allows fast solvent evaporation, it is hypothesized that the growing crystal front is given only limited time to crystallize. Hence, the material gets kinetically entrapped in a metastable state with superior properties compared to the equilibrium morphology.

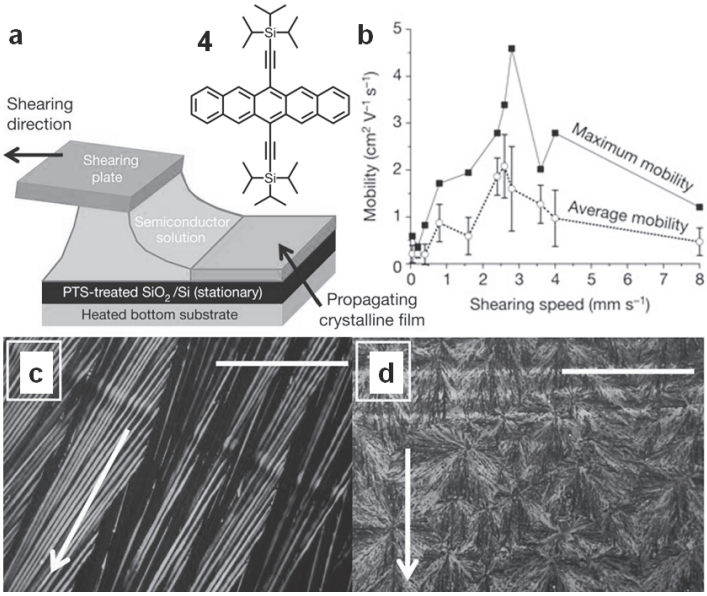

Figure 1.5 | Pentacene crystals prepared via a solution-shearing process have a different morphology that conducts better. (a) Schematic representation of the solution-shearing process (a), by which the charge carrier mobility in crystals of pentacene derivative **4** can be optimized (b). (c, d) Shearing results in metastable crystals with a higher conductance compared to bulk, equilibrium crystals. However, this effect is counteracted by a loss in anisotropy if the shear speed is too fast (c, shear speed 1.6 mm/s; d, 8 mm/s, scale bars represent 200 μm). Image from ref. 29.

1.2.2 Metastability in π-conjugated fibres in solution

Aida and co-workers assembled graphitic nanotubes with semiconducting properties from hexabenzocoronenes (HBC, **5**, Fig 1.6).[30] These nanotubes can become micrometers long but have a very uniform diameter of 20 nm. The wall of the tubes consists of a 3 nm thick bilayer of π-stacked HBCs, facilitated by the amphiphilic character of the HBC molecule that has two aliphatic dodecyl tails on one side and two hydrophilic triethylene glycol chains on the other. Assembly of HBC **5** in pure THF results in exclusive formation of nanotubes. However, in the presence of 20 volume% water in THF, helical coils are obtained next to the nanotubes. These coils, comprising helically folded bilayer ribbons, are considered as the topological precursor for the nanotubes, suggesting that they are only kinetically stable.[31] To further investigate the different structures involved in the HBC assembly pathways, HBC **6** was functionalized with

two polymerizable norbornene groups to the triethylene glycol chains.[32] Diffusion of diethylether vapour into a solution of **6** in dichloromethane at 25 °C yields nanotubes, whereas vapour diffusion at 15 °C results in helical coils only. The metastable character of these coils is demonstrated by annealing at 25 °C, which results in a gradual transformation into nanotubes. To stabilize the nanocoils that are only kinetically stable at low temperatures, the norbornene groups are polymerized using a Grubbs catalyst. Whereas non-polymerized assemblies are disrupted completely, covalently fixed nanocoils maintain their structure up to 75 °C, clearly indicating the stabilizing effect of covalent fixation on the metastable architectures.

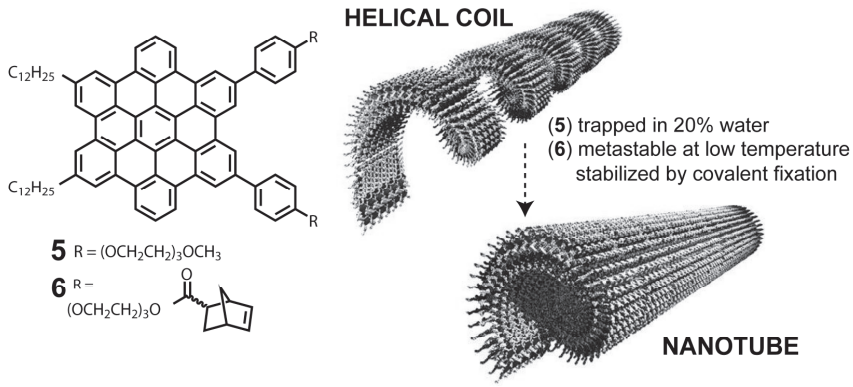

Figure 1.6 | Hexabenzocoronene (HBC) derivatives **5** and **6** assemble under equilibrium conditions in nanotubes. HBC **5** can be trapped in metastable helical coils upon addition of 20 volume% water to the solution. For HBC **6**, these coils can be obtained at low temperature and thereafter stabilized by covalent fixation upon polymerization of the norborene groups.[30–32] Image from ref. 31.

The hierarchical assembly pathways of bismerocyanine **7** (Fig 1.7) are studied in detail by Würthner and co-workers.[33–35] The two merocyanine units of this V-shaped molecule have a large dipole moment that allows both of them to dimerize with the merocyanine unit of another molecule, resulting in randomly oriented oligomer chains (*D* aggregates). In apolar solvents like methylcyclohexane (MCH), these chains assemble further into helical rods (*H* aggregates) that consists of six intertwined chains (Fig 1.7). These intertwined chains are visible in Atomic Force Microscopy (AFM) and cryo-Transmission Electron Microscopy (cryo-TEM). Molecular simulations have provided insight into the number of intertwined chains. To rationalize this hierarchical assembly process, a kinetic experiment is performed. Molecularly dissolved **7** in THF is added to MCH, yielding a 30:70 v/v THF/MCH solution. Time-dependent UV/Vis spectroscopy reveals the transition from instantaneously assembled *D* aggregates into *H* aggregates. Together with the rise of *H* aggregates, a strong negative Cotton effect appears in the CD spectra, indicative for a helical organization of the chromophores within the intertwined chains of the helical rods. Surprisingly however, the assembly process proceeds after the appearance of the negative Cotton effect as revealed by a total inversion of the CD spectrum. This stereomutation indicates that the initially formed *H* aggregates, referred to as *H1*, are metastable and reorganize in time into a more stable structure *H2* that has an

opposite Cotton effect. To understand this process further, the *D*→*H1*→*H2* conversions are studied using AFM on solutions that have been spin coated in different stages of the assembly process. Right-handed structures appear in the AFM micrographs for *H1* aggregates corresponding to the structure with a negative Cotton effect. Remarkably, AFM on dried fibres corresponding to *H2* aggregates also show this handedness, even though for this state an opposite Cotton effect is observed. To rationalize these results, it is hypothesized that the helicity of the intertwined chains is not affected during the conversion from *H1* to *H2* aggregates. Only the molecular organization of the merocyanine units within these chains, which is responsible for the sign of the Cotton effect, shifts from a left- to a right-handed fashion. Applying a higher fraction of MCH delays the *H1*→*H2* conversion and results in entrapment of *H1* aggregates for weeks. This suggests that (re)-dissolved molecules play an important role in the stereomutation process from metastable to stable assemblies.

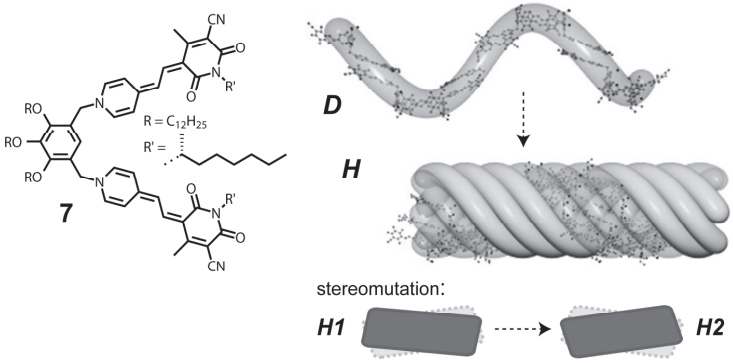

Figure 1.7 | Hierarchical assembly process of bismerocynanine **7** into subsequently oligomer chains (*D*) and helical rods (*H*). The helical organization of the merocyanine units in these rods inverts in time, from metastable *H1* to stable *H2*.[33–35] Image from ref. 33.

1.3 Mechanistic insights into aggregation pathways

The examples discussed in the previous paragraph make clear that metastable morphologies appear frequently in π-conjugated materials. Avoiding or attenuating entrapment of material in these metastable nanostructures requires in-depth understanding of the individual pathways as well as their mutual interactions. In this respect, every pathway can be simplified to a one-dimensional aggregation process that (often) starts with a nucleation event. Here, the building blocks are individual molecules in the case of small molecule systems, and oligomer segments for polymer systems.[36–38] The onset of the aggregation process can be described as a purely one-dimensional (1D) assembly process where all monomers stack on top of each other into a fibre, driven by π-π stacking. Alternatively, a fibre can be formed via lateral growth of multiple stacks, as illustrated in Figure 1.8. It should be mentioned that processing of π-conjugated materials occurs in concentrated solutions and involves multiple aggregation steps beyond the formation of these fibrous structures. Nevertheless, mechanistic insights derived from assembly of fibres under dilute conditions hold important lessons to unravel and control aggregation pathways in π-conjugated materials. To this end, this paragraph is focused on the mechanisms of one-dimensional and lateral assembly processes.

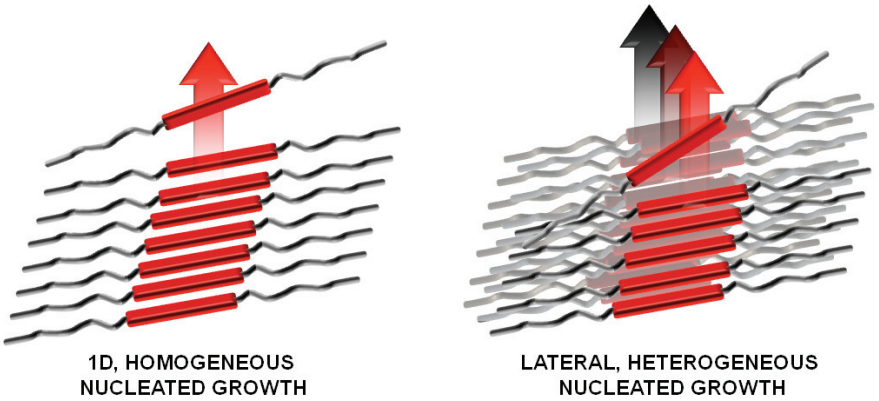

Figure 1.8 | Schematic representation of 1D, homogeneous (left) and lateral, heterogeneous nucleated growth (right).

1.3.1 Self-assembly under equilibrium conditions

Self-assembly processes can be described under equilibrium conditions as a sequence of monomer association equilibria, as depicted in Figure 1.9a. Two major classes of self-assembly mechanisms are the isodesmic and cooperative mechanism.[39, 40] Whereas in isodesmic assembly the monomer association equilibrium constant K is independent of the chain length i, cooperative assembly starts with a relatively unfavourable nucleation up to the nucleus size n, followed by more favourable elongation. Hence, the equilibrium constant of nucleation K_n is smaller than the equilibrium constant of elongation K_e, and this difference is characterized by the cooperativity $\sigma = K_n/K_e$. Via analysis of the monomer association equilibria, as

demonstrated by Goldstein and Stryer[41], the characteristic features of isodesmic and cooperative assembly can be reconstructed. To this end, the dimensionless concentration $x_{tot} = K_e \cdot c_{tot}$ is defined. The dimensionless quantity x_{tot} increases with total concentration c_{tot} and, as the assembly of most π-conjugated systems in non-aqueous solutions is enthalpy driven, decreases with temperature. In Figure 1.9b, the degree of aggregation φ, which equals the fraction of material in aggregates larger than the monomer ($i \geq 2$) for an isodesmic system or aggregates larger than the nucleus ($i > n$) for a cooperative system, is displayed as a function of x_{tot}. A sigmoidal, symmetric curve is obtained for isodesmic assembly. In contrast, cooperative aggregation results in a transition at $x_{tot} = 1$, which becomes sharper for smaller values of the cumulative cooperativity σ^{n-1}.[41] The critical transition at $x_{tot} = 1$ implies that cooperative growth only occurs beyond a critical concentration and below a critical temperature. Next to the onset of the temperature- or concentration-dependent aggregation process, nucleation also influences the equilibrium length of the assemblies. While isodesmic assembly yields many relatively short chains, an unfavourable nucleation event results in a few assemblies with much larger length, since monomer addition to long aggregates is preferred over the nucleation of new, short assemblies.[39] This implies that the formation of fibres or crystals, such as shown in Figures 1.4, 1.5, 1.6 and 1.7, is likely to originate from a nucleation event.

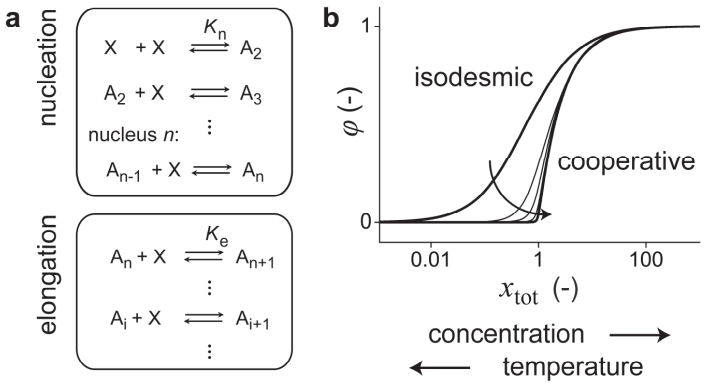

Figure 1.9 | (a) Thermodynamic model for assembly, as developed by Goldstein and Stryer[41], that describes the assembly of monomer X via a sequence of monomer association equilibria into assemblies A_i. (b) The degree of aggregation φ increases gradually with the dimensionless concentration x_{tot} for isodesmic assembly ($\sigma = 1$), and a critical transition at $x_{tot} = 1$ is obtained for cooperative assembly. The arrow indicates a decrease in cooperativity σ.

1.3.2 Kinetics of nucleated aggregation along one pathway

Aggregation pathways towards metastable morphologies, as observed for many self-assembling systems, emphasize the importance of kinetic phenomena. However, detailed kinetic studies on the aggregation of artificial molecular systems are rare in comparison to the vast amount of studies on self-assembly under thermodynamic control. Most theories employed to analyse fibre growth kinetics are originally developed in the field of protein

aggregation, to describe protein aggregation pathways involved in the formation of actin filaments or amyloid fibrils related to diseases like Alzheimer's disease.[42] The following part of this paragraph provides an overview of the kinetic insights into nucleated aggregation along a single pathway that are most relevant to the unravelling of multiple aggregation pathways.

In the initial stages of a cooperative self-assembly process, nucleation has to take place before the first elongated fibres can be formed. As the formation of a nucleus is an unfavourable event, the formation of the initial aggregates is relatively slow. However, when more nuclei and large aggregates appear, further growth can take place more rapidly since monomer association is more favourable in the elongation regime. As a result, the initial rate of the aggregation increases after $t = 0$, resulting in a lag phase in the time-dependent degree of aggregation for a cooperative assembly process.[43] Next to the critical temperature and concentration, such a lag phase is a hallmark for cooperative growth. It should be mentioned however that also pseudo lag phases can be observed for isodesmic systems if the experimental method is not sensitive to aggregates below a certain threshold size.[44]

The previously introduced 1D and lateral growth processes have different nucleation mechanisms. In a 1D process, the growth in the initial phases of the process is dominated by monomer, nucleus and eventually pre-nucleus species, and can be considered as homogenously nucleated growth.[45] For lateral growth, different nucleation pathways are involved as the surface of existing stacks nucleates the formation of new stacks. As a consequence of this secondary or heterogeneous nucleation, the aggregates catalyse their own formation (*i.e.* autocatalytic growth).[46] Here, two models are discussed that describe 1D and lateral growth.

1.3.3 One-dimensional, homogeneous nucleated growth kinetics

An insightful kinetic model developed by Powers and Powers forms the basis of the approach applied in this thesis to analyse nucleated 1D assembly kinetics.[45] Analogous to the equilibrium model, the model describes the growth of 1D assemblies in a single pathway as a sequence of monomer addition steps, as shown in Figure 1.10a. In the nucleation part of this mechanism, oligomers can change size upon monomer association and dissociation, with rate constants a and b, respectively. Beyond the nucleus with size n, further elongation takes place with monomer association rate constant a, and monomer dissociation rate constant c. The decrease of the dissociation rate for elongation (c) relative to nucleation (b) reflects the cooperative character of the mechanism. The equilibrium constants for nucleation K_n and elongation K_e are equal to a/b and a/c, respectively, and the cooperativity σ follows from c/b. It should be mentioned however, that whereas Powers and Powers reduced the number of reaction-rate equations by assuming irreversible monomer additions to the nucleus, the models applied in this thesis describe the full system in a reversible fashion by applying a quasi-equilibrium approach, as further elaborated in Chapter 2.

Kinetic simulations, where the degree of aggregation φ is followed in time, are performed by numerically solving the system of differential equations that describe the subsequent monomer association and dissociation steps. Simulations performed for a cooperative system ($\sigma = 0.01$ and $n = 5$) show that indeed in the initial stages of the growth process a lag phase can be observed (Fig 1.10f). In contrast, such a lag phase is absent in simulations assuming isodesmic growth (*i.e.* $\sigma = 1$, Fig 1.10h). Remarkably, the time at which 50% of the monomers are assembled into aggregates (t-50) levels off at the highest concentrations for a cooperative system ($\sigma = 0.01$ and $n = 5$), as shown in Figure 1.10bc. Analogous simulations assuming isodesmic growth ($\sigma = 1$) do not show such a concentration independence at high concentrations. The levelling off of t-50 at high concentrations for cooperative 1D aggregation is related to the formation of pre-nucleus oligomers[45, 47]: following the time-dependent fraction of material assembled in oligomers up to the nucleus size shows that for the highest concentrations a significant amount of material is accumulated in pre-nucleus assemblies (Fig 1.10e). In the high concentration regime, the conversion rate from these oligomers to elongated assemblies becomes concentration-independent. Again, this phenomenon can also be observed for isodesmic systems if the smallest species are not captured by the experimental assay.

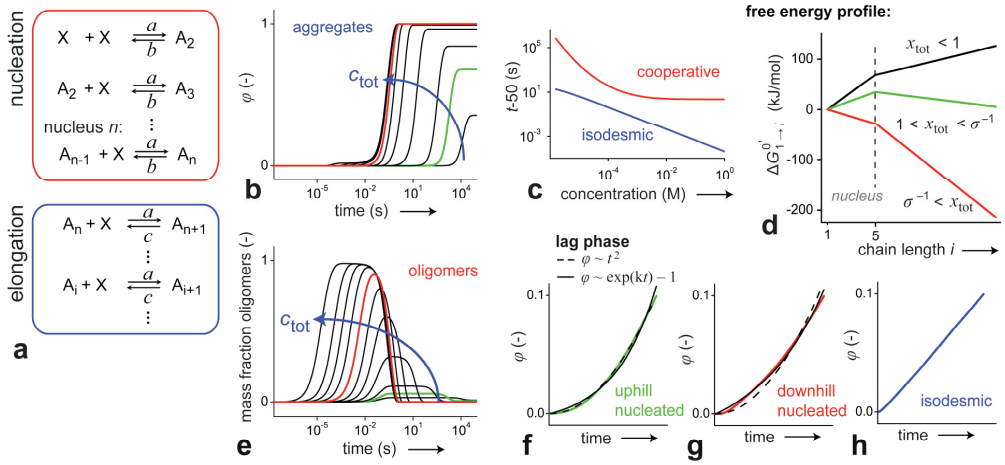

Figure 1.10 | Analysis of assembly kinetics along a single pathway, assuming homogeneous nucleated growth. (a) Schematic representation of the kinetic model that describes the nucleated assembly process as a sequence of monomer addition and dissociation steps. (b) The degree of aggregation φ is simulated as a function of time. Simulations performed for the case of homogeneous nucleated growth ($a = 10^4$ M^{-1}s^{-1}, $b = 1$ s^{-1}, $c = 0.01$ s^{-1}, $n = 5$) show faster growth at higher concentrations, although the rate levels off at high concentration (c) due to accumulation of material in pre-nucleus oligomers (e). For low concentrations (e.g. 3.2 μM, f), the lag phase can be described with a quadratic scaling relation $\varphi \sim t^2$, whereas this approximation fails at high concentrations (e.g. 1.8 mM, g). This behaviour corresponds to uphill and downhill nucleation, as depicted in the free energy profiles at 25 °C (d). Isodesmic growth ($a = 10^4$ M^{-1}s^{-1}, $b = c = 0.01$ s^{-1}) results in a monotonic decrease of t-50 with concentration (c), and no lag phase (h).

1.3.4 Lateral, heterogeneous nucleated growth kinetics

To describe lateral growth, a minimalistic, phenomenological model has been developed by Finke and Watzky.[46, 48] First, the conversion of monomer *X* into aggregated state *A* is defined with activation rate constant *a*. Next, *X* reacts with *A* to yield 2 *A*, with rate constant *b*. As $b > a$, *A* enhances its own formation in an autocatalytic fashion (Fig 1.11a). Also in this mechanism, the resulting kinetic curves display a lag phase (Fig 1.11c). Besides, the rate increases monotonically with concentration (Fig 1.11bd), unless the concentration is very low and formation of *A* takes mainly place via the monomolecular activation.

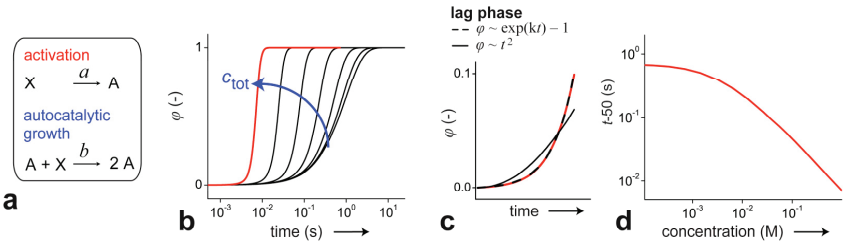

Figure 1.11 | Analysis of assembly kinetics along a single pathway, assuming lateral, heterogeneous nucleated growth. (a) Schematic representation of the phenomenological model developed by Finke and Watzky. (b) Simulations show that the rate increases monotonically with concentration (b, d) and the lag phase can be approximated with an exponential relation $\varphi \sim \exp(k \cdot t) - 1$ (c). The blue arrows indicate increasing concentration. Parameters: $a = 1\ s^{-1}$, $b = 10^3\ M^{-1}s^{-1}$.

1.3.5 Unravelling lag phases in nucleation pathways

Since the lag phase is one of the characteristics of cooperative assembly, special attention is paid to the early stages of the aggregation process, both for homogeneous and heterogeneous nucleation. To this end, we focus first on the description of cooperative assembly via Gibbs free energy profiles. We start from the well-known equation $\Delta G^0 = -RT \ln(K)$, where *K* equals the equilibrium constant in M^{-1}, *i.e.* K_n in the nucleation regime and K_e in the elongation regime. It can be shown that for the dimensionless concentration x_{tot} which equals $K \cdot c_{tot}$, $-RT \ln(x_{tot}) = -RT \ln(K) - RT \ln(c_{tot})$ holds. If we now define a new Gibbs free energy $\Delta G^{0\prime}_{i \rightarrow i+1}$ that equals $-RT \ln(x_{tot})$, the free energy profile can be constructed, *i.e.* $\Delta G^{0\prime}_{1 \rightarrow i}$ as a function of chain length *i*, starting with $\Delta G^{0\prime} = 0$ for the monomer. As shown in Figure 1.10d, the free energy profile is concentration-dependent. Formally, here the total concentration c_{tot} is taken as the reference state, whereas the standard state is defined at 1 M.[49] Three concentration regimes can now be recognized:[45] (1) If $x_{tot} < 1$, the free energy keeps increasing with chain length. Hence, the monomer is the lowest energy species, and no aggregation takes place in agreement with the simulations employing the equilibrium model. (2) If $1 < x_{tot} < \sigma^{-1}$, the nucleus is the highest energy species, but $\Delta G^{0\prime}_{1 \rightarrow i}$ decreases after the nucleus and hence elongation can take place (3) If $x_{tot} > \sigma^{-1}$, the monomer is the highest energy species. A clear difference between the second and third regime is the development of $\Delta G^{0\prime}$ during the

nucleation phase, which is uphill for regime 2 and downhill for regime 3. Hence, the formation of pre-nucleus oligomers is unfavourable in regime 2, whereas significant amounts of oligomeric species appear in the initial stages of the aggregation process for regime 3, as demonstrated in the kinetic simulations (Fig 1.10e).

In the case of homogeneous uphill nucleation, monomer and nucleus are the most dominant species during nucleation. This means that the rate in the initial stages of the aggregation (up to 10% conversion) can be approximated by: $d\varphi/dt \sim k\cdot[monomer][nucleus]$. It can be shown that under these conditions the lag phase can be described by the quadratic relation $\varphi(t) \sim t^2$.[50, 51] For a homogeneous downhill aggregation however, pre-nucleic oligomers cannot be neglected and therefore the lag phase does not have a quadratic dependence on time (Fig 1.10fg).

If the aggregation process is dominated by lateral growth, the aggregation rate in the initial stages of the growth process is expected to be proportional to the amount of aggregated material present. Alternatively, also secondary nucleation effects like fragmentation which facilitate formation of new nuclei are proportional to the degree of aggregation and hence autocatalytic. Therefore, the aggregation rate in the initial stages of the nucleated growth can be approximated by $d\varphi/dt \sim k\cdot\varphi$. Hence, autocatalytic lag phases can be approximated by an exponential relation, *i.e.* $\varphi(t) \sim \exp(k\cdot t) - 1$, as shown in Figure 1.11c.[50, 51] In contrast, it is not possible to describe these lag phases with the quadratic scaling relation corresponding to homogeneous nucleation regime. *Vice versa*, the exponential relation does not describe the lag phases obtained with the homogeneous nucleation model.

1.3.6 Nucleation in one-dimensional *vs*. three-dimensional aggregation

The involvement of a nucleus in the cooperative formation of 1D assemblies holds an intriguing resemblance to classical nucleation phenomena well known in ice formation, precipitation of organic crystals[52] and colloidal crystallization.[53] However, notable differences can be recognized, for instance in the physical principles responsible for the involvement of a nucleus. The formation of a three-dimensional crystal depends on the competition between 1) the free-energy gain due to the liquid–crystal phase transition and 2) the free-energy loss due to the unfavourable formation of the liquid–crystal interface. More specifically, the total change in free energy ΔG upon forming a spherical crystal with radius R equals[54, 55]:

$$\Delta G = \frac{4}{3}\pi R^3 \rho_S \Delta\mu + 4\pi R^2 \gamma, \tag{1.1}$$

where ρ_S is the number-density of the crystal, $\Delta\mu$ (< 0) is the difference in chemical potential of the solid and liquid phase and γ is the solid-liquid interfacial free energy density. As a result, the formation of a crystal only becomes favourable beyond a critical nucleus size where the free energy gain, *i.e.* the volume term that is proportional to R^3 compensates the interface free energy loss, *i.e.* the surface term that is proportional to R^2. Nuclei involved in 1D aggregation often originate from molecular phenomena, like the formation of a macrodipole that favours molecular association to an existing assembly over the formation of a new one. Alternatively,

structural rearrangements like the completion of the first turn of a helix can facilitate cooperative growth.[39]

Another difference between the formation of bulk crystals and 1D assemblies appears in the transition itself. The formation of bulk crystals is marked by a sharp first-order phase-transition. For example, above 0 °C no ice is formed at all, and below 0 °C the thermodynamic equilibrium prescribes that all water is the system is frozen. Also in spherical colloid systems, coexistence of colloids in the crystal and colloids in the fluid phase is only found in a narrow volume fraction regime.[53] In contrast, 1D assembly under equilibrium conditions results in the coexistence of assemblies and free monomers in a wide temperature or concentration regime. Even for highly cooperative assembly processes, both assemblies and free monomers are predicted well beyond the critical dimensionless concentration ($x_{tot} = K_e \cdot c_{tot} = 1$), as evidenced from the non-saturated degree of aggregation *vs.* x_{tot} shown in Figure 1.9b. Formally, 1D assembly processes approximate with increasing cooperativity (*i.e.* a diminishing equilibrium constant of nucleation K_n) a second-order phase-transition.[56–58]

The Gibbs free energy barrier that has to be overcome in order to form a spherical crystal of the critical nucleus size can be derived from eq. 1.1[54, 55]:

$$\Delta G_{crit} = \frac{16\pi}{3} \gamma^3 \Big/ \left(\rho_S \left|\Delta\mu\right|\right)^2 . \tag{1.2}$$

From this free energy barrier the crystal-nucleation rate I can be approximated via $I = \kappa \cdot \exp(-\Delta G_{crit}/k_B T)$ where κ equals the kinetic pre-factor and k_B is Boltzmann's constant. Further development of crystallization models to match theory and experimental results is still topic of ongoing research and involves for instance metastable pre-crystallization phases[59], critical density fluctuations[60] and supersaturation-dependent solid-liquid interface energies.[61] Nevertheless, the principle of crystal nucleation can be understood from the classical nucleation theory. At the critical transition (e.g. $T = 0$ °C for ice formation), the driving force for forming crystals, $\Delta\mu$, is zero. This implies an infinite free energy barrier that prohibits the formation of a nucleus under these conditions, even though the thermodynamic equilibrium dictates that removal of heat at 0 °C should result in ice formation. Indeed, it is well known that – under homogeneous conditions – supercooling is required in order to overcome the free energy barrier. The same holds for the formation of organic crystals for supersaturated solutions.[52] In contrast to this, the formation of a 1D assembly in solution at the critical temperature of elongation is not associated with an infinite free energy barrier.

1.4 Aim and outline of this thesis

The existence of multiple pathways towards different morphologies, as illustrated above, prompts us to develop new strategies to unravel and obtain control over the aggregation of π-conjugated material. Experiments and theories that are limited to equilibrium conditions are insufficient to understand the consequences of metastable pathways for the final outcome of the aggregation process. Metastable pathways can only be unravelled by kinetic experiments that start from the free monomer and probe the assembly process along the multiple pathways that can be followed. Furthermore, kinetic models are required to clarify the influence of these pathways on the overall aggregation process.

Therefore, the aim of this thesis is to develop experiments and models to 1) unravel, 2) understand and 3) obtain control over chemical assembly pathways.

To this end, in **Chapter 2** a π-conjugated molecular model system is introduced that assembles into 1D aggregates. Kinetic experiments reveal metastable assemblies that appear in the initial stages of the assembly process. By developing a kinetic model, inspired by models applied in the field of protein aggregation, the phenomenon of pathway complexity is unravelled. Different assembly pathways are competing for the molecular building block. As a consequence, entrapment of monomers in the metastable pathway hampers the formation of thermodynamically stable assemblies.

Since π-conjugated materials are often processed by manipulating the solvent conditions – *i.e.* going from good to poor solvent – we elaborate on the influence of solvent conditions on the stability and dynamics of the aggregates in **Chapter 3**. By combining experiments and simulations, it is demonstrated that the destabilizing effect of a good solvent results in a critical solvent composition that marks the onset of a nucleated aggregation process. Moreover, the rate of the aggregation process is the slowest close to this critical point. Since the rates and stabilities of different aggregation pathways are a critical aspect in the selection of the desired morphology, these insights provide an interesting approach to control the aggregation process by tuning the solvent conditions.

Based on the insights obtained into assembly pathways, **Chapter 4** introduces an engineering approach to circumvent spurious, metastable assembly pathways. The co-assembly of two π-conjugated enantiomers is studied both experimentally as well as via the development of a kinetic model. Detailed analyses of the metastable pathways that appear in the co-assembly process provide further insights to optimize self-assembly processes by avoiding the entrapment of material in metastable assemblies.

In **Chapter 5**, we analyse how different preparation protocols to assemble peptide-amphiphiles in water can result in different morphologies. Even though these peptide-amphiphiles differ in many respects from π-conjugated molecules, the kinetic insights derived from studies on those π-conjugated molecules apply to peptide-amphiphiles as well. It is shown that conditions temporarily encountered during the preparation of peptide-amphiphile

assemblies, for instance upon injecting the dissolved monomers into a poor solvent that induces assembly, have a large impact on the supramolecular structures obtained.

In **Chapter 6**, the self-assembly mechanisms are analysed for different supramolecular systems that cannot be described with regular one-dimensional assembly models under equilibrium control. Hence, novel assembly models are required to clarify the aggregation behaviour, and this chapter presents a couple of examples to demonstrate a model-driven *modus operandi* to unravel assembly processes. Furthermore, the kinetic models developed in previous chapters are revisited to analyse the effect of fragmentation and nucleation pathways. Finally, this chapter outlines how the kinetic insights into assembly pathways, derived from a combination of kinetic experiments and models, can pave the way towards model-driven engineering of more complex assemblies.

1.5 References

[1] Henson, Z. B.; Müllen, K.; Bazan G. C. *Nature Chem.* **2012**, *4*, 699.
[2] Beaujuge P. M.; Fréchet, J. M. J. *J. Am. Chem. Soc.* **2011**, *133*, 20009.
[3] Greatzel, M.; Janssen, R. A. J.; Mitzi, D. B.; Sargent, E. H. *Nature*, **2012**, *488*, 304.
[4] Hoeben, F. J. M.; Jonkheijm, P.; Meijer, E. W.; Schenning, A. P. H. J. *Chem. Rev.* **2005**, *105*, 1491.
[5] Mei, J.; Diao, Y.; Appleton, A. L.; Fang, L.; Bao, Z. *J. Am. Chem. Soc.* **2013**, *135*, 6724.
[6] Rand, B. P.; Cheyns, D.; Vasseur, K.; Giebink, N. C.; Mothy, S.; Yi, Y.; Coropceanu, V.; Beljonne, D.; Cornil, J.; Brédas, J.-L.; Genoe, J. *Adv. Funct. Mater.* **2012**, *22*, 2987.
[7] Aiyar, A. R.; Hong, J.-I.; Reichmanis, E. *Chem. Mater.* **2012**, *24*, 2845.
[8] Rahimi, K.; Botiz, I.; Stingelin, N.; Kayunkid, N.; Sommer, M.; Koch, F. P. V.; Nguyen, H.; Coulembier, O.; Dubois, P.; Brinkmann, M.; Reiter, G. *Angew. Chem. Int. Ed.* **2012**, *51*, 11131.
[9] Gentili, D.; Di Maria, F.; Liscio, F.; Ferlauto, L.; Leonardi, F.; Maini, L.; Gazzano, M.; Milita, S.; Barbarella, G.; Cavallini, M. *J. Mater. Chem.* **2012**, *22*, 20852.
[10] Treat, N. D.; Nekuda Malik, J. A.; Reid, O.; Yu, L.; Shuttle, C. G.; Rumbles, G.; Hawker, C. J.; Chabinyc, M. L.; Smith, P.; Stingelin, N. *Nat. Mater.*, **2013**, *12*, 628.
[11] Ajayaghosh, A.; Varghese, R.; Praveen, V. K.; Mahesh, S. *Angew. Chem. Int. Ed.* **2006**, *45*, 3261.
[12] Tidhar, Y.; Weissman, H.; Wolf, S. G.; Gulino, A.; Rybtchinski, B. *Chem. Eur. J.* **2011**, *17*, 6068.
[13] Wolffs, M.; Korevaar, P. A.; Jonkheijm, P.; Henze, O.; Feast, W. J.; Schenning, A. P. H. J.; Meijer, E. W. *Chem. Commun.* **2008**, 4613.
[14] Percec, V.; Sun, H.-J.; Leowanawat, P.; Peterca, M.; Graf, R.; Spiess, H. W.; Zeng, X.; Ungar, G.; Heiney, P. A. *J. Am. Chem. Soc.* **2013**, *135*, 4129.
[15] Lakhwani, G.; Meskers, S. C. J. *Macromolecules* **2009**, *42*, 4220.
[16] Wedl, B.; Resel, R.; Leising, G.; Kunert, B.; Salzmann, I.; Oehzelt, M.; Koch, N.; Vollmer, A.; Duhm, S.; Werzer, O.; Gbabode, G.; Sferrazza, M.; Geerts, Y. *RSC Adv.* **2012**, *2*, 4404.
[17] Gopal, A.; Varghese, R.; Ajayaghosh, A. *Chem. Asian J.* **2012**, *7*, 2061.
[18] Lin, Z.-Q.; Sun, P.-J.; Tay, Y.-Y.; Liang, J.; Liu, Y.; Shi, N.-E.; Xie, L.-H.; Yi, M.-D.; Qian, Y.; Fan, Q.-L.; Zhang, H.; Hng, H. H.; Ma, J.; Zhang, Q.; Huang, W. *ACS Nano* **2012**, *6*, 5309.
[19] Mei, J.; Graham, K. R.; Stalder, R.; Tiwari, S. P.; Cheun, H.; Shim, J.; Yoshio, M.; Nuckolls, C.; Kippelen, B.; Castellano, R. K.; Reynolds, J. R. *Chem. Mater.* **2011**, *23*, 2285.
[20] Yu, L.; Li, X.; Pavlica, E.; Koch, F. P. V.; Portale, G.; Da Silva, I.; Loth, M. A.; Anthony, J. E.; Smith, P.; Bratina, G.; Kjellander, B. K. C.; Bastiaansen, C. W. M.; Broer, D. J.; Gelinck, G. H.; Stingelin, N. *Chem. Mater.* **2013**, *25*, 1823.
[21] Vakhshouri, K.; Gomez, E. D. *Macromol. Rapid Commun.* **2012**, *33*, 2133.
[22] Dang, M. T.; Hirsch, L.; Wantz, G.; Wuest, J. D. *Chem. Rev.* **2013**, *113*, 3734.
[23] Yao, Y.; Dong, H.; Hu, W. *Polym. Chem.* **2013**, *4*, 5197.

[24] www.pv-tech.org/news/nrel_validates_konarkas_8.3_power_plastic_efficiency_record.
[25] Bouman, M. M.; Meijer, E. W. *Adv. Mater.* **1995**, *7*, 385.
[26] Satrijo, A.; Meskers, S. C. J.; Swager, T. M. *J. Am. Chem. Soc.* **2006**, *128*, 9030.
[27] Satrijo, A.; Swager, T. M. *Macromolecules* **2005**, *38*, 4054.
[28] Tevis, I. D.; Palmer, L. C.; Herman, D. J.; Murray, I. P.; Stone, D. A.; Stupp, S. I. *J. Am. Chem. Soc.* **2011**, *133*, 16486.
[29] Giri, G.; Verploegen, E.; Mannsfeld, S. C. B.; Atahan-Evrenk, S.; Kim, D. H.; Lee, S. Y.; Becerril, H. A.; Aspuru-Guzik, A.; Toney, M. F.; Bao, Z. *Nature* **2011**, *480*, 504.
[30] Hill, J. P.; Jin, W.; Kosaka, A.; Fukushima, T.; Ichihara, H.; Shimomura, T.; Ito, K.; Hashizume, T.; Ishii, N.; Aida, T. *Science* **2004**, *304*, 1481.
[31] Jin, W.; Fukushima, T.; Niki, M.; Kosaka, A.; Ishii, N.; Aida, T. *Proc. Natl. Acad. Sci. USA* **2005**, *102*, 10801.
[32] Yamamoto, T.; Fukushima, T.; Yamamoto, Y.; Kosaka, A.; Jin, W.; Ishii, N.; Aida, T. *J. Am. Chem. Soc.* **2006**, *128*, 14337.
[33] Würthner, F.; Yao, S.; Beginn, U. *Angew. Chem. Int. Ed.* **2003**, *42*, 3247.
[34] Lohr, A.; Lysetska, M.; Würthner, F. *Angew. Chem. Int. Ed.* **2005**, *44*, 5071.
[35] Lohr, A.; Würthner, F. *Angew. Chem. Int. Ed.* **2008**, *47*, 1232.
[36] Ihn, K. J.; Moulton, J.; Smith, P. *J. Polym. Sci., Part B: Polym. Phys.* **1993**, *31*, 735.
[37] Liu, J.; Arif, M.; Zou, J.; Khondaker, S. I.; Zhai, L. *Macromolecules* **2009**, *42*, 9390.
[38] Takizawa, Y.; Shimomura, T.; Miura, T. *J. Phys. Chem. B* **2013**, *117*, 6282.
[39] De Greef, T. F. A.; Smulders, M. M. J.; Wolffs, M.; Schenning. A. P. H. J.; Sijbesma, R. P.; Meijer, E. W. *Chem. Rev.* **2009**, *109*, 5687.
[40] Zhao, D.; Moore, J. S. *Org. Biomol. Chem.* **2003**, *1*, 3471.
[41] Goldstein, R. F.; Stryer, L. *Biophys. J.* **1986**, *50*, 583.
[42] Frieden, C. *Protein Sci.* **2007**, *16*, 2334.
[43] Roberts, C. J. *Biotechnol. Bioeng.* **2007**, *98*, 927.
[44] Powers, E. T.; Powers, D. L. *Biophys. J.* **2006**, *91*, 122.
[45] Morris, A. M.; Watzky, M. A.; Agar, J. N.; Finke, R. G. *Biochemistry* **2008**, *47*, 2413.
[46] Morris, A. M.; Watzky, M. A.; Finke, R. G. *Biochim. Biophys. Acta* **2009**, *1794*, 375.
[47] Kodaka, M. *Biophys. Chem.* **2004**, *109*, 325.
[48] Watzky, M. A.; Finke, R. G. *J. Am. Chem. Soc.* **1997**, *119*, 10382.
[49] Xue, W.-F.; Homans, S. W.; Radford, S. E. *Proc. Natl. Acad. Sci. USA* **2008**, *105*, 8926.
[50] Bishop, M. F.; Ferrone, F. A. *Biophys. J.* **1984**, *46*, 631.
[51] Ferrone, F. A. *Methods Enzymol.* **1999**, *309*, 256.
[52] Davey, R. J.; Schroeder, S. L. M.; Ter Horst, J. H. *Angew. Chem. Int. Ed.* **2013**, *52*, 2166.
[53] Anderson, V. J.; Lekkerkerker, H. N. W. *Nature* **2002**, *416*, 811.
[54] Kawasaki, T.; Tanaka, H. *Proc. Natl. Acad. Sci. USA* **2010**, *107*, 14036.
[55] Auer, S.; Frenkel, D. *Nature* **2001**, *409*, 1020.
[56] Percec, V.; Ungar, G.; Peterca, M. *Science* **2006**, *313*, 55.
[57] Douglas, J. F.; Dudowicz, J.; Freed, K. F. *J. Chem. Phys.* **2008**, *128*, 224901.
[58] Dudowicz, J.; Freed, K. F.; Douglas, J. F. *J. Chem. Phys.* **2000**, *113*, 434.
[59] Ten Wolde, P. R.; Frenkel, D. *Phys. Chem. Chem. Phys.* **1999**, *1*, 2191.
[60] Ten Wolde, P. R.; Frenkel, D. *Science* **1997**, *277*, 1975.
[61] Auer, S.; Frenkel, D. *Nature* **2001**, *413*, 711.

2

Pathway complexity in one-dimensional assembly

Abstract: The assembly pathways of a chiral, π-conjugated oligo(*p*-phenylene vinylene) derivative into one-dimensional helical assemblies are studied. Experiments under kinetic control reveal kinetically favoured, metastable helices that are formed fast but then transform into the equilibrium structures that have the opposite helical twist. Quantitative insights into the kinetic experiments are obtained by developing a kinetic model, inspired on theories developed in the field of protein aggregation. The model describes in parallel both the metastable as well as the thermodynamically stable pathway as a cooperative one-dimensional assembly process. Simulations reveal that, due to the competition of these pathways for the same monomer, at high concentration the metastable helices sequester the free monomer and thereby hamper the formation of the stable assemblies. As a result of this pathway complexity, the overall assembly rate of these equilibrium structures decreases upon increasing the concentration: a counterintuitive phenomenon that is also observed experimentally. Based on the insights, finally a two-step non-covalent synthetic methodology is developed in which a chiral auxiliary is temporarily attached to the chiral monomers. Upon attachment of the auxiliary, the assemblies can be forced completely down the kinetically favoured pathway so that, on removal of the auxiliary, metastable helices are obtained exclusively.

Part of this work has been published as:

"Pathway complexity in supramolecular polymerization" P. A. Korevaar, S. J. George, A. J. Markvoort, M. M. J. Smulders, P. A. J. Hilbers, A. P. H. J. Schenning, T. F. A. de Greef, E. W. Meijer, *Nature* **2012**, *481*, 492–496.

2.1 Introduction

The performance of artificial self-assembled systems in functional materials is highly dependent on the molecular organization. This holds for the previously introduced π-conjugated materials, but also for supramolecular polymers with applications in self-healing or bioactive materials.[1] However, most studies focus on structural and functional characteristics of these materials. In-depth mechanistic studies on the formation of one-dimensional supramolecular polymers are rare and in most cases limited to a thermodynamic analysis.[2] In sharp contrast, fundamental insights into the aggregation of protein fibrils have reached a high level of sophistication. Detailed understanding of these processes has emerged from a combination of kinetic and thermodynamic studies. Over the last fifty years, the experimental data on a wide variety of different protein aggregations have been analysed by applying increasingly complex kinetic models. Nowadays, it is well established that most protein aggregations occur via a homogeneous primary nucleation mechanism. Here, the formation of high-energy oligomers (*i.e.* nuclei) from soluble proteins acts as a bottleneck that limits the rate of fibril formation.[3–5] In addition, secondary nucleation mechanisms, either occurring via fragmentation of filaments or surface catalysed growth, have been identified and shown to have a dominant influence on the growth of protein fibrils.[6–9]

Next to the insights into protein fibrillization along a single pathway ("on-pathway"), recent theoretical and experimental efforts in this field have shown the effect of pathway complexity on the growth of amyloidal protein fibrils.[10–13] Pathway complexity is a result of a multitude of different assembly intermediates, constituting both on- as well as off-pathway aggregates. These aggregates are competing for the free monomer (*i.e.* the soluble protein) and thereby exert their influence on the equilibrium fibrils. Due to entrapment of monomers into metastable, off-pathway aggregates that are formed fast, the appearance of equilibrium fibrils is even further slowed down.[10, 13] The existence of multiple aggregation pathways, *i.e.* pathway complexity, is also recognized in non-natural systems, as discussed in the previous chapter for π-conjugated molecules. Recent studies on block-copolymer micelles have also shown that these self-assembled structures can controllably be forced down specific aggregation pathways, resulting in kinetically trapped structures.[14] However, more quantitative insights into the phenomenon of pathway complexity are a prerequisite to control one-dimensional assembly processes that involve multiple aggregation pathways. This chapter discloses the first step to describe such a kinetic analysis in detail, by taking advantage of kinetic models that are developed in the field of protein aggregation. First, a molecular model system is introduced that assembles into one-dimensional helices. Then, kinetic experiments are discussed that reveal the presence of a kinetically favoured metastable assembly which appears quickly but then transforms into the thermodynamically favoured form. Quantitative insights into the kinetic experiments are obtained by developing a kinetic model that involves two parallel assembly pathways: one towards the metastable form and one to the thermodynamically favoured form. Based on these insights, a non-covalent multi-step synthesis is developed that enables to exclusively select the metastable pathway.

2.2 Model system oligo(*p*-phenylene vinylene)

As a model system to unravel the occurrence of multiple assembly pathways, *S*-chiral oligo(*p*-phenylene vinylene) (SOPV, Fig 2.1a) is used.[15] This molecule consists of a π-conjugated oligo(*p*-phenylene vinylene) with chiral side chains, capped on one end by a tridodecylbenzene and on the other end by an ureidotriazine moiety. Because of the large π-system, OPV can easily be probed in diluted solution via spectroscopic techniques in the UV/Vis regime. Moreover, the absence of turbidity or precipitation makes it possible to follow the entire aggregation process. The assembly pathway is initiated by self-complementary, fourfold hydrogen bonding, and in apolar solvents the resulting hydrogen-bonded OPV dimers aggregate into long one-dimensional helices (Fig 2.1b). Due to the chiral side groups, one helicity is energetically favoured over the other and hence the formation of these helices in solution can be probed with CD spectroscopy.[16, 17]

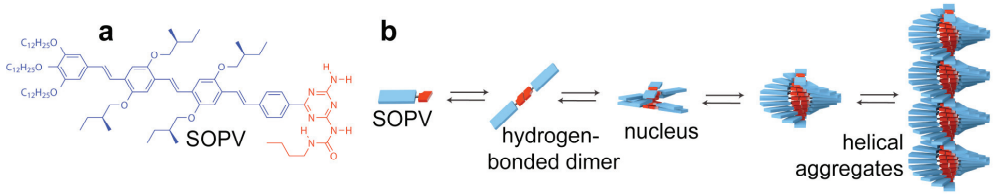

Figure 2.1 | Cooperative assembly of model system SOPV. (a) Molecular structure of SOPV (b) SOPV forms a hydrogen-bonded dimer that subsequently forms a disordered nucleus prior to elongation into helical stacks.

To characterize the assembly mechanism of SOPV in detail, temperature-dependent studies on OPV in apolar, aliphatic solvents have been conducted by Jonkheijm *et al*.[18] At high temperatures, no CD effect is observed for a solution of SOPV in methylcyclohexane (MCH). Also the UV/Vis and fluorescence spectra are comparable to those acquired in good solvent chloroform, indicative for molecularly dissolved OPV molecules and hydrogen-bonded dimers. At low temperatures however, CD shows a bisignated, negative Cotton effect corresponding to left-handed, *M*-type helices (Fig 2.2a). Concomitantly, UV/Vis reveals a shoulder at 490 nm. Following CD at the wavelength where the maximum intensity can be observed, 466 nm, upon cooling slowly with a temperature ramp of 60 °C/hr, reveals a critical temperature at which the formation of helical assemblies starts (Fig 2.2b). This indicates a cooperative growth process. However, the shoulder in UV/Vis at 490 nm appears gradually upon cooling, prior to the critical transition in CD. Combining these spectroscopic data suggests that upon cooling initially small, disordered aggregates are formed. These small species result in a shoulder in UV/Vis at 490 nm but are CD silent as they have no helical organization. Only after the formation of a nucleus that contains multiple (*i.e.* more than two) hydrogen-bonded dimers, a helical twist is introduced in the assembly and further elongation takes place more favourably (Fig 2.1b).

The gradual appearance of pre-nucleus oligomers above the critical elongation temperature can be rationalized by simulations with the equilibrium model that is introduced in Chapter 1. In this cooperative equilibrium model, developed by Goldstein and Stryer[19], monomer addition to pre-nucleus oligomers is described with an equilibrium constant of nucleation K_n that is smaller compared to the equilibrium constant of elongation K_e, and this difference is characterized by the cooperativity $\sigma = K_n/K_e$ (Fig 2.2d). It should be mentioned that in this analysis, the hydrogen-bonded SOPV dimer is considered as the building block, *i.e.* the monomer, of the one-dimensional aggregation process. By using a Van 't Hoff relation for both K_n and K_e, both the fraction of monomers assembled in species larger than the free monomer ($i > 1$), as well as the fraction of monomers assembled in species larger than the nucleus ($i > n$), can be reconstructed as a function of temperature (Fig 2.2c, see details in paragraph 2.7). Simulations reveal a gradual increase in the amount of assembled monomers ($i > 1$) upon decreasing the temperature. Assembly into elongated stacks ($i > n$) however only occurs at lower temperatures compared to the formation of pre-nucleus oligomers. This corroborates the hypothesis that the transition in UV/Vis at 490 nm can be attributed to the overall assembly of the SOPV monomers, *i.e.* $i > 1$, whereas the fraction of aggregates of all species larger than the nucleus in the simulations can be attributed to the CD effect. Moreover, the onset of the simulated temperature-dependent elongation curves becomes sharper when a larger nucleus size is applied. This phenomenon led Goldstein and Stryer to define the cumulative cooperativity $\omega = \sigma^{n-1}$, a parameter that represents the effect that the free energy barrier required to form the nucleus becomes larger when the nucleus size increases. Hence, even though the value of σ at $T = 50$ °C equals only 0.44 in the simulation, a sharp transition can be observed for larger values of n.

The exact reason for cooperativity in the OPV system has not been unravelled completely yet. It has been suggested that the cooperativity is related to the unfavourable completion of the first helical turn, that involves, based on a rotation angle between adjacent monomers of 6° to 12°, 15 to 30 monomers.[18] Alternatively, the cooperativity has been attributed to the unfavourable planarization of the SOPV molecule, *i.e.* rotation of the ureidotriazine unit with respect to the oligo(*p*-phenylene vinylene) unit, which penalizes the start of the aggregation process.[2] More recently however, Kulkarni *et al*. suggested, based on preliminary quantum chemical calculations, that the tridodecylbenzene wedges in the periphery of the helical stacks form weak C—H···O hydrogen bonds between two OPV molecules.[20] Previously, it has been shown that hydrogen-bonding within helical benzene-tricarboxamide (BTA) stacks results in the formation of a macro-dipole along the direction of the stack.[21] As a result, the association of a BTA monomer via three-fold hydrogen bonding to a long stack that has developed a macro-dipole becomes more favourable compared to association of a free BTA monomer to another monomer. Hence, the nucleation of a new stack becomes unfavourable compared to elongation of an existing stack. In a similar fashion, the C—H···O hydrogen bonds can give rise to a macro-dipole along the direction of a helical SOPV stack, and a free SOPV hydrogen-bonded dimer prefers to associate to an elongated stack rather than nucleating a new assembly that lacks a macro-dipole.

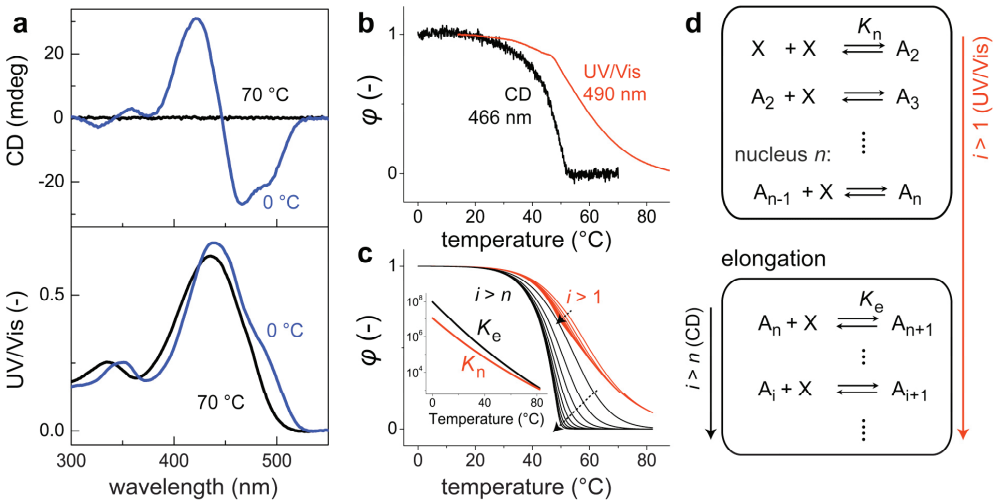

Figure 2.2 | Analysis of cooperative assembly of SOPV under equilibrium conditions. (a) CD (top) and UV/Vis (bottom) spectra of SOPV in methylcyclohexane (MCH, 100 μM) in the molecularly dissolved state (70 °C) and at the assembled state (0 °C). (b) Temperature-dependent degree of aggregation φ, derived from transitions in CD (466 nm) and UV/Vis (490 nm) acquired upon cooling SOPV in MCH (46 μM) with a temperature ramp of 60 °C/hr. (c) The temperature-dependent assembly of monomers in species larger than the monomer ($i > 1$) and in species larger than the nucleus ($i > n$) is simulated with the thermodynamic equilibrium model (d), using temperature-dependent equilibrium constants K_n and K_e as depicted in the inset of (c): the nucleus size increases from $n = 2$ up to $n = 10$ along the dashed arrows.

2.3 Kinetic experiments reveal a metastable pathway

In order to unravel the influence of kinetically controlled pathways towards metastable assemblies, the assembly of SOPV is examined under non-equilibrium conditions. Rapid quenching of SOPV from the molecularly dissolved state at 70 °C to 0 °C yields a mixture of *M*-SOPV and aggregates with opposite helicity, as evidenced by the opposite sign of the bisignated Cotton effect (Fig 2.3a). At 25 °C, these right-handed *P*-type aggregates (*P*-SOPV) slowly convert into thermodynamically stable *M*-SOPV aggregates (Fig 2.3b). The observation of metastable *P*-SOPV aggregates indicates that the assembly of SOPV involves two different aggregation pathways which we term the on-pathway (*M*) and off-pathway (*P*, Fig 2.3c).

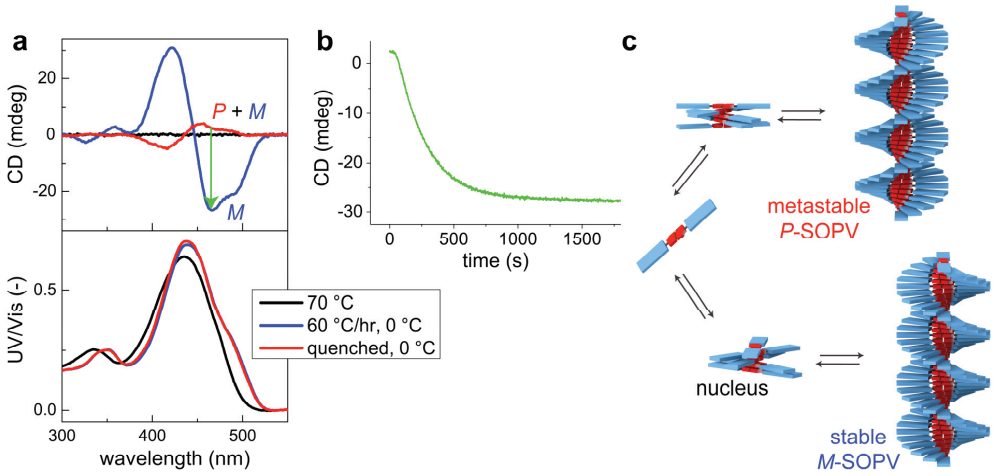

Figure 2.3 | Pathway complexity in the self-assembly of SOPV. (a) CD (top) and UV/Vis (bottom) spectra of SOPV in MCH (100 μM) in the disassembled state at 70 °C, thermodynamically stable *M*-SOPV and metastable *P*-SOPV (+ *M*-SOPV) at 0 °C. (b) Conversion of metastable *P*-SOPV to *M*-SOPV, probed in CD (466 nm) at 25 °C. (c) Schematic representation of the two nucleated assembly pathways of SOPV towards metastable *P*-SOPV (off-pathway) and thermodynamically stable *M*-SOPV (on-pathway).

To study the aggregation mechanism of SOPV and quantify the self-assembly pathways under kinetic control, stopped-flow experiments are conducted in which a concentrated solution of molecularly dissolved SOPV in chloroform is mixed with an excess of methylcyclohexane (MCH) to initiate self-assembly. The subsequent formation of helical SOPV aggregated in MCH is probed using CD spectroscopy. The kinetic experiments are conducted at 20 °C and 35 °C, with different concentrations of SOPV. At 20 °C and the lowest SOPV concentrations, the rate of aggregate formation initially increases with time, characteristic of a lag phase (Fig 2.4ac). The time-dependent CD signal is always negative under these conditions, suggesting the direct formation of thermodynamically stable on-pathway *M*-SOPV aggregates. However, at higher concentrations (≥9 μM) a positive CD signal appears in the initial stages of the assembly process and then develops into a negative CD signal at later times. This suggests the initial formation of off-pathway *P*-SOPV aggregates that then convert into thermodynamically stable *M*-SOPV aggregates. Remarkably, the time at which 50% of the

aggregation process is completed (*t*-50) is longer at 15 μM than at 10 μM (Fig 2.4d). Analogous kinetic studies at 35 °C also reveal the presence of a lag phase in experiments at the lowest concentrations (Fig 2.4be) and an inverted dependence of *t*-50 on concentration, although the shortest *t*-50 time shifts to a higher SOPV concentration (20 μM; Fig 2.4d).

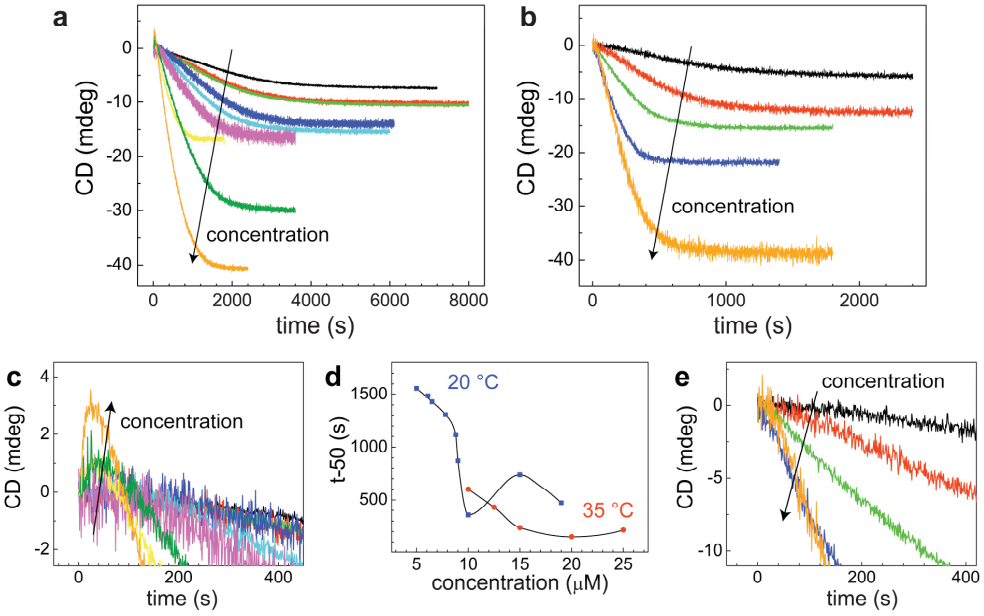

Figure 2.4 | Stopped-flow experiments on self-assembly of SOPV. (a) Concentration-dependent kinetics at 20 °C. SOPV concentrations (arrow shows increasing concentration) are colour-coded as follows: 5 μM (black), 6.1 μM (red), 6.5 μM (light green), 7.8 μM (dark blue), 8.7 μM (light blue), 9 μM (pink), 10 μM (yellow), 15 μM (dark green) and 19 μM (orange). (b) Concentration-dependent kinetics at 35 °C. SOPV concentrations are 10 μM (black), 12.5 μM (red), 15 μM (green), 20 μM (blue) and 25 μM (orange). (c) Zoom in for initial stages of growth process studied at 20 °C in panel a. (d) Time at which 50% of final CD intensity is reached (*t*-50) versus concentration at 20 °C and 35 °C. The lines serve to guide the eye. (e) Zoom in for initial stages of growth process studied at 35 °C in panel c.

To investigate if the off-pathway towards *P*-SOPV involves a nucleation step, similar to the on-pathway, SOPV in MCH is quenched from different temperatures to 0 °C in an ice bath (Fig 2.5ab). Only the CD spectrum that is obtained upon quenching from 30 °C to 0 °C coincides with the CD spectrum acquired at 0 °C under equilibrium conditions, *i.e.* after cooling with a cooling rate of 60 °C/hr. The CD spectra that are obtained upon quenching from higher temperatures (45 °C, 40 °C, 38 °C and 35 °C) to 0 °C differ from the equilibrium CD spectrum at 0 °C. However, the corresponding UV/Vis spectra indicate a fully aggregated state for the quenched solutions as well. Therefore, the lower intensity of the CD spectra obtained upon quenching from higher temperatures indicate the formation of a distribution of *P*-SOPV and *M*-SOPV helices.

The CD spectra that are acquired upon quenching can be described by a linear combination of a pure *M*-SOPV spectrum and a pure *P*-SOPV spectrum (Fig 2.5c). A pure *P*-SOPV CD spectrum, *i.e.* a CD spectrum of a solution that contains solely *P*-type helices, is obtained via a procedure that is elaborated in paragraph 2.5. The linear combination of *M*- and *P*-type CD spectra allows determining the fraction of monomers present in *M*- and *P*-type helices for the different CD spectra that are obtained upon quenching. As shown in Figure 2.5d, only quenching from higher temperatures (≥ 35 °C) yields *P*-SOPV helices at 0 °C. This means that no *P*-SOPV is obtained upon quenching from 30 °C to 0 °C. However, the fraction of free SOPV monomer that is present under equilibrium conditions prior to the quenching step (derived from the corresponding CD spectra assuming $\varphi_{\text{monomer}} = 1 - \varphi_{\text{helical aggregate}}$) shows that also at 30 °C SOPV monomers are available to form *P*-SOPV aggregates upon quenching. This suggests that a critical free monomer concentration is involved in the self-assembly of metastable *P*-SOPV aggregates, which is a hallmark of a cooperative growth mechanism.

Furthermore, previous studies revealed that the cooperative formation of long helical *M*-SOPV assemblies is reflected in changes of the extinction coefficient at 335 nm.[18] The temperature-dependent UV/Vis spectra in Figure 2.2a clearly show a red shift upon cooling in this wavelength regime, and by detailed temperature-dependent UV/Vis experiments it has been demonstrated that this transition at 335 nm coincides with the critical temperature of elongation in CD, which marks the onset of the formation of long helical assemblies. Hence, the coinciding UV/Vis spectra of *P*- and *M*-SOPV at 0 °C, as shown in Figure 2.3a, corroborate that the metastable *P*-SOPV assemblies are long helices formed by a cooperative mechanism.

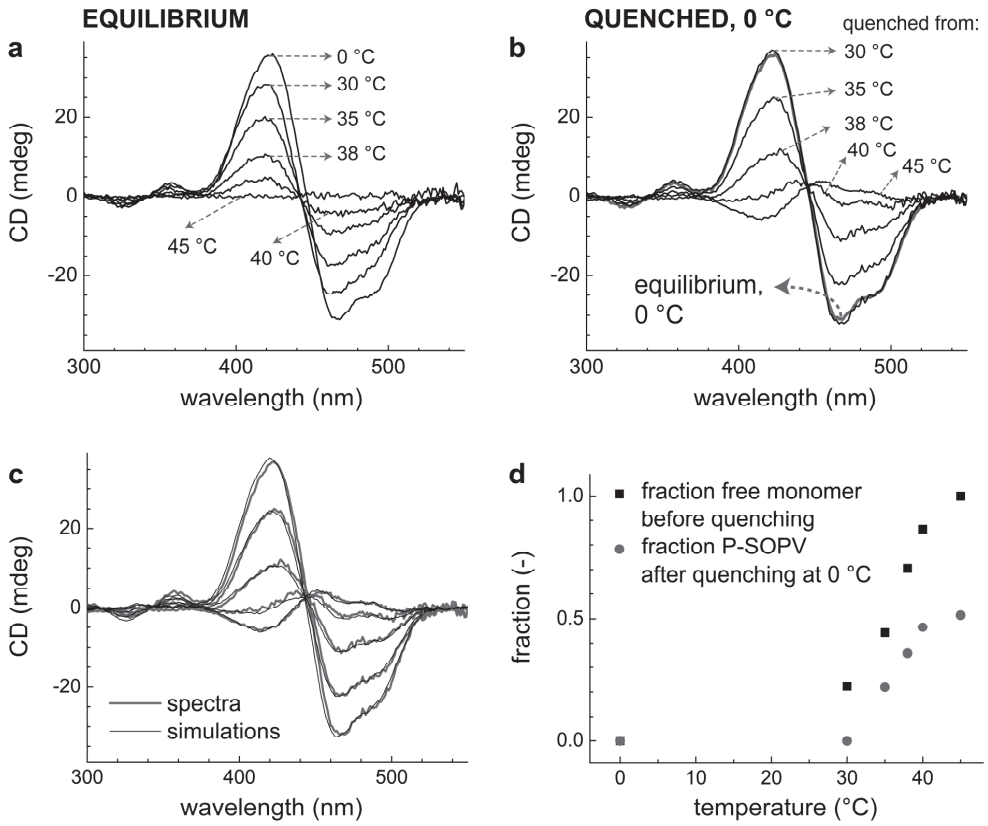

Figure 2.5 | Nucleation in off-pathway assembly revealed by quenching experiments. (a) CD spectra of SOPV at different temperatures under equilibrium conditions (MCH, 13 μM). (b) Corresponding CD spectra acquired after quenching SOPV from different temperatures to 0 °C, compared to the CD spectrum of SOPV at 0 °C under equilibrium conditions. (c) Simulations of linear combinations of the CD spectra of pure *P*-SOPV and *M*-SOPV helices to CD spectra acquired after quenching SOPV from different temperatures to 0 °C. (d) Fraction of free SOPV monomer present under equilibrium conditions before quenching, and fraction of *P*-SOPV present after quenching at 0 °C. The fraction of material present in *P*-SOPV after quenching is evaluated from the ratio by which *P*- and *M*-type CD spectra are combined to describe the respective CD spectrum obtained at 0 °C, as in pane c.

2.4 Kinetic model of two parallel assembly pathways

To rationalize the experimental aggregation kinetics, models known in the field of protein fibrillization[5, 10] are extended by incorporating two competing, nucleated assembly pathways, in which pre-nucleus oligomers (oligomer aggregates below the critical nucleation size) and helical aggregates change size through monomer association and dissociation (Fig 2.6a). For the *M*-SOPV aggregates, non-helical pre-nucleus oligomers change size with rate constants for association and dissociation of a and b, respectively. Once the critical nucleus (with size n) is reached, the helical aggregates are in the elongation regime and change size through monomer association with the same rate constant a, while dissociation proceeds with rate constant c. The steady-state concentration of the aggregates in the nucleation phase is determined by the nucleation equilibrium constant $K_n = a/b$, while in the elongation phase it is determined by the elongation equilibrium constant $K_e = a/c$. The nucleated growth of off-pathway *P*-SOPV aggregates is described analogously, with nucleus size n^*, rate constants a^*, b^* and c^*, and equilibrium constants K_n^* and K_e^*. An essential model assumption is that the transition from metastable to thermodynamically stable aggregates occurs via disassembly of *P*-SOPV aggregates and subsequent growth of *M*-SOPV aggregates. This is justified by the high helix reversal penalty of 8.1 k_BT obtained by "majority rules" experiments, which rules out intrastack stereomutation as an alternative transition mechanism.

Although only monomer association and dissociation are taken into account in the model, the number of association and dissociation steps is in principle infinite. In previous kinetic models the required number of rate equations has been reduced either by truncating at a certain polymer length, or by using a lumped set of reaction-rate equations under the assumption of irreversible monomer association to the nucleus. A drawback of truncating the rate equations is that the concentration of high-molecular species is assumed to be zero, which is unrealistic in a cooperative growth mechanism. A lumped set of reaction-rate equations successfully describes the formation of a single type of aggregate.[5] However, if off-pathway aggregation is included, the assumption of irreversible monomer association to the nucleus is unrealistic as off-pathway aggregates have to disassemble in order for the thermodynamically stable aggregates to grow in length. An insightful model analysed by Powers and Powers[10] describes the off-pathway aggregation as an isodesmic growth process in which all species are assumed to be in fast (pre)equilibrium with the free monomer. The cooperative on-pathway reactions are described by a lumped set of rate equations under the assumption of irreversible monomer addition. Inspired by their approach, here an alternative approach is introduced to describe competition between two cooperative aggregation pathways. All aggregates up to a certain length N, with N much larger than the nucleus sizes (n and n^*) are described explicitly. The aggregates with size larger than N are described per type together (*i.e. P*-SOPV and *M*-SOPV) as fibrils by considering both the fibril number concentration, that is the total concentration of species larger than N monomers, as well as the fibril mass concentration, that is the total concentration of monomers assembled in species larger than N monomers. As demonstrated in paragraph 2.7, by assuming that for $i > N$, $[X_{i+1}] = \alpha \cdot [X_i]$, the required number of differential equations can be reduced from infinity to $2 \cdot (N+2)$.

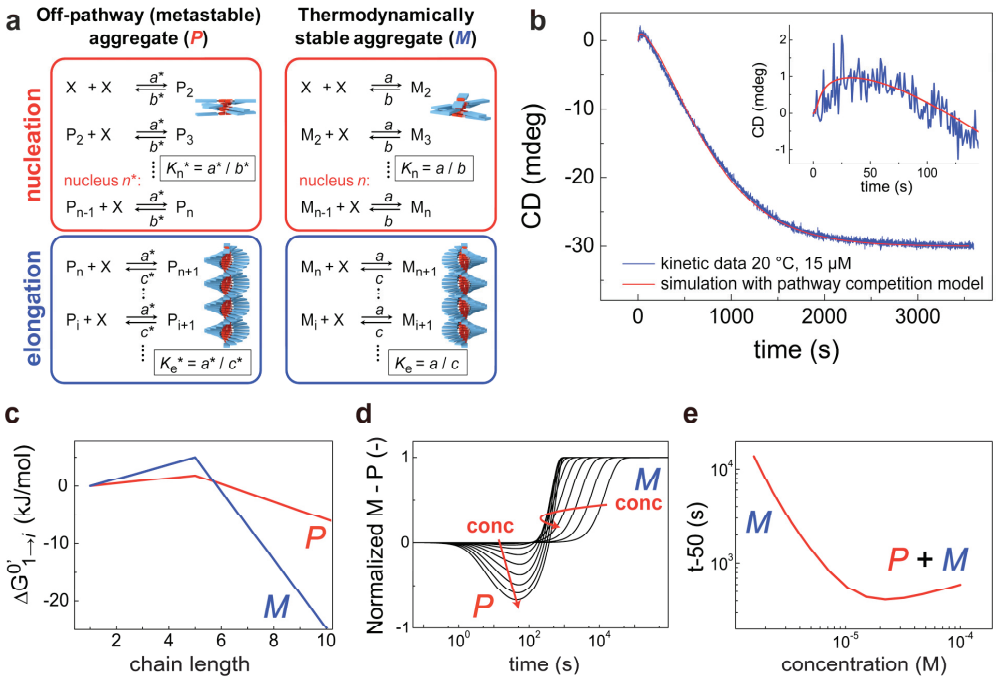

Figure 2.6 | **Analysis of aggregation pathway competition with kinetic model.** (a) Schematic representation of reversible kinetic model for nucleated aggregation, including a metastable off-pathway (*P*) and a thermodynamically stable on-pathway (*M*) competing for free monomer (*X*). (b) Kinetic data on the self-assembly of SOPV simulated with pathway competition model. The inset to b shows a zoom in for the initial stages of the growth process. (c) Calculated Gibbs free energy diagram for formation of *P*- and *M*-SOPV. (d) Concentration-dependent simulation of kinetics with pathway competition model. (e) *t*-50 versus SOPV hydrogen-bonded dimer concentration for concentration-dependent simulated kinetics. (Parameters: $n = n^* = 5$; $a = 2.9 \cdot 10^4$ $M^{-1}s^{-1}$; $K_e = 1.52 \cdot 10^6$ M^{-1}; $K_n/K_e = 0.0526$; $K_n^*/K_n = 1.38$; $K_e^*/K_e = 0.164$ and $a^*/a = 3.79$, $N = 100$).

Simulations with the two-pathway kinetic model show that off-pathway *P*-SOPV aggregates only appear in the initial stages of the self-assembly process if sufficient monomers are present and *P*-SOPV formation is kinetically favoured over that of *M*-SOPV. Specifically, the total monomer concentration (c_{tot}) has to exceed the critical concentration of *P*-SOPV ($c_{tot} > K_e^{*-1}$), which depends on the elongation equilibrium constant of this species. Moreover, the initial formation of *P*-SOPV is kinetically favoured when the forward rate constant of nucleation and elongation is larger for the off-pathway aggregates ($a^* > a$) or if the pre-nucleus oligomers of *P*-SOPV are kinetically more stable ($K_n^* > K_n$, or $a^*/b^* > a/b$) (Fig 2.7ab). As a result, off-pathway *P*-SOPV aggregates can only self-assemble at high concentrations and low temperatures (high K_e^*), as is observed experimentally (Fig 2.4). With $a^* > a$, the kinetic model successfully describes the experimental kinetic data, including the initial formation of *P*-SOPV (Fig 2.6b). The calculated Gibbs free energy diagram reveals that the *P*-SOPV nucleus is thermodynamically less unstable than the *M*-SOPV nucleus (that is, $K_n^* > K_n$), whereas *M*-

SOPV aggregates are more stable in the elongation phase (Fig 2.6c). Kinetic studies on protein fibrillation have shown that for the initial stages of homogeneously nucleated aggregation involving a thermodynamically unstable nucleus, the conversion to the stable product is proportional to time squared, t^2. In the experiments with the lowest SOPV concentrations, the changes of the CD signal in the lag phases indeed can be described as being proportional to t^2, demonstrating homogeneous nucleation in the aggregation of SOPV (Fig 2.7c).

To corroborate the proposed involvement of two aggregation pathways, the concentration dependence of the kinetic data is further analysed. The changes in the *t*-50 values with concentration, in particular the inverted dependence of *t*-50 on concentration as shown in Figure 2.4d, can only be rationalized by taking off-pathway aggregation into account (Fig 2.6de). The relatively large amount of metastable *P*-type aggregates formed at higher concentrations sequesters monomers and lowers their solution concentration, thereby hampering the formation of the thermodynamically stable *M*-type aggregates. The simulations however do not show a further decrease of *t*-50 at higher concentrations with reasonable model parameters. Because our model only considers monomer addition and dissociation, oligomer reactions and fragmentation – which become more important at higher concentrations – may explain this difference between simulated and observed behaviour. Simulations exploring the effect of temperature show that the aggregation rate gets faster (that is, *t*-50 values get lower) on increasing temperature. Furthermore, the maximum in the aggregation rate shifts to higher concentrations, as is observed experimentally (Fig 2.4d, Fig 2.7d). This effect can be rationalized by the fact that K_e^* decreases upon increasing temperature. Hence, the critical concentration c_{tot}^* (= $1/K_e^*$) at which the metastable *P*-type helices appear and retard the assembly of *M*-type helices increases with temperature.

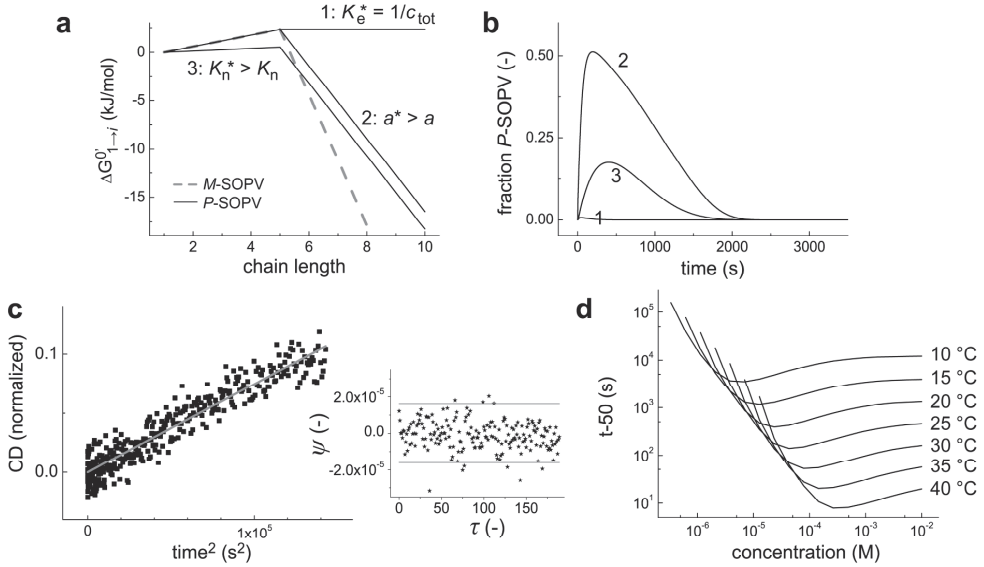

Figure 2.7 | Further details on the aggregation of *P*- and *M*-SOPV. Simulations with pathway competition model for (*1*) $K_e^* = 1/c_{tot}$ ($K_n^*/K_n = 1$; $K_e^*/K_e = 0.065$; $a^*/a = 1$); (2) $a^* > a$ ($K_n^*/K_n = 1$; $K_e^*/K_e = 0.3$; $a^*/a = 10$); (*3*) $K_n^* > K_n$ ($K_n^*/K_n = 1.2$; $K_e^*/K_e = 0.3$; $a^*/a = 1$). (a) Calculated Gibbs free energy diagram for formation of *P*- and *M*-SOPV. (b) Fraction of *P*-SOPV formed *vs.* time, calculated with $K_e^* = 1/c_{tot}$ (1), $a^* > a$ (2) and $K_n^* > K_n$ (3, *vide supra*). Significant amounts of metastable *P*-SOPV are only formed if $K_e^* > 1/c_{tot}$, if $a^* > a$ or $K_n^* > K_n$. (c) Normalized CD *vs*. time squared for initial stages (up to 10% conversion) of aggregation of SOPV (20 °C, 6.5 μM). The linear relation indicates a homogeneous nucleated mechanism. The inset shows the autocorrelation $\psi(\tau)$ of residual sequence (data – fit) estimated via $\psi(\tau) = \frac{1}{L}\sum_{i=1}^{L}\xi(i)\xi(i+\tau)$, where L represents half of the length of the dataset and ξ the residual sequence. The grey lines indicate the boundaries of the 95% confidence interval as computed via $\pm 1.96 \cdot \sigma_\xi^2 \cdot L^{-0.5}$, where σ_ξ^2 is the estimated variance of the residual. 95% of the autocorrelation estimates are in between the boundaries. (d) Temperature-dependent simulations with pathway competition model show that the optimum rate shifts to higher concentrations and lower *t*-50 values upon increasing temperature, as is observed experimentally.

2.5 Select the metastable pathway with an auxiliary

The discovery of the two different assembly pathways, producing structurally different aggregates, encouraged us to attempt to direct the assembly of SOPV towards metastable products. To force the assembly of SOPV into exclusively *P*-type aggregates instead of the mixture obtained upon fast cooling (Fig 2.3a), a two-step non-covalent synthetic method has been developed in our group by dr. Subi George (Fig 2.8ab). A chiral auxiliary is used to direct the assembly so that, upon removal of the auxiliary, the thermodynamically unstable *P*-type aggregates are obtained. In the first step, *S*-chiral dibenzoyl tartaric acid (DTA) is used to dictate its chirality to the SOPV monomer via two-fold hydrogen bonding, orthogonal to the SOPV dimerization. Aggregates having opposite helicity (*P*-DTA-SOPV) compared to equilibrium conditions (*M*-SOPV) are formed, as demonstrated by the opposite CD spectrum (Fig 2.8c). In the second step, the complete removal of DTA from the SOPV aggregates by aqueous extraction at 0 °C using ethylene diamine results in the formation of transiently stable *P*-SOPV aggregates at this temperature. The exclusive formation of *P*-SOPV is demonstrated by the absolute ellipticity of *P*-SOPV, which equals the ellipticity of a solution containing exclusively *M*-SOPV aggregates under equilibrium conditions. The kinetic lability of *P*-SOPV is demonstrated by annealing at 25 °C, resulting in a time-dependent stereomutation of the CD spectra indicative of a conversion from *P*-SOPV towards *M*-SOPV aggregates (Fig 2.8d). The single isosbestic point in these time-dependent CD spectra indicates that two distinct states are involved in the conversion process: *P*-SOPV and *M*-SOPV.

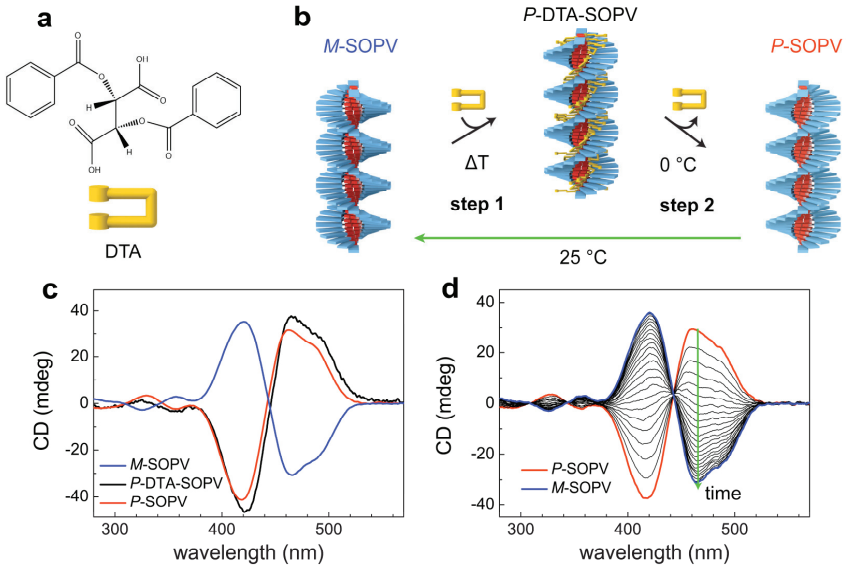

Figure 2.8 | Controlled formation of exclusively metastable aggregates via two-step non-covalent synthetic methodology. (a) Molecular structure of *S*-chiral dibenzoyl tartaric acid (DTA). (b) Schematic representation of preparation of pure *P*-SOPV via two-step non-covalent synthetic methodology. (c) CD spectra of *M*-SOPV, *P*-DTA-SOPV and *P*-SOPV in MCH (100 μM). (d) CD spectra acquired during conversion from metastable *P*-SOPV towards *M*-SOPV upon annealing at 25 °C.

To investigate if the observed transition from metastable *P*- to thermodynamically stable *M*-type helices can be attributed to the disassembly of *P*-SOPV aggregates and subsequent assembly of *M*-SOPV aggregates, *i.e.* via the free monomer as suggested in the previous paragraph, the stereomutation kinetics are further analysed. The stereomutation kinetics experimentally acquired at 20 °C, 25 °C, and 30 °C follow first order kinetics, as shown in Figure 2.9b. To analyse if this behaviour can also be predicted by the kinetic model, simulations are performed, starting at t = 0 with an equilibrium distribution of monomers exclusively assembled in *P*-SOPV stacks. The initial concentrations [P_i] of these metastable assemblies for every aggregate length i are computed with the equilibrium model. Based on these start concentrations the subsequent development of the system is simulated with the kinetic model that includes two pathways towards *P*- and *M*-SOPV. Indeed, the simulated stereomutation curves display first order kinetics, as is observed experimentally as well. A critical parameter for the simulated rate of the stereomutation is the value of the equilibrium constant of elongation K_e*(0 °C) that is used to define the initial equilibrium distribution of *P*-SOPV assemblies at 0 °C. Larger values of K_e*(0 °C) yield slower stereomutation kinetics upon annealing at 20 °C.

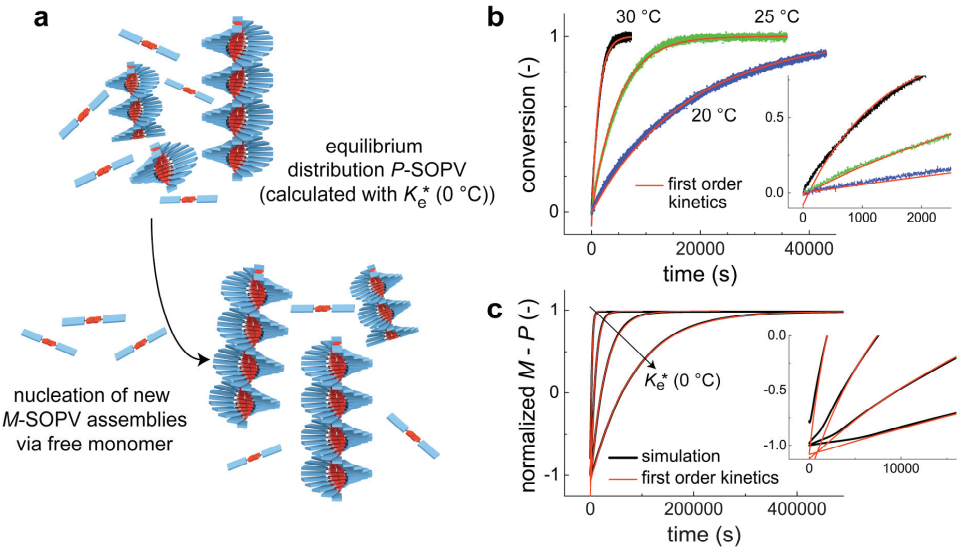

Figure 2.9 | Analysis of stereomutation kinetics from *P*-SOPV to *M*-SOPV aggregates. (a) Schematic representation of followed approach to simulate stereomutation from *P*- to *M*-type helices. First the equilibrium distribution of *P*-SOPV assemblies is calculated, based on the equilibrium constant of elongation K_e*(0 °C). Based on these start concentrations the subsequent transition from *P*- to *M*-SOPV is simulated with the kinetic model. (b) Stereomutation kinetics from *P*- to *M*-SOPV at different temperatures, fitted with first order kinetics: conversion ~ 1 – exp(–k·(t–t_0)). The inset focuses on the initial stages of the stereomutation process. (c) The conversion from *P*- to *M*-SOPV is simulated with the kinetic model, using different values of K_e* at 0 °C to compute the distribution of *P*-type aggregates at t = 0. K_e*(0 °C) increases along the arrow: 10^5 M^{-1}; 10^6 M^{-1}; 10^7 M^{-1}; 10^8 M^{-1}. The simulated curves are fitted with first order kinetics. The inset focuses on the initial stages of the simulated conversion.

This can be rationalized by the fact that a larger equilibrium constant of elongation results in longer *P*-type assemblies at the beginning of the process. As the disassembly of these helices is simulated via monomer dissociation from the ends, longer helices need more time to be fully re-assembled via the free monomer into helices with opposite twist.

2.6 Conclusions and discussion

Via experiments under kinetic control it is established that the aggregation of SOPV involves two aggregation pathways leading to assemblies with opposite helicity, one of which is favoured kinetically and the other thermodynamically. Kinetically controlled formation of one-dimensional supramolecular aggregates has been reported previously for different systems.[22, 23] However, in most cases the metastable states involved are only probed in terms of their static properties, such as morphology or photophysical properties. Kinetic studies as shown in this chapter, by probing the full aggregation process starting from free monomers, reveal that the influence of the metastable off-pathway aggregates on the overall assembly process is mediated through the equilibrium with free monomers. As a result, entrapment of material in the metastable pathway hampers the formation of thermodynamically favoured assemblies at high concentration. This phenomenon, a hall mark of pathway complexity, has been observed in protein aggregation before[13, 24, 25]. By taking advantage of theories developed in this field of research, further quantitative insights into the consequences of pathway complexity for the aggregation of π-conjugated material can be obtained.[10] Furthermore, these results indicate that by influencing the subtleties of the self-assembly process generating these materials, through tuning of the on-pathway or off-pathway mechanisms, the resulting morphologies could potentially be controlled to arrive at optimized self-assembled functional materials. To this end, the next chapter will focus on the influence of solvent conditions on the stability and dynamics of aggregation processes.

Although not the main scope of this chapter, it did not escape our attention that kinetically and thermodynamically favoured helices with opposite helicity, like *P*- and *M*-type in the case of SOPV, are often obtained in the assembly of chiral π-conjugated molecules. Examples reported in literature include thiophene[26, 27], perylene[28], bismerocyanine[23], *p*-phenylene vinylene[29, 30], squaraine[31], fluorene[32], terphenyl[33] and azobenzene[34] derivatives. The occurrence of both types of helices suggests that the energy landscape as a function of the rotation angle between subsequent monomers within the helix contains two local minima at a positive and a negative angle. For achiral molecules, both minima are anticipated to be equal in energy, which implies the formation of a racemic mixture of left- and right-handed helices. However, introduction of chirality in the system results in an asymmetric energy landscape in which one handedness yields a lower energy minimum compared to the opposite handedness.[17, 28] The initial appearance of a metastable helix – *i.e.* the one that corresponds to the rotation angle with the unfavourable local energy minimum – bears a resemblance with the *Ostwald rule of stages* that is observed in crystallization processes. Similar to the metastable helices, here the least stable polymorph – *i.e.* the one that is closest in energy to the solution phase – crystallizes first whereas the more stable polymorphs appear later in the process.[35]

2.7 Details of experiments and simulations

Instrumentation and Material. The synthesis of SOPV has been described previously, all solvents are used as received.[36] CD, linear dichroism and corresponding UV/Vis spectra are recorded using a Jasco J-815 CD spectrometer. Sensitivity, response time and scanning speed are chosen appropriately. The temperature is controlled using a Jasco Peltier temperature controller with a range of -10 – 110 °C and adjustable temperature slope. Stopped-flow studies are performed using a Biologic SFM 400 stopped-flow setup with Berger Ball mixer, Biologic TC 100 cuvet (optical path length 1 cm), and Biologic MPS-60 controller unit. The stopped-flow cuvet is connected in-line with a Jasco J-815 CD spectrometer. To control the temperature of the cuvet and syringes, SFM 400 is connected to a Julabo F12 temperature controller (ethylene glycol bath with thermostat). ^{1}H-NMR spectra are recorded at 298 K on a Varian Unita Inova Spectrometer (500 MHz), in $CDCl_3$ (Cambridge Isotope Laboratories). Temperature-dependent UV/Vis data are recorded on a PerkingElmer L40 photospectrometer equipped with a Perkin Elmer PTP-1 Peltier temperature controller with a range of 0 – 100 °C and adjustable temperature slope.

Experiments under thermodynamic and kinetic control. Thermodynamically stable *M*-SOPV (100 μM) in methylcyclohexane (MCH, spectroscopic grade, Sigma-Aldrich) is obtained upon slow cooling (60 °C/hr) from the molecularly dissolved state (70 °C) to 0 °C; equilibrium conditions are verified by time-dependent measurements, showing no further change in time. Metastable *P*-SOPV (MCH, 100 μM) is obtained upon quenching molecularly dissolved SOPV from 70 °C to 0 °C (ice bath). The optical path length for the reported CD spectra is 1 mm, no linear dichroism (LD) artefacts are observed. The corresponding temperature-dependent CD and UV/Vis experiments are performed with SOPV concentrations of 46.7 μM and 46.2 μM, respectively, and optical path lengths of 1 mm and 1 cm, respectively. The fraction of *P*-SOPV and *M*-SOPV obtained upon quenching SOPV (MCH, 13 μM) from different temperatures is evaluated from the CD spectra by simulation of a linear combination of the spectra corresponding to a solution consisting of pure *P*-SOPV (obtained via the two-step non-covalent synthetic methodology) and a solution containing *M*-SOPV exclusively. The fraction of free SOPV monomer present before quenching is derived from the CD spectra under equilibrium conditions assuming $\varphi_{\text{monomer}} = 1 - \varphi_{\text{helical aggregate}}$; where $\varphi_{\text{helical aggregate}}$ is derived from the CD intensity devided by the saturated CD intensity at 0 °C. It should be noted that this assumption implies that the concentration of material present in pre-nucleus oligomers (*i.e.* dimer, trimer, etc.) is neglected. The optical path length of the reported spectra for these quenching experiments is 1 cm.

Stopped-flow experiments. To probe the kinetics of the supramolecular polymerization of SOPV, SOPV in chloroform (spectroscopic grade, Sigma-Aldrich) is mixed with MCH (50:1; 1508 μl:30 μl, injection rate 8–9 ml/s, mixing time <10 ms), after which CD is followed in time (λ = 466 nm; $\Delta\lambda$ = 1 nm; Δt = 1 s; standard sensitivity; high tension (HT) voltage adjusted to get a direct-current voltage around 1 V). The SOPV concentration and the duration of the measurement are adjusted appropriately. Kinetic curves are averaged over multiple stopped-flow experiments as follows. At 293 K: 5 μM, 9; 6.1 μM, 2; 6.5 μM, 6; 7.8 μM, 1; 8.7 μM, 4; 9 μM, 2; 10 μM, 9; 15 μM, 3; 19 μM, 6. At 308 K: 10 μM, 6; 12.5 μM, 6; 15 μM, 11; 20 μM, 9; 25 μM, 6. After the measurement, the concentration is verified using CD (466 nm) and UV/Vis (438 nm) spectra.

The molecular dissolved state of SOPV in chloroform at the start of the stopped-flow experiment is experimentally based on the absence of a Cotton effect in CD spectra, and the absence of the band at 490 nm in UV/Vis absorption which is characteristic for aggregation. To verify the molecular dissolved state of SOPV in chloroform at the start of the kinetic experiment, concentration-dependent ^{1}H-NMR experiments are performed on SOPV in $CDCl_3$ in the concentration regime 0.15 – 8.3 mM at T = 298 K. As stacking of SOPV changes the local magnetic field of the aromatic protons, formation of small oligomers is expected to result in shifted resonances in the aromatic regime (7 – 8 ppm) of the ^{1}H-NMR spectra. However, no shifts occur upon changing the concentration. Moreover, no broadening of peaks

in the aromatic regime is observed, indicating that in chloroform no stacking of hydrogen-bonded SOPV dimers occurs in this concentration regime, which largely covers the concentrations used in the kinetic experiments.

Based on the SOPV dimerization constant K_{dim} = (2.1 ± 0.3)·10^4 M^{-1} at T = 25 °C[15], the fraction of hydrogen-bonded SOPV dimer in chloroform is estimated to be >70 % for all kinetic experiments. It has been shown that the dimerization constant for a three-fold hydrogen-bonded module increases two orders of magnitude when MCH is used as solvent instead of chloroform.[37] Hence, it is assumed that upon addition of the chloroform solution to MCH, the dimerization constant of SOPV increases considerably, resulting in a full conversion of the remaining SOPV molecules into hydrogen-bonded SOPV dimers and the concomitant formation of helical stacks. As hydrogen-bonding typically occurs via a diffusion-controlled reaction[38], the fraction of hydrogen-bonded SOPV dimers is expected to approach 100% immediately after mixing of the chloroform solution with MCH.

The influence of chloroform on the self-assembly of SOPV is assessed by temperature-dependent CD measurements (λ = 466 nm) of solutions of SOPV in MCH containing varying amounts of chloroform (0 – 5 v/v%). The addition of small percentages of chloroform leads to a reduction in the critical elongation temperature T_e and hence, stability of the helical stacks. However, the shape of the cooling curves is similar as in pure MCH, indicating that the addition of chloroform does not affect the cooperative growth mechanism. Furthermore, full CD spectra of SOPV in MCH/chloroform solutions obtained at 0 °C demonstrate that the shape of the CD signal is not affected by addition of chloroform, a clear sign that the supramolecular organization of the SOPV chromophores within the stack is similar as in pure MCH.

Two-step non-covalent synthetic methodology. To obtain *P*-DTA-SOPV, the DTA (Syncom, Groningen, NL) and SOPV are mixed in chloroform (1:1). Subsequently, chloroform is evaporated by purging with nitrogen gas; the residual DTA-SOPV complex (red colour) is dissolved in MCH (100 μM) upon sonication and heating until the sample turns green, indicating molecular dissolution. Cooling from this molecularly dissolved state to 0 °C results in *P*-DTA-SOPV aggregates. On adding an equal volume of aqueous ethyl diamine solution (0.15 M) at 0 °C, vigorous mixing of the water and MCH phase (1 min) and full separation of both phases, the top MCH layer containing metastable *P*-SOPV could be isolated.

Equilibrium model. The equilibrium model describes the one-dimensional aggregation process as a sequence of monomer addition equilibria:

$$
\begin{aligned}
&\mathrm{X} + \mathrm{X} \overset{K_n}{\rightleftarrows} \mathrm{M}_2 && [\mathrm{M}_2] = K_n [\mathrm{X}]^2 \\
&\mathrm{M}_2 + \mathrm{X} \overset{K_n}{\rightleftarrows} \mathrm{M}_3 && [\mathrm{M}_3] = K_n [\mathrm{M}_2][\mathrm{X}] \\
&\quad\vdots \\
&\mathrm{M}_{n-1} + \mathrm{X} \overset{K_n}{\rightleftarrows} \mathrm{M}_n && [\mathrm{M}_n] = K_n [\mathrm{M}_{n-1}][\mathrm{X}] \\
&\mathrm{M}_n + \mathrm{X} \overset{K_e}{\rightleftarrows} \mathrm{M}_{n+1} && [\mathrm{M}_{n+1}] = K_e [\mathrm{M}_n][\mathrm{X}] \\
&\quad\vdots \\
&\mathrm{M}_{i-1} + \mathrm{X} \overset{K_e}{\rightleftarrows} \mathrm{M}_i && [\mathrm{M}_i] = K_e [\mathrm{M}_{i-1}][\mathrm{X}]. \\
&\quad\vdots
\end{aligned}
\qquad (2.1)
$$

Here X represents the monomer, *i.e.* the hydrogen-bonded dimer in case of SOPV assembly. In case of a cooperative aggregation process, $K_n < K_e$ (with K_n the equilibrium constant of nucleation, K_e the equilibrium constant of elongation and cooperativity $\sigma = K_n / K_e$). Obviously, in an isodesmic aggregation process, $K_n = K_e$ ($\sigma = 1$). The concentration of each species M_i equals $[M_i] = K_n^{i-1}[X]^i$ for $i \leq n$ and $[M_i] = K_e^{i-n} K_n^{n-1} [X]^i$ for $i > n$. With dimensionless concentration $m_i = K_e[M_i]$, dimensionless monomer

concentration $x = K_e[X]$, the dimensionless concentration of each species M_i equals $m_i = \sigma^{i-1}x^i$ for $i \leq n$ and $m_i = \sigma^{n-1}x^i$ for $i > n$. Hence, the dimensionless mass balance is

$$x_{tot} = \sigma^{-1}\sum_{i=1}^{n} i(\sigma x)^i + \sigma^{n-1}\sum_{i=n+1}^{\infty} ix^i \,. \tag{2.2}$$

with dimensionless total concentration $x_{tot} = K_e \cdot c_{tot}$ and c_{tot} the total monomer concentration in mol/L. Evaluating both sums in eq. 2.2 using standard expressions for converging series yields:

$$x_{tot} = \sigma^{-1}\left(\frac{(\sigma x)^{n+1}(n\sigma x - n - 1)}{(\sigma x - 1)^2} + \frac{\sigma x}{(\sigma x - 1)^2}\right) - \sigma^{n-1}\left(\frac{x^{n+1}(nx - n - 1)}{(x-1)^2}\right). \tag{2.3}$$

Solving eq. 2.3 using standard numerical methods in Matlab yields the dimensionless monomer concentration x. Subsequently, if all species with $i > 1$ are considered as aggregates (as is the case for the UV/Vis data on SOPV) the degree of aggregation φ can be defined as:

$$\varphi = \frac{x_{tot} - x}{x_{tot}} \,. \tag{2.4}$$

In the case of the helical SOPV aggregates however, the degree of aggregation that follows from the CD signal is considered to be equal to:

$$\varphi = \frac{x_{tot} - x - \sum_{2}^{n} i \cdot m_i}{x_{tot}}. \tag{2.5}$$

The temperature-dependent equilibrium constants in Figure 2.2c are defined via the Van't Hoff equation: $K = \exp(-(\Delta H^0 - T\Delta S^0) / R \cdot T)$ with gas constant R and temperature T. ΔH^0 and ΔS^0 here represent the standard enthalpy and entropy of nucleation (ΔH_n^0 and ΔS_n^0) and elongation (ΔH_e^0 and ΔS_e^0), respectively. Parameters: $\Delta H_n^0 = -90$ kJ/mol; $\Delta S_n^0 = -195$ J/K.mol; $\Delta H_e^0 = -110$ kJ/mol; $\Delta S_e^0 = -250$ J/K.mol.

Kinetic model describing competition between two cooperative aggregation pathways. The reactions for the aggregation of monomer *X* into two aggregates of different helicities (*P*-type and *M*-type) are shown in Figure 2.6a. It is assumed that all association (forward) rate constants for each aggregate type are the same and that the dissociation rate constants only differ between pre- and post-nucleus aggregates. This assumption has been used previously in other cooperative reversible association models. Although it has been shown by Hill that, in general, the rate constants depend continuously on the polymer length, this dependence is proven to be very weak when aggregates grow by monomer addition only.[39] To limit the number of reaction rate equations required to describe the system, only the aggregates up to a certain length *N*, with *N* much larger than the nucleus sizes (*n* and *n**) are described explicitly. The aggregates with size larger than *N* are described per type together as fibrils by considering both the fibril number concentrations,

$$\left[F^M\right] = \left[M_{N+1}\right] + \left[M_{N+2}\right] + \left[M_{N+3}\right] + \ldots, \tag{2.6}$$

similarly for the *P*-type fibrils:

$$\left[F^P\right] = \left[P_{N+1}\right] + \left[P_{N+2}\right] + \left[P_{N+3}\right] + \ldots, \tag{2.7}$$

and the fibril mass concentrations,

$$\left[Z^M\right] = (N+1)\left[M_{N+1}\right] + (N+2)\left[M_{N+2}\right] + (N+3)\left[M_{N+3}\right] + \ldots, \tag{2.8}$$

similarly for the *P*-type fibrils:

$$\left[Z^P\right] = (N+1)\left[P_{N+1}\right] + (N+2)\left[P_{N+2}\right] + (N+3)\left[P_{N+3}\right] + \ldots . \tag{2.9}$$

In order to keep the fibril formation reversible, an estimation is needed for the number of fibrils of length *N*+1, the species that upon monomer dissociation results in the explicitly described aggregate of length *N*. Assuming that for all $i > N$, $\left[M_{i+1}\right] = \alpha_M \left[M_i\right]$, one obtains

$$\begin{aligned} \left[F^M\right] &= \sum_{i=0}^{\infty} \left(\alpha_M\right)^i \left[M_{N+1}\right], \\ \left[Z^M\right] &= \sum_{i=0}^{\infty} \left(N+1+i\right)\left(\alpha_M\right)^i \left[M_{N+1}\right]. \end{aligned} \tag{2.10}$$

Using the standard series $\sum_{i=0}^{\infty} x^i = \frac{1}{1-x}$ and $\sum_{i=0}^{\infty} i \cdot x^i = \frac{x}{\left(x-1\right)^2}$ for x < 1, this yields

$$\left[F^M\right] = \left[M_{N+1}\right]\frac{1}{1-\alpha_M}, \qquad \left[Z^M\right] = \left[M_{N+1}\right]\left(\frac{N+1}{1-\alpha_M} + \frac{\alpha_M}{\left(1-\alpha_M\right)^2}\right). \tag{2.11}$$

Substituting the equation for $\left[F^M\right]$ in $\left[Z^M\right]$ yields

$$\left[Z^M\right] = \left[F^M\right]\left(N+1+\frac{\alpha_M}{\left(1-\alpha_M\right)}\right), \tag{2.12}$$

from which α_M can be solved as

$$\alpha_M = 1 - \frac{\left[F^M\right]}{\left[Z^M\right] - N\left[F^M\right]}. \tag{2.13}$$

The estimated concentration of *M*-type aggregates of length *N*+1 is thus

$$\left[M_{N+1}\right] = \left(1-\alpha_M\right)\left[F^M\right]. \tag{2.14}$$

Similarly, for the *P*-type aggregates

$$\alpha_P = 1 - \frac{\left[F^P\right]}{\left[Z^P\right] - N\left[F^P\right]}, \tag{2.15}$$

and

$$\left[P_{N+1}\right] = \left(1-\alpha_P\right)\left[F^P\right]. \tag{2.16}$$

The rate equations for the aggregation pathway competition model then finally become:

- for the monomers

$$\begin{aligned} \frac{d\left[X\right]}{dt} = &-a\left[X\right]\left(2\left[X\right] + \sum_{i=2}^{N}\left[M_i\right] + \left[F_M\right]\right) + b\left(2\left[M_2\right] + \sum_{i=3}^{n}\left[M_i\right]\right) + c\left(\sum_{i=n+1}^{N}\left[M_i\right] + \left[F_M\right]\right) \\ &- a^*\left[X\right]\left(2\left[X\right] + \sum_{i=2}^{N}\left[P_i\right] + \left[F_P\right]\right) + b^*\left(2\left[P_2\right] + \sum_{i=3}^{n^*}\left[P_i\right]\right) + c^*\left(\sum_{i=n^*+1}^{N}\left[P_i\right] + \left[F_P\right]\right), \end{aligned} \tag{2.17}$$

- for the oligomers

$$\frac{d[M_i]}{dt} = a[X]([M_{i-1}]-[M_i]) + b([M_{i+1}]-[M_i]),$$
$$\frac{d[P_i]}{dt} = a^*[X]([P_{i-1}]-[P_i]) + b^*([P_{i+1}]-[P_i]), \quad (2.18)$$

- for the nucleus

$$\frac{d[M_n]}{dt} = a[X]([M_{n-1}]-[M_n]) + (c[M_{n+1}]-b[M_n]),$$
$$\frac{d[P_{n^*}]}{dt} = a^*[X]([P_{n^*-1}]-[P_{n^*}]) + (c^*[P_{n^*+1}]-b^*[P_{n^*}]), \quad (2.19)$$

- for polymers larger than the nucleus size n (M-type) or n^* (P-type)

$$\frac{d[M_i]}{dt} = a[X]([M_{i-1}]-[M_i]) + c([M_{i+1}]-[M_i]),$$
$$\frac{d[P_i]}{dt} = a^*[X]([P_{i-1}]-[P_i]) + c^*([P_{i+1}]-[P_i]), \quad (2.20)$$

- for the last explicitly considered aggregate with length N

$$\frac{d[M_N]}{dt} = a[X]([M_{N-1}]-[M_N]) + c((1-\alpha_M)[F_M]-[M_N]),$$
$$\frac{d[P_N]}{dt} = a^*[X]([P_{N-1}]-[P_N]) + c^*((1-\alpha_P)[F_p]-[P_N]), \quad (2.21)$$

- for the fibril number concentration

$$\frac{d[F_M]}{dt} = a[X][M_N] - c(1-\alpha_M)[F_M],$$
$$\frac{d[F_P]}{dt} = a^*[X][P_N] - c^*(1-\alpha_P)[F_P], \quad (2.22)$$

- and finally for the fibril mass concentration

$$\frac{d[Z_M]}{dt} = (N+1)(a[X][M_N] - c(1-\alpha_M)[F_M]) + a[X][F_M] - c([F_M]-(1-\alpha_M)[F_M]),$$
$$\frac{d[Z_P]}{dt} = (N+1)(a^*[X][P_N] - c^*(1-\alpha_P)[F_P]) + a^*[X][F_P] - c^*([F_P]-(1-\alpha_P)[F_P]), \quad (2.23)$$

which can be rewritten into

$$\frac{d[Z_M]}{dt} = a[X]((N+1)[M_N]+[F_M]) - c([F_M]+N(1-\alpha_M)[F_M]),$$
$$\frac{d[Z_P]}{dt} = a^*[X]((N+1)[P_N]+[F_P]) - c^*([F_P]+N(1-\alpha_P)[F_P]). \quad (2.24)$$

The resulting system of differential equations, combined with the relation between α, F and Z for both P-type as well as M-type aggregates, is solved using the *ode15s* solver in Matlab. The influence of N on the simulated aggregation kinetics is assessed by comparing kinetic curves simulated with different values of N, using the rate constants and nucleus sizes corresponding to the concentration-dependent

kinetic simulations shown in Figure 2.6d. No differences in the simulated curves are found for $N = 50$, $N = 100$ and $N = 200$, demonstrating that, at least if $N > 50$, the size of the largest aggregate that is explicitly described in a rate equation does not affect the simulated growth kinetics. To verify the influence of truncating the differential equations at a specific length (*i.e.* excluding the filaments), simulations are performed with a maximum aggregate size of 50. Compared to the simulations in which the filaments are included via the quasi-equilibrium approach ($N = 50$), large differences are observed. Only if the differential equations are truncated at a larger aggregate size of 2000, the simulations approach the simulated kinetics with filaments included.

The simulations in Figure 2.7ab are performed with the following parameters: $n = n^* = 5$; $a = 2.9 \cdot 10^4$ $M^{-1}s^{-1}$; $K_e = 1.52 \cdot 10^6$ M^{-1}; $K_n/K_e = 0.0526$; $N = 100$; $c_{tot} = 10$ μM). For the temperature-dependent simulations in Figure 2.7d, the temperature-dependency of the forward rate constant is described by the Arrhenius equation: $a = A\exp(-E_{act}/RT)$, where A is the kinetic prefactor and E_{act} the activation energy. The temperature-dependency of K_e is described using the Van't Hoff equation. Parameters: $A = 2.38 \cdot 10^{13}$ $M^{-1}s^{-1}$, $E_{act} = 50$ kJ/mol, $\Delta H_e^0 = -100$ kJ/mol, $\Delta S_e^0 = -223$ J/K.mol, $K_n / K_e = 0.052$, $K_n^*/K_n = 1.38$, $K_e^*/K_e = 0.16$, $a^*/a = 3.8$. The stereomutation kinetics in Figure 2.9d are simulated with the following parameters: $n = n^* = 5$; $a = 2.9 \cdot 10^4$ $M^{-1}s^{-1}$; $K_e = 1.52 \cdot 10^6$ M^{-1}, $K_n/K_e = 0.0526$, $K_n^*/K_n = 1.38$, $K_e^*/K_e = 0.164$ and $a^*/a = 3.79$, $K_n^*/K_e^* = 0.05$ at 273 K, $c_{tot} = 50$ μM.

To further assess the influence of the metastable pathway (P) on the stable pathway towards the equilibrium structures (M), kinetic simulations are performed at different concentrations. As a function of concentration, the times at which 50% and 99% of the conversion towards M is completed (t-50 and t-99, respectively) are followed. Next, the maximum fraction of monomers assembled in metastable P (P_{max}) and the minimum net helicity, *i.e.* the difference between the fraction of monomers assembled in M and P, $(M - P)_{min}$, are followed as a function of the concentration as well. If $a^* > a$, $K_e^* < K_e$ and both pathways are cooperative, the rate decreases with concentration well beyond the concentration where the metastable P-type assemblies can be formed ($c_{tot} \sim 10 \times 1/K_e^*$), as shown in Figure 2.10a. However, if both nucleated pathways have the same rate constant of monomer association ($a^* = a$), the initial appearance of metastable P becomes less pronounced and only a slight decrease in t-99 in the high concentration regime is obtained (Fig 2.10b). This can be rationalized by the fact that the small fraction of material that is accumulated in the metastable pathway is released slower upon increasing the concentration, and hence the last 1% of the assembly into M is retarded as well. To increase the initial appearance of P with respect to M, despite the fact that $a^* = a$, the nucleation barrier of the metastable pathway is omitted by defining the cooperativity σ^* equal to 1. Indeed, a larger fraction of the material is initially accumulated into the metastable pathway. However, this does not result in slower assembly of the equilibrium state M at higher concentrations (Fig 2.10c). Only if $a^* > a$, an inverted relation between rate and concentration can be obtained with an isodesmic system ($\sigma^* = \sigma = 1$, Fig 2.10d).

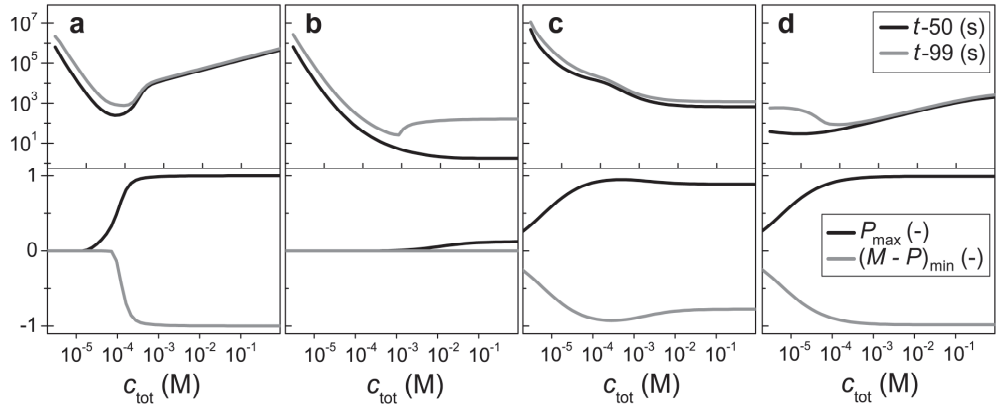

Figure 2.10 | Analysis of competition between two parallel assembly pathways under kinetic and thermodynamic control. Kinetic simulations are performed at different concentrations. The top panes represent the concentration-dependent times at which 50% and 99% of the conversion towards *M* is completed (*t*-50 and *t*-99 respectively). The bottom panes represent the maximum fraction of monomers assembled in metastable *P* (P_{max}) and the minimum net helicity, *i.e.* the difference between the fraction of monomers assembled in *M* and *P*, $(M - P)_{min}$, as a function of the concentration. Parameters: (a) $a^* = 10^6$ $M^{-1}s^{-1}$; $a = 10^4$ $M^{-1}s^{-1}$; $K_e^* = 10^5$ M^{-1}; $K_e = 10^6$ M^{-1}; $\sigma^* = 0.01$; $\sigma = 0.01$; $n^* = 5$; $n = 5$. (b) $a^* = a = 10^4$ $M^{-1}s^{-1}$; $K_e^* = 10^5$ M^{-1}; $K_e = 10^6$ M^{-1}; $\sigma^* = 0.01$; $\sigma = 0.01$; $n^* = 5$; $n = 5$. (c) $a^* = a = 10^4$ $M^{-1}s^{-1}$; $K_e^* = 10^5$ M^{-1}; $K_e = 10^6$ M^{-1}; $\sigma^* = 1$ (isodesmic); $\sigma = 0.01$; $n = 5$. (d) $a^* = 10^6$ $M^{-1}s^{-1}$; $a = 10^4$ $M^{-1}s^{-1}$; $K_e^* = 10^5$ M^{-1}; $K_e = 10^6$ M^{-1}; $\sigma^* = \sigma = 1$ (isodesmic). For the isodesmic pathways, all species larger than the monomer are included in the weight concentration of the respective type of aggregate.

2.8 References

[1] Aida, T.; Meijer, E. W.; Stupp, S. I. *Science* **2012**, *335*, 813.

[2] De Greef, T. F. A.; Smulders, M. M. J.; Wolffs, M.; Schenning, A. P. H. J.; Sijbesma, R. P.; Meijer, E. W. *Chem. Rev.* **2009**, *109*, 5687.

[3] Ferrone, F. A. *Methods Enzymol.* **1999**, *309*, 256.

[4] Oosawa, F.; Kasai, M. *J. Mol. Biol.* **1962**, *4*, 10.

[5] Powers, E. T.; Powers, D. L. *Biophys. J.* **2006**, *91*, 122.

[6] Bishop, M. F.; Ferrone, F. A. *Biophys. J.* **1984**, *46*, 631.

[7] Xue, W.-F.; Homans, S. W.; Radford, S. E. *Proc. Natl. Acad. Sci. USA* **2008**, *105*, 8926.

[8] Knowles, T. P. J.; Waudby, C. A.; Devlin, G. L.; Cohen, S. I. A.; Aguzzi, A.; Vendruscolo, M.; Terentjev, E. M.; Welland, M. E.; Dobson, C. M. *Science* **2009**, *326*, 1533.

[9] Cohen, S. I. A.; Linse, S.; Luheshi, L. M.; Hellstrand, E.; White, D. A.; Rajah, L.; Otzen, D. E.; Vendruscolo, M.; Dobson, C. M.; Knowles, T. P. J. *Proc. Natl. Acad. Sci. USA* **2013**, *110*, 9758.

[10] Powers, E. T.; Powers, D. L. *Biophys. J.* **2008**, *94*, 379.

[11] Baskakov, I. V.; Legname, G.; Baldwin, M. A.; Prusiner, S. B.; Cohen, F. E. *J. Biol. Chem.* **2002**, *277*, 21140.

[12] Mulder, A. M.; Yoshioka, C.; Beck, A. H.; Bunner, A. E.; Milligan, R. A.; Potter, C. S.; Carragher, B.; Williamson, J. R. *Science* **2010**, *330*, 673.

[13] Deva, T.; Lorenzen, N.; Vad, B. S.; Petersen, S. V.; Thørgersen, I.; Enghild, J. J.; Kristensen, T.; Otzen, D. E. *Biochim. Biophys. Acta* **2013**, *1834*, 677.

[14] Cui, H.; Chen, Z.; Zhong, S.; Wooley, K. L.; Pochan, D. J. *Science* **2007**, *317*, 647.

[15] Schenning, A. P. H. J.; Jonkheijm, P.; Peeters, E.; Meijer, E. W. *J. Am. Chem. Soc.* **2001**, *123*, 409.

[16] Beljonne, D.; Hennebicq, E.; Daniel, C.; Herz, L. M.; Silva, C.; Scholes, G. D.; Hoeben, F. J. M.; Jonkheijm, P.; Schenning, A. P. H. J.; Meskers, S. C. J.; Phillips, R. T.; Friend, R. H.; Meijer, E. W. *J. Phys. Chem. B* **2005**, *109*, 10594.
[17] George, S. J.; De Bruijn, R.; Tomović, Ž.; Van Averbeke, B.; Beljonne, D.; Lazzaroni, R.; Schenning, A. P. H. J.; Meijer, E. W. *J. Am. Chem. Soc.* **2012**, *134*, 17789.
[18] Jonkheijm, P.; Van der Schoot, P.; Schenning, A. P. H. J.; Meijer, E. W. *Science* **2006**, *313*, 80.
[19] Goldstein, R. F.; Stryer, L. *Biophys. J.* **1986**, *50*, 583.
[20] Kulkarni, C.; Balusubramanian, S.; George, S. J. *ChemPhysChem* **2013**, *14*, 661.
[21] Filot, I. A. W.; Palmans, A. R. A.; Hilbers, P. A. J.; Van Santen, R. A.; Pidko, E. A.; De Greef, T. F. A. *J. Phys. Chem. B* **2010**, *114*, 13667.
[22] Pashuck, E. T.; Stupp, S. I. *J. Am. Chem. Soc.* **2010**, *132*, 8819.
[23] Lohr, A.; Würthner, F. *Angew. Chem. Int. Ed.* **2008**, *47*, 1232.
[24] Souillac, P. O.; Uversky, V. N.; Fink, A. L. *Biochemistry*, **2003**, *42*, 8094.
[25] Souillac, P. O.; Uversky, V. N.; Millett, I. S.; Khurana, R.; Doniach, S.; Fink, A. L. *J. Biol. Chem.* **2002**, *277*, 12666.
[26] Wolffs, M.; Korevaar, P. A.; Jonkheijm, P.; Henze, O.; Feast, W. J.; Schenning, A. P. H. J.; Meijer, E. W. *Chem. Commun.* **2008**, 4613.
[27] Bouman, M. M.; Meijer, E. W. *Adv. Mater.* **1995**, *7*, 385.
[28] Hu, J.; Kuang, W.; Deng, K.; Zou, W.; Huang, Y.; Wei, Z.; Faul, C. F. J. *Adv. Funct. Mater.* **2012**, *22*, 4149.
[29] Satrijo, A.; Meskers, S. C. J.; Swager, T. M. *J. Am. Chem. Soc.* **2006**, *128*, 9030.
[30] Jonkheijm, P.; Miura, A.; Zdanowska, M.; Hoeben, F. J. M.; De Feyter, S.; Schenning, A. P. H. J.; De Schryver, F. C.; Meijer, E. W. *Angew. Chem. Int. Ed.* **2004**, *43*, 74.
[31] Jyothish, K.; Hariharan, M.; Ramaiah, D. *Chem. Eur. J.* **2007**, *13*, 5944.
[32] Lakhwani, G.; Meskers, S. C. J. *Macromolecules* **2009**, *42*, 4220.
[33] Cui, J.; Liu, A.; Guan, Y.; Zheng, J.; Shen, Z.; Wan, X. *Langmuir* **2010**, *26*, 3615.
[34] Del Barrio, J.; Tejedor, R. M.; Chinelatto, L. S.; Sánchez, C.; Piñol, M.; Oriol, L. *J. Mater. Chem.* **2009**, *19*, 4922.
[35] Chung, S.-Y.; Kim, Y.-M.; Kim, J.-G.; Kim, Y.-J. *Nature Phys.* **2009**, *5*, 68.
[36] Jonkheijm, P.; Hoeben, F. J. M.; Kleppinger, R.; Van Herrikhuyzen, J.; Schenning, A. P. H. J.; Meijer, E. W. *J. Am. Chem. Soc.* **2003**, *125*, 15941.
[37] Würthner, F.; Thalacker, C.; Sautter, A.; Schärtl, W.; Ibach, W.; Hollricher, O. *Chem. Eur. J.* **2000**, *6*, 3871.
[38] Hammes, G. H.; Park, A. C. *J. Am. Chem. Soc.* **1969**, *91*, 956.
[39] Hill, T. L. *Biophys. J.* **1983**, *44*, 285.

3

Controlling self-assembly by solvent-dependent dynamics

Abstract: The influence of the ratio between poor and good solvent on the stability and dynamics of one-dimensional assemblies is studied via a combination of experiments and simulations. Stepwise addition of good solvent to aggregates formed via a cooperative growth mechanism results in complete disassembly at a critical good/poor solvent ratio. In contrast, gradual disassembly profiles upon addition of good solvent are observed for isodesmic systems. Due to the weak association of good solvent molecules to monomers, the solvent-dependent aggregate stability can be described by a linear free-energy relationship. With respect to dynamics, the disassembly of π-conjugated oligo(*p*-phenylene vinylene) (OPV) assemblies in methylcyclohexane (MCH) upon addition of chloroform as a good solvent is shown to proceed with a minimum rate around the critical chloroform/MCH solvent ratio. This minimum disassembly rate bears an intriguing resemblance to phenomena observed in protein unfolding, where minimum rates are observed at the thermodynamic midpoint of a protein denaturation experiment. A kinetic nucleation-elongation model in which the rate constants explicitly depend on the good solvent fraction is developed to rationalize the kinetic traces and further extend the insights by simulation. It is shown that cooperativity – *i.e.* the nucleation of new aggregates – plays a key role in the minimum assembly and disassembly rate at the critical solvent composition. Importantly, this shows that the mixing protocol by which one-dimensional aggregates are prepared via solution-based processing using good/poor solvent mixtures is of major influence on self-assembly dynamics.

Part of this work has been published as:

"Controlling Chemical Self-Assembly by Solvent-Dependent Dynamics" P. A. Korevaar, C. Schaefer, T. F. A. de Greef, E. W. Meijer, *J. Am. Chem. Soc.* **2012**, *134*, 13482–13491.

3.1 Introduction

The solvent conditions selected in self-assembly processes play a key role in the stability of the aggregated structures[1–5] and even the morphology[6–12]. By tuning the ratio between good solvent, in which the molecules are molecularly dissolved, and poor solvent, in which the molecules are less soluble and therefore assemble, these processes can be controlled. In the previous chapter, it is shown that the formation of self-assembled structures can be affected by metastable, off-pathway aggregates that compete with the thermodynamically stable state for free monomers and thereby exert their influence on the rate of the overall assembly process.[9] These insights emphasize the importance of control over assembly pathways, both in terms of stability as well as dynamics. For this reason, different processing methodologies are applied in self-assembly processes that are induced by a transfer from good to poor solvent, varying from fast dispersion to (slow) vapour diffusion.[13] However, although a start has been made to control the subtleties in self-assembly processes by tuning the solvent conditions, more detailed insight is needed to arrive at optimized nanoscopically ordered materials.

The role of solvent in the control over non-covalent interactions has been studied for decades in protein folding.[14] It is for example well known that proteins can unfold, or denaturate, by the addition of urea. The denaturation process in case of simple peptides is often described as a two-state equilibrium between a folded (F) and an unfolded (U) state. Due to the linear dependence of the Gibbs free energy of folding on the denaturant concentration, addition of a denaturant results in a gradual destabilisation of the folded state.[15–17] Remarkably, the unfolding as well as the folding processes have a minimum rate at the denaturant concentration corresponding to the thermodynamic midpoint of the denaturation curve, which results in characteristic "chevron plots".[18–20] This phenomenon can be rationalized by assuming that the rate constant of folding decreases upon adding denaturant, whereas the rate constant of unfolding increases with denaturant. Consequently, the overall observed relaxation rate shows a V-shaped dependence on the denaturant concentration, with a minimum at the midpoint of the denaturation equilibrium curve.

The insights developed in the field of protein folding prompted us to investigate how the influence of solvent conditions on assembly processes can be rationalized, both in terms of stability (thermodynamics) and dynamics (kinetics). In the first part of this chapter a clear relation is shown between the assembly mechanism and the stability of the aggregates upon addition of good solvent. Assemblies formed via a cooperative (nucleated) growth mechanism are demonstrated to disassemble completely at a critical good/poor solvent ratio. In the second part, it is shown that the disassembly of oligo(*p*-phenylene vinylene) (OPV) aggregates proceeds with the slowest dynamics close to this critical solvent composition. This phenomenon bears an intriguing resemblance to denaturant-dependent rate effects observed in protein unfolding. In the third part, the influence of the mixing protocol on the time-dependent development of the self-assembled system after addition of good solvent is shown and rationalized. Finally, the kinetic model as introduced in the previous chapter is modified

to describe the solvent-dependent assembly and disassembly processes, and to further expand the insights by simulations.

3.2 Thermodynamic relation between solvent composition and stability of self-assembled structures

The assembly of *R*-chiral oligo(*p*-phenylene vinylene)-ureidotriazine (ROPV) **1**, *S*-chiral benzene-1,3,5-trithioamide **2**, *R*-chiral 3,3′-diamino-2,2′-bipyridine C_3-discotic **3**, and perylene tetracarboxylic acid bisimide **4** (Fig 3.1) are probed with circular dichroism (CD, **1**, **2** and **3**) and UV/Vis spectroscopy (**4**), respectively.

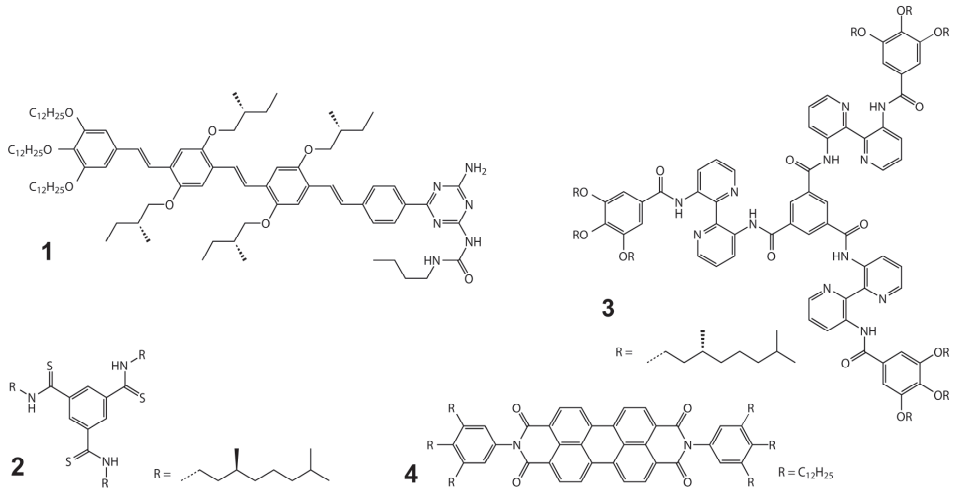

Figure 3.1 | Molecular structures of self-assembling moieties **1**, **2**, **3** and **4**.

These monomers self-assemble in methylcylohexane (MCH), whereas their molecularly dissolved states can be obtained in pure chloroform. In analogy to protein denaturation studies, the self-assembly is studied in different solvent mixtures of poor (MCH) and good (chloroform) solvent, as shown for **1** in Figure 3.2.

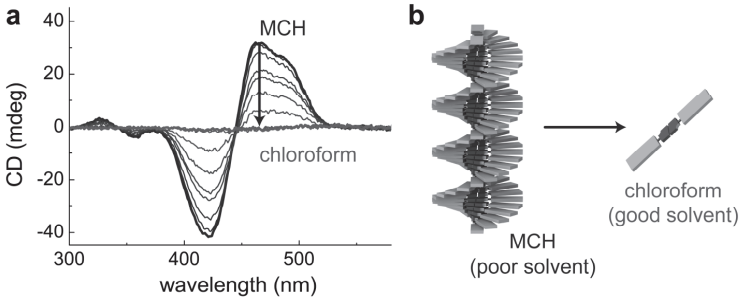

Figure 3.2 | **Disassembly of ROPV by addition of chloroform.** (a) CD spectra of ROPV **1** in MCH with increasing chloroform volume fraction along the arrow (20 °C, 24 μM). (b) The addition of chloroform induces the disassembly of the ROPV helices.

Since each of these moieties displays a clear transition in CD and/or UV/Vis upon aggregation, the degree of aggregation can be deduced from the normalized changes in CD or UV/Vis under equilibrium conditions. The degree of aggregation *vs*. the chloroform volume fraction (*f*) reveals a critical solvent composition for the self-assembly of **1** and **2**, whereas a gradual "denaturation" curve is observed for **3** and **4** (Fig 3.3). The occurrence of a critical solvent composition holds a similarity with the critical temperature of aggregation, typically attributed to a nucleation phenomenon involved in the aggregation process. Indeed, temperature-dependent studies reveal a cooperative aggregation mechanism for **1** and **2**, whereas isodesmic growth is observed for **3** and **4**.[21–23] For **1**, the degree of aggregation *vs*. volume fraction of good solvent *f* is determined at different temperatures and concentrations (Fig 3.3). The critical chloroform volume fraction (f_{crit}) increases with concentration and decreases with temperature.

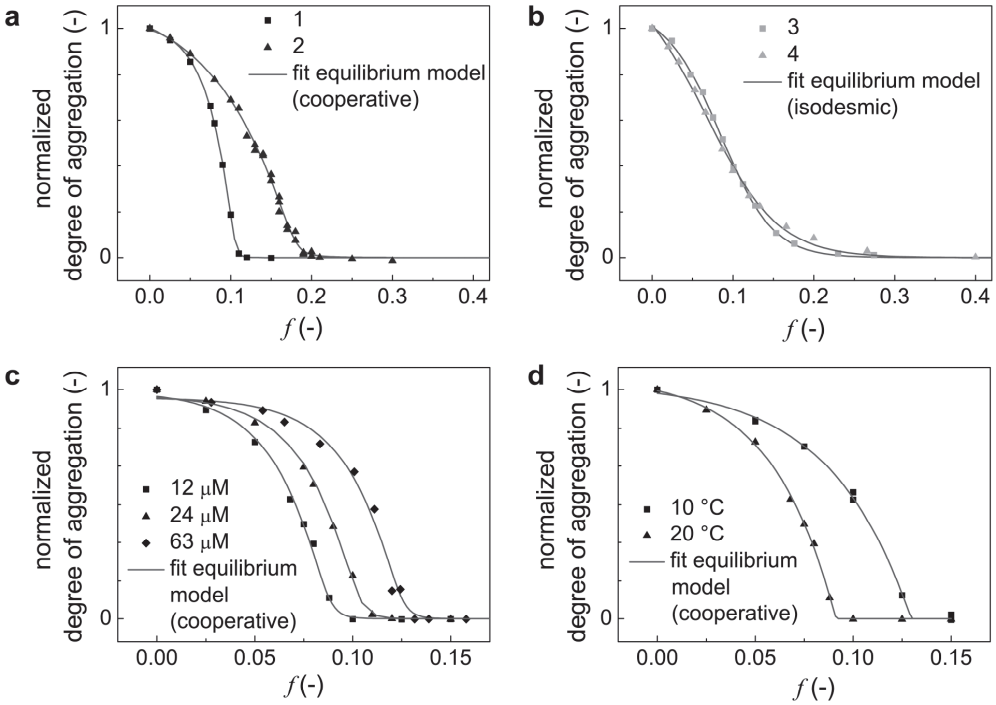

Figure 3.3 | Denaturation curves of nucleated and isodesmic systems. The normalized degree of aggregation *vs*. chloroform volume fraction *f* is fitted with the equilibrium model for both cooperative assemblies (a, **1** and **2**) as well as isodesmic assemblies (b, **3** and **4**). The equilibrium model includes a Gibbs free energy of monomer association that is linearly dependent on the chloroform volume fraction (20 °C; **1**, 24 μM; **2**, 19 μM; **3**, 14 μM; **4**, 146 μM). The critical chloroform volume fraction at which the aggregates of **1** are fully disassembled is found to increase with concentration (c, 20 °C) and decrease with temperature (d, 12 μM), in agreement with the equilibrium model.

To further rationalize the effect of solvent-composition on the self-assembly, the data are analysed by expanding the general nucleation-elongation equilibrium model as introduced in Chapter 1 (Fig 3.4a). In the analysis here, the equilibrium constant of elongation K_e is defined via $K_{e,f} = \exp(-\Delta G^{0\prime} / RT)$, with $\Delta G^{0\prime}$ being the Gibbs free energy gain upon monomer addition, R the gas constant and T the temperature. In analogy with protein denaturation models, the Gibbs free energy is assumed to be linearly dependent on the volume fraction of chloroform:

$$\Delta G^{0\prime} = \Delta G^{0} + m \cdot f, \tag{3.1}$$

where ΔG^0 represents the Gibbs free energy gain upon monomer addition in pure MCH and the dependence of $\Delta G^{0\prime}$ on f is described by the m-value. The cooperativity parameter σ is assumed to be independent of f (*i.e.* the m-value involved in the nucleation Gibbs free energy equals the m-value during elongation).

Simulations with the equilibrium model, shown in Figure 3.4, reveal a critical solvent composition below which cooperative growth of the assemblies occurs ($\sigma < 1$), whereas a gradual denaturation curve is obtained in case of an isodesmic growth mechanism ($\sigma = 1$). Furthermore, the position of the critical solvent composition is found to increase with the stability of the aggregate in pure MCH (proportional to the free energy release upon monomer addition, $-\Delta G^0$), and with the total monomer concentration, as is also observed experimentally.

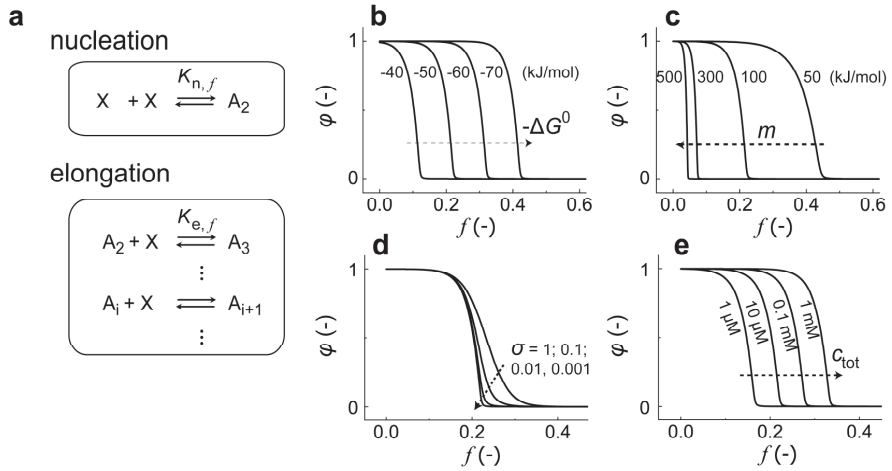

Figure 3.4 | Simulations with solvent-dependent equilibrium model. (a) Nucleation-elongation equilibrium model, where the dependence of the equilibrium constant of elongation $K_{e,f}$ on the chloroform volume fraction f is defined via $K_{e,f} = \exp(-\Delta G^{0\prime} / RT)$, with $\Delta G^{0\prime} = \Delta G^0 + m \cdot f$. The equilibrium constant of nucleation $K_{n,f}$ is defined via $K_{n,f} = \sigma \cdot K_{e,f}$. The influence of different parameters (ΔG^0, b; m-value, c; σ, d and c_{tot}, e) on the denaturation curves, *i.e.* degree of aggregation φ *vs.* f, is assessed by simulations with the equilibrium model. Parameters: nucleus size = 2, T = 293 K, ΔG^0 = –50 kJ/mol, m = 100 kJ/mol, σ = 0.001 and c_{tot} = 10 μM, unless stated differently.

Curve fitting by applying a global non-linear least square procedure using the equilibrium model gives a very good description of the data for both the assemblies growing via a cooperative (**1** and **2**) as well as an isodesmic (**3** and **4**) mechanism (Fig 3.3ab). The details of the fitting procedure are given in paragraph 3.7, Table 3.1 shows the fitted parameters for the different datasets. The enormous standard deviations obtained for the values of ΔG^0 and σ for the denaturation of **1** at a concentration of 12 μM can be rationalized by the fact that in these denaturation curves data points are lacking around the critical chloroform volume fraction. Especially this region of the denaturation curve is very dependent on σ, as shown in Figure 3.4d, and hence important for an accurate determination of the value of σ via the curve fitting procedure. Indeed, if σ is fixed during the curve fitting procedure, ΔG^0 can be determined with a much higher accuracy, as discussed in paragraph 3.7.

Table 3.1. Results of fitting the equilibrium model to the denaturation curves.

Compound	c_{tot} [μM]	T [°C]	ΔG^0 [kJ/mol]	m-value [kJ/mol]	σ [-]	p[a] [-]
1	12	20	-36 ± 1·10^5 [d]	75 ± 4	0 ± 2·10^4 [d]	1.06 ± 0.02
1	24	20	-37.1 ± 0.1	83 ± 3	0.16 ± 0.03	1.023 ± 0.008
1	63	20	-39 ± 3	(1.0 ± 0.2) ·10^2	0.2 ± 0.2	0.97 ± 0.03
1	12	10	-36 ± 1·10^6 [d]	57 ± 7	0 ± 2·10^5	1.03 ± 0.03
2	19	20	-31.5 ± 0.5	29 ± 3	(8 ± 8)·10^{-4} [d]	1.14 ± 0.05
3	14	20	-32.7 ± 0.3	81 ± 2	1[b]	1.09 ± 0.01
4	146	20	-24.0 ± 0.5	58 ± 3	1[b]	1.27 ± 0.05
1[c]	12 24 63	20	-39.9 ± 0.4	109 ± 3	0.25 ± 0.04	0.96 ± 0.01 0.99 ± 0.02 0.98 ± 0.02

[a] Normalization factor; [b] isodesmic fit; [c] multiple curve fit; [d] See text and paragraph 3.7 for a discussion of these standard deviations.

Moreover, the accuracy of the parameter values determined via the parameter estimation procedure depends on the correlation between the different parameters, which is a measure for the influence that a change in the value of one parameter (e.g. ΔG^0) has on the value of another parameter (e.g. σ) that is found via the optimization procedure. Whereas fitting the equilibrium model to the individual denaturation datasets of **1** acquired at concentrations of respectively 12 μM, 24 μM and 63 μM yields in all cases a significant correlation between ΔG^0 and the m-value, much lower correlation values are obtained when the datasets are fitted together via a multiple curve fitting procedure (see details in paragraph 3.7). Furthermore, also the problem of insufficient data around the critical solvent composition can be reduced via this multiple curve fitting approach. The values of ΔG^0 and σ obtained via multiple curve fitting (Table 3.1) are in good agreement with temperature-dependent analyses. As in the curve fitting procedure multiple denaturation curves obtained at different total concentrations of **1** are used, it can be concluded that the m-value that describes the decrease in stability of the aggregated state is independent of the total monomer concentration (Fig 3.3c).

In protein denaturation studies, a linear decrease of the Gibbs free energy of folding upon addition of denaturant is rationalized by the weak association of many denaturant molecules to the polyamide backbone which competes with the hydrogen bond formation involved in the protein folding itself.[24–26] As a consequence of the manifold of weak interactions of the denaturant molecules to one amide group, the resulting stability of the folded state can be described via a linear Gibbs free energy relation rather than taking into account all the denaturant association equilibria. Interestingly, detailed investigations by Moore and co-workers revealed a similar phenomenon in the folding of synthetic foldamers, in which the weak association of chloroform to the π-conjugated units of a foldamer results in a linear relation between Gibbs free energy of folding and chloroform concentration.[27] The results presented here show that this behaviour is not limited to intramolecular folding of proteins or synthetic foldamers but is more general and can also be observed in supramolecular systems with molecular components assembling via intermolecular association.

Traditionally, self-assembly mechanisms are often identified via concentration- or temperature-dependent studies.[28] However, the concentration-dependent transition from the monomeric to the fully aggregated state typically covers three (cooperative) to four (isodesmic) orders of magnitude in concentration.[28–30] Such an extended concentration-window often exceeds the limits of an experimental technique. Furthermore, temperature-dependent studies can be hampered by solubility, stability or lower critical solution temperature (LCST) issues as well. The denaturation studies on **1** and **2** show that cooperative aggregation processes display a critical solvent composition: an easily recognizable characteristic to distinguish between cooperative and isodesmic growth. Hence, denaturation studies provide the chemist with an alternative methodology to unravel self-assembly pathways involved in systems that cannot be studied by concentration- or temperature-dependent studies. Moreover, the influence of solvent composition on the stability of an assembly plays an important role in the dynamics of cooperative systems, as shown in the next part of this chapter.

3.3 Kinetic studies on disassembly by co-solvent addition

The disassembly kinetics of **1** are studied by manually mixing a solution of molecularly dissolved ROPV in chloroform (12 μM) with a solution of ROPV assemblies in MCH (12 μM) in different ratios. The chloroform-induced disappearance of the helical ROPV assemblies in time is followed by probing the CD effect at 466 nm (Fig 3.5a). Intriguingly, the rate, characterized by the time at which 90% of the conversion towards the equilibrium state is obtained (*t*-90), shows a minimum close to the critical chloroform volume fraction as obtained from the equilibrium denaturation curves (*i.e.* f_{crit}, Fig 3.5b). In a similar experiment performed at a higher total concentration of **1** (24 μM), the chloroform volume fraction at which the slowest disassembly is observed again coincides with the critical chloroform volume fraction obtained from the thermodynamic denaturation curve, which has a higher value at this concentration (Fig 3.5cd).

3.4 Influence of mixing protocol on self-assembly kinetics

To further investigate the disassembly kinetics, a manual mixing experiment is performed at a higher total concentration of **1** (63 μM, Fig 3.6a). Again, the disassembly kinetics is slowest at the critical chloroform volume fraction. However, disassembly experiments with chloroform volume fractions below 12% show an increasing CD intensity in time. Apparently, directly after mixing of the MCH and chloroform solutions, an overshoot in the disassembly occurs, and subsequently the system reassembles back to the equilibrium state.

The disassembly overshoot as shown in Figure 3.6 can be rationalized by the influence of inefficient mixing in the initial stages of the experiment. Imagine a mixing experiment that aims for a homogeneous mixture of 7.5 v/v% chloroform in MCH (Fig 3.6b). The experiment is performed such that halfway in the mixing procedure, the upper half of the cuvette contains 15 v/v% chloroform, whereas the lower half contains 0 v/v% chloroform. Since the chloroform volume fraction in the top part exceeds f_{crit} (12.5 v/v%), aggregated material in the upper half of the cuvette disassembles quickly, whereas no disassembly takes place in the lower half of the cuvette. Further mixing results in a homogeneous system with 7.5 v/v% chloroform and containing 50% of the assemblies present in the MCH solution before the addition of the chloroform solution (*i.e.* the average of complete disassembly in one half of the cuvette and no disassembly in the other half). As a result, after complete mixing, the degree of aggregation equals 50% of the degree of aggregation in pure MCH (0.5). However, the degree of aggregation under equilibrium conditions at $f = 0.075$ equals 0.9, resulting in a reassembly in time.

Although in reality the experiment does not occur via a two-step mixing protocol, this *Gedankenexperiment* clearly demonstrates the influence of the mixing efficiency on the disassembly dynamics of one-dimensional assemblies. Gratifying, no overshoot in the disassembly kinetics is observed when the disassembly experiments are performed in a stopped-flow setup that enables very fast and efficient mixing using a Berger Ball mixer.

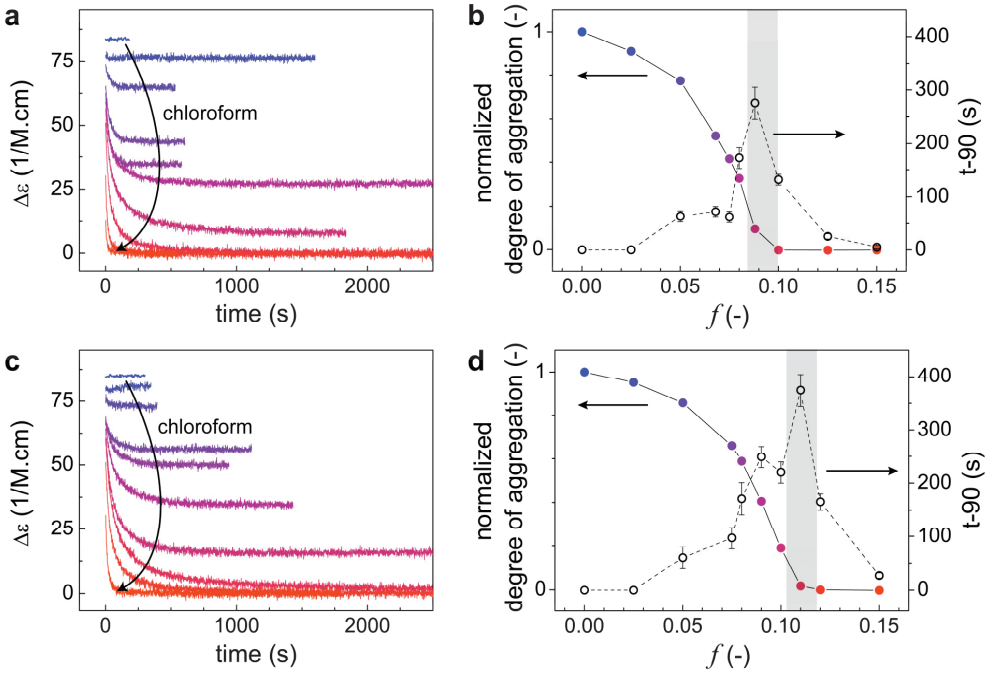

Figure 3.5 | Solvent-dependent disassembly rate of ROPV. The disassembly of **1** in MCH induced by addition of **1** in chloroform is followed in molar ellipticity ($\Delta\varepsilon$) *vs.* time for different chloroform volume fractions. The experiments are performed at a concentration of 12 μM (a,b) and 24 μM (c,d) at 20 °C. The normalized degree of aggregation *vs.* chloroform volume fraction is derived from the steady state CD intensities in the kinetic experiments. For both concentrations, the time at which 90% of the conversion towards the equilibrium state is obtained (t-90) *vs.* f shows a maximum close to the critical chloroform volume fraction f_{crit} at which just enough chloroform is added to induce full disassembly.

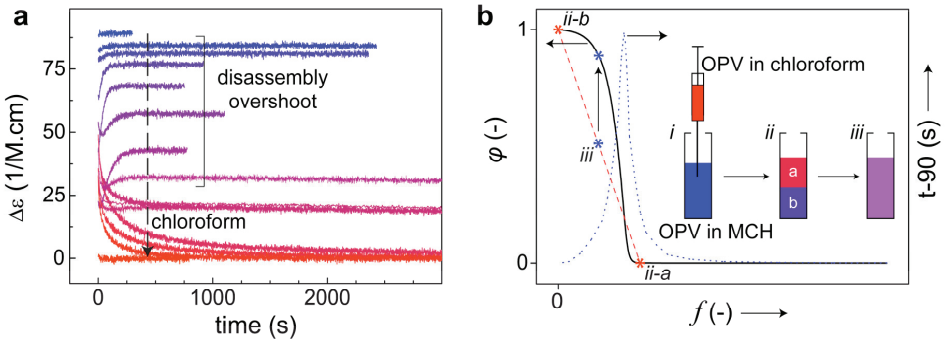

Figure 3.6 | Mixing effects cause overshoot in disassembly of ROPV helices. (a) Disassembly kinetics of **1** in MCH, induced by addition of **1** in chloroform at high concentration (63 μM, 20 °C). (b) The disassembly overshoot can be rationalized by inefficient mixing in the initial stages of the disassembly experiment. To illustrate this, we consider the mixing of OPV in MCH with OPV in chloroform, aiming for f = 0.075 (*i*). Due to insufficient mixing however, initially in the upper half of the cuvette f equals 0.15

(*ii-a*), whereas in the lower half of the cuvette *f* equals 0 (*ii-b*). As a consequence, rapid disassembly is obtained in *ii-a*, whereas no disassembly takes place in *ii-b*. Subsequently, further mixing results in a homogeneous mixture (*iii*, $f = 0.075$), with an average degree of aggregation on the red dashed line. However, the equilibrium average degree of aggregation at $f = 0.075$ (0.90) is larger than the degree of aggregation obtained after mixing (0.50), resulting in reassembly.

3.5 Unravelling and simulating the influence of solvent composition on aggregation dynamics via a kinetic model

The minimum rate encountered in the disassembly of ROPV assemblies close to f_{crit} holds an intriguing resemblance to protein unfolding dynamics, where a minimum rate is observed at the thermodynamic midpoint of the denaturation curve. In protein unfolding, this phenomenon is rationalized by explicitly taking into account the effect of the denaturant concentration [denaturant] on the rate constants of folding (k_F) and unfolding (k_U) using the relation $\log(k_F) = \log(k_F^0) - m_F \cdot$[denaturant] and $\log(k_U) = \log(k_U^0) + m_U \cdot$[denaturant], with k_U^0 and k_F^0 the rate constants in pure water.[18–20] Inspired by this approach, here we modify the kinetic model introduced in the previous chapter in an attempt to simulate the disassembly kinetics. Thereafter, we will – guided by these simulations – unravel what is the cause of the observed disassembly results, and further analyse the generality of the observed effect of solvent-composition on assembly and disassembly dynamics.

3.5.1 Kinetic model with solvent-dependent rate constants

To simulate the disassembly kinetics, the kinetic model introduced in Chapter 2 is extended with solvent dependent rate constants. For simplicity, only one pathway, *i.e.* the thermodynamically stable pathway, is taken into account. The solvent dependency of the forward and backward rate constants a_f and c_f is defined via

$$\log(a_f) = \log(a) - m_a \cdot f, \tag{3.2}$$

$$\log(c_f) = \log(c) + m_c \cdot f, \tag{3.3}$$

respectively, with a_f and c_f the rate constants in pure MCH. Rate constant b_f is defined via

$$b_f = c_f/\sigma, \tag{3.4}$$

with cooperativity parameter σ. Equilibrium constants of nucleation K_n and elongation K_e in pure MCH are defined via $K_e = a/c$ and $K_n = \sigma \cdot K_e$. Again, σ is assumed to be independent of *f*.

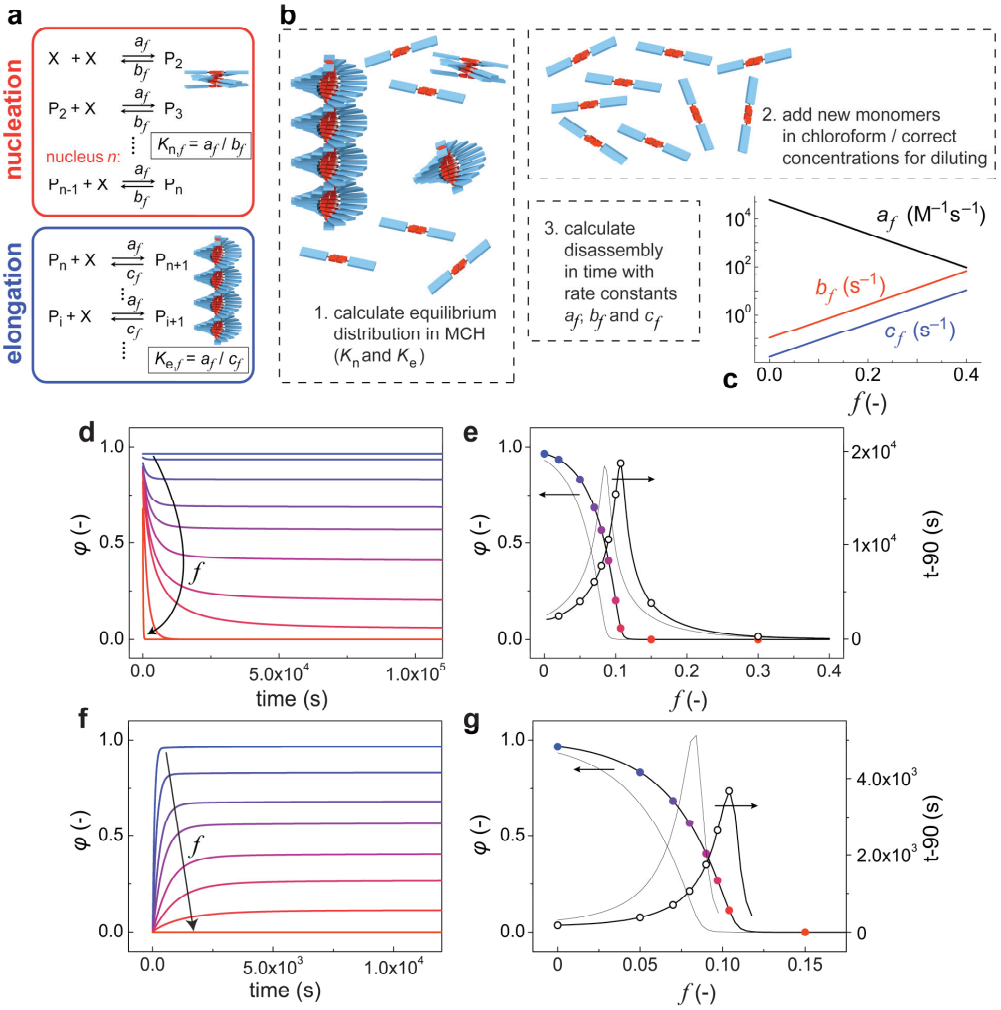

Figure 3.7 | Simulated solvent-dependent disassembly and assembly kinetics. (a) Kinetic nucleation-elongation model to simulate (dis)assembly of ROPV helices, in which the hydrogen-bonded OPV dimer (X) is considered as the monomer. (b) Schematic representation of followed approach to simulate the disassembly kinetics: (1) The equilibrium distribution of all species with different stack lengths (i = 1, i = 2, etc.) in pure MCH is calculated via the equilibrium model, using K_n and K_e. (2) New monomers that originate from the chloroform phase are added to the monomers present in the MCH solution, and the resulting monomer concentration as well as the concentrations of all aggregate species are corrected for dilution due to mixing of the MCH and chloroform phases. (3) Using these concentrations as start conditions, the subsequent disassembly kinetics are simulated using the rate constants a_f, b_f and c_f with values in accordance with the chloroform/MCH ratio. (c) Relation between rate constants a_f, b_f and c_f and chloroform volume fraction in MCH (based on equations 3.2–3.4, $a = 6{\cdot}10^4$ $M^{-1}s^{-1}$, $c = 1.71{\cdot}10^{-2}$ s^{-1}, $m_a = 7$, $m_c = 7$, $\sigma = 0.16$). (d) Simulated disassembly kinetics with increasing amounts of chloroform. (e) The time at which 90% of the conversion towards the equilibrium state is obtained (t-90) shows a minimum rate

close to the critical chloroform volume fraction. (f) The assembly kinetics are simulated starting from only free monomers in different chloroform/MCH ratios, with solvent-dependent rate constants defined similar to the disassembly simulations. (g) The time at which 90% of the conversion towards the equilibrium state is obtained (*t*-90) shows a minimum assembly rate around the critical chloroform volume fraction. The kinetic curves are simulated with a concentration of 12 μM (n = 2); the thin black lines in pane e and g display results simulated with a concentration of 6 μM.

To simulate the disassembly kinetics induced by the addition of ROPV in chloroform to the solution of ROPV assemblies in MCH, first the concentrations of all oligomers and helical aggregates in pure MCH are calculated via the equilibrium model using realistic values of K_n and K_e (Fig 3.7b). Subsequently, starting concentrations for the dynamic simulations are obtained by addition of fresh monomers to the monomer pool in MCH and correcting the resulting monomer concentration as well as the concentrations of all aggregate species for dilution due to mixing of the MCH and chloroform phases. Thereafter, the disassembly kinetics at the respective chloroform/MCH ratio are simulated using these starting concentrations together with the rate constants a_f, b_f and c_f, defined via equations 3.2–3.4 (Fig 3.7bc). The value of the forward rate constant a (*i.e.* in pure MCH) is chosen close to the value found in the assembly of OPV (Chapter 2). The values of the backward rate constant c (which equals a/K_e), m_a, m_c and σ are chosen so as to match the experimental melting and denaturation curves obtained under thermodynamic control. Indeed, simulations of the disassembly dynamics performed at different chloroform volume fractions reveal a minimum disassembly rate around f_{crit}, as is observed experimentally (Fig 3.7de). However, the simulated maximum values of *t*-90 at both OPV concentrations are approximately two orders of magnitude larger than the experimentally observed values. This difference can be explained by the fact that the kinetic model describes disassembly of aggregates by monomer addition and dissociation reactions only and does not consider fragmentation of aggregates into two oligomers. Involvement of these fragmentation reactions results in much faster disassembly kinetics and hence lower values of *t*-90, as discussed in Chapter 6. Nevertheless, the qualitative kinetic model presented here correctly predicts a minimum disassembly rate at the critical chloroform volume fraction, even though it does not capture the full complexity of the disassembly kinetics because fragmentation of one-dimensional aggregates is not taken into account. It should be mentioned that involvement of oligomer reactions or fragmentation in the disassembly process has no influence on the thermodynamic analysis. Even though the equilibrium model describes the assembly process by sequential monomer association and dissociation, also oligomer reactions and fragmentation are implicitly taken into account due to the principle of detailed balance.

3.5.2 What causes the minimum rate at the critical solvent composition?

The resemblance between the minimum protein (un)folding rate at the midpoint of the denaturation curve and the minimum disassembly rate of ROPV at the critical solvent composition is remarkable, because of the differences in non-covalent interactions involved (dipolar *vs*. hydrogen-bonding), reaction order (intermolecular *vs*. intramolecular) and solvent conditions (non-aqueous *vs*. aqueous). To further analyse this phenomenon, the influence of the cooperativity in the growth of the aggregates is assessed by kinetic simulations with the model. Interestingly, if cooperative effects are diminished ($\sigma \rightarrow 1$), the minimum disassembly rate appears at lower values of f and in case of isodesmic growth ($\sigma = 1$), the rate continuously increases with f. This demonstrates that cooperativity is a key parameter in observing the chevron-type disassembly kinetics (Fig 3.8).

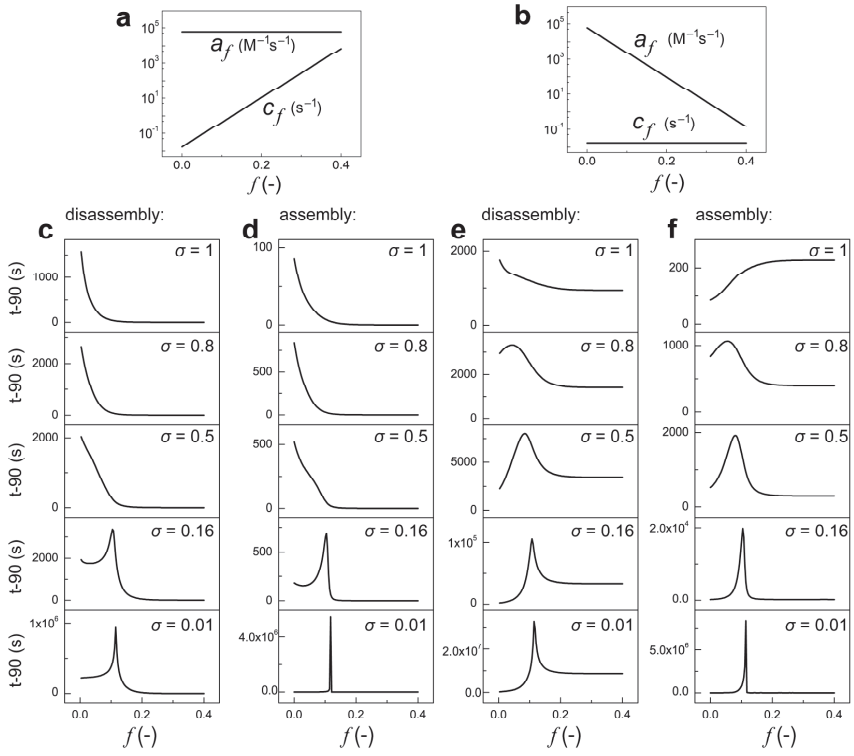

Figure 3.8 | Influence of cooperativity on minimum assembly and disassembly rate at critical solvent composition. The influence of cooperativity σ on the disassembly and assembly rate is assessed by performing simulations with the kinetic model. t-90 is followed as a function of chloroform volume fraction f for different values of σ, 1) for a mechanism in which c_f increases with f and a_f is constant (m_a = 0, m_c = 14, a) and 2) for a mechanism in which the forward rate constant a_f decreases with f and backward rate constant c_f is solvent-independent (m_a = 14, m_c = 0, b). In both cases only a minimum disassembly (c, e) or assembly (d, f) rate is obtained around f_{crit} if σ is small: cooperativity is required to obtain a minimum rate at the critical solvent composition.

The minimum disassembly rate observed around the critical chloroform volume fraction can be rationalized by the influence of solvent composition on the length distribution. Upon increasing the fraction of good solvent (f), the equilibrium concentration of long stacks decreases, whereas the concentration of short stacks, (pre-nucleus) oligomers and monomers increases (Fig 3.9ab). As a consequence, addition of free monomers in chloroform to a solution of long stacks in pure MCH results in two effects which occur simultaneously: 1) disassembly of long aggregates to their new (shorter) equilibrium length as a consequence of the increased chloroform/MCH ratio; 2) assembly of new monomers, either originating from the chloroform phase or from disassembly of long stacks, into new oligomers and short aggregates (Fig 3.9c). The first effect becomes stronger upon increasing f, either as a result of an increasing backward rate constant c_f or due to the decreasing forward rate constant a_f, both hampering elongation of long stacks. However, the same influence of chloroform on the rate constants deactivates the second effect, thereby slowing down the formation of new oligomers and short aggregates upon increasing f. Since the concentration of short aggregates and oligomers is negligible beyond f_{crit}, the first effect dominates the disassembly rate in the regime $f > f_{crit}$, resulting in a rate that increases with the fraction of good solvent in this regime. However, in the regime $f < f_{crit}$, the monomers resulting from the disassembly of long stacks aggregate into new short stacks, as demonstrated in Figure 3.9b. This formation of short aggregates is slowed down upon increasing the chloroform volume fraction, both due to the decreasing forward rate constant a_f as well as the increasing backward rate constants b_f (nucleation) and c_f (elongation). For a cooperative assembly process in which a nucleation step is involved in the formation of new aggregates, this results in a minimum equilibration rate at the critical chloroform volume fraction.

Next, the influence of solvent composition on the aggregation kinetics is investigated by simulating the build-up of aggregates starting from a solution of free monomers (Fig 3.7fg). Again, an important influence of nucleation is encountered (Fig 3.8df). Only for small values of σ, a minimum aggregation rate is observed at f_{crit}. In analogy to the influence of nucleation on the equilibration of ROPV assemblies upon addition of chloroform, this phenomenon can be rationalized by the fact that for aggregation kinetics the rate of equilibration is determined by 1) the amount of material that is aggregated under equilibrium conditions, and 2) the formation rate of new aggregates. Both the amount of material that aggregates under equilibrium conditions as well as the formation rate decrease with f. In case of cooperative growth, the nucleation of new aggregates – which is hampered upon increasing f – dominates the process. As a result, the simulated assembly rate for cooperative systems decreases up to f_{crit}.

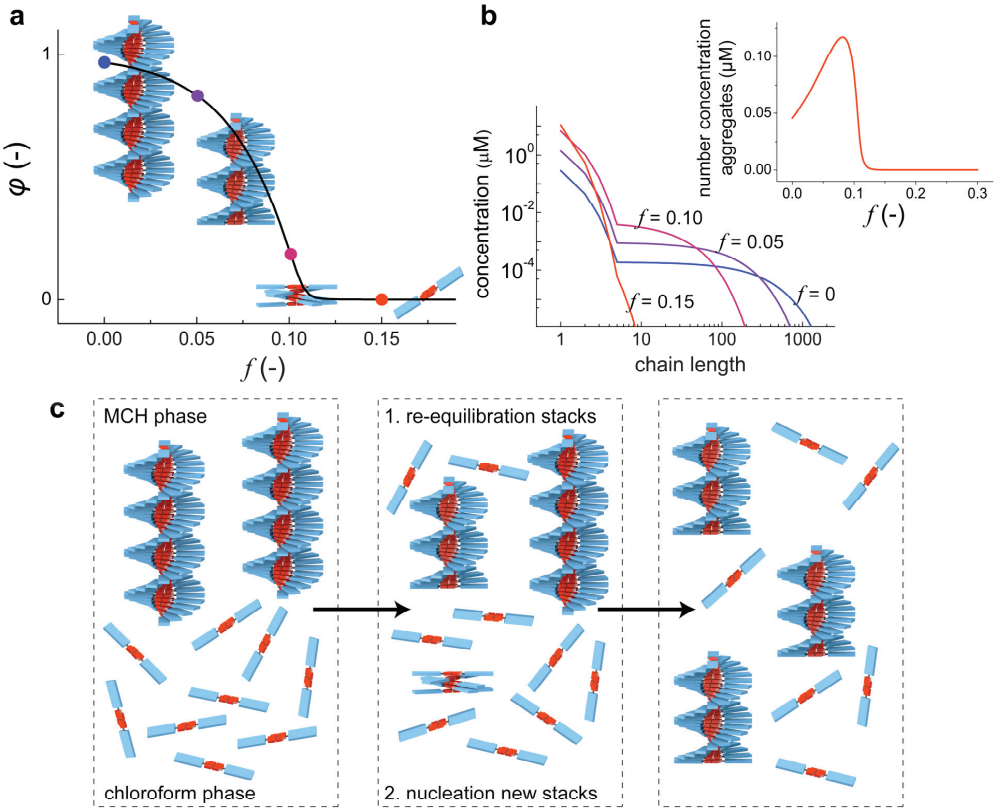

Figure 3.9 | Influence of co-solvent on chain length distribution. (a) Degree of aggregation φ *vs.* volume fraction of good solvent f calculated under equilibrium conditions ($K_e = 3.5 \cdot 10^6$ M^{-1}, OPV dimer concentration = 12 μM, $m = 7.9 \cdot 10^4$ J/mol, $n = 5$, $\sigma = 0.16$). (b) For different points on the denaturation curve, the equilibrium distribution (concentration *vs.* chain length) is calculated via the equilibrium model. The inset shows the total number concentration of aggregates as a function of f. (c) Schematic representation of development of assemblies in time after mixing the MCH and chloroform phase: both the long stacks as well as the new monomers re-equilibrate towards the new equilibrium state via disassembly and nucleation of new stacks, respectively.

3.5.3 Analysing the generality of the effect of solvent-composition on assembly and disassembly dynamics

To further extend the insights from the kinetic model, simulations are performed on the aggregation kinetics in which the dependence of the forward and backward rate constants on the solvent composition is varied. In general, the thermodynamic stability of the assemblies as a function of chloroform volume fraction, f, is determined by the value of m in eq. 3.1, with $m > 0$. On the other hand, the stability of the assemblies can be represented by the equilibrium constant of elongation $K_{e,f} = a_f / c_f$, in which the dependence of rate constants a_f and c_f on f is

determined via m_a and m_c, respectively (eq. 3.2 and 3.3). Combining these two relations, it can be derived that $K_{e,f}$ decreases with f if $m_a + m_c > 0$, as shown in paragraph 3.7. Hence, disassembly upon addition of chloroform occurs when both rate constants increase with f, when both rate constants decrease with f and all possibilities in between, as long as the requirement $m_a + m_c > 0$ is met (Fig 3.10). The kinetic assembly simulations show that if rate constants a_f and c_f are both decreasing functions with respect to f, a minimum assembly rate is obtained at f_{crit} as a result of the decreasing rate of monomer association. If rate constant a_f decreases with respect to f and rate constant c_f increases with f, also the increasing rate of monomer dissociation slows down the assembly towards f_{crit}. However, if rate constant a_f increases with f, an interesting dependence of t-90 on solvent composition can be observed. Initially, the assembly rate increases with f, and subsequently slows down towards f_{crit}. Apparently, for low values of f the increasing a_f dominates the assembly rate, whereas close to f_{crit} the increasing c_f is dominant and slows down the assembly. In analogy to this behaviour, comparable results are obtained in simulations on disassembly kinetics (Fig 3.10). This indicates that, independent of the actual influence of solvent composition on the forward and backward rate constants, addition of a destabilizing co-solvent results in a slowing down of the rate of both assembly as well as disassembly close to the critical solvent composition.

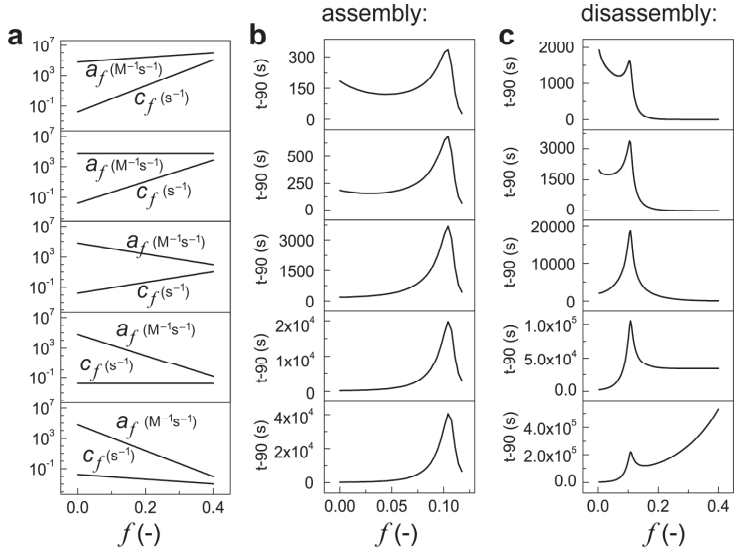

Figure 3.10 | Influence of the dependence of the rate constant on f for assembly and disassembly kinetics. Assembly (b) and disassembly (c) kinetics simulated with the kinetic nucleation-elongation model show that if the slope of backward rate constant c_f as a function of f is less negative compared to the slope of forward rate constant a_f (*i.e.* $m_a + m_c > 0$), a minimum assembly or disassembly rate is obtained close to the critical solvent composition. Pane (b) and (c) show the dependence of t-90 on f for the different relations between rate constants and solvent composition that are shown in the pane (a). From top to bottom: $m_a = -3$, $m_c = 17$; $m_a = 0$, $m_c = 14$; $m_a = 7$, $m_c = 7$; $m_a = 14$, $m_c = 0$; $m_a = 17$, $m_c = -3$. The rate constants are based on equations 3.2–3.4, $a = 6{\cdot}10^4$ $M^{-1}s^{-1}$, $c = 1.71{\cdot}10^{-2}$ s^{-1}, $\sigma = 0.16$, $n = 5$, $c_{tot} = 12$ μM.

3.6 Conclusions and discussion

The present study shows the influence of solvent conditions on the stability and dynamics of self-assembled systems. In analogy to protein denaturation models and studies on the unfolding of synthetic foldamers, addition of a co-solvent that weakly associates with the monomer (thereby acting as a "good" solvent) results in a linear decrease of the Gibbs free energy for monomer addition. The resulting disassembly process reveals a critical solvent composition for aggregates that assemble via a cooperative mechanism, whereas a gradual disassembly profile is observed for assemblies that grow via an isodesmic mechanism.

The disassembly experiments reveal a minimum rate of OPV disassembly close to the critical volume fraction of the good solvent. Because of the solvent-dependent dynamics, the mixing protocol applied to induce disassembly is shown to have important consequences for the time-dependent development of the aggregates. Insufficient mixing can initially result in a (fast) disassembly in one part of the solution, whereas in the final obtained homogeneous solution aggregation is again initiated. The time scale of its assembly and disassembly, which is in the order of 5 – 30 min., makes OPV an ideal model system to study one-dimensional assembly mechanisms in detail. Analysis of the dynamics of the other systems studied in this chapter, **2** – **4**, have shown that it is too fast for reliable studies on the assembly and disassembly kinetics, meaning that their assembly can only be studied under equilibrium conditions. However, the experimental results on OPV disassembly provide us general insights, as evidenced by the kinetic model developed in this chapter. By taking into account the influence of solvent on the rate constants, the model captures the experimentally observed behaviour and predicts a minimum disassembly rate at the critical solvent composition as well. By simulating the solvent-dependent kinetics using this model, we trace the origin of the slowest dynamics (both in assembly and disassembly) at the critical good/poor solvent ratio observed in cooperative systems back to *de novo* nucleation of aggregates.

The observed relations between solvent composition and time-dependent development of a self-assembled system are envisioned to have important consequences for the formation of functional supramolecular systems. Previously it has been shown that the development of 1D self-assemblies can be performed via a fast process by rapid dispersion of molecules into a poor solvent. However, if the association is too strong (e.g. due to strong interactions between the side chains), this methodology produces large agglomerates that precipitate.[13] To slow down the assembly process, the mixing of good and poor solvent can be retarded via phase transfer[13, 31] (using a non-miscible combination of good and poor solvent) or vapour diffusion.[32–34] However, the current study shows that the self-assembly rate can be further controlled by the ratio between good and poor solvent as well. This finding expands the toolbox to control the formation of one-dimensional nanomaterials across multiple length and time scales.

Moreover, in the stepwise assembly of multicomponent structures, a critical aspect that needs to be achieved is the exclusive growth of a new molecular building block on previously formed assemblies without nucleation of the new material. The most convenient way to

achieve this is by addition of a new component in a good solvent to a solution containing aggregates in such a way that the new component cannot form new nuclei *de novo*. However, unless the assemblies formed in previous steps are locked by covalent fixation[35–37], extremely strong noncovalent interactions such as metal-ion binding[38] or crystallization[39–41], the addition of a good solvent affects their stability as well. These factors complicate the design of multistep noncovalent syntheses. For example, the highly nonlinear relation between dynamics and solvent composition can, in case of an inhomogeneous addition of good solvent, result in a disassembly overshoot of the initially formed architectures. Only by understanding the influence of good and poor solvents on the thermodynamics and kinetics of self-assembly processes optimized noncovalent synthetic strategies can be developed which will pave the way towards functional multicomponent supramolecular systems.

3.7 Details of experiments and simulations

Instrumentation and Material. The syntheses of molecules **1**[42], **2**[21], **3**[43] and **4**[22] are described elsewhere. **1** is kindly provided by dr. Christophe Grenier and dr. Subi J. George; **2** is provided by dr.ir. Tristan Mes; **3** is provided by dr.ir. Anja R. A. Palmans and **4** by dr.ir. Floris A. Helmich. CD spectra are recorded using a Jasco J-815 CD spectrometer. Sensitivity, response time and scanning rate are chosen appropriately. The temperature is controlled using a Jasco Peltier temperature controller with a range of -10 – 110 °C and adjustable temperature slope. UV/Vis spectra are recorded using a Jasco V-650 UV/Vis spectrometer. The temperature is controlled using a Jasco Peltier temperature controller with a range of -10 – 110 °C and adjustable temperature slope. The stopped-flow experiments are conducted via a procedure as described in Chapter 2. Solvents were obtained from Sigma-Aldrich (MCH, spectrophotometric grade, 99%) and Biosolve (chloroform, AR, > 99.9%) and used as received.

Denaturation experiments. The denaturation experiments are performed by adding solutions of the monomer in chloroform (good solvent) in different amounts to solutions of the aggregates in methylcyclohexane (MCH). The disassembly is probed by CD (**1**, 466 nm; **2**, 316 nm; **3**, 286 nm) or UV/Vis (**4**, at maximum intensity ranging from 518–528 nm) spectroscopy under equilibrium conditions verified by time-dependent experiments. The kinetic experiments on the disassembly of ROPV described in Figure 3.5 and Figure 3.6 are performed by manually mixing of the solutions of ROPV in chloroform and ROPV in MCH. The experiments are conducted in quartz cuvettes with optical path lengths of 1 cm (12 μM), 5 mm (24 μM) and 1 mm (63 μM). Molar ellipticity $\Delta\varepsilon$ in [1/M·cm] is found via $\Delta\varepsilon$ = CD [mdeg] / (32982 x concentration OPV [M] x optical path length [cm]). The time at which 90% of the conversion towards the equilibrium state is obtained (*t*-90) is determined by the time *t* at which (CD_0 – CD(*t*)) / (CD_0 – $CD_{steady\ state}$) = 0.90. In this equation, $CD_{steady\ state}$ represents the final CD-value, CD(*t*) the CD-value at time *t*, and CD_0 the initial CD-value in pure MCH corrected for dilution with the chloroform phase (*i.e.* $CD_0 = CD_{MCH}\cdot(1 - f)$).

Fitting the solvent-equilibrium model to denaturation curves. To analyse the denaturation curves acquired under equilibrium conditions, the equilibrium model as explained in paragraph 2.7 is applied. To fit the equilibrium model to the denaturation data acquired on **1** – **4**, the normalized degree of aggregation is deduced from the changes observed in CD or UV/Vis. For **1** – **3**,

$$\text{normalized degree of aggregation } (f) = \frac{\mathrm{CD}(f)}{\mathrm{CD}(f=0)}, \tag{3.5}$$

whereas for **4**,

$$\text{normalized degree of aggregation } (f) = \frac{\text{UV/Vis}(f) - \text{UV/Vis}(f=0)}{\text{UV/Vis}(f=1) - \text{UV/Vis}(f=0)}. \quad (3.6)$$

It should be mentioned that the normalized degree of aggregation obtained via eq. 3.5 and 3.6 equals 1 in pure MCH (f = 0). However, if the experimental CD or UV/Vis value obtained in pure MCH is not yet saturated at the temperature at which the experiment is performed, a normalization factor p should be introduced to match the normalized degree of aggregation found via eq. 3.5 or 3.6 and the calculated degree of aggregation φ. The calculated degree of aggregation φ is defined as

$$\varphi = \frac{x_{tot} - x}{x_{tot}} \quad (3.7)$$

for **2** – **4** (*i.e.* all species with $i > 1$ are considered as aggregates). In the case of **1**, the CD signal is assumed to originate from solely post-nucleus aggregates. Hence, the degree of aggregation for **1** is considered to be equal to:

$$\varphi = \frac{x_{tot} - x - \sum_{2}^{n} i \cdot p_i}{x_{tot}}, \quad (3.8)$$

with n = 5. In eq. 3.7 and 3.8, x represents the dimensionless concentration of the monomer (which is the hydrogen-bonded ROPV dimer in case of **1**). In eq. 3.8, p_i represents the dimensionless concentration of aggregate P with length i.

Taken together, four parameters need to be optimized to fit the equilibrium model to the data (normalized degree of aggregation *vs*. f): ΔG^0, m, σ and p. The optimized parameters are found via a non-linear least-squares analysis where the sum of the squared residuals is minimized using Matlab (*lsqnonlin* solver). The data are fitted with non-linear least squared regression, using the Levenberg-Marquardt algorithm. To analyse the data acquired at multiple concentrations in one curve fitting procedure, the sum of all squared residuals is minimized using the same procedure. To avoid the program getting trapped in a local minimum, 100 different initial parameter sets are defined, and the best fit is taken as the final solution for the values of ΔG^0, m, σ and p. The different initial parameter sets are defined using a *Latin hypercube sampling* method (Matlab function *lhsdesign*). Initial parameter values are in the intervals $\Delta G^0 \in$ [–50, –20] kJ/mol, $m \in$ [50, 120] kJ/mol, $\sigma \in$ [0, 1] and $p \in$ [0.9, 1.1], the boundaries are adjusted if necessary.

The covariance matrix *Cov* is found via:

$$Cov = \frac{resnorm}{\#DOF}\left(Jacobian^T \cdot Jacobian\right)^{-1}, \quad (3.9)$$

where *resnorm* is the sum of the normalized residuals in the fitting procedure, *#DOF* is the number of degrees of freedom (which equals the number of data points minus the number of fitting parameters).[44, 45] The *Jacobian* is a matrix in which the number of columns is given by the number of free parameters and the number of rows equals the number of data points. Each element $Jacobian_{ij}$ represents the derivative of the residual for data point i to parameter j. The standard deviation of each parameter i can be found by taking the square root of Cov_{ii}. Subsequently, the elements of the correlation matrix *Corr* (Pearson correlation coefficients) are obtained via:

$$Corr_{ij} = \frac{Cov_{ij}}{\sqrt{Cov_{ii} Cov_{jj}}}. \quad (3.10)$$

The off-diagonal values $Corr_{ij}$ (with $i \neq j$) represent the correlation between parameter i and j, with $Corr_{ij} = 0$ indicating no correlation and $C_{ij} = \pm 1$ indicating maximum correlation. Furthermore, $Corr_{ij} = Corr_{ji}$, and $Corr_{ii} = 1$.

To illustrate the fact that lower correlation values are obtained when the datasets are fitted together via the multiple curve fitting procedure, rather than individually, the correlation matrices of the individual and multiple curve fits are displayed below.

Individual fits:

1, 12 μM, 20 °C

	ΔG^0	m	σ	p
ΔG^0	1	0.01	-1.00	-0.01
m		1	-0.01	-0.88
σ			1	0.01
p				1

1, 24 μM, 20 °C

	ΔG^0	m	σ	p
ΔG^0	1	-0.98	-0.86	0.77
m		1	0.76	-0.82
σ			1	-0.47
p				1

1, 63 μM, 20 °C

	ΔG^0	m	σ	p
ΔG^0	1	-0.99	-0.86	0.71
m		1	0.80	-0.74
σ			1	-0.43
p				1

Multiple curve fits:

1, 12 μM (1), 24 μM (2), 63 μM (3), 20 °C

	ΔG^0	m	σ	p_1	p_2	p_3
ΔG^0	1	-0.94	-0.74	-0.16	0.38	0.13
m		1	0.48	0.12	-0.46	-0.21
σ			1	0.26	0.00	0.15
p_1				1	0.07	0.11
p_2					1	0.25
p_3						1

The equilibrium model is also fitted to temperature-dependent data on the assembly of ROPV (24 μM, 102 μM). Based on the obtained values for the enthalpies and entropies of nucleation and elongation (ΔH_e^0 = (–140.9 ± 0.3) kJ/mol, ΔS_e^0 = (–343.3 ± 0.9) J/K.mol, ΔH_n^0 = (–141 ± 0.3) kJ/mol, ΔS_n^0 = (–356.8 ± 0.9) J/K.mol), $\Delta G^0 = \Delta H_e^0 - T \cdot \Delta S_e^0$ = –40.4 kJ/mol and σ = 0.20 at 20 °C. The resemblance of these values, found via temperature-dependent experiments, to the results obtained upon analysing the solvent-dependent assembly of **1** at multiple concentrations corroborates the validity of the latter methodology.

The very low correlations obtained upon fitting the equilibrium model to the first dataset (12 μM) are probably related to the lacking data points around f_{crit}, that result in very large standard deviations as well. If σ is fixed at a value of σ = 0.16, the following parameter values are obtained: ΔG^0 = (–37.5 ± 0.4) kJ/mol; m = (83 ± 5) kJ/mol; p = 1.04 ± 0.02, indicating that fixing one parameter can reduce the standard deviations on the other parameters. However, this strategy does not yield a reduction in the correlation values:

1, 12 μM, 20 °C, σ = 0.16

	ΔG^0	m	p
ΔG^0	1	-1	0.87
m		1	-0.85
p			1

Kinetic experiments and modelling. In the supramolecular polymerization model, the hydrogen bonded OPV dimer is considered as the building-block (*i.e.* monomer) in the aggregation process, similar to the model applied in Chapter 2. In the previous chapter, two assembly pathways are taken into account to describe the assembly process: a kinetically *vs*. thermodynamically controlled pathway that are competing for the same free monomer. However, in the analysis followed here only one assembly pathway towards the thermodynamically stable aggregate is considered. This simplification is justified because of the limited influence of the kinetic assembly pathway in the simulation of disassembly kinetics. Moreover, this simplification extends the applicability of the simulations to other supramolecular systems.

Also if the addition of pure chloroform – rather than OPV monomers in chloroform – to OPV assemblies in MCH is simulated, a minimum depolymerisation rate at f_{crit} is observed for cooperative systems. The overshoot in disassembly, as is observed at the highest concentration (63 μM, Fig 3.6), could potentially also be explained by the fact that the curve which represents the degree of aggregation under equilibrium conditions as a function of f exceeds the initial degree of aggregation obtained upon homogeneous mixing, which is on the line $y = 1 - f$. However, at this concentration this is not the case.

As follows from eq. 3.1, $\Delta G^{0\prime}$ increases with f if $m > 0$, resulting in a decrease of $K_{e,f}$ with f. Alternatively, $K_{e,f}$ can be found via the rate constants of monomer addition and dissociation:

$$\begin{aligned} \log(K_{e,f}) &= \log\left(\frac{a_f}{c_f}\right) = \log\left(\frac{a}{c}\right) - \left(m_a + m_c\right) f = \log\left(K_e\right) - \left(m_a + m_c\right) f, \\ \ln(K_{e,f}) &= \ln\left(K_e\right) - 2.3026\left(m_a + m_c\right) f. \end{aligned} \tag{3.5}$$

Subsequently expressing $K_{e,f}$ and K_e in $\Delta G^{0\prime}$ and ΔG^0, respectively, yields:

$$\Delta G^{0'} = \Delta G^0 + 2.3026 \cdot \mathrm{R}T\left(m_a + m_c\right) f. \tag{3.6}$$

As a result, m equals $2.3026 \cdot \mathrm{R}T\,(m_a + m_c)$ and $m_a + m_c > 0$ if $m > 0$.

3.8 References

[1] Mes, T.; Smulders, M. M. J.; Palmans, A. R. A.; Meijer, E. W. *Macromolecules*, **2010**, *43*, 1981.
[2] Mammen, M.; Simanek, E. E.; Whitesides, G. M. *J. Am. Chem. Soc.* **1996**, *118*, 12614.
[3] Bouteiller, L.; Van der Schoot, P. *J. Am. Chem. Soc.* **2012**, *134*, 1363.
[4] Cook, J. L.; Hunter, C. A.; Low, C. M. R.; Perez-Velasco, A.; Vinter, J. G. *Angew. Chem., Int. Ed.* **2007**, *46*, 3706.
[5] Ponnuswamy, N.; Pantoş, G. D.; Smulders, M. M. J.; Sanders, J. K. M. *J. Am. Chem. Soc.* **2012**, *134*, 566.
[6] Oh, J. H.; Lee, H. W.; Mannsfeld, S.; Stoltenberg, R. M.; Jung, E.; Jin, Y. W.; Kim, J. M.; Yoo, J.-B.; Bao, Z. *Proc. Natl. Acad. Sci. USA* **2009**, *106*, 6065.
[7] Boekhoven, J.; Brizard, A. M.; Van Rijn, P.; Stuart, M. C. A.; Eelkema, R.; Van Esch, J. H. *Angew. Chem., Int. Ed.* **2011**, *50*, 12285.
[8] Obert, E.; Bellot, M.; Bouteiller, L.; Andrioletti, F.; Lehen-Ferrenbach, C.; Boué, F. *J. Am. Chem. Soc.* **2007**, *129*, 15601.
[9] Dasgupta, D.; Srinivasan, S.; Rochas, C.; Ajayashosh, A.; Guenet, J.-M. *Soft Matter* **2011**, *7*, 9311.
[10] Bouteiller, L.; Colombani, O.; Lortie, F.; Terech, P. *J. Am. Chem. Soc.* **2005**, *127*, 8893.
[11] Tidhar, Y.; Weissman, H.; Wolf, S. G.; Gulino, A.; Rybtchinski, B. *Chem. Eur. J.* **2011**, *17*, 6068.
[12] Canevet, D.; Pérez del Pino, Á.; Amabilino, D. B.; Sallé, M. *J. Mater. Chem.* **2011**, *21*, 1428.
[13] Zang, L.; Che, Y.; Moore, J. S. *Acc. Chem. Res.* **2008**, *41*, 1596.
[14] England, J. L.; Haran, G. *Annu. Rev. Phys. Chem.* **2011**, *62*, 257.
[15] Tanford, C. *J. Am. Chem. Soc.* **1964**, *86*, 2050.

[16] Scholtz, J. M.; Grimsley, G. R.; Pace, C. N. *Methods Enzymol.* **2009**, *466*, 549.
[17] Greene, R. F.; Pace, C. N. *J. Biol. Chem.* **1974**, *249*, 5388.
[18] Tanford, C. *Adv. Prot. Chem.* **1968**, *23*, 121.
[19] Matthews, C. R. *Methods Enzymol.* **1987**, *154*, 498.
[20] Liu, Z.; Reddy, G.; O'Brien, E. P.; Thirumalai, D. *Proc. Natl. Acad. Sci. USA* **2011**, *108*, 7787.
[21] Mes, T.; Cantekin, S.; Balkenende, D. W. R.; Frissen, M. M. M.; Gillissen, M. A. J.; De Waal, B. F. M.; Voets, I. K.; Meijer, E. W.; Palmans, A. R. A. *Chem. Eur. J.* **2013**, *19*, 8642.
[22] Chen, Z.; Stepanenko, V.; Dehm, V.; Prins, P.; Siebbeles, L. D. A.; Seibt, J.; Marquetand, P.; Engel, V.; Würthner, F. *Chem. Eur. J.* **2007**, *13*, 436.
[23] Metzroth, T.; Hoffmann, A.; Martín-Rapún, R.; Smulders, M. M. J.; Pieterse, K.; Palmans, A. R. A.; Vekemans, J. A. J. M.; Meijer, E. W.; Spiess, H. W.; Gauss, J. *Chem. Sci.* **2011**, *2*, 69.
[24] Schellman, J. A. *Biopolymers* **1975**, *14*, 999.
[25] Schellman, J. A. *Biophys. Chem.* **2002**, *96*, 91.
[26] Auton, M.; Holthauzen, L. M. F.; Bolen, D. W. *Proc. Natl. Acad. Sci. USA* **2007**, *104*, 15317.
[27] Prince, R. B.; Saven, J. G.; Wolynes, P. G.; Moore, J. S. *J. Am. Chem. Soc.* **1999**, *121*, 3114.
[28] Smulders, M. M. J.; Nieuwenhuizen, M. M. L.; De Greef, T. F. A.; Van der Schoot, P.; Schenning, A. P. H. J.; Meijer, E. W. *Chem. Eur. J.* **2010**, *16*, 362.
[29] de Greef, T. F. A.; Smulders, M. M. J.; Wolffs, M.; Schenning, A. P. H. J.; Sijbesma, R. P.; Meijer, E. W. *Chem. Rev.* **2009**, *109*, 5687.
[30] Zhao, D.; Moore, J. S. *Org. Biomol. Chem.* **2003**, *1*, 3471.
[31] Balakrishnan, K.; Datar, A.; Naddo, T.; Huang, J.; Oitker, R.; Yen, M.; Zhao, J.; Zang. L. *J. Am. Chem. Soc.* **2006**, *128*, 7390.
[32] Che, Y.; Yang, X.; Loser, S.; Zang, L., *Nano Lett.* **2008**, *8*, 2219.
[33] Wang, S.; Dössel, L.; Mavrinskiy, A.; Gao, P.; Feng, X.; Pisula, W.; Müllen, K. *Small* **2011**, *7*, 2841.
[34] Xu, G.; Tang, Y.-B.; Tsang, C.-H.; Zapien, J.-A.; Lee, C.-S.; Wong, N.-B. *J. Mater. Chem.* **2010**, *20*, 3006.
[35] Grill, L.; Dyer, M.; Lafferentz, L.; Persson, M.; Peters, M. V.; Hecht, S. *Nat. Nanotechnol.* **2007**, *2*, 687.
[36] Fujita, N.; Sakamoto, Y.; Shirakawa, M.; Ojima, M.; Fujii, A.; Ozaki, M.; Shinkai, S. *J. Am. Chem. Soc.* **2007**, *129*, 4134.
[37] Dautel, O. J.; Robitzer, M.; Lère-Porte, J.-P.; Serein-Spirau, F.; Moreau, J. J. E. *J. Am. Chem. Soc.* **2006**, *128*, 16213.
[38] Zhang, W.; Jin, W.; Fukushima, T.; Saeki, A.; Seki, S.; Aida, T. *Science* **2011**, *334*, 340.
[39] Wang, X.; Guerin, G.; Wang, H.; Wang, Y.; Manners, I.; Winnik, M. A. *Science* **2007**, *317*, 644.
[40] Gilroy, J. B.; Gädt, T.; Whittell, G. R.; Chabanne, L.; Mitchels, J. M.; Richardson, R. M.; Winnik, M. A.; Manners, I. *Nature Chem.* **2010**, *2*, 566.
[41] Zheng, J. Y.; Yan, Y.; Wang, X.; Zhao, Y. S.; Huang, J.; Yao, J. *J. Am. Chem. Soc.* **2012**, *134*, 2880.
[42] Korevaar, P. A.; Grenier, C.; Markvoort, A. J.; Schenning, A. P. H. J.; De Greef, T. F. A.; Meijer, E. W. *Proc. Natl. Acad. Sci. USA* **2013**, *110*, 17205.
[43] Palmans, A. R. A.; Vekemans, J. A. J. M.; Havinga, E. E.; Meijer, E. W. *Angew. Chem. Int. Ed.* **1997**, *36*, 2648.
[44] Ashyraliyev, M.; Fomekong-Nanfack, Y.; Kaandorp, J. A.; Blom, J. G. *FEBS Journal* **2009**, *276*, 886.
[45] Geier, F.; Fengos, G.; Felizzi, F.; Iber, D. Analysing and constraining signalling networks: parameter estimation for the user, in *Computational Modelling of Signalling Networks* (Editors Xuedong Liu, Meredith D. Betterton), **2012**, Humana Press.

4

Model-driven optimization of multi-component self-assembly processes

Abstract: This chapter describes an engineering approach towards multi-component self-assembly processes by developing a methodology to circumvent spurious, metastable assemblies. The formation of metastable aggregates often hampers self-assembly of molecular building blocks into the desired nanostructures. Strategies are explored to control pathway complexity and avoid off-pathway aggregates by optimizing the rate of assembly along the correct pathway. As a model system, we study the co-assembly of two monomers, the *R*- and *S*-chiral enantiomers of a π-conjugated oligo(*p*-phenylene vinylene) derivative. Co-assembly kinetics are analysed by developing a kinetic model, which reveals the initial assembly of metastable structures buffering free monomers and thereby slowing down the formation of thermodynamically stable assemblies. These metastable assemblies exert greater influence on the thermodynamically favoured self-assembly pathway if the ratio between both monomers approaches 1:1; in agreement with experimental results. Moreover, competition by metastable assemblies is highly temperature-dependent and most effectively hampers assembly of equilibrium nanostructures at intermediate temperatures. It is demonstrated that the rate of the assembly process can be optimized by tuning the cooling rate. Finally, it is shown by simulation that stepwise increasing the driving force for assembly by changing solvent composition can circumvent metastable pathways and thereby force the assembly process directly into the correct pathway.

Part of this work has been published as:

"Model-driven optimization of multicomponent self-assembly processes" P. A. Korevaar, C. Grenier, A. J. Markvoort, A. P. H. J. Schenning, T. F. A. de Greef, E. W. Meijer, *Proc. Natl. Acad. Sci. USA* **2013**, *110*, 17205–17210.

4.1 Introduction

Self-assembled nanostructures are often considered to be in fast exchange with their molecular building blocks.[1] Although this is true for highly dynamic systems, the assembly of more rigid systems – *i.e.* systems most often used in applications – have relatively slow dynamics and are often not in equilibrium.[2–7] The long lifetime of the resulting assemblies allows the hierarchical construction of functional nanostructures from self-assembly of multiple components, since aggregates formed in earlier steps will not re-equilibrate after addition of subsequent components. Via this approach one-dimensional multi-segment nanorods[8] have been assembled, as well as supramolecular electronic structures containing different types of wires[9] and p–n junctions.[10] Also in the processing of organic materials like bulk heterojunction solar cells, slow self-assembly dynamics play a critical role. For example, prolonged annealing is often required to obtain optimal morphologies of electron donor and acceptor components.[11–13] A drawback of the slow monomer exchange dynamics, however, is that the molecular components can easily get trapped in metastable off-pathway assemblies which hamper assembly along the correct pathway; a phenomenon known as pathway complexity.[14] Hence, obtaining the desired supramolecular morphology is often non-trivial, and many variables like solvent composition, concentration, temperature and preparation methodology have to be optimized to obtain the correct molecular architectures.[15–20]

The presence of kinetically controlled self-assembly pathways clearly emphasizes the necessity of developing kinetic models which take into account the growth mechanism and pathway complexity leading to a diversity of various aggregate morphologies. Such a model-driven approach is common in synthetic biology, where it aids the development of systems which can for instance control gene expression.[21–24] Typically, a kinetic model is developed first that includes all modular elements and the interactions between them. Next, to identify the most critical parameters that have to be optimized in order to achieve the targeted function, the combinatorial design variable space of the model is mapped by running many simulations with different parameter combinations.

Inspired by this forward engineering approach, in this chapter we computationally screen self-assembly strategies which circumvent formation of metastable aggregates and thereby optimize the rate of self-assembly into thermodynamically stable aggregates. First a molecular model system is introduced consisting of two different molecules which co-assemble into one-dimensional, helical aggregates. Next, the co-assembly is experimentally studied under thermodynamic and kinetic control, and a model is developed to analyse the co-assembly kinetics in detail. Simulations reveal the initial formation of metastable structures which buffer free monomers and thereby slow down the formation of the thermodynamically stable assemblies. In the third part, we analyse the temperature-dependent entrapment of monomers in these assemblies. The competition exerted by the metastable pathway is found to be highly dependent on the applied cooling rate, and a temperature-dependent kinetic model is developed to rationalize this behaviour. Based on the resulting insights into the co-assembly pathways, methodologies are proposed and assessed by simulation to circumvent these

metastable pathways during the aggregation process, whilst providing the fastest route to arrive at the desired structure. Alternatively, this strategy allows the design of methodologies to obtain the kinetically favoured assemblies if required.

4.2 Model system: co-assembly of two enantiomers

As a model system, the co-assembly of *R*- and *S*-chiral oligo(*p*-phenylene vinylene)-ureidotriazine (ROPV and SOPV, Fig 4.1a) is selected.[25, 26] To investigate the co-assembly of ROPV and SOPV, "majority rules" experiments are performed by dr. Christophe Grenier, which assess the capability of the major enantiomer to amplify its chirality by forcing all assemblies in the system to take over its preferred helicity.[27] Solutions of R- and SOPV (200 μM) are mixed at 20 °C in different ratios characterized by the enantiomeric excess *ee*, which equals the difference between the molar fractions of R- and SOPV. The resulting anisotropy factor $\Delta\varepsilon/\varepsilon$ (460 nm) depends linearly on *ee*, indicative of the lack of chiral amplification (Fig 4.1c). However, annealing above the critical temperature of elongation T_e at which all helices are disassembled, followed by slow cooling (1 °C/min) back to 20 °C strongly influences the relation between $\Delta\varepsilon/\varepsilon$ and *ee*. For $ee < -0.2$ and $ee > 0.2$, $\Delta\varepsilon/\varepsilon$ is now saturated and equals the anisotropy factor corresponding to the excess enantiomer in its pure form. The strong chiral amplification obtained upon annealing and subsequent cooling implies that initial mixing of the assemblies at 20 °C does not result in notable monomer exchange, and hence the net helicity equals the weighted sum of the helicities of homo-aggregates consisting of R- and SOPV monomers only. Annealing results in disassembly of enantiopure aggregates after which the monomers can mix upon cooling, resulting in chirally amplified hetero-aggregates.

The majority rules experiment is also performed at a lower concentration of 10 μM (Fig 4.1d) and again, no chiral amplification is observed upon mixing the assemblies at 20 °C. However, also after annealing above T_e and subsequent cooling (1 °C/min) no chiral amplification is observed. To investigate if this absence of chiral amplification is related to *kinetic* phenomena, a 10 μM OPV solution with $ee = -0.3$ is cooled and subsequently heated with a rate of 1 °C/min (Fig 4.1e). Indeed, a large hysteresis is obtained, and only cooling with a much slower rate from the molecular dissolved state (0.1 °C/min) results in a $\Delta\varepsilon/\varepsilon$-value indicative of chiral amplification. Since the UV/Vis spectrum obtained after cooling with 1 °C/min at 20 °C coincides with the UV/Vis spectrum of the mixture of S- and ROPV assemblies at this temperature prior to annealing, it can be concluded that also in the non-amplified state most monomers are assembled. This means that the small helicity of the non-amplified state is not related to failure of monomers to assemble upon cooling with a rate of 1 °C/min. Furthermore, fluorescence lifetime measurements on a 1:1 mixture of S- and ROPV assemblies result in lifetimes that are identical to the results obtained on enantiopure helices, *i.e.* solely SOPV assemblies or solely ROPV assemblies in solution. Only heating the 1:1 mixture of S- and ROPV assemblies and subsequent cooling with a rate of 1 °C/min yields a significant change in the fluorescence decay time, consistent with mixing of both enantiomers into hetero-aggregates. Hence, this observation excludes the involvement of conglomerates, *i.e.* separated R- and SOPV assemblies, in the non-amplified state that is obtained after annealing.

These metastable co-assemblies bear a relation with the assembly of enantiopure OPV: As shown in Chapter 2, SOPV monomers assemble fast into metastable *P**-type helices and subsequently form stable *M*-type helices. *Vice versa*, ROPV forms metastable *M**-type helices prior to the slower assembly into stable *P*-type helices (Fig 4.1b).

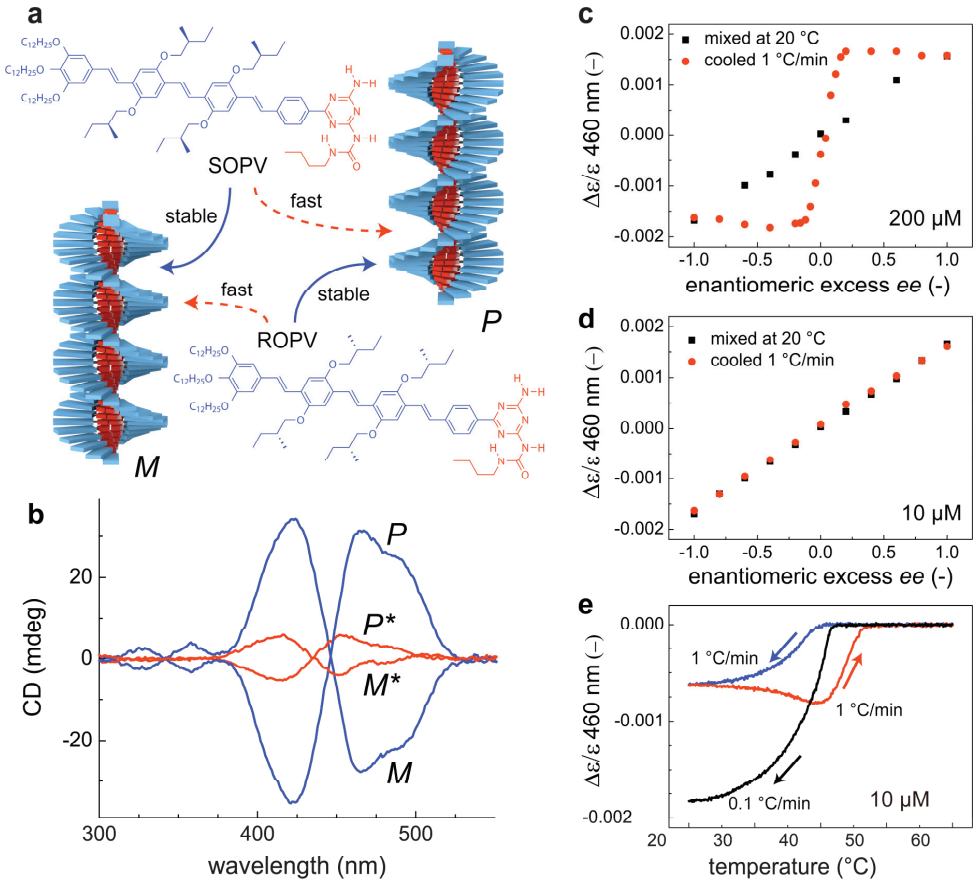

Figure 4.1 | Assembly and co-assembly of S- and ROPV. (a) Molecular structures of S- and ROPV. Both enantiomers assemble into helical stacks: for SOPV, *M*-type helices are thermodynamically favoured whereas *P**-type helices appear under kinetic control. *Vice versa*, ROPV forms *P*-type helices under thermodynamic control and *M**-type helices under kinetic control, as demonstrated by the CD spectra in pane (b). To study the co-assembly of both enantiomers, majority rules experiments are performed for mixtures of R- and SOPV in MCH. Both for high (200 μM, c) and low concentration (10 μM, d) no chiral amplification is obtained after mixing the assemblies at 20 °C. Heating to 80 °C, well above the elongation temperature T_e, and cooling with 1 °C/min to 20 °C yields only chiral amplification at 200 μM. (e) For a 10 μM OPV solution (*ee* = –0.3), chiral amplification is only obtained upon cooling with 0.1 °C/min, whereas cooling and heating with 1 °C/min results in a large hysteresis.

4.3 Analysis of co-assembly kinetics

To unravel the origin of the metastable aggregates that appear in the co-assembly of S- and ROPV, a deterministic kinetic model is developed that approximates a previously developed stochastic simulation algorithm for majority-rules kinetics.[27] The co-assembly model, schematically depicted in Figure 4.2a, describes the assembly of both types of monomers in left-handed *M*-type and right-handed *P*-type helical stacks. Nucleation occurs by association of two monomers into *M*- and *P*-type nuclei. Further elongation of the stacks occurs via stepwise monomer association, with association rate constant *a*. In contrast to the stochastic simulations, the exact monomer sequence of each aggregate is not considered, which greatly decreases computational time. Hence, to describe dissociation of the two different monomers from *M*- and *P*-type stacks, the dissociation probabilities of *S*- and *R*-chiral monomers are computed from the ratio of both monomers present in the respective aggregate type. Monomer dissociation is described with rate constant *c*. For dissociation of monomers from aggregates of their non-preferred type of helicity, this dissociation rate constant increases with a mismatch penalty factor *MMP* (for details in the kinetic model see paragraph 4.7).

Simulations with the co-assembly model, starting with a mixture of *R*- and *S*-chiral monomers in different ratios show that the time-dependent net helicity ($P_{tot} - M_{tot}$), defined as the difference in concentration of monomers present in *P*- and *M*-type aggregates, is strongly dependent on *ee* and has a minimum rate at *ee*-values close to zero (Fig 4.2b). Under steady-state conditions, the calculated net helicity as a function of *ee* is comparable to the experimentally observed chiral amplification curve, assuming a *MMP* of 1.1. However, during equilibration the net helicity initially depends linearly on the *ee*, indicative of a non-amplified state (Fig 4.2c). Congruently, the equilibration of the total assembled material ($P_{tot} + M_{tot}$) is much faster compared to equilibration of the net helicity, supporting the fact that during the initial stages of the assembly process aggregates are formed that do not contribute to chiral amplification. To analyse this in detail, the time-dependent concentrations of the two monomers (*R*- and *S*-chiral) in the different stacks (*P*- and *M*-type) are followed for different values of *ee*, varying from 0 to 1 (Fig 4.2d-g). The results show that initially part of the monomer pool assembles into aggregates with a helicity corresponding to the minority enantiomer and that the kinetic stability of these aggregates becomes larger if the *ee* approaches 0. As a result, the subsequent conversion into the stable aggregate type is delayed for smaller *ee* values, resulting in a slower rate of chiral amplification for less enantiopure systems. The kinetic curves as well as the equilibrium data predicted by the co-assembly model are in good agreement with stochastic simulations (Fig 4.8a).

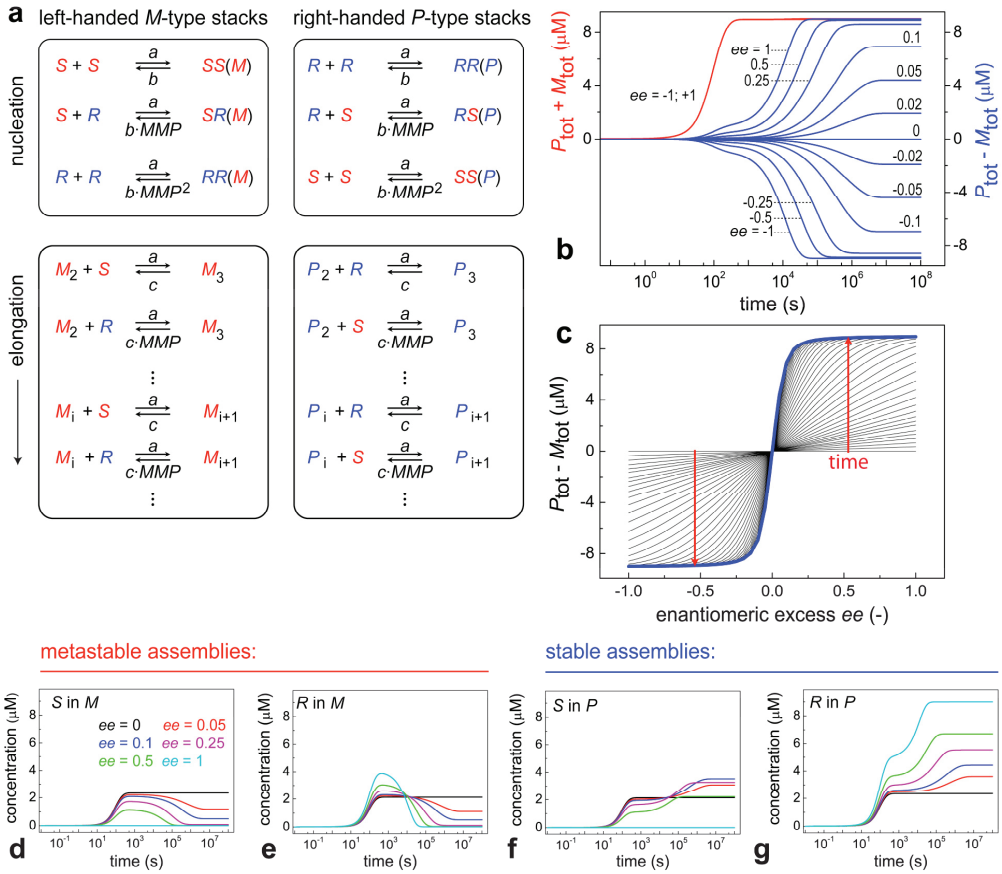

Figure 4.2 | Analysis of the co-assembly kinetics of two different monomers by simulation. (a) Schematic representation of the kinetic model describing the nucleated co-assembly of *R*- and *S*-chiral monomers in *P*- and *M*-type helical stacks, with a mismatch penalty factor *MMP* for *R*-chiral monomers in *M*-type stacks and *S*-chiral monomers in *P*-type stacks. (b, c) The time-dependent development of net helicity ($P_{tot} - M_{tot}$) and total assembled material ($P_{tot} + M_{tot}$) simulated with different values of *ee*, and a *MMP* of 1.1. The rate of chiral amplification decreases as the *ee* approaches 0. For different *ee* values from 0 to 1, the time-dependent concentration of both monomers in *M*- (d, e) and *P*-type stacks (f, g) is analysed. When the *ee* approaches 0 the monomers are buffered for a longer time in the metastable *M*-type stacks, resulting in slower amplification kinetics. Parameters: $a = 4 \cdot 10^4$ $M^{-1}s^{-1}$; b = 400 s^{-1}; c = 0.04 s^{-1}; c_{tot} = 10 μM.

The strong dependence of the chiral amplification rate on the *ee*, as predicted by the co-assembly model, is verified by kinetic experiments. OPV solutions (10 μM) with different *ee*'s are cooled from above the T_e to 20 °C with 8 °C/min and subsequently the increase of $\Delta\varepsilon/\varepsilon$ is followed in time (Fig 4.3). In agreement with previous chiral amplification studies[28, 29], the *ee* has a large effect on the annealing kinetics. Slower rates are obtained for less enantiopure compositions, in agreement with the co-assembly model.

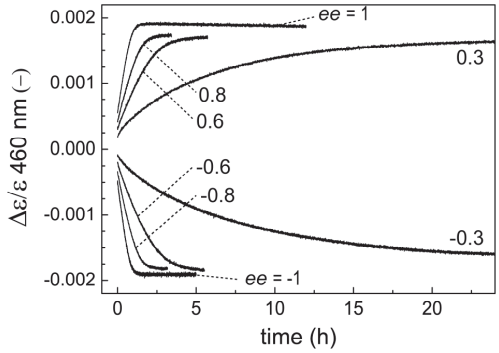

Figure 4.3 | The rate of chiral amplification is strongly dependent on the *ee*, as shown by kinetic experiments where $\Delta\varepsilon/\varepsilon$ is followed in time at 20 °C for OPV solutions with different *ee*'s that have been cooled from above the T_e to 20 °C (8 °C/min, 10 μM).

4.4 Temperature-dependent entrapment of monomers in metastable assemblies

The majority rules experiments at a low concentration of 10 μM show that fast cooling results in metastable assemblies that fail to display chiral amplification and contribute to the strong hysteresis observed. To further corroborate the role of these metastable assemblies in the hysteresis, the influence of cooling rate on the co-assembly of R- and SOPV is assessed. An OPV solution (10 μM, *ee* = –0.3) is cooled from above the T_e to 0 °C with different cooling rates: 1 °C/min, 8 °C/min and via quenching of the solution in an ice bath. Thereafter, the evolution of the amplified state is probed by CD at 20 °C (Fig 4.4a). Surprisingly, a maximum rate in net helicity is observed after rapid quenching, whereas a significantly slower rate is observed after cooling with 1 °C/min. This counterintuitive effect cannot be explained by an aggregation mechanism in which monomers assemble via a single pathway: in this case longer re-equilibration times would be expected for faster cooling rates, as demonstrated in Figure 4.5a. A possible way to rationalize the kinetic results is via the buffering of monomers into parallel operating, kinetically controlled pathways, comparable to the metastable assemblies that appear in the simulations with the co-assembly model (Fig 4.2). During slow cooling (*i.e.* 1 °C/min), free monomers get entrapped into these pathways. Hence, the assembly into thermodynamically favoured aggregates that contribute to chiral amplification occurs slower.

In the co-assembly model all monomer association reactions are described with the same rate constant *a*, independent of the helicity of the aggregate. This results in an initial appearance of aggregates that show no chiral amplification, as well as a correct prediction of the relation between *ee* and the rate of chiral amplification. The experiments discussed in Chapter 2 on the assembly of enantiopure SOPV revealed a fast, kinetically controlled assembly into *P**-type helices. *Vice versa*, a metastable *M**-type helix can be obtained for ROPV (Fig 4.1b). Upon co-assembling S- and ROPV, both enantiomerically related monomers will also be incorporated in these metastable aggregates, meaning that SOPV slowly assembles into

the kinetically controlled *M**-type helix that is initially formed by ROPV, and thereby increases its stability. Analogously, ROPV slowly stabilizes the metastable *P**-type helix that is initially formed by SOPV. As a result, the stability of the metastable hetero-aggregates as well as the rate constants that describe the association and dissociation of both monomers to these assemblies depend on the exact composition of the aggregate. Effectively, this results in multiple, parallel operating metastable pathways that compete with the thermodynamically controlled hetero-aggregates for available monomers. Giving an exact description of all these assembly pathways by further expanding the co-assembly model is possible but will introduce a great number of additional constants which would complicate further analysis. Therefore, we analyse the system by applying a simplified kinetic model that describes the nucleated assembly of one monomer *X* into a single metastable pathway *A* that shows no chiral amplification and one stable pathway *B* that does show chiral amplification.

The model, introduced before in Chapter 2 and ref. 14, describes both assembly pathways as a sequence of monomer dissociation and association reactions (Fig 4.4b). Monomer association is described with rate constants a_A and a_B for the metastable and stable pathway, respectively. The higher thermodynamic stability of aggregates in pathway *B* is reflected by $a_B/c_B > a_A/c_A$, with rate constants of monomer dissociation c_B and c_A for pathway *B* and *A*. We note that in the kinetic experiments after rapid quenching a $\Delta\varepsilon/\varepsilon$-value of –0.001 is reached within 20 minutes, whereas it would take more than a day to reach this $\Delta\varepsilon/\varepsilon$-value after cooling with 1 °C/min (Fig 4.4a). This indicates that metastable assemblies sequester monomers most effectively in intermediate temperature regimes. Hence, the assembly of metastable assemblies in the kinetic model is assumed to be only faster than the stable pathway (*i.e.* $a_A > a_B$) for temperatures above 20 °C (Fig 4.4c).

Simulations with the kinetic model, based on the temperature-dependency of the various rate constants as depicted in Figure 4.4c, indeed reveal that metastable assemblies only appear above 20 °C (Fig 4.4d). As a result, the assembly of thermodynamically stable aggregates, characterized by the time at which 50% of its conversion is completed (t-50B), is significantly slowed down above 20 °C. Using the kinetic model and the temperature-dependent rate constants we simulate the assembly of free monomers during cooling from 50 °C to 0 °C with different temperature ramps (Fig 4.4e). In the simulations, a $\Delta\varepsilon/\varepsilon$-value of –0.0005 is assigned to metastable *A*-type assemblies and a $\Delta\varepsilon/\varepsilon$-value of –0.0018 to stable *B*-type assemblies. The resulting cooling curves reveal for slow cooling the direct formation of thermodynamically stable aggregates ($\Delta\varepsilon/\varepsilon \sim -0.0018$), for fast cooling no assembly and for intermediate cooling rates kinetically controlled assemblies ($\Delta\varepsilon/\varepsilon \sim -0.0005$), in agreement with our experimental results. Moreover, simulation of the subsequent equilibration kinetics at 20 °C yields the slowest rate for intermediate cooling rates like 1 °C/min. These simulations demonstrate that upon cooling with intermediate temperature ramps, monomers are efficiently sequestered in metastable assemblies that are easily formed above 20 °C. This buffering of free monomers significantly slows down their re-assembly into the thermodynamically stable aggregates at room temperature.

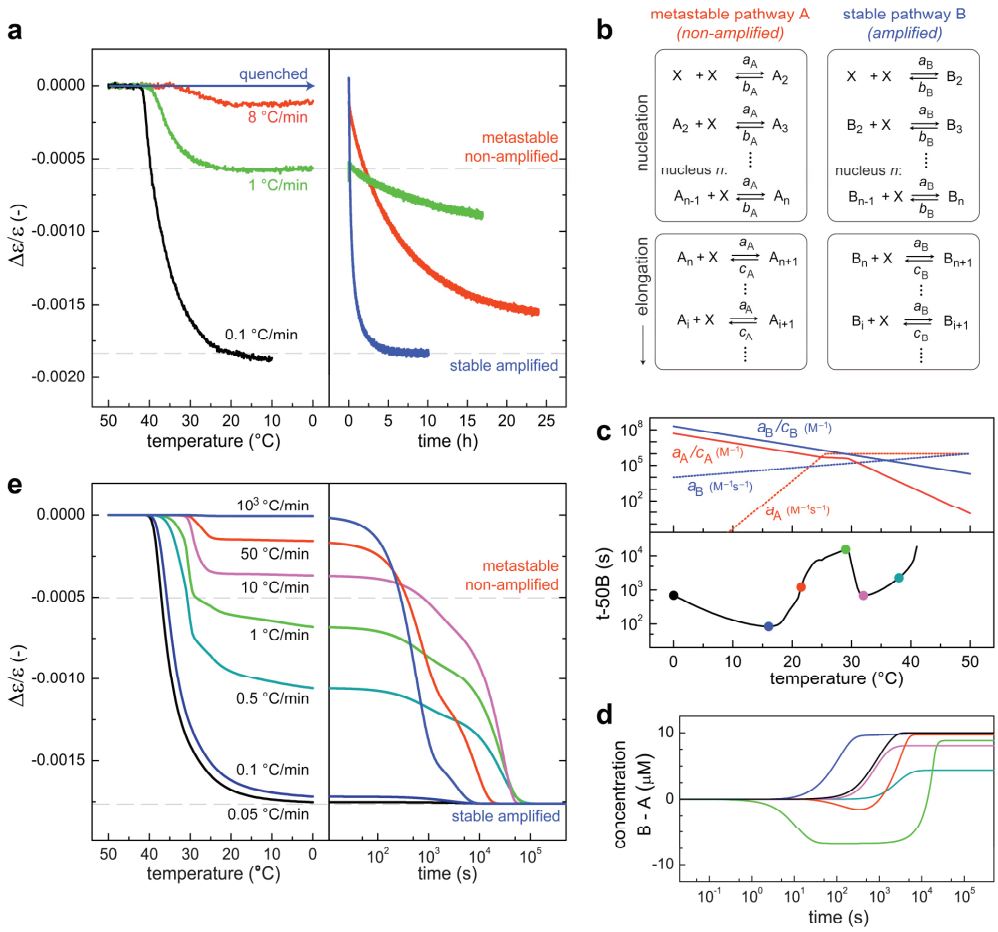

Figure 4.4 | Experiments under kinetic control reveal that the competition for free monomer exerted by the metastable assembly pathway is strongly temperature-dependent. (a) Temperature-dependent net-helicity of an OPV solution (10 μM, *ee* = –0.3) upon cooling from above T_e to 0 °C with different rates (left pane). During subsequent equilibration at 20 °C, faster rates are observed after higher cooling rates (right pane). (b) Schematic representation of the kinetic model describing the parallel assembly of a kinetically controlled pathway *A* and a slower pathway *B* resulting in thermodynamically stable aggregates. Both pathways compete for the same monomer *X*. (c) Influence of temperature on rate constants used in simulations (top pane) and simulated assembly time, characterised by *t*-50B, of stable *B*-type assemblies (bottom pane). (d) Time-dependent assembly in metastable *A*-type and thermodynamically favoured *B*-type assemblies, simulated at different temperatures (colour coding corresponds to coloured dots in c, also the black line represents simulated *t*-50B values). (e) Simulated temperature-dependent assembly of free monomer into metastable (Δε/ε-value of –0.0005) and stable assemblies (Δε/ε-value of –0.0018) upon cooling (left pane). Subsequent equilibration kinetics at 20 °C (right pane) reveal the slowest rate after cooling with intermediate cooling rates due to entrapment of monomers in metastable assemblies. Parameters: $b_A = c_A / 0.1$; $b_B = c_B / 0.01$, $n = 5$; $N = 100$, $c_{tot} = 10$ μM.

The simulations, based on the assumption that the metastable pathway sequesters monomers most effectively in the intermediate temperature regime, qualitatively capture the kinetic results that are at first glance counterintuitive. However, two other questions remain to be addressed: (1) Why does cooling from 80 °C with a temperature ramp of 1 °C/min at concentration of 200 μM not result in the metastable, non-amplified state, as shown in Figure 4.1e? One of the conclusions of Chapter 2 is that the metastable pathways exert their influence on the equilibrium state in particular at higher concentrations: hence the non-amplified state would be expected at this higher concentration as well. (2) Why does the net helicity initially increase upon heating the non-amplified state, as shown in the red curve in Figure 4.1e?

To address the first point, it should be noted that a higher concentration results in a higher temperature of elongation that marks the onset of the assembly process. Since the monomer association rate increases with temperature, this means that at the start of the assembly of the stable aggregates, at the critical temperature, a faster cooling rate can be tolerated to maintain equilibrium conditions. Indeed, temperature-dependent simulations with a concentration of 200 μM reveal the amplified, stable state after cooling with 1 °C/min (Fig 4.5b).

To address the second point, the increase of the net helicity upon heating the non-amplified state is simulated with the temperature-dependent kinetic model as well (Fig 4.5b). The effect can be rationalized by the fact that the system, after being "frozen in" in the non-amplified state at 0 °C, reaches elevated temperatures during heating again. At these temperatures, it can continue to self-assemble into the equilibrium structures, which means a temporary rise in the net helicity. Only at temperatures close to the temperature of elongation, the assemblies become too unstable and the net helicity decreases again.

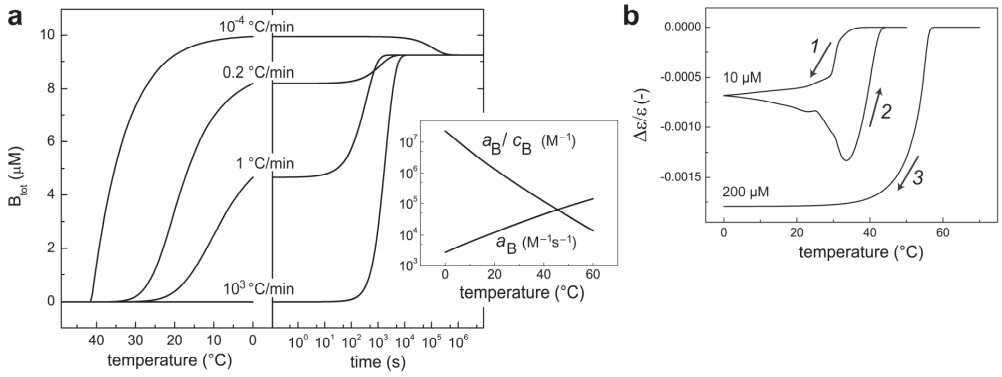

Figure 4.5 | Analysing the effect of metastable pathways on temperature-dependent assembly via modelling. (a) Temperature-dependent assembly simulated with different cooling rates (left pane) and subsequent equilibration kinetics at 20 °C. Only the pathway towards *B*-type assemblies is considered. The inset shows the temperature-dependency of the forward rate constant a_B and the ratio a_B/c_B. Parameters: b_B/c_B = 0.01; n = 5; N = 100; c_{tot} = 10 μM. (b) Simulated temperature-dependent assembly of free monomer into metastable (Δε/ε-value of –0.0005) and stable assemblies (Δε/ε-value of –0.0018). The assembly is simulated during (*1*) cooling and (*2*) subsequent heating of a system at a concentration of 10 μM. Besides, the temperature-dependent assembly is simulated for a system at much higher

concentration (200 μM) upon cooling (*3*). For curves 1–3, the temperature ramp equals 1 °C/min. Parameters are analogous to Figure 4.4; for T > 50 °C all temperature-dependent parameters are extrapolated in agreement with Figure 4.4c, with $a_B = 10^6$ $M^{-1}s^{-1}$.

4.5 Fast assembly: circumventing the metastable state

The entrapment of monomers in metastable pathways slows down the final formation of the equilibrium assemblies. Hence, only strategies to avoid metastable aggregates allows optimization of the rate of the self-assembly into the thermodynamically stable structures. In this paragraph, we demonstrate by simulation two approaches by which the assembly rate can be optimized upon circumventing the metastable pathway.

4.5.1 Optimizing the assembly rate by tuning the cooling rate

Since the slowest assembly rate of the stable aggregates in the system discussed above is obtained using intermediate cooling rates, the assembly process can be optimized by 1) decreasing the cooling rate such that the monomers can assemble directly into the thermodynamically stable pathway at elevated temperatures, or 2) by rapidly quenching the molecularly dissolved monomers from a high temperature. To demonstrate this, we assess by simulation how the cooling rate influences the rate at which the stable aggregates appear. Via the temperature-dependent two-pathway model (Fig 4.4b) we calculate the time at which 99% conversion of the equilibrium $\Delta\varepsilon/\varepsilon$-value is obtained, corresponding to the thermodynamically stable aggregate (Fig 4.6). Indeed, optimum assembly times are obtained upon employing slow and high cooling rates.

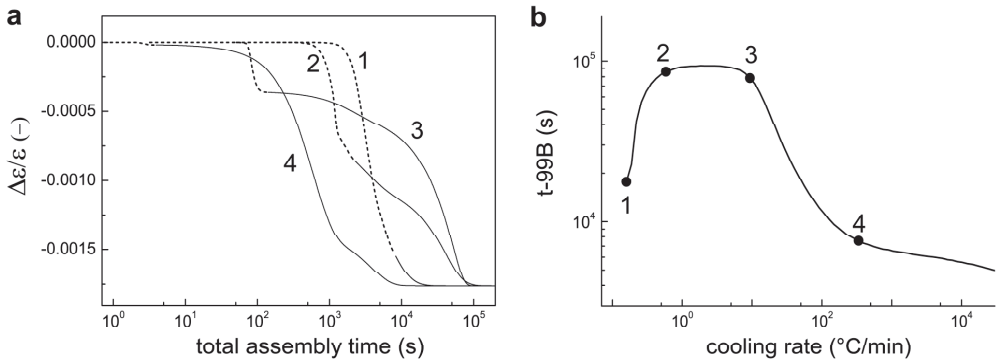

Figure 4.6 | Optimizing the overall rate of temperature-dependent assembly processes by varying the cooling rate. (a) Analogous to the temperature-dependent assembly simulations in Figure 4.4e, $\Delta\varepsilon/\varepsilon$ is followed in time during *I*) cooling with different cooling rates from 42 °C to 20 °C (dashed curves) and *II*) subsequent equilibration at 20 °C (solid curves). (b) The total assembly time at which 99% of the equilibrium $\Delta\varepsilon/\varepsilon$-value at 20 °C is obtained (*t*-99B) *vs*. the cooling rate. Next to points 1–4, the black line represents simulated *t*-99B values as well.

4.5.2 Optimizing the assembly rate by addition of a co-solvent

Next to tuning the cooling rate, the assembly of a system in which metastable pathways buffer the molecular building blocks can also be optimized by adjusting solvent conditions. Typically, addition of a destabilizing co-solvent (*i.e.* good solvent) decreases the rate of monomer association and increases the rate of monomer dissociation, as shown in Chapter 3 (Fig 4.7a).[30] Here we demonstrate by simulation how this effect can be utilized to circumvent metastable pathways. First we analyse the equilibrium free monomer concentration for both the kinetically and thermodynamically controlled pathways independently as a function of the volume fraction of a good solvent f, assuming a total monomer concentration of X equal to 10 μM. In the example shown in Figure 4.7b, the stable assemblies are formed below $f = 0.40$, and the metastable assemblies below $f = 0.33$.

Simulating the assembly of free monomers at this concentration without the presence of a destabilizing solvent ($f = 0$) results in sequestering of monomers in metastable assemblies which subsequently slows down the formation of the thermodynamically stable aggregates (Fig 4.7c). To circumvent the initial formation of metastable assemblies, we attempt by simulation an alternative methodology in which the assembly of free monomers dissolved in a good solvent (corresponding to $f = 1$) is initiated by changing the solvent composition such that the total yield of metastable assemblies is zero (*i.e.* $f = 0.33$). After equilibration, further assembly is induced by decreasing f such that the concentration of free monomers that remain from the first step just equals the critical concentration of monomers required for the formation of metastable assemblies at this new f-value. In this way, the formation of metastable assemblies is also avoided during the second assembly step. Upon repeating this stepwise approach of lowering the fraction of good solvent, a full conversion of all monomers into stable assemblies is obtained in the pure solvent ($f = 0$) at the sixth step. The advantage of this stepwise assembly approach is clearly demonstrated by the fact that the rate is 21 times faster compared to the direct assembly of free monomers by changing the solvent fraction from $f = 1$ to $f = 0$ in a single step (Fig 4.7c).

To further optimize this stepwise assembly strategy, we analyse the combinatorial design variable space by investigating the influence of 1) the conversion per step p and 2) the applied method to decrease f every step. In the example described above, f is decreased such that the concentration of free monomers remaining from the previous step equals the critical monomer concentration required for the formation of metastable assemblies (black lines in Fig 4.7b). However, to optimize the process, the decrease in f per step is varied by adding a factor Δf for every step (green lines in Fig 4.7b). 10000 different parameter sets for p and Δf are assessed, in the range $p = [0.1, 1]$ and $\Delta f = [-0.35, 0.05]$. For all parameter sets, the simulated assembly rate obtained via stepwise decreasing f to zero is compared to the rate of directly assembling by changing the solvent fraction from $f = 1$ to $f = 0$ in a single step. A maximum rate is obtained with $p = 0.99$ and $\Delta f = -0.12$; well beyond the critical f-value where metastable assemblies initially appear (*i.e.* $\Delta f = 0$) and hamper the formation of thermodynamically stable assemblies (Fig 4.7d). Nevertheless, these conditions yield a Pareto optimal situation which is a trade-off

between buffering of free monomers in metastable assemblies, which increases upon lowering the fraction of good solvent, and the monomer association rate, which increases upon decreasing *f*. This example clearly emphasizes that finding the optimal self-assembly route involves the optimization of multiple parameters, which can only be done by computationally analysing the full combinatorial design variable space.

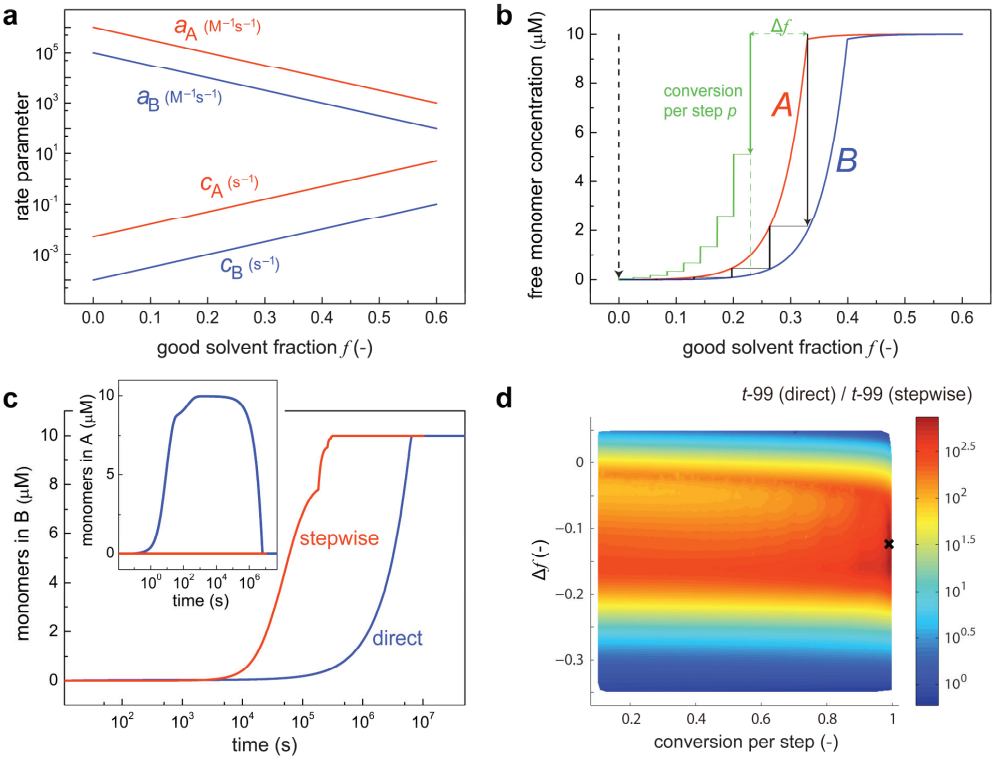

Figure 4.7 | Stepwise assembly methodology to avoid entrapment of monomers in metastable pathways. (a) A destabilizing (good) co-solvent is applied which decreases the monomer association rate and increases the monomer dissociation rate. (b) Equilibrium free monomer concentration for metastable (*A*) and stable assemblies (*B*) *vs.* good solvent fraction *f*. To circumvent the initial formation of metastable assemblies, the assembly starts at $f = 0.33$, and *f* is decreased stepwise to $f = 0$ (black lines). The vertical lines indicate the different assembly steps, the horizontal lines the decrease of *f*. (c) The formation of stable assemblies *B* via the stepwise assembly is significantly faster compared to direct assembly of free monomers at $f = 0$ (dotted arrow in pane b). The inset shows the concentration of monomers entrapped in metastable assemblies *A* during the direct and stepwise assembly. (d) To optimize the stepwise assembly, the method to decrease *f* stepwise is modified by adjusting 1) the conversion per step *p* and 2) the factor Δ*f* ($\Delta f = -0.1$ for green lines in pane b). The influence of *p* and Δ*f* on the assembly rate is characterized by the time at which the total conversion into the stable assemblies is 99%: *t*-99 (direct) / *t*-99 (stepwise). 10000 different parameter sets are assessed. The highest rate (*t*-99 (direct) / *t*-99 (stepwise) = 744) is found with $p = 0.99$ and $\Delta f = -0.12$ (black cross).

4.6 Conclusions and discussion

Kinetic experiments combined with detailed simulations on the co-assembly of the *R*- and *S*-chiral enantiomers of OPV reveal the appearance of multiple, parallel operating self-assembly pathways. The resulting pathway complexity enables metastable aggregates to exert their influence on the total co-assembly process, as entrapment of the chiral monomers results in a slow assembly of the thermodynamically stable co-assemblies. Since the kinetic stability of these metastable aggregates increases if the ratio between both chiral monomers approaches one, the co-assembly rate is highly dependent on the enantiomeric excess of the monomer pool.

Competition between different nanostructures via cross-talk of parallel operating self-assembly pathways results in counterintuitive phenomena with important consequences. For example, if a certain preparation protocol results in entrapment of monomers in metastable nanostructures, subsequent conversion to a nanofibre morphology with increased stability is much slower compared to the situation where monomers can directly assemble into the most stable aggregate morphology. Kinetic studies can identify parallel operating assembly pathways and more importantly yield information which of the pathways are under kinetic control. For example, self-assembly of a π-conjugated monomer resulting in short fibres with limited length might be due to entrapment in kinetically controlled off-pathway aggregates. However, these short fibres can also be the result of incomplete assembly of monomers in the thermodynamically controlled pathway as fast solvent evaporation can effectively freeze-in nanostructures due to the slow monomer association rate compared to the rate of evaporation. In the first case, the rate can be optimized by addition of a co-solvent which destabilizes the metastable pathway with respect to on-pathway aggregates, whereas in the second case a stabilizing solvent or a higher concentration is required to increase the assembly rate into the stable structure.

Model-driven optimization provides a practical approach for the design of preparation protocols to circumvent spurious, metastable self-assembled nanostructures. Especially if multiple components are involved in the assembly process, alternative pathways are likely to occur. Combining simulations and experiments, the results presented in this chapter demonstrate that the competition exerted by metastable assembly pathways can be highly temperature-dependent, providing a unique handle to tune the assembly process by optimizing the cooling rate. More general, if the driving force for self-assembly, e.g. fraction of poor solvent, is increased in a stepwise manner such that entrapment of monomers in metastable pathways is avoided, the assembly rate can be improved significantly. A comparable step-wise approach is now widely applied in the self-assembly of DNA origami [31–36] in which often temperature or solvent annealing steps are applied to direct the assembly towards the desired structures by optimizing the differential stability between on and off-pathway nanostructures.

In this study the two monomers used in the co-assembly of helical nanostructures are enantiomers and hence experience the same mismatch penalty in their non-preferred assembly

type. However, the phenomena observed in this study are general applicable to the assembly of multiple building blocks. For instance, nanofibres used in tissue engineering often include bioactive epitopes together with molecules that provide mechanical strength to the material.[37, 38] In bulk heterojunction solar cells, the functional properties are highly dependent on the supramolecular organization of the molecular components, e.g. fullerene and poly(3-hexylthiophene). Although these materials do not really co-assemble but rather phase separate, both molecular components have mutual interactions and their concomitant aggregation processes are competing for available space.[39] Perhaps for this reason, manipulating the aggregation pathways by adding co-solvents such as 1,8-diiodooctane has a strong effect on the resulting morphology of organic devices.[40–43]

4.7 Details of experiments and simulations

Instrumentation and Material. CD spectra are recorded using a Jasco J-815 CD spectrometer. Sensitivity, response time and scanning rate are chosen appropriately. The temperature is controlled using a Jasco Peltier temperature controller with a range of -10 – 110 °C and adjustable temperature slope.

Co-assembly kinetics model. To analyse the co-assembly kinetics of S- and ROPV (*S* and *R*) into *M*- and *P*-type helical aggregates, a deterministic kinetic model is developed. We note that hydrogen-bonding of S- and ROPV results in both homo- and hetero-dimers. However, the kinetic model describes the assembly process of the helical stacks as a sequence of OPV molecule (*i.e.* monomer) additions. This implies that it is assumed that the OPV molecules experience upon assembly in the non-preferred type of stack a mismatch penalty that is independent of the chirality of the opposite hydrogen-bonded OPV molecule.

Formation of the nucleus. The assembly of both *M*- and *P*-type stacks starts off by association of two monomers (*i.e.* SOPV, ROPV or a combination of both) into *M*- and *P*-type nuclei M_2 and P_2. In Chapter 2 it is described that the nucleus size involved in OPV aggregation is larger than 2. However, for simplicity a nucleus size of 2 is assumed in the co-assembly model.

$$\begin{aligned}\frac{\mathrm{d}[M_2]}{\mathrm{d}t} &= a_\mathrm{n}[S]^2 + 2a_\mathrm{n}[S][R] + a_\mathrm{n}[R]^2 \\ &- b_\mathrm{n}\left(\frac{[M(S)]}{[M(S)]+[M(R)]}\right)^2[M_2] - 2b_\mathrm{n}\cdot MMP\cdot\left(\frac{[M(S)]}{[M(S)]+[M(R)]}\right)\left(\frac{[M(R)]}{[M(S)]+[M(R)]}\right)[M_2] \\ &- b_\mathrm{n}\cdot MMP^2\cdot\left(\frac{[M(R)]}{[M(S)]+[M(R)]}\right)^2[M_2],\end{aligned} \tag{4.1}$$

$$\begin{aligned}\frac{\mathrm{d}[P_2]}{\mathrm{d}t} &= a_\mathrm{n}[S]^2 + 2a_\mathrm{n}[S][R] + a_\mathrm{n}[R]^2 \\ &- b_\mathrm{n}\left(\frac{[P(R)]}{[P(S)]+[P(R)]}\right)^2[P_2] - 2b_\mathrm{n}\cdot MMP\cdot\left(\frac{[P(S)]}{[P(S)]+[P(R)]}\right)\left(\frac{[P(R)]}{[P(S)]+[P(R)]}\right)[P_2] \\ &- b_\mathrm{n}\cdot MMP^2\cdot\left(\frac{[P(S)]}{[P(S)]+[P(R)]}\right)^2[P_2].\end{aligned} \tag{4.2}$$

Here, a_n and b_n represent the nucleation rate constants of monomer association and dissociation, respectively. The disassembly rate of the dimer is dependent on its composition: dissociation of monomers from their non-preferred aggregate helicity (*i.e. S* in *P*-type and *R* in *M*-type assemblies) is increased with a mismatch penalty factor *MMP* and disassembly of the *SS*(*P*) and *RR*(*M*) dimers is increased with a factor MMP^2. The concentration of each type of dimer (*i.e.* [*SS*(*M*)], [*SR*(*M*)], [*RR*(*M*)],

[*SS*(*P*)], [*SR*(*P*)], [*RR*(*P*)]) is approximated via the ratio of both monomers in the respective aggregate type, where [*M*(*S*)] represents the concentration of *S* in *M*-type assemblies, [*M*(*R*)] the concentration of *R* in *M*-type assemblies, [*P*(*R*)] the concentration of *R* in *P*-type assemblies and [*P*(*S*)] the concentration of *S* in *P*-type assemblies. As the probability to form a heterodimer (*i.e. SR* or *RS*) is two times larger than the probability to form the homodimers *RR* or *SS*, a factor 2 is included in the description of the formation rate of the heterodimers. Analogously, a factor 2 is included in the description of the dissociation of the heterodimers.

Similar to eq. 4.1 the following differential equations for the free monomer concentrations [*S*] and [*R*] as well as [*M*(*S*)] and [*M*(*R*)] can be derived:

$$\frac{\mathrm{d}[S]}{\mathrm{d}t} = -2a_\mathrm{n}[S]^2 - 2a_\mathrm{n}[S][R] + 2b_\mathrm{n}\left(\frac{[M(S)]}{[M(S)]+[M(R)]}\right)^2[M_2] + 2b_\mathrm{n}\cdot MMP\cdot\left(\frac{[M(S)]}{[M(S)]+[M(R)]}\right)\left(\frac{[M(R)]}{[M(S)]+[M(R)]}\right)[M_2], \tag{4.3}$$

$$\frac{\mathrm{d}[R]}{\mathrm{d}t} = -2a_\mathrm{n}[S][R] - 2a_\mathrm{n}[R]^2 + 2b_\mathrm{n}\cdot MMP\cdot\left(\frac{[M(S)]}{[M(S)]+[M(R)]}\right)\left(\frac{[M(R)]}{[M(S)]+[M(R)]}\right)[M_2] + 2b_\mathrm{n}\cdot MMP^2\cdot\left(\frac{[M(R)]}{[M(S)]+[M(R)]}\right)^2[M_2], \tag{4.4}$$

$$\frac{\mathrm{d}[M(S)]}{\mathrm{d}t} = 2a_\mathrm{n}[S]^2 + 2a_\mathrm{n}[S][R] - 2b_\mathrm{n}\left(\frac{[M(S)]}{[M(S)]+[M(R)]}\right)^2[M_2] - 2b_\mathrm{n}\cdot MMP\cdot\left(\frac{[M(S)]}{[M(S)]+[M(R)]}\right)\left(\frac{[M(R)]}{[M(S)]+[M(R)]}\right)[M_2], \tag{4.5}$$

$$\frac{\mathrm{d}[M(R)]}{\mathrm{d}t} = 2a_\mathrm{n}[S][R] + 2a_\mathrm{n}[R]^2 - 2b_\mathrm{n}\cdot MMP\cdot\left(\frac{[M(S)]}{[M(S)]+[M(R)]}\right)\left(\frac{[M(R)]}{[M(S)]+[M(R)]}\right)[M_2] - 2b_\mathrm{n}\cdot MMP^2\cdot\left(\frac{[M(R)]}{[M(S)]+[M(R)]}\right)^2[M_2]. \tag{4.6}$$

Analogously to eq. 4.2 the following differential equations for the free monomer concentrations, [*P*(*S*)] and [*P*(*R*)] can be derived. It should be noted that eq. 4.7 and 4.8 are extensions of eq. 4.3 and 4.4, respectively.

$$\frac{\mathrm{d}[S]}{\mathrm{d}t} = \frac{\mathrm{d}[S]}{\mathrm{d}t}(eq.\ 4.3) - 2a_\mathrm{n}[S]^2 - 2a_\mathrm{n}[S][R] + 2b_\mathrm{n}\cdot MMP\cdot\left(\frac{[P(S)]}{[P(S)]+[P(R)]}\right)\left(\frac{[P(R)]}{[P(S)]+[P(R)]}\right)[P_2] + 2b_\mathrm{n}\cdot MMP^2\cdot\left(\frac{[P(S)]}{[P(S)]+[P(R)]}\right)^2[P_2], \tag{4.7}$$

$$\frac{\mathrm{d}[R]}{\mathrm{d}t} = \frac{\mathrm{d}[R]}{\mathrm{d}t}(eq.\ 4.4) - 2a_\mathrm{n}[S][R] - 2a_\mathrm{n}[R]^2 + 2b_\mathrm{n}\left(\frac{[P(R)]}{[P(S)]+[P(R)]}\right)^2[P_2] + 2b_\mathrm{n}\cdot MMP\cdot\left(\frac{[P(S)]}{[P(S)]+[P(R)]}\right)\left(\frac{[P(R)]}{[P(S)]+[P(R)]}\right)[P_2], \tag{4.8}$$

$$\frac{\mathrm{d}[P(S)]}{\mathrm{d}t} = 2a_\mathrm{n}[S]^2 + 2a_\mathrm{n}[S][R] - 2b_\mathrm{n}\cdot MMP\cdot\left(\frac{[P(S)]}{[P(S)]+[P(R)]}\right)\left(\frac{[P(R)]}{[P(S)]+[P(R)]}\right)[P_2] - 2b_\mathrm{n}\cdot MMP^2\cdot\left(\frac{[P(S)]}{[P(S)]+[P(R)]}\right)^2[P_2], \tag{4.9}$$

$$\frac{\mathrm{d}[P(R)]}{\mathrm{d}t} = 2a_\mathrm{n}[S][R] + 2a_\mathrm{n}[R]^2 - 2b_\mathrm{n}\left(\frac{[P(R)]}{[P(S)]+[P(R)]}\right)^2[P_2] - 2b_\mathrm{n}\cdot MMP\cdot\left(\frac{[P(S)]}{[P(S)]+[P(R)]}\right)\left(\frac{[P(R)]}{[P(S)]+[P(R)]}\right)[P_2]. \tag{4.10}$$

Assembly of S monomer in M-type stacks. The build-up of *M*-type stacks via stepwise association and dissociation of *S* monomers is described subsequently for every length *i*, with *i* increasing stepwise from 3 up to *N*:

$$\begin{aligned} &Q = a[S][M_{i-1}] - c[M_i]\left(\frac{[M(S)]}{[M(S)]+[M(R)]}\right), \\ &\frac{\mathrm{d}[M_i]}{\mathrm{d}t}(new) = \frac{\mathrm{d}[M_i]}{\mathrm{d}t}(old) + Q, \quad \frac{\mathrm{d}[M_{i-1}]}{\mathrm{d}t}(new) = \frac{\mathrm{d}[M_{i-1}]}{\mathrm{d}t}(old) - Q, \\ &\frac{\mathrm{d}[S]}{\mathrm{d}t}(new) = \frac{\mathrm{d}[S]}{\mathrm{d}t}(old) - Q, \quad \frac{\mathrm{d}[M(S)]}{\mathrm{d}t}(new) = \frac{\mathrm{d}[M(S)]}{\mathrm{d}t}(old) + Q, \end{aligned} \tag{4.11}$$

where *a* and *c* represent the rate constants of monomer association and dissociation, respectively. *Q* is calculated stepwise for every length *i*, from *i* = 3 up to *i* = *N*. In every step, the value of Q is added to (or subtracted from) the differential equations that describe the concentrations of the different species in the system.

To describe also the formation of species with length larger than *N*, we apply the methodology that is introduced in Chapter 2. The assemblies with size larger than *N* are described per type (*i.e. M*- and *P*-type) together as fibrils by considering the fibril number concentrations [F_M] and [F_P], with [F_M] = [M_{N+1}] + [M_{N+2}] + [M_{N+3}] + …, and [F_P] = [P_{N+1}] + [P_{N+2}] + [P_{N+3}] +…, and the fibril mass concentrations [Z_M] and [Z_P], with [Z_M] = (*N*+1)·[M_{N+1}] + (*N*+2)·[M_{N+2}] + (*N*+3)·[M_{N+3}] + …, and [Z_P] = (*N*+1)· [P_{N+1}] + (*N*+2)·[P_{N+2}] + (*N*+3)·[P_{N+3}] +… Assuming that for *i* > *N*, [M_{i+1}] = α_M[M_i] and [P_{i+1}] = α_P[P_i], it can be shown that

$$\alpha_M = 1 - \frac{[F_M]}{[Z_M] - N[F_M]} \quad \text{and} \quad \alpha_P = 1 - \frac{[F_P]}{[Z_P] - N[F_P]}, \tag{4.12}$$

by which the concentrations [M_{N+1}] and [P_{N+1}] can be found via

$$[M_{N+1}] = (1-\alpha_M)[F_M] \quad \text{and} \quad [P_{N+1}] = (1-\alpha_P)[F_P]. \tag{4.13}$$

With the expressions for [M_{N+1}], *i.e.* eq. 4.12 and 4.13, the formation of *M*-type stacks with length *N*+1 upon association and dissociation of *S* monomers can be described:

$$\begin{aligned} &Q = a[S][M_N] - c[M_{N+1}]\left(\frac{[M(S)]}{[M(S)]+[M(R)]}\right), \\ &\frac{\mathrm{d}[M_N]}{\mathrm{d}t}(new) = \frac{\mathrm{d}[M_N]}{\mathrm{d}t}(old) - Q, \quad \frac{\mathrm{d}[F_M]}{\mathrm{d}t}(new) = \frac{\mathrm{d}[F_M]}{\mathrm{d}t}(old) + Q, \quad \frac{\mathrm{d}[Z_M]}{\mathrm{d}t}(new) = \frac{\mathrm{d}[Z_M]}{\mathrm{d}t}(old) + (N+1)Q, \\ &\frac{\mathrm{d}[S]}{\mathrm{d}t}(new) = \frac{\mathrm{d}[S]}{\mathrm{d}t}(old) - Q, \quad \frac{\mathrm{d}[M(S)]}{\mathrm{d}t}(new) = \frac{\mathrm{d}[M(S)]}{\mathrm{d}t}(old) + Q, \end{aligned} \tag{4.14}$$

as well as the assembly of stacks with size larger than *N*+1:

$$\begin{aligned} &Q = a[S][F_M] - c([F_M] - [M_{N+1}])\left(\frac{[M(S)]}{[M(S)]+[M(R)]}\right), \\ &\frac{\mathrm{d}[Z_M]}{\mathrm{d}t}(new) = \frac{\mathrm{d}[Z_M]}{\mathrm{d}t}(old) + Q, \quad \frac{\mathrm{d}[S]}{\mathrm{d}t}(new) = \frac{\mathrm{d}[S]}{\mathrm{d}t}(old) - Q, \quad \frac{\mathrm{d}[M(S)]}{\mathrm{d}t}(new) = \frac{\mathrm{d}[M(S)]}{\mathrm{d}t}(old) + Q. \end{aligned} \tag{4.15}$$

Assembly of R monomer in M-type stacks. Analogously, the build-up of *M*-type stacks via stepwise association and dissociation of *R* monomers is described subsequently for every length *i*, with *i* increasing stepwise from 3 up to *N*:

$$\begin{aligned}
&Q = a[R][M_{i-1}] - c \cdot MMP \cdot [M_i]\left(\frac{[M(R)]}{[M(S)]+[M(R)]}\right),\\
&\frac{\mathrm{d}[M_i]}{\mathrm{d}t}(new) = \frac{\mathrm{d}[M_i]}{\mathrm{d}t}(old) + Q, \quad \frac{\mathrm{d}[M_{i-1}]}{\mathrm{d}t}(new) = \frac{\mathrm{d}[M_{i-1}]}{\mathrm{d}t}(old) - Q,\\
&\frac{\mathrm{d}[R]}{\mathrm{d}t}(new) = \frac{\mathrm{d}[R]}{\mathrm{d}t}(old) - Q, \quad \frac{\mathrm{d}[M(R)]}{\mathrm{d}t}(new) = \frac{\mathrm{d}[M(R)]}{\mathrm{d}t}(old) + Q,
\end{aligned} \tag{4.16}$$

With the expressions for $[M_{N+1}]$, *i.e.* eq. 4.12 and 4.13, the formation of *M*-type stacks with length *N*+1 upon association and dissociation of *R* monomers can be described:

$$\begin{aligned}
&Q = a[R][M_N] - c \cdot MMP \cdot [M_{N+1}]\left(\frac{[M(R)]}{[M(S)]+[M(R)]}\right),\\
&\frac{\mathrm{d}[M_N]}{\mathrm{d}t}(new) = \frac{\mathrm{d}[M_N]}{\mathrm{d}t}(old) - Q, \quad \frac{\mathrm{d}[F_M]}{\mathrm{d}t}(new) = \frac{\mathrm{d}[F_M]}{\mathrm{d}t}(old) + Q, \quad \frac{\mathrm{d}[Z_M]}{\mathrm{d}t}(new) = \frac{\mathrm{d}[Z_M]}{\mathrm{d}t}(old) + (N+1)Q,\\
&\frac{\mathrm{d}[R]}{\mathrm{d}t}(new) = \frac{\mathrm{d}[R]}{\mathrm{d}t}(old) - Q, \quad \frac{\mathrm{d}[M(R)]}{\mathrm{d}t}(new) = \frac{\mathrm{d}[M(R)]}{\mathrm{d}t}(old) + Q,
\end{aligned} \tag{4.17}$$

as well as the assembly of stacks with size larger than *N*+1:

$$\begin{aligned}
&Q = a[R][F_M] - c \cdot MMP \cdot ([F_M] - [M_{N+1}])\left(\frac{[M(R)]}{[M(S)]+[M(R)]}\right),\\
&\frac{\mathrm{d}[Z_M]}{\mathrm{d}t}(new) = \frac{\mathrm{d}[Z_M]}{\mathrm{d}t}(old) + Q, \quad \frac{\mathrm{d}[R]}{\mathrm{d}t}(new) = \frac{\mathrm{d}[R]}{\mathrm{d}t}(old) - Q, \quad \frac{\mathrm{d}[M(R)]}{\mathrm{d}t}(new) = \frac{\mathrm{d}[M(R)]}{\mathrm{d}t}(old) + Q.
\end{aligned} \tag{4.18}$$

Assembly of R monomer in P-type stacks. The build-up of *P*-type stacks via stepwise association and dissociation of *R* monomers is described subsequently for every length *i*, with *i* increasing stepwise from 3 up to *N*:

$$\begin{aligned}
&Q = a[R][P_{i-1}] - c \cdot [P_i]\left(\frac{[P(R)]}{[P(S)]+[P(R)]}\right),\\
&\frac{\mathrm{d}[P_i]}{\mathrm{d}t}(new) = \frac{\mathrm{d}[P_i]}{\mathrm{d}t}(old) + Q, \quad \frac{\mathrm{d}[P_{i-1}]}{\mathrm{d}t}(new) = \frac{\mathrm{d}[P_{i-1}]}{\mathrm{d}t}(old) - Q,\\
&\frac{\mathrm{d}[R]}{\mathrm{d}t}(new) = \frac{\mathrm{d}[R]}{\mathrm{d}t}(old) - Q, \quad \frac{\mathrm{d}[P(R)]}{\mathrm{d}t}(new) = \frac{\mathrm{d}[P(R)]}{\mathrm{d}t}(old) + Q.
\end{aligned} \tag{4.19}$$

With the expressions for $[P_{N+1}]$, *i.e.* eq. 4.12 and 4.13, the formation of *P*-type stacks with length *N*+1 upon association and dissociation of *R* monomers can be described:

$$\begin{aligned}
&Q = a[R][P_N] - c[P_{N+1}]\left(\frac{[P(R)]}{[P(S)]+[P(R)]}\right),\\
&\frac{\mathrm{d}[P_N]}{\mathrm{d}t}(new) = \frac{\mathrm{d}[P_N]}{\mathrm{d}t}(old) - Q, \quad \frac{\mathrm{d}[F_P]}{\mathrm{d}t}(new) = \frac{\mathrm{d}[F_P]}{\mathrm{d}t}(old) + Q, \quad \frac{\mathrm{d}[Z_P]}{\mathrm{d}t}(new) = \frac{\mathrm{d}[Z_P]}{\mathrm{d}t}(old) + (N+1)Q,\\
&\frac{\mathrm{d}[R]}{\mathrm{d}t}(new) = \frac{\mathrm{d}[R]}{\mathrm{d}t}(old) - Q, \quad \frac{\mathrm{d}[P(R)]}{\mathrm{d}t}(new) = \frac{\mathrm{d}[P(R)]}{\mathrm{d}t}(old) + Q,
\end{aligned} \tag{4.20}$$

as well as the assembly of stacks with size larger than *N*+1:

$$\begin{aligned}
&Q = a[R][F_P] - c([F_P] - [P_{N+1}])\left(\frac{[P(R)]}{[P(S)]+[P(R)]}\right),\\
&\frac{\mathrm{d}[Z_P]}{\mathrm{d}t}(new) = \frac{\mathrm{d}[Z_P]}{\mathrm{d}t}(old) + Q, \quad \frac{\mathrm{d}[R]}{\mathrm{d}t}(new) = \frac{\mathrm{d}[R]}{\mathrm{d}t}(old) - Q, \quad \frac{\mathrm{d}[P(R)]}{\mathrm{d}t}(new) = \frac{\mathrm{d}[P(R)]}{\mathrm{d}t}(old) + Q.
\end{aligned} \tag{4.21}$$

Assembly of S monomer in P-type stacks. The build-up of *P*-type stacks via stepwise association and dissociation of *S* monomers is described subsequently for every length *i*, with *i* increasing stepwise from 3 up to *N*:

$$\begin{aligned} &Q = a[S][P_{i-1}] - c \cdot MMP \cdot [P_i]\left(\frac{[P(S)]}{[P(S)]+[P(R)]}\right), \\ &\frac{d[P_i]}{dt}(new) = \frac{d[P_i]}{dt}(old) + Q, \quad \frac{d[P_{i-1}]}{dt}(new) = \frac{d[P_{i-1}]}{dt}(old) - Q, \\ &\frac{d[S]}{dt}(new) = \frac{d[S]}{dt}(old) - Q, \quad \frac{d[P(S)]}{dt}(new) = \frac{d[P(S)]}{dt}(old) + Q. \end{aligned} \tag{4.22}$$

With the expressions for $[P_{N+1}]$, *i.e.* eq. 4.12 and 4.13, the formation of *P*-type stacks with length *N*+1 upon association and dissociation of *S* monomers can be described:

$$\begin{aligned} &Q = a[S][P_N] - c \cdot MMP \cdot [P_{N+1}]\left(\frac{[P(S)]}{[P(S)]+[P(R)]}\right), \\ &\frac{d[P_N]}{dt}(new) = \frac{d[P_N]}{dt}(old) - Q, \quad \frac{d[F_P]}{dt}(new) = \frac{d[F_P]}{dt}(old) + Q, \quad \frac{d[Z_P]}{dt}(new) = \frac{d[Z_P]}{dt}(old) + (N+1)Q, \\ &\frac{d[S]}{dt}(new) = \frac{d[S]}{dt}(old) - Q, \quad \frac{d[P(S)]}{dt}(new) = \frac{d[P(S)]}{dt}(old) + Q, \end{aligned} \tag{4.23}$$

as well as the assembly of stacks with size larger than *N*+1:

$$\begin{aligned} &Q = a[S][F_P] - c \cdot MMP \cdot ([F_P] - [P_{N+1}])\left(\frac{[P(S)]}{[P(S)]+[P(R)]}\right), \\ &\frac{d[Z_P]}{dt}(new) = \frac{d[Z_P]}{dt}(old) + Q, \quad \frac{d[S]}{dt}(new) = \frac{d[S]}{dt}(old) - Q, \quad \frac{d[P(S)]}{dt}(new) = \frac{d[P(S)]}{dt}(old) + Q. \end{aligned} \tag{4.24}$$

The total concentrations of monomers assembled in *M*-type stacks (M_{tot}) and *P*-type stacks (P_{tot}) are defined as:

$$M_{tot} = \sum_{i=2}^{N} i \cdot [M_i] + [Z_M], \quad P_{tot} = \sum_{i=2}^{N} i \cdot [P_i] + [Z_P]. \tag{4.25}$$

In order to simulate the time-dependent development of $P_{tot} - M_{tot}$ and $P_{tot} + M_{tot}$, the total system of ordinary differential equations (ODEs) is solved by applying the Matlab *ode15s* solver. The total concentration of *S* and *R* monomers, S_{tot} and R_{tot}, is determined by the enantiomeric excess *ee* = $(R_{tot} - S_{tot}) / c_{tot}$, where c_{tot} is the total concentration. The co-assembly kinetics are simulated for a variety of *ee*-values, with parameters $a_n = 2 \cdot 10^4$ $M^{-1}s^{-1}$; $b_n = 200$ s^{-1}; $a = 4 \cdot 10^4$ $M^{-1}s^{-1}$; $c = 0.04$ s^{-1}; $MMP = 1.1$; $c_{tot} = 10$ μM and $N = 200$, as shown in Figure 4.2.

To verify the assumption that the dissociation probability of *S* and *R* monomers can be computed from the overall ratio of both monomers present in the respective aggregate type, the simulated results are compared to stochastic simulations performed by dr. Bart Markvoort, in which the exact monomer sequence of every stack is considered. The methodology employed in these stochastic simulations is described in detail in ref. 27. As shown in Figure 4.8a, the kinetic curves predicted by the co-assembly model are in perfect agreement with the stochastic simulations.

Moreover, the steady state fractions of *R* monomers present in *P*-type stacks and *S* monomers in *M*-type stacks, as predicted by the co-assembly model, are verified with an equilibrium model. In ref. 44, it has been demonstrated by ten Eikelder *et al.* that

$$\frac{[P(R)]}{[P(R)]+[P(S)]} = \frac{K[R]}{K[R] + \frac{K}{MMP}[S]}, \quad \frac{[M(S)]}{[M(S)]+[M(R)]} = \frac{K[S]}{K[S] + \frac{K}{MMP}[R]}, \tag{4.26}$$

where K represents the equilibrium constant of elongation, equal to a/c. As shown in Figure 4.8b, the co-assembly kinetic model obeys under steady state conditions also to these equilibrium relations.

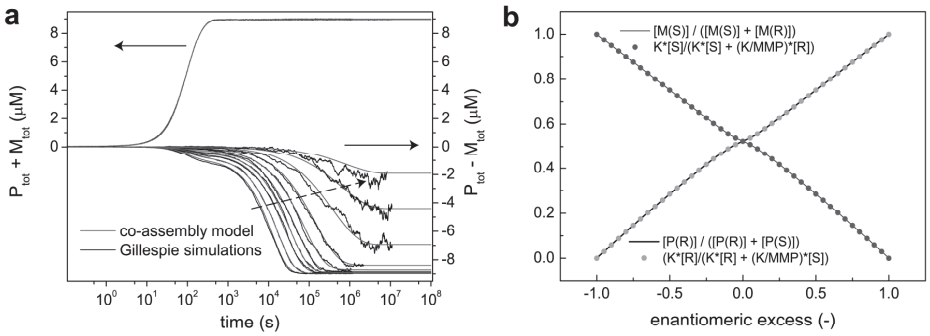

Figure 4.8 | (a) Comparison of the time-dependent net helicity ($P_{tot} - M_{tot}$) and total amount of assembled material ($P_{tot} + M_{tot}$) obtained via kinetic simulations with the co-assembly model and the Gillespie methodology.[27] (b) The steady state fractions of R monomers present in P-type stacks and S monomers in M-type stacks, as predicted by the co-assembly model, are in perfect agreement with the equilibrium model (eq. 26). Parameters: $a_n = 2{\cdot}10^4$ $M^{-1}s^{-1}$; $b_n = 200$ s^{-1}; $a = 4{\cdot}10^4$ $M^{-1}s^{-1}$; $c = 0.04$ $M^{-1}s^{-1}$; $MMP = 1.1$ $c_{tot} = 10$ μM; $N = 200$; ee increases along the dashed arrow: $ee = -1$; $ee = -0.8$, $ee = -0.6$; $ee = -0.5$; $ee = -0.4$; $ee = -0.3$; $ee = -0.2$; $ee = -0.1$; $ee = -0.05$; $ee = -0.02$. In the stochastic simulations, a system of 10^5 monomers is considered.

Temperature-dependent kinetic simulations. The kinetic curves in Figure 4.4d are simulated using the two pathway kinetics model as introduced in Chapter 2 with the temperature-dependent rate constants as shown in Figure 4.4c. The other rate constants are defined via temperature-independent ratios: $b_A = c_A / 0.1$, $b_B = c_B / 0.01$, the nucleus size for both the stable and metastable pathway is 5 and $N = 100$. To simulate the cooling curves with the different cooling rates, for every curve, at $T = 50$ °C, the assembly of monomer X (10 μM) is simulated for a time interval t_{step}, using the temperature-dependent rate constants. This time interval is determined via the time that is spent to decrease the temperature with 0.5 °C; *i.e.* $t_{step} = \frac{0.5\ °C}{\text{cooling rate in °C/min}} \times 60\ \text{s/min}$. Next, the final concentrations of all species at 50 °C are taken as the starting conditions for the subsequent simulation step performed at 49.5 °C. This step has a length of t_{step} as well, and is performed with rate parameters applicable to this temperature. Via this approach, T is decreased in steps of $\Delta T = 0.5$ °C to 0 °C, and subsequently the equilibration kinetics are simulated at 20 °C, by using the final concentrations obtained at 0 °C as starting conditions. The kinetic curves in Figure 4.6 are simulated using the same methodology and parameters.

To verify if the maximum rate in net helicity that is observed after rapid quenching (Fig 4.4a) can be rationalized by an aggregation mechanism that follows a single pathway, we perform, comparable to the temperature-dependent simulations described above with the two pathway kinetics model, temperature-dependent simulations with a single pathway kinetic model. In analogy to the kinetic model shown in Figure 4.4, the single pathway kinetics model, (*i.e.* the two pathway kinetics model with $a_A = 0$) describes the nucleated assembly of aggregates B as a sequence of monomer dissociation and association reactions, described with rate constants a_B and c_B, respectively. In the nucleation regime, monomer dissociation is described with rate constant b_B, with $b_B > c_B$. The equilibration curves simulated after cooling with different cooling rates reveal no significant relation between the equilibration rate and the preceding cooling rate, in contrast to the experimental results. Only for the slowest cooling rates, a

slow disassembly is observed which is related to the formation of long stacks at low temperatures that partly disassemble again at 20 °C.

Optimizing the assembly rate upon stepwise changing the good solvent fraction. To simulate the stepwise assembly of monomers by adjusting the solvent conditions, we assume that both the rate constants of monomer association and dissociation for the stable pathway *B* in the elongation regime, $a_{B,f}$ and $c_{B,f}$ respectively, depend on the good solvent fraction *f* via:

$$\begin{aligned} \log\left(a_{B,f}\right) &= \log\left(a_B\right) - m_a f, \\ \log\left(c_{B,f}\right) &= \log\left(c_B\right) + m_c f, \end{aligned} \tag{4.27}$$

where a_B and c_B represent the rate constants in pure poor solvent. The equilibrium constant of elongation $K_{eB,f}$ is defined via $K_{eB,f} = a_{B,f} / c_{B,f}$, and the equilibrium constant of nucleation $K_{nB,f}$ via $K_{nB,f} = \sigma \cdot K_{eB,f}$, with cooperativity parameter σ which is assumed to be independent of *f*. The rate constant of dissociation in the nucleation regime $b_{B,f}$ can be found via $b_{B,f} = a_{B,f} / K_{nB,f}$. Next, the rate constant of monomer association for the metastable pathway *A* is defined via $a_{A,f} = r_A \cdot a_{B,f}$, and the equilibrium constant of elongation $K_{eA,f}$ via $K_{eA,f} = x_A \cdot K_{eB,f}$, with both factors r_A and x_A independent of *f*. Hence, $c_{A,f} = a_{A,f} / K_{eA,f}$ and $b_{A,f} = a_{A,f} / (\sigma \cdot K_{eA,f})$.

Using these equilibrium constants and the equilibrium model as explained in paragraph 2.7, the equilibrium monomer concentration can be calculated as a function of *f* for both the metastable pathway as well as the stable pathway independently. To define the solvent fraction f_1 at which the first assembly step is simulated, *i.e.* point **i** in Figure 4.9, we first determine the critical equilibrium constant that marks the onset of the assembly of the metastable assemblies: $K_{eA,f} = 1/c_{tot}$. Hence, the corresponding value of $K_{eB,f}$ can be found via

$$K_{eB,f} = \frac{K_{eA,f}}{x_A} = \frac{1}{x_A \cdot c_{tot}}. \tag{4.28}$$

Since $K_{eB,f} = a_{B,f} / c_{B,f}$, the general relation between *f* and K_{eB} can be found via eq. 4.27:

$$\begin{aligned} &\log\left(K_{eB,f}\right) = \left(\log\left(a_B\right) - m_a f\right) - \left(\log\left(c_B\right) + m_c f\right) = \log\left(\frac{a_B}{c_B}\right) - \left(m_a + m_c\right) f, \\ &f = \frac{\log\left(K_{eB}\right) - \log\left(K_{eB,f}\right)}{m_a + m_c}, \end{aligned} \tag{4.29}$$

where K_{eB} represents the equilibrium constant of elongation in pure poor solvent. Via eq. 4.28 and 4.29, the critical solvent composition f_1 at which the first assembly step is simulated is obtained, and subsequently the equilibrium monomer concentration at f_1, $[X]_{eq}$ can be determined via the equilibrium model. If the conversion per simulation step equals *p*, the final monomer concentration for the first step $[X]_1$ (*i.e.* point **ii** in Figure 4.9) equals:

$$\left[X\right]_1 = \left[X\right]_{eq} + \left(1 - p\right)\left(c_{tot} - \left[X\right]_{eq}\right). \tag{4.30}$$

After the first assembly step, further assembly is induced by decreasing *f* such that the concentration of free monomers remaining from the first assembly step just equals the concentration of monomers required for the formation of metastable assemblies at this new good solvent fraction f_2. To find this value of f_2, *i.e.* point **iii** in Figure 4.9, we apply a numerical approach in which *f* is decreased in small steps of 0.0006 until the value of $[X]_{eq}$ according to the metastable pathway equals $[X]_1$. Next, $[X]_2$ (*i.e.* point **iv** in Figure 4.9) can be calculated comparable to the determination of $[X]_1$ via eq. 4.30. Via a similar approach, the next solvent compositions f_3, f_4, f_5 etc. are determined, until *f* equals 0.

To simulate the kinetics, first the assembly of free monomers with a total concentration of c_{tot} is simulated at f_1, with rate constants determined according to this solvent composition (eq. 4.27). When the conversion equals p, the first assembly step is stopped, and the concentrations of all species are taken as the start conditions for the next assembly step at f_2. This second assembly step is simulated with new values for the rate constants, in agreement with this solvent composition, again up to a conversion which equals p. This stepwise decrease of f is continued at f_3, f_4, f_5 etc., until f equals 0. The last assembly step at $f = 0$ is continued up to $t = 10^7$ s.

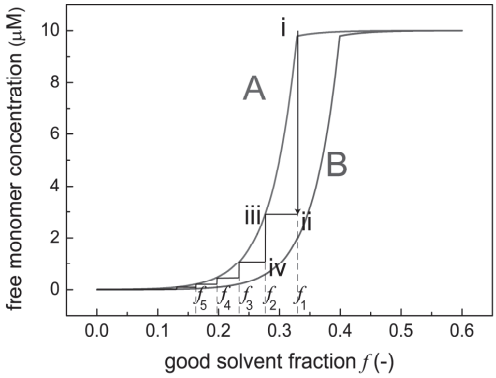

Figure 4.9 | Optimizing the assembly process by stepwise decreasing the good solvent fraction. Equilibrium free monomer concentration calculated independently for the metastable (*A*) and the stable (B) pathway as a function of good solvent fraction *f*, via the equilibrium model. The assembly process starts at point **i**, the vertical lines represent the different assembly steps performed at different solvent fractions f_i, the horizontal lines represent the rapid decrease of *f* in between these steps.

4.8 References

[1] De Greef, T. F. A.; Smulders, M. M. J.; Wolffs, M.; Schenning, A. P. H. J.; Sijbesma, R. P.; Meijer, E. W. *Chem. Rev.* **2009**, *109*, 5687.

[2] Pashuck, E. T.; Stupp, S. I. *J. Am. Chem. Soc.* **2010**, *132*, 8819.

[3] Cui, H.; Chen, Z.; Zhong, S.; Wooley, K. L.; Pochan, D. J. *Science* **2007**, *317*, 647.

[4] Tidhar, Y.; Weissman, H.; Wolf, S. G.; Gulino, A.; Rybtchinski, B. *Chem. Eur. J.* **2011**, *17*, 6068.

[5] Danila, I.; Riobé, F.; Piron, F.; Puigmartí-Luis, J.; Wallis, J. D.; Linares, M.; Ågren, H.; Beljonne, D.; Amabilino, D. B.; Avarvari, N. *J. Am. Chem. Soc.* **2011**, *133*, 8344.

[6] Ajayaghosh, A.; Varghese, R.; Praveen, V. K.; Mahesh, S. *Angew. Chem. Int. Ed.* **2006**, *45*, 3261.

[7] Boekhoven, J.; Poolman, J. M.; Maity, C.; Li, F.; Van der Mee, L.; Minkenberg, C. B.; Mendes, E.; Van Esch, J. H.; Eelkema, R. *Nature Chem.* **2013**, *5*, 433.

[8] Rupar, P. A.; Chabanne, L.; Winnik, M. A.; Manners, I. *Science* **2012**, *337*, 559.

[9] Zheng, J. Y.; Yan, Y.; Wang, X.; Zhao, Y. S.; Huang, J.; Yao, J. *J. Am. Chem. Soc.* **2012**, *134*, 2880.

[10] Zhang, W.; Jin, W.; Fukushima, T.; Saeki, A.; Seki, S.; Aida, T. *Science* **2011**, *334*, 340.

[11] Henson, Z. B.; Müllen, K.; Bazan, G. C. *Nature Chem.* **2012**, *4*, 699.

[12] Graetzel, M.; Janssen, R. A. J.; Mitzi, D. B.; Sargent, E. H. *Nature* **2012**, *488*, 304.

[13] Beaujuge, P. M.; Fréchet, J. M. J. *J Am Chem Soc* **2011**, *133*, 20009.

[14] Korevaar, P. A.; George, S. J.; Markvoort, A. J.; Smulders, M. M. J.; Hilbers, P. A. J.; Schenning, A. P. H. J.; De Greef, T. F. A.; Meijer, E. W. *Nature* **2012**, *481*, 492.

[15] Hayward, R. C.; Pochan, D. J. *Macromolecules* **2010**, *43*, 3577.

[16] Moore, J. S.; Kraft, M. L. *Science* **2008**, *320*, 620.
[17] Ladet, S.; David, L.; Domard, A. *Nature* **2008**, *452*, 76.
[18] Tevis, I. D.; Palmer, L. C.; Herman, D. J.; Murray, I. P.; Stone, P. A.; Stupp, S. I. *J. Am. Chem. Soc.* **2011**, *133*, 16486.
[19] Kim, K. T.; Zhu, J.; Meeuwissen, S. A.; Cornelissen, J. J. L. M.; Pochan, D. J.; Nolte, R. J. M.; Van Hest, J. C. M. *J. Am. Chem. Soc.* **2010**, *132*, 12522.
[20] Zhang, X.; Douglas, J. F.; Jones, R. L. *Soft Matter* **2012**, *8*, 4980.
[21] François, P.; Hakim, V. *Proc. Natl. Acad. Sci. USA* **2004**, *101*, 580.
[22] Elowitz, M. B.; Leibler, S. *Nature* **2000**, *403*, 335.
[23] Gardner, T. S.; Cantor, C. R.; Collins, J. J. *Nature* **2000**, *403*, 339.
[24] Carothers, J. M.; Goler, J. A.; Juminaga, D.; Keasling, J. D. *Science* **2011**, *334*, 1716.
[25] Jonkheijm, P.; Van der Schoot, P.; Schenning, A. P. H. J.; Meijer, E. W. *Science* **2006**, *313*, 80.
[26] Kulkarni, C.; Balasubramanian, S.; George, S. J. *ChemPhysChem* **2013**, *14*, 661.
[27] Markvoort, A. J.; Ten Eikelder, H. M. M.; Hilbers, P. A. J.; De Greef, T. F. A.; Meijer, E. W. *Nat. Commun.* **2011**, *2*, 509.
[28] Lohr, A.; Würthner, F. *Angew. Chem. Int. Ed.* **2008**, *47*, 1232.
[29] Wolffs, M.; Van Velthoven, J. L. J.; Lou, X.; Bovee, R. A. A.; Pouderoijen, M.; Van Dongen, J. L. J.; Schenning, A. P. H. J.; Meijer, E. W. *Chem. Eur. J.* **2012**, *18*, 15057.
[30] Korevaar, P. A.; Schaefer, C.; De Greef, T. F. A.; Meijer, E. W. *J. Am. Chem. Soc.* **2012**, *134*, 13482.
[31] Zhang, D. Y.; Chen, S. X.; Yin, P. *Nature Chem* **2012**, *4*, 208.
[32] Leunissen, M. E.; Dreyfus, R.; Cheong, F. C.; Grier, D. G.; Sha, R.; Seeman, N. C.; Chaikin, P. M. *Nature Mater.* **2009**, *8*, 590.
[33] Jungmann, R.; Liedl, T.; Sobey, T. L.; Shih, W.; Simmel, F. C. *J. Am. Chem. Soc.* **2008**, *130*, 10062.
[34] Sobczak, J.-P. J.; Martin, T. G.; Gerling, T.; Dietz, H. *Science* **2012**, *338*, 1458.
[35] Macfarlane, R. J.; Lee, B.; Hill, H. D.; Senesi, A. J.; Seifert, S.; Mirkin, C. A. *Proc. Natl. Acad. Sci. USA* **2009**, *106*, 10493.
[36] Schulman, R.; Winfree, E. *Proc. Natl. Acad. Sci. USA* **2007**, *104*, 15236.
[37] Shah, R. N.; Shah, N. A.; Del Rosario Lim, M. M.; Hsieh, C.; Nuber, G.; Stupp, S. I. *Proc. Natl. Acad. Sci. USA* **2010**, *107*, 3293.
[38] Dankers, P. Y. W.; Boomker, J. M.; Huizinga-van der Vlag, A.; Wisse, E.; Appel, W. P. J.; Smedts, F. M. M.; Harmsen, M. C.; Bosman, A. W.; Meijer, E. W.; Van Luyn, M. J. A. *Biomaterials* **2011**, *32*, 723.
[39] Wu W.-R.; Jeng, U.-S.; Su, C.-J.; Wei, K.-H.; Su, M.-S.; Chiu, M.-Y.; Chen, C.-Y.; Su, W.-B.; Su, C.-H.; Su, A.-C. *ACS Nano* **2011**, *5*, 6233.
[40] Yao, Y.; Hou, J.; Xu, Z.; Li, G.; Yang, Y. *Adv. Funct. Mater.* **2008**, *18*, 1783.
[41] Di Nuzzo, D.; Aguirre, A.; Shahid, M.; Gevaerts, V. S.; Meskers, S. C. J.; Janssen, R. A. J. *Adv. Mater.* **2010**, *22*, 4321.
[42] Graham, K. R.; Wieruszewski, P. M.; Stalder, R.; Hartel, M. J.; Mei, J.; So, F.; Reynolds, J. R. *Adv. Funct. Mater.* **2012**, *22*, 4801.
[43] Lee, J. K.; Ma, W. L.; Brabec, C. J.; Yuen, J.; Moon, J. S.; Kim, J. Y.; Lee, K.; Bazan, G. C.; Heeger, A. J. *J. Am. Chem. Soc.* **2008**, *130*, 3619.
[44] Ten Eikelder, H. M. M.; Markvoort, A. J.; De Greef, T. F. A.; Hilbers, P. A. J. *J. Phys. Chem. B* **2012**, *116*, 5291.

5

Pathway selection in peptide-amphiphile assembly

Abstract: This chapter demonstrates how different preparation protocols to assemble peptide-amphiphiles in water can result in different morphologies. Conditions temporarily encountered during the preparation of the assemblies, for instance upon injecting the dissolved monomers into a poor solvent that induces assembly, can have a large impact on the supramolecular structures obtained. Two effects that play a key role during the preparation are unravelled: 1) The assembly rate decreases in the presence of a destabilizing "good" solvent like hexafluoroisopropanol. 2) The assemblies have a high kinetic stability and, once formed, do not rapidly fall apart. Insights into the characteristic dynamics of the supramolecular system are envisioned to provide an efficient approach to select the optimum assembly pathway.

Part of this work will be published as:

"Pathway selection in peptide-amphiphile assembly" P. A. Korevaar, C. J. Newcomb, E. W. Meijer, S. I. Stupp, *close to submission.*

5.1 Introduction

The molecular design of peptide-amphiphiles is completely different from π-conjugated polymers that are of interest for the development of functional electronic materials, or the OPV molecules that have been studied as a model system in the previous three chapters. Nevertheless, the aggregation of peptide-amphiphiles (PAs) – an interesting class of self-assembling materials on itself owing to its biomedical relevance – shows several intriguing similarities to the kinetic behaviour of the OPV system as discussed before. Therefore, a chapter that focuses on the assembly pathways of PAs is included in this thesis. The work described here is a collaboration with dr. Christina Newcomb and prof.dr. Samuel Stupp, Northwestern University, Evanston (IL) USA.

The assembly of PA molecules into long, rigid nanofibres yields scaffold materials that can be applied to support cells and, when functionalized with bioactive epitopes, stimulate the development of these cells into a specific type of tissue.[1] *In vivo* studies have demonstrated the applicability of this approach to repair injured spinal cord[2] and to regenerate blood vessels[3], bone[4–6] and cartilage[7]. In order to assemble these PAs in water, their molecular design typically comprises (subsequently) an aliphatic tail, a peptide segment suitable for β-sheet formation and a peptide segment with hydrophilic side groups. The hydrophilic part facilitates the solution of the PA structures in water, whereas their assembly is induced by the hydrophobic interactions among the aliphatic tails together with the formation of β-sheets via hydrogen bonding.[8–12] Modelling studies have shown that the subtle interplay between the latter two types of interactions is critical to the morphology of the assemblies, varying from single β-sheets to spherical or long cylindrical micelles.[13]

To arrive at functional PA systems, many different molecular designs have been investigated since the introduction of this intriguing material by Hartgerink, Beniash and Stupp in 2001.[14] A decade of experience with PA assemblies in the Stupp laboratory – varying from mechanistic studies on their assembly to their application as biomaterial – has resulted in several methodologies to obtain the PA fibres in aqueous solution.[7, 14–16] The development of all these different preparation protocols emphasizes that the pathway selected to create these materials is critical to their morphology. In general, creating self-assemblies in water starts with the material being molecularly dissolved in a "good" solvent. Subsequently, the assembly is induced by switching to "poor" solvent conditions that can be obtained upon changing parameters like pH, temperature and salt concentration, or by the addition of the monomers that are dissolved in a co-solvent to water.[17–24] This implies that the assemblies are formed while going from good to poor solvent conditions, and that conditions temporarily encountered by the system during this process can significantly affect the morphology of the structures as well. Therefore, non-covalent synthesis of assemblies in water can be very dependent on the exact preparation methodology that is applied, similar to organic synthesis.[25–39] In this chapter it is demonstrated how different preparation protocols result in different outcomes of the PA assembly process. This can be rationalized by kinetic phenomena like hysteresis and the effect of solvent conditions on the assembly rate.

5.2 Solvent-dependent assembly of peptide-amphiphiles

The assembly of palmitoyl-$V_3A_3E_3$-NH_2, PA1 (Fig 5.1a) is studied. PA1 is assumed to be molecularly dissolved in hexafluoroisopropanol (HFIP, *i.e.* good solvent) and forms long cylindrical micelles in pure water (*i.e.* poor solvent, Fig 5.1b). To characterize a typical preparation of PA assemblies induced by a change from good to poor solvent conditions, we study the assembly of PA1 (50 μg/mL) in mixtures of water and HFIP, using circular dichroism (CD) and UV spectroscopy.

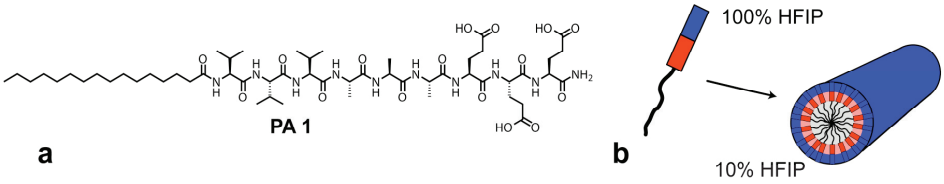

Figure 5.1 | The assembly of peptide-amphiphile PA1 into nanofibres. (a) Molecular structure of PA1. (b) PA1 is molecularly dissolved in pure HFIP and assembles under aqueous conditions via β-sheet formation into cylindrical micelles.

5.2.1 Peptide-amphiphile assembly under steady state conditions

In the CD and UV spectra, three solvent-composition regimes can be recognized (Fig 5.2ab). In pure HFIP, a CD spectrum with a negative maximum at 200 nm is obtained, indicating a random coil conformation of the oligopeptides. In more aqueous solutions of e.g. 10% (*i.e.* volume%) HFIP, β-sheet-like CD spectra are obtained, and concomitantly a clear red-shift appears in UV. Intermediate water/HFIP fractions (e.g. 50% HFIP) result in red-shifted CD spectra reminiscent of random coil structures. Detailed analysis with Dynamic Light Scattering (DLS) techniques reveals that only under the solvent conditions where β-sheets are obtained (<20% HFIP) larger PA assemblies are present in solution (Fig 5.3a). If spherical dimensions are assumed, a radius >100 nm is anticipated. However, couette flow experiments disclose an alignment of anisotropic PA structures in the presence of 10% HFIP (Fig 5.3b), thereby corroborating the formation of high-aspect ratio β-sheet nanofibres under these conditions. In the presence of 20%, 30%, 50% and 70% HFIP, time-correlation graphs are obtained suggesting the presence of small particles in solution. One might conclude that these DLS results correspond to the formation of PA micelles. This cannot be unambiguously demonstrated, however, since HFIP itself forms micelles in water as well under these conditions, as reported in literature before[40] and evidenced by the time-correlation graphs of pure water/HFIP mixtures (Fig 5.3a). The hydrophobic core of the β-sheet nanofibres is evidenced by the inclusion of the solvatochromic dye Nile red, which fluorescence depends on the local solvent conditions. Only at 10% HFIP, *i.e.* the β-sheet regime, significant differences between the fluorescence of the solution with and without PA1 are observed. This suggests that only under these conditions inclusion of the Nile red molecules in the hydrophobic core of the cylindrical PA micelles occurs. Therefore, we propose that the shifted random coil CD spectrum in intermediate HFIP percentages is related to either different conformational states of the PA, or

to the formation of small, oligomeric species that cannot be clarified by DLS or Nile red inclusion.

5.2.2 Kinetics of peptide-amphiphile assembly

To further investigate the formation of β-sheets that is dependent on the solvent composition, PA1 dissolved in HFIP is manually injected together with pure HFIP into water. Subsequently, the formation of β-sheets in time is probed in CD and UV at 200 nm (Fig 5.2cd). All kinetic experiments with different water/HFIP ratios are performed at a total PA1 concentration of 50 μg/mL. The CD data acquired under steady state conditions (Fig 5.2e) show that β-sheets (*i.e.* positive CD at 200 nm) only appear below 21% HFIP. At higher HFIP contents the random coils (*i.e.* negative CD at 200 nm) appear immediately after the injection, and both in CD and UV no further changes are observed in time (Fig 5.2cd). Remarkably, the kinetic curves show a minimum rate in the formation of β-sheets at the critical HFIP content of 21%. This phenomenon holds an intriguing resemblance to the kinetic studies on π-conjugated molecules in organic solvents as presented in Chapter 3. Furthermore, kinetic studies on the assembly of natural polypeptides have revealed a slower appearance of β-sheets in the presence of higher amounts of HFIP as well, whereas beyond a certain HFIP content only α-helices are formed.[41] This further emphasizes the generality of the interplay between solvent interactions and assembly dynamics, despite the variety of molecular interactions and solvent conditions that can be involved.

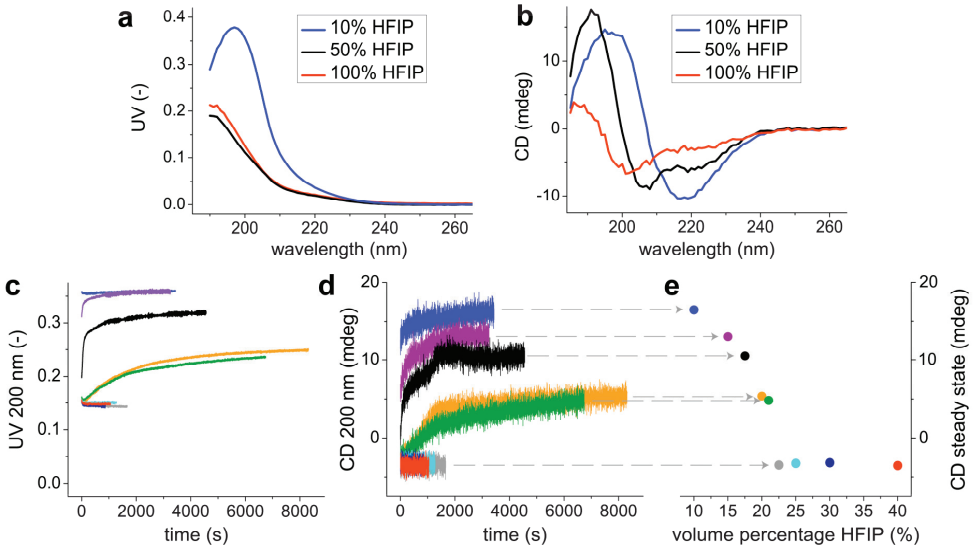

Figure 5.2 | The dynamics and stability of peptide-amphiphile assemblies depends on the solvent composition. (a, b) CD and UV spectra of PA1 in 10% HFIP / 90% water, 50% HFIP / 50% water and 100% HFIP. (c, d) The assembly kinetics of the PA β-sheets are followed in UV and CD, revealing a decrease in the rate upon increasing the HFIP content. (e) Beyond the critical HFIP content (21 volume%), no β-sheets are formed (50 μg/mL, 20 °C). The HFIP percentages are expressed in volume%.

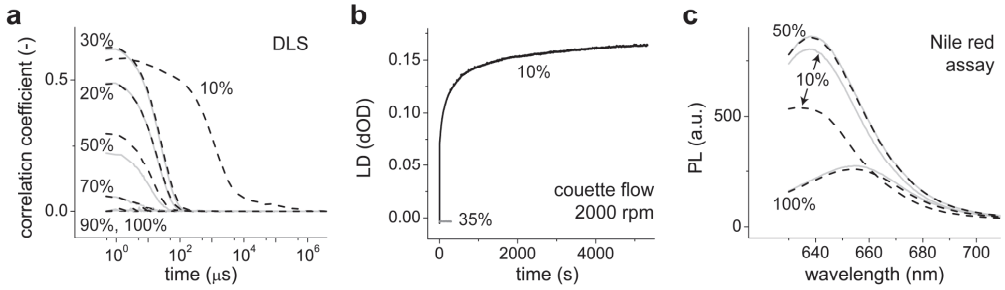

Figure 5.3 | Evidence for β-sheet nanofibres with high aspect-ratio and hydrophobic core in 10% HFIP. (a) Time-correlation graphs, obtained via Dynamic Light Scattering (DLS), on PA1 (50 μg/mL) in water/HFIP mixtures (dashed curves). The grey curves represent the scattering results obtained on pure water/HFIP mixtures. (b) Time-dependent alignment of β-sheet structures in a couette flow (2000 rpm), probed in linear dichroism (LD, 200 nm) for a PA1 solution in 10% HFIP and 35% HFIP, respectively. (c) Assessment of hydrophobic interactions within PA1 assemblies in different solvent compositions by fluorescence of solvatochromic dye Nile red (dashed curves, Nile red 1 μM, PA1 50 μg/mL, λ_{ex} = 600 nm). The grey curves represent the fluorescence of Nile red in the absence of PA1. The HFIP percentages are expressed in volume%.

5.3 The influence of preparation protocol on peptide-amphiphile assembly

The effect of solvent conditions on both the stability and the dynamics of the PA assemblies prompted us to further explore the effect of the preparation protocol on the assembly process. The assemblies are formed during the transition from good to poor solvent conditions. Hence, it is anticipated that a focus on the dynamic effect of solvent conditions that are temporarily encountered by the PAs during the assembly process clarifies the relation between preparation protocol and the structures obtained. This aspect is addressed in the first part of this paragraph. Next, increasing temperature is often considered as an attractive strategy to modify the assembly rate and erase spurious hysteresis of kinetic structures. In the second part of this paragraph, this aspect will be addressed.

5.3.1 Clarifying the effect of solvent conditions on the assembly

To illustrate the importance of the preparation protocol, we prepare a sample of the same composition in two different ways: sample 1 and 2 (see Fig 5.4). The kinetic effects discussed above have a significant influence on the preparation of an aqueous solution of PA1 (50 μg/mL) in 20% HFIP. Even though both solutions, prepared via different methods as shown in Figure 5.4a, have the same HFIP and PA content, clear differences can be observed between the CD spectra of solution 1 and 2 (Fig 5.4b). Whereas solution 1 yields a random coil CD spectrum, the spectrum acquired on solution 2 has some β-sheet character. The presence of β-sheets in solution 2 can be rationalized by the fact that for this solution first the stock solution of PA1 in HFIP is added to water. After this addition step, *i.e.* in the presence of 10% HFIP,

PA1 forms β-sheets as evidenced by the CD spectrum of solution 2▪. After the addition of the remaining amount of pure HFIP, *i.e.* in 20% HFIP, these β-sheets do not disassemble completely. To characterize the stability of these β-sheets in the presence of 20% HFIP in solution 2, CD is followed in time at 200 nm. However, no transition back to the random coil spectrum is observed. *Vice versa*, no conversion from random coils to β-sheets is observed for solution 1 (Fig 5.4b). These results demonstrate that the β-sheets formed by PA1 are sensitive to hysteresis. Once formed in a solution with 10% HFIP, as evidenced by the spectrum of solution 2▪, these structures do not disassemble on an observable time scale when the HFIP content is increased to 20%. The hysteresis of β-sheets in solution 2 is corroborated by DLS experiments (Fig 5.4c), that reveal for solution 2 correlation at much larger time scales as compared to solution 1, indicating that larger structures are present in solution 2.

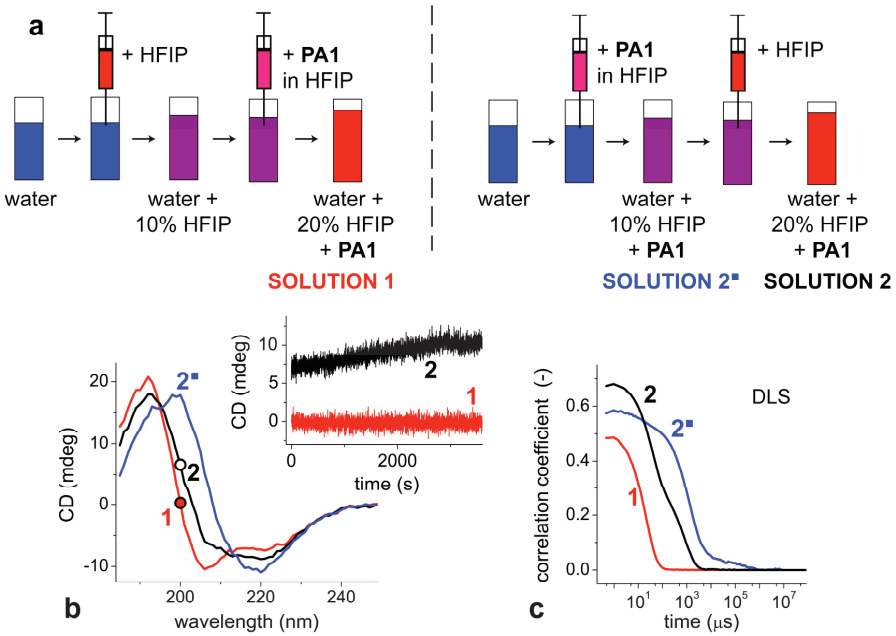

Figure 5.4 | The peptide-amphiphile assembly depends on the preparation protocol applied. (a) Two PA1 solutions (50 μg/mL) in 20% HFIP are prepared via two methods that differ by the order in which pure HFIP and the PA/HFIP stock solution are added to water. Even though both solutions 1 and 2 contain the same PA concentration and HFIP content, clear differences can be observed in CD (b) and DLS (c). The time-dependent CD (200 nm) acquired on solutions 1 and 2, shown in the inset of pane b, demonstrates the large hysteresis involved. The HFIP percentages are expressed in volume%.

To further demonstrate the effect of the non-linear relation between assembly rate and solvent composition, as shown in Figure 5.2, together with the hysteresis effect as shown in Figure 5.4, we prepare four solutions of equal PA1 concentration (93 μg/mL) and HFIP content (20%). Again, both pure HFIP as well as a stock solution of PA1 in HFIP are added to water, in four different ways as schematically depicted in Figure 5.5a. However, in this case the addition steps are performed right after each other, within 10–20 seconds, meaning that after

homogenizing of the solution the next addition is performed. As shown in Figure 5.5b, the resulting kinetic curves for solution 1 and 2 are similar, but solution 3 and 4 yield different kinetic curves, and even different final CD spectra (Fig 5.5c). These differences can be rationalized by two effects that play a key role: 1) the rate of the assembly process decreases in the presence of a destabilizing solvent like HFIP, 2) the formed β-sheets have a high kinetic stability and, once formed, do not rapidly fall apart when more HFIP is added (*i.e.* hysteresis). Combining these two effects implies that if the PAs during injection from HFIP into the water phase (temporarily) experience a pure water environment, as is likely the case for solution 1, they will quickly form β-sheets. Due to their large hysteresis, these β-sheets do no directly fall apart if another 15% HFIP is added to the solution. However, if the PAs are injected in a solution that contains 15% HFIP, the driving force for making β-sheets is much smaller, and hence random coil spectra are obtained, as is the case for solution 4. Especially when the final HFIP content approximates the critical solvent composition, this hysteresis effect will have major consequences for the assembly process. *Vice versa*, this implies that an accurate determination of the critical solvent composition, as shown in Figure 5.2e, is also subject to subtle effects in the injection and mixing methodology applied.

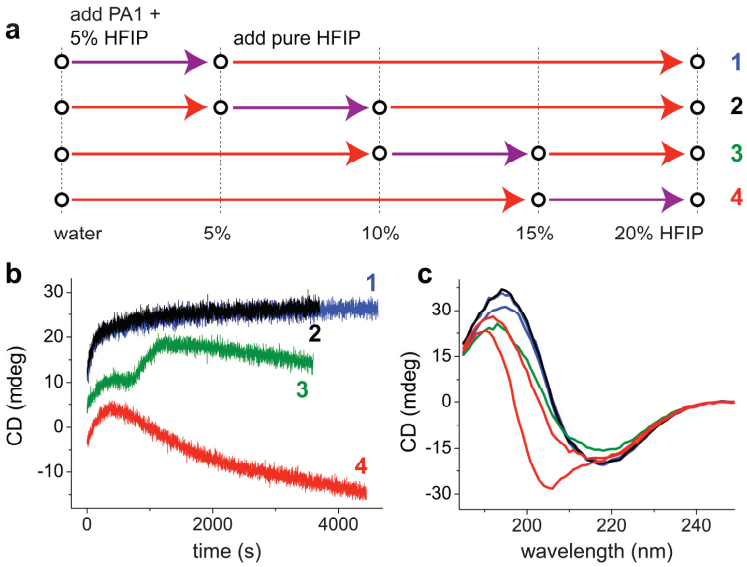

Figure 5.5 | Further evidence of solvent-dependent hysteresis in the assembly process. Four PA1 solutions (93 μg/mL) in 20% HFIP are prepared by adding 5% PA1/HFIP and aliquots of pure HFIP to water, in different order (a). The purple arrows indicate the addition of the PA1/HFIP stock solution; the red arrows indicate the additions of pure HFIP to the aqueous solution. The black circles at 5%, 10% and 15% HFIP represent intermediate stages, at which the solution is homogenized for only 10–20 seconds. Pane (b) displays CD (200 nm) *vs*. time after the preparation of solution 1–4, and (c) displays the CD spectra acquired after the respective time course measurements. The HFIP percentages are expressed in volume%.

5.3.2 The effect of temperature history on the assembly process

Often it is assumed that hysteresis effects can be erased by heating the assemblies, as the fast dynamics at elevated temperatures allow entrapped monomers to re-equilibrate or disassemble. To analyse if this is the case for PA1 assemblies, we prepare PA1 solutions (50 μg/mL) at 50 °C in different HFIP contents of 10%, 15%, and 20%. Then, the solutions are cooled to 0 °C and subsequently heated to 50 °C with a temperature ramp of 1 °C/min, while the assembly is analysed with CD (Fig 5.6ab). As shown in Figure 5.6, cooling and heating does not significantly affect the morphology of the assemblies in the solution that contains 10% HFIP. β-sheets are formed immediately at 50 °C, and these assemblies do not disappear upon cooling to 0 °C and heating back to 50 °C as evidenced by the CD spectra acquired at these temperatures. In the presence of 20% HFIP, random coil structures are obtained at 50 °C, and again the cooling and heating run does not significantly change the morphology (Fig 5.6c). For the PAs in 15% HFIP however, cooling the random coils that are initially obtained after the preparation of the sample at 50 °C yields around 40 °C a clear transition from random coils to β-sheets (Fig 5.6b). After the cooling-heating run, again with a temperature ramp of 1 °C/min, these β-sheets are still present, as demonstrated by the CD spectrum acquired at 50 °C; a clear sign of hysteresis (Fig 5.6c).

To analyse whether the equilibrium state for the 15% HFIP solution at 50 °C is either represented by the random coil CD spectrum, as obtained before the cooling-heating run, or by the β-sheet CD spectrum as obtained afterwards, the stability of both states at 50 °C is assessed in time. For a fresh prepared solution of PA1 (50 μg/mL) at 50 °C in 15% HFIP, no changes in CD are observed (Fig 5.6d). However, also for a similar solution that has been subjected to a cooling-heating run, the β-sheets do not disappear at 50 °C. Formally, this experiment does not elucidate the equilibrium morphology under these conditions (15% HFIP, 50 °C). However, these results do emphasize the strong hysteresis involved in the formation of these β-sheets fibres in 15% HFIP: they cannot be formed at 50 °C, but once they have been formed, upon cooling, they do not disassemble again at this elevated temperature.

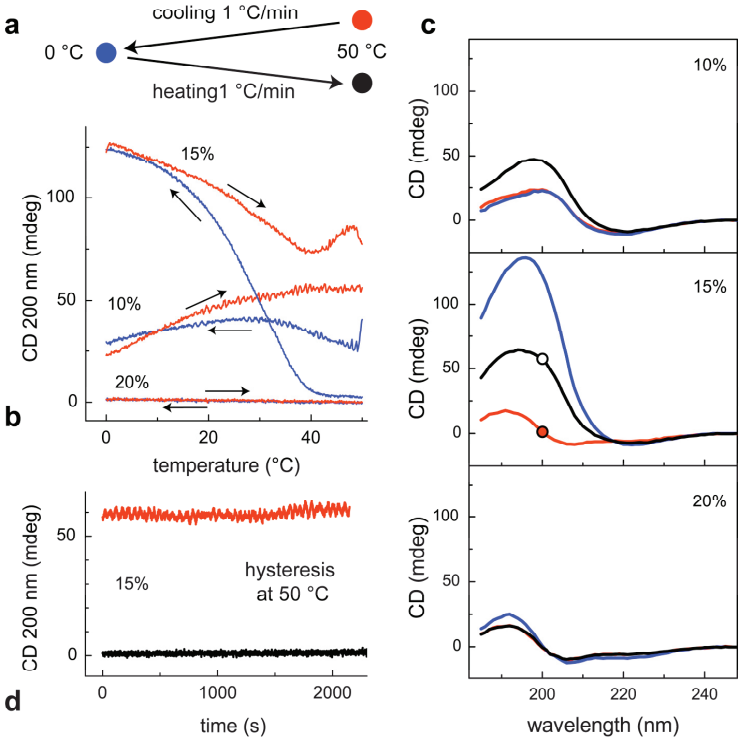

Figure 5.6 | Hysteresis effect in temperature-dependent peptide-amphiphile assembly. (a) The PA1 solutions are prepared at 50 °C (red), subsequently cooled to 0 °C (blue) and, to analyse the effect of hysteresis, subsequently heated back to 50 °C (black). (b) CD *vs.* temperature, during cooling (blue) and heating (red) of different PA solutions (50 μg/mL) with a temperature ramp of 1 °C/min. (c) The CD spectra that are subsequently acquired at 50 °C before cooling (red), at 0 °C (blue) and at 50 °C after the cooling-heating run (black) display a large hysteresis for the PA solution that contains 15% HFIP, as further demonstrated by time-dependent CD experiments (d). The HFIP percentages are expressed in volume%.

5.4 Conclusions and discussion

In summary, these experiments show that kinetic effects like hysteresis or the influence of the solvent composition on the dynamics of the assemblies can have a large impact on the supramolecular structures obtained. Due to these effects, conditions temporarily encountered during the preparation of the assemblies exert their influence on the morphology obtained. We hypothesize that, comparable to the kinetic phenomena demonstrated here for one type of PA in water/HFIP mixtures, the dynamics play a critical role in the preparation of other PA systems as well. Even if their assembly processes are controlled by other parameters like pH, salt concentration or the addition of co-assembling molecular components. Hence, every molecular system requires its own optimized preparation protocol to circumvent entrapment of material into spurious assemblies and select the pathway that is aimed for. These optimized

strategies can be very dependent on the molecular design. For example, performing the experiments with another PA in which the final amide group at the hydrophilic end was replaced by a carboxylic acid resulted in assemblies that are less sensitive to hysteresis. Analysing the dynamics of the respective system of interest requires a lot of experiments. Nevertheless, it is foreseen that considering the consequences of kinetics and hysteresis – especially on the short time scale of obvious preparation steps like injection and mixing – will advance our capability to master self-assembly in water.

5.5 Details of experiments

PA1 is kindly provided by dr. Christina Newcomb, Northwestern University, USA. HFIP and Nile red are obtained from Sigma-Aldrich and used as received. MilliQ water is used in all experiments. Circular dichroism (CD) and linear dichroism (LD) data, as well as the UV kinetics are recorded using a Jasco J-815 CD spectrometer. Sensitivity, response time and scanning rate were chosen appropriately. The temperature is controlled using a Jasco Peltier temperature controller with a range of -10 – 110 °C and adjustable temperature slope. The UV spectra are recorded using a Jasco V-650 UV/Vis spectrometer with a Jasco Peltier temperature controller. Dynamic Light Scattering (DLS) experiments are performed on a Malvern μV Zetasizer with an 830 nm laser. Fluorescence spectra are acquired on a Jasco FP-6500 spectrofluorometer. Couette flow experiments are performed with a Dioptica Scienctific Ltd. Linear Dichroism 2 setup, equipped with a quartz sample holder, connected in line with the Jasco J-815 spectrometer.

The kinetic experiments in CD and UV are performed in a 1mm quartz cuvette; the samples are prepared by injecting the respective solvents and solutions directly into the cuvette. The fluorescence experiments are performed in a 1cm x 1cm fluorescence quartz cuvette, with an excitation wavelength of 600 nm. The optical density of all solutions is kept below 0.1, verified by UV measurements, to avoid inner filter effects. DLS experiments are performed using a 1cm x 1cm fluorescence quartz cuvette. DLS samples are filtered through a 0.2 μm PTFE filter (Whatman) prior to the measurement; the presence of PA assemblies after the filtering step is verified by CD spectroscopy.

5.6 References

[1] Cui, H.; Webber, M. J.; Stupp, S. I. *PeptideScience* **2010**, *94*, 1.
[2] Tysseling-Mattiace, V. M.; Sahni, V.; Niece, K. L.; Birch, D.; Czeisler, C.; Fehlings, M. G.; Stupp, S. I.; Kessler, J. A. *J. Neurosci.* **2008**, *28*, 3814.
[3] Rajangam, K.; Behanna, H. A.; Hui, M. J.; Han, X.; Hulvat, J. F.; Lomasney, J. W.; Stupp, S. I. *Nano Lett.* **2006**, *6*, 2086.
[4] Mata, A.; Geng, Y.; Henrikson, K. J.; Aparicio, C.; Stock, S. R.; Satcher, R. L.; Stupp, S. I. *Biomaterials* **2010**, *31*, 6004.
[5] Spoerke, E. D.; Anthony, S. G.; Stupp, S. I. *Adv. Mater.* **2009**, *21*, 425.
[6] Newcomb, C. J.; Bitton, R.; Velichko, Y. S.; Snead, M. L.; Stupp, S. I. *Small* **2012**, *8*, 2195.
[7] Shah, R. N.; Shah, N. A.; Del Rosario Lim, M. M.; Hsieh, C.; Nuber, G.; Stupp, S. I. *Proc. Natl. Acad. Sci. USA* **2010**, *107*, 3293.
[8] Lee, O.-S.; Cho, V.; Schatz, G. C. *Nano Lett.* **2012**, *12*, 4907.
[9] Tovar, J. D.; Claussen, R. C.; Stupp, S. I. *J. Am. Chem. Soc.* **2005**, *127*, 7337.
[10] Lee, O.-S.; Stupp, S. I.; Schatz, G. C. *J. Am. Chem. Soc.* **2011**, *133*, 3677.
[11] Paramonov, S. E.; Jun, H.-W.; Hartgerink, J. D. *J. Am. Chem. Soc.* **2006**, *128*, 7291.
[12] Pashuck, E. T.; Cui, H.; Stupp, S. I. *J. Am. Chem. Soc.* **2010**, *132*, 6041.
[13] Velichko, Y. S.; Stupp, S. I.; Olvera de la Cruz, M. *J. Phys. Chem. B* **2008**, *112*, 2326.
[14] Hartgerink, J. D.; Beniash, E.; Stupp, S. I. *Science* **2001**, *294*, 1684.

[15] Zhang, S.; Greenfield, M. A.; Mata, A.; Palmer, L. C.; Bitton, R.; Mantei, J. R.; Aparicio, C.; Olvera de la Cruz, M.; Stupp, S. I. *Nature Mater.* **2010**, *9*, 594.
[16] Pashuck, E. T.; Stupp, S. I. *J. Am. Chem. Soc.* **2010**, *132*, 8819.
[17] Percec, V.; Wilson, D. A.; Leowanawat, P.; Wilson, C. J.; Hughes, A. D.; Kaucher, M. S.; Hammer, D. A.; Levine, D. H.; Kim, A. J.; Bates, F. S.; Davis, K. P.; Lodge, T. P.; Klein, M. L.; DeVane, R. H.; Aqad, E.; Rosen, B. M.; Argintaru, A. O.; Sienkowska, M. J.; Rissanen, K.; Nummelin, S.; Ropponen, J. *Science* **2010**, *328*, 1009.
[18] Besenius, P.; Portale, G.; Bomans, P. H. H.; Janssen, H. M.; Palmans, A. R. A.; Meijer, E. W. *Proc. Natl. Acad. Sci USA* **2010**, *107*, 17888.
[19] Van Eldijk, M. B.; Wang, J. C.-Y.; Minten, I. J.; Li, C.; Zlotnick, A.; Nolte, R. J. M.; Cornelissen, J. J. L. M.; Van Hest, J. C. M. *J. Am. Chem. Soc.* **2012**, *134*, 18506.
[20] Von Gröning, M.; De Feijter, I.; Stuart, M. C. A.; Voets, I. K.; Besenius, P. *J. Mater. Chem. B.*, **2013**, *1*, 2008.
[21] Frisch, H.; Unsleber, J. P.; Lüdeker, D.; Peterlechner, M.; Brunklaus, G.; Waller, M.; Besenius, P. *Angew. Chem. Int. Ed.* **2013**, *52*, 10097.
[22] Ghosh, A.; Haverick, M.; Stump, K.; Yang, X.; Tweedle, M. F.; Goldberger, J. E. *J. Am. Chem. Soc.* **2012**, *134*, 3647.
[23] Boekhoven, J.; Koot, M.; Wezendonk, T. A.; Eelkema, R.; Van Esch, J. H. *J. Am. Chem. Soc.* **2012**, *134*, 12908.
[24] Leenders, C. M. A.; Albertazzi, L.; Mes, T.; Koenigs, M. M. E.; Palmans, A. R. A.; Meijer, E. W. *Chem. Commun.* **2013**, *49*, 1963.
[25] Hayward, R. C.; Pochan, D. J. *Macromolecules* **2010**, *43*, 3577.
[26] Moore, J. S.; Kraft, M. L. *Science* **2008**, *320*, 620.
[27] Ladet, S.; David, L.; Domard, A. *Nature* **2008**, *452*, 76.
[28] Sorrells, J. L.; Tsai, Y.-H.; Wooley, K. L. *J. Polym. Sci. Part A: Polym. Chem.* **2010**, *48*, 4465.
[29] Cui, H.; Chen, Z.; Zhong, S.; Wooley, K. L.; Pochan, D. J. *Science* **2007**, *317*, 647.
[30] Huang, J.; Bonduelle, C.; Thévenot, J.; Lecommandoux, S.; Heise, A. *J. Am. Chem. Soc.* **2012**, *134*, 119.
[31] Lee, S. J.; Kim, E.; Seo, M. L.; Do, Y.; Lee, Y.-A.; Lee, S. S.; Jung, J. H.; Kogiso, M.; Shimizu, T. *Tetrahedron* **2008**, *64*, 1301.
[32] Tidhar, Y.; Weissman, H.; Wolf, S. G.; Gulino, A.; Rybtchinski, B. *Chem. Eur. J.* **2011**, *17*, 6068.
[33] Carnall, J. M. A.; Waudby, C. A.; Belenguer, A. M.; Stuart, M. C. A.; Peyralans, J. J.-P.; Otto, S. *Science* **2010**, *327*, 502.
[34] Hermans, T. M.; Broeren, M. A. C.; Gomopoulos, N.; Van der Schoot, P.; Van Genderen, M. H. P.; Sommerdijk, N. A. J. M.; Fytas, G.; Meijer, E. W. *Nat. Nanotechnol.* **2009**, *4*, 721.
[35] Kieltyka, R. E.; Pape, A. C. H.; Albertazzi, L.; Nakano, Y.; Bastings, M. M. C.; Voets, I. K.; Dankers, P. Y. W.; Meijer, E. W. *J. Am. Chem. Soc.* **2013**, *135*, 11159.
[36] Kaeser, A.; Fischer, I.; Abbel, R.; Besenius, P.; Dasgupta, D.; Gillissen, M. A. J.; Portale, G.; Stevens, A. L.; Herz, L. M.; Schenning, A. P. H. J. *ACS Nano* **2013**, *7*, 408.
[37] Capito, R. M.; Azevedo, H. S.; Velichko, Y. S.; Mata, A.; Stupp, S. I. *Science* **2008**, *319*, 1812.
[38] Wang, Q.; Mynar, J. L.; Yoshida, M.; Lee, E.; Lee, M.; Okuro, K.; Kinbara, K.; Aida, T. *Nature* **2010**, *463*, 339.
[39] Petzetakis, N.; Robin, M. P.; Patterson, J. P.; Kelley, E. G.; Cotanda, P.; Bomans, P. H. H.; Sommerdijk, N. A. J. M.; Dove, A. P.; Epps, III, T. H.; O'Reilly, R. K. *ACS Nano* **2013**, *7*, 1120.
[40] Kuprin, S.; Gräslund, A.; Ehrenberg, A.; Koch, M. H. J. *Biochem. Biophys. Res. Commun.* **1995**, *217*, 1151.
[41] Yanagi, K.; Ashizaki, M.; Yagi, H.; Sakurai, K.; Lee, Y.-H.; Goto, Y. *J. Biol. Chem.* **2011**, *286*, 23959.

6

Mechanisms of self-assembly: from analysing curiosities to a model-driven *modus operandi*

Abstract: In this chapter, the self-assembly mechanisms of different supramolecular systems are analysed. Firstly, the aggregation behaviour of a perylene bisimide derivative is clarified, which appears to follow a nucleation pathway but nevertheless yields only small nanoparticles rather than elongated structures that might be anticipated based on a nucleated assembly mechanism. Secondly, the involvement of secondary aggregation in the bundling of one-dimensional assemblies of fluorinated benzene-1,3,5-tricarboxamide derivatives is unravelled via temperature-dependent and kinetic experiments, combined with equilibrium and kinetic models. Thirdly, the co-assembly pathways of different oligo(*p*-phenylene vinylene) derivatives are investigated, and fourth, the behaviour of π-conjugated poly(diketopyrrolopyrrole-terthiophene) in chloroform is investigated. This polymer aggregates in chloroform – prior to spin coating – and since the resulting fibrils are anticipated to influence the performance of the solar cell that is finally obtained, a better understanding of this aggregation process will further advance the processing of these materials. In the second part of this chapter, we revisit the kinetic models that are applied in Chapter 2 and 3 to describe the competition between on- and off-pathway aggregates as well as solvent-dependent dynamics. In particular, the influence of fragmentation is addressed and the effect of nucleation pathways on the competition between on- and off-pathway aggregates is further investigated. In the last part of this chapter, we attempt to generalize the approach applied so far to analyse assembly mechanisms by using models, and outline how this model-driven approach can lead to the design of new systems.

Part of this work has been published as:

"Small sized perylene-bisimide assemblies controlled by both cooperative and anti-cooperative assembly processes" R. van der Weegen, P. A. Korevaar, P. Voudouris, I. K. Voets, T. F. A. de Greef, J. A. J. M. Vekemans, E. W. Meijer, *Chem. Commun.* **2013**, *49*, 5532–5534.

"Symmetry Breaking in the Self-Assembly of Partially Fluorinated Benzene-1,3,5-tricarboxamides" P. J. M. Stals, P. A. Korevaar, M. A. J. Gillissen, T. F. A. de Greef, C. F. C. Fitié, R. P. Sijbesma, A. R. A. Palmans, E. W. Meijer, *Angew. Chem. Int. Ed.* **2012**, *51*, 11297–11301.

6.1 Introduction

Mechanistic insights into chemical self-assembly processes are a prerequisite to control the formation of supramolecular assemblies. The two major mechanisms to describe one-dimensional self-assembly, isodesmic and cooperative growth, are now well understood and a vast amount of supramolecular systems reported in literature can be classified according to these mechanisms. Furthermore, the formation of many of these one-dimensional assemblies can be analysed with these mechanisms. This means that the data acquired on the assembly processes can be described with an equilibrium model, and via a curve-fitting procedure thermodynamic values can be extracted. However, in other cases unravelling the self-assembly process is less trivial, for instance due to assembly steps that go beyond one-dimensional growth, or due to kinetic phenomena that hamper an analysis under thermodynamic equilibrium. If certain effects are experienced, new models are required to clarify the assembly mechanism: a process that involves iterations of developing a hypothetical model and comparing the behaviour predicted by the model with the experimental observations. In the first part of this chapter we demonstrate with several examples different aspects of this model-driven *modus operandi* to unravel supramolecular assembly processes.

Understanding self-assembly processes however is not a goal on itself but should improve our capabilities to create functional supramolecular systems. Currently, the design of supramolecular systems is often limited to the chemical design of the molecular building blocks. However, we anticipate that considering the mechanistic aspects of the assembly process are prerequisite, since phenomena like association-dissociation rates, metastable pathways, nucleation steps etc. affect the construction of supramolecular architectures as well. Therefore, the last part of this chapter presents an outline how the model-driven approach to unravel self-assembly mechanisms and pathways can pave the way towards model-driven engineering of functional supramolecular materials and systems.

6.2 Unravelling assembly mechanisms: a model-driven approach

This paragraph presents four examples of assembling systems that display self-assembly behaviour of the “less trivial” category. We attempt to unravel the mechanisms and pathways involved here, by developing new models or by combining insights from models analysed previously.

6.2.1 Cooperative formation of small sized perylene bisimide assemblies

The self-assembly of perylene bisimide PBI (Fig 6.1a) is experimentally investigated by ir. Rob van der Weegen.[1] To characterize the growth mechanism, temperature-dependent UV/Vis experiments are conducted in methylcyclohexane (MCH). At elevated temperatures, the UV/Vis spectrum displays characteristic features for PBIs in the molecularly dissolved state, whereas at low temperatures the red-shifted shoulder indicates the formation of PBI aggregates (Fig 6.1b).[2] To characterize the assembly mechanism, UV/Vis is probed at 542 nm

upon cooling a PBI solution of 20 μM with a rate of 0.2 °C/min (Fig 6.1b). The slow cooling rate is required to maintain the system under equilibrium conditions during the cooling process. The cooling curve reveals a critical temperature that marks the onset of the assembly process, suggesting a cooperative growth mechanism. Further analysis of the temperature-dependent data with the equilibrium model as introduced in paragraph 2.7 of Chapter 2 suggests that at room temperature long one-dimensional assemblies of more than 1000 monomers should be present in solution. Surprisingly however, small angle X-ray scattering (SAXS) experiments on PBI in MCH (1 mM) reveal the presence of small objects in solution with a radius of gyration of 1.9 nm. Assuming a typical π-π distance of 0.35 nm, this yields only 11 monomers present in the aggregate; a value much smaller compared to the amount of monomers that is expected based on the UV/Vis data, especially since the SAXS experiments are performed at a higher concentration.

The formation of small, discretely sized objects has been reported before, even at high concentrations.[3–6] Rather than following an isodesmic assembly mechanism, increasing repulsive interactions, for instance due to steric hindrance, in those cases diminish the monomer association constant and thereby halt the assembly process at the stage of small aggregates. This can, at least qualitatively, be rationalized by an anti-cooperative mechanism, assuming that the equilibrium constant of nucleation K_n is larger than the equilibrium constant of elongation K_e. Hence, we analyse the dependence of the degree of aggregation φ as a function of the dimensionless concentration x_{tot}. The dimensionless concentration x_{tot} equals $K_e \cdot c_{tot}$, and typically can be increased upon increasing the total concentration c_{tot} or, as K_e increases upon cooling, by decreasing the temperature. Besides, we follow the weight averaged degree of polymerisation DP_w as predicted by the equilibrium model. Even though the equilibrium model with $K_n = 10 \cdot K_e$ (anti-cooperative) predicts the formation of short assemblies when the degree of aggregation φ approximates 1, no critical temperature or concentration is found (Fig 6.1d), which is in contrast to the experimental observations. Hence, several alternative equilibrium models are analysed. First, an attenuated equilibrium model is considered, in which every subsequent monomer addition step proceeds with a diminished equilibrium constant; $K_i = K/i$, with i the length of the respective aggregate to which the monomer addition takes place. Further details of the attenuated model are given in paragraph 6.5. Although this model predicts the formation of small assemblies, again no critical point can be observed in the plots of φ *vs.* x_{tot} (Fig 6.1d). However, after modifying the model such that the attenuated assembly starts off with an energetically unfavourable nucleation of two monomers (*i.e.* $K_2 = \sigma \cdot K/i$, with $\sigma < 1$), the formation of small aggregates only occurs beyond a critical concentration or temperature (Fig 6.1d).

A molecular explanation for the cooperative formation of PBI assemblies would be the relatively unfavourable formation of a hydrogen-bonded dimer via two-fold hydrogen bonding of two PBI molecules. Formation of hydrogen bonds between the non-substituted imide sides of two PBI molecules has been confirmed by IR spectroscopy in solution.[1] However, formation of such a hydrogen-bonded dimer occurs via a relatively weak interaction, and the subsequent π-π stacking of these dimers is expected to be energetically

more favourable. Hence, this results in a nucleated growth of the aggregates. Further elongation proceeds according to an attenuated mechanism that yields only small sized assemblies. A hypothetical explanation is that the π-π stacking of the perylene dimers prefers a co-facial arrangement that is not able to facilitate the optimum arrangement for the aliphatic side chains. Thereby, steric crowding of the side chains diminishes the aggregation tendency with increasing length. We model this scenario by assuming that the formation of a hydrogen-bonded dimer occurs with equilibrium constant K_h. The subsequent elongation is described – in analogy to the attenuated assembly as described above – with equilibrium constant $K_i = K/i$, where the hydrogen-bonded PBI dimer is considered as the monomer (Fig 6.1c). Again, both the degree of aggregation and DP_w as a function of x_{tot} capture the experimental results: a critical point is obtained and small values for DP_w are predicted, even at high values of x_{tot}.

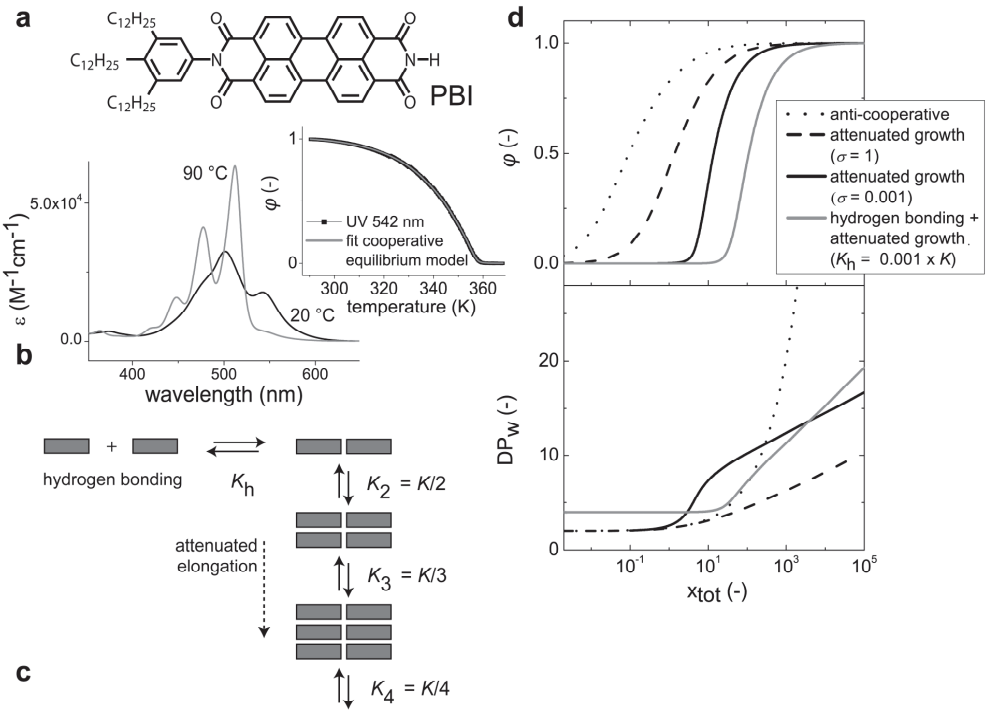

Figure 6.1 | Attenuated assembly of small sized perylene aggregates. (a) Molecular structure of perylene bisimide PBI. (b) Temperature-dependent UV/Vis spectra of PBI (20 μM) in MCH. The inset shows the degree of aggregation, derived from the UV/Vis absorption at 542 nm and analysed with the nucleation-elongation equilibrium model. (c) Schematic representation of the equilibrium model describing attenuated growth of PBI assemblies, with the formation of a hydrogen-bonded dimer as the unfavourable nucleation step. (d) Degree of aggregation (φ, top pane) and weight averaged degree of polymerisation (DP_w, bottom pane) *vs.* dimensionless concentration x_{tot}, simulated with equilibrium model assuming (1) anti-cooperative growth, (2) attenuated growth, (3) nucleated attenuated growth and (4) attenuated growth that starts off with the formation of a hydrogen-bonded dimer.[1]

The role of hydrogen-bonding in the nucleated assembly mechanism is corroborated by the fact that no critical point in the temperature-dependent assembly is observed when this interaction is selectively removed by N-methylation of the imide.[1] In general, an unfavourable association event (*i.e.* nucleation, formation of a hydrogen-bonded dimer) is required to obtain a critical point in the temperature-dependent assembly. It should be noted that, in order to obtain assemblies of limited size, alternative relations between the association constant K_i and chain length can be selected to predict a limited size of the aggregates formed.

6.2.2 Symmetry-breaking via secondary aggregation of fluorinated BTAs

In this paragraph we analyse the role of secondary nucleation in symmetry breaking of fluorinated benzene-1,3,5-tricarboxamide (BTA) assemblies.[7] This phenomenon is experimentally investigated by dr.ir. Patrick Stals on a library of achiral BTA derivatives that are all functionalized with two *n*-decyl chains and one partially fluorinated chain (Fig 6.2a). BTAs are well known to assemble into one-dimensional helical stacks in a cooperative fashion due to three-fold hydrogen bonding.[8–10] In case of an achiral BTA, a racemic mixture of left- and right-handed helices is expected. However, despite the fact that all members of the fluorinated BTA library are achiral, the BTAs that bear a hydrogen atom at the ω-position of the fluorinated chain (*i.e.* BTA-F_8H and BTA-$F_{12}H$) yield a CD effect when dissolved in MCH. This CD effect is not related to artefacts like linear dichroism, linear birefringence or precipitation. Hence, it is suggested that this phenomenon is related to symmetry breaking, in which the chirality of the BTA aggregates is induced by a – probably very small – trace of a chiral impurity.

Analysis via the classic approach: under "equilibrium" conditions. To unravel the mechanism involved in the appearance of the chiral assemblies, we study the aggregation of BTA-F_8H as a function of temperature via a combination of UV and CD spectroscopy (Fig 6.2c). Upon cooling from 90 °C with a rate of 1 °C/min, first a sharp transition occurs in the UV absorption at 223 nm. This transition at the critical temperature of elongation T_e corresponds to a blue-shift of the UV absorbance, typical for aggregation of BTA moieties into one-dimensional helices.[11] Further cooling results in a second sharp transition in UV, that coincides with the appearance of the CD effect. The sharp, non-sigmoidal character of these transitions indicates that nucleation steps are involved in the formation of the optically silent 1D helices, below T_e, as well as in the subsequent appearance of the aggregates that are responsible for the CD effect. The BTA derivatives that lack a hydrogen atom at the ω-position of the fluorinated chain display only a critical transition in UV at elevated temperatures (T_e), corresponding to the formation of 1D helices (Fig 6.2b).

Analysis of the CD active species in solution with Dynamic Light Scattering (DLS) as well as with Atomic Force Microscopy (AFM) on dried material reveals the presence of large aggregates.[7] This indicates that the optically active aggregates have a larger diameter compared to 1D BTA helices, implying that they are formed by bundling of multiple BTA helices. The optical activity of these bundles is likely to be induced by the inclusion of a chiral species in these structures. This species acts as a seed and thereby forces the majority of the

material to assemble into structures with either positive or negative helicity. Indeed, the CD sign of these structures is shown to be affected by the addition of chiral crystals.[7]

Analysis of the concentration-dependent values of T_e for BTA-F$_8$H via the Van't Hoff relation results in an enthalpy of elongation ΔH_e = –63 kJ/mol. This value is close to previously reported values for the nucleated assembly on non-fluorinated BTAs into 1D helices (Fig 6.3ab) and corroborates that the transition in UV at T_e corresponds to the formation of 1D BTA helices.[11] In contrast to the concentration-dependence of T_e, the concentration has a much smaller influence on T_b, the critical temperature that marks the onset of the formation of CD active bundles. To rationalize this concentration-independence, we develop a phenomenological equilibrium model that describes the temperature-dependent, nucleated formation of both 1D helices as well as higher order assemblies (*i.e.* bundles), as described in detail in paragraph 6.5. Whereas the 1D helices have a higher stability at elevated temperatures, the bundles are defined to be more stable in the lower temperature regime (Fig 6.3c). Temperature-dependent simulations performed at different concentrations reveal that the T_e that marks the onset of the assembly of the 1D helices increases with concentration, as is observed experimentally (Fig 6.3de).

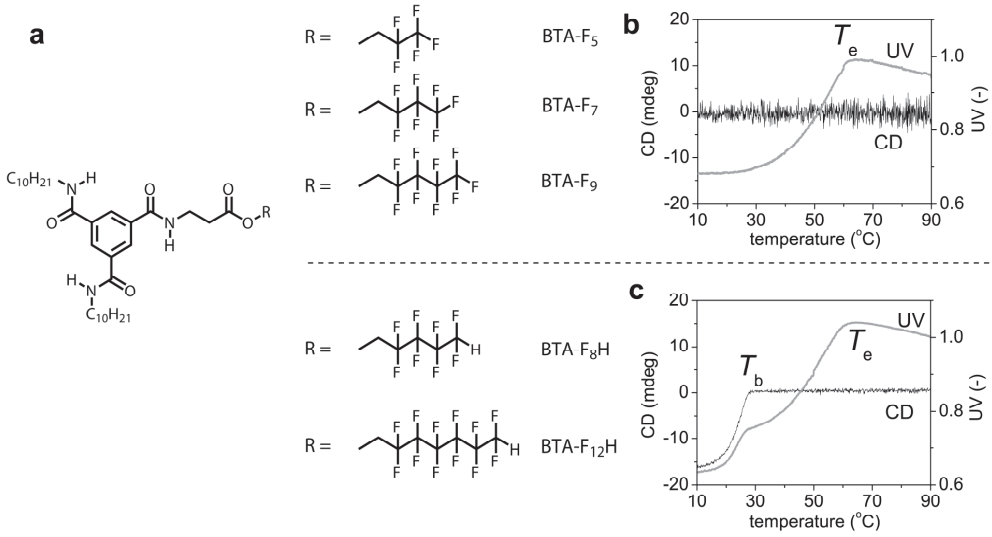

Figure 6.2 | Symmetry breaking in fluorinated BTA derivatives. (a) Molecular structures of the partially fluorinated BTAs, without (BTA-F$_5$, BTA-F$_7$, BTA-F$_9$) and with (BTA-F$_8$H, BTA-F$_{12}$H) a hydrogen at the ω-position of the fluorinated chain. (b) Temperature-dependent UV and CD spectroscopy (223 nm) reveals for the structures without the hydrogen at the ω-position of the fluorinated chain only a transition in UV (T_e), as shown for BTA-F$_9$ (30 μM, MCH). (c) Temperature-dependent UV on structures with a hydrogen at the ω-position of the fluorinated chain displays, next to the transition at T_e, a second transition in UV at T_b that coincides with the appearance of the CD effect, as shown for BTA-F$_8$H (30 μM, MCH).[7]

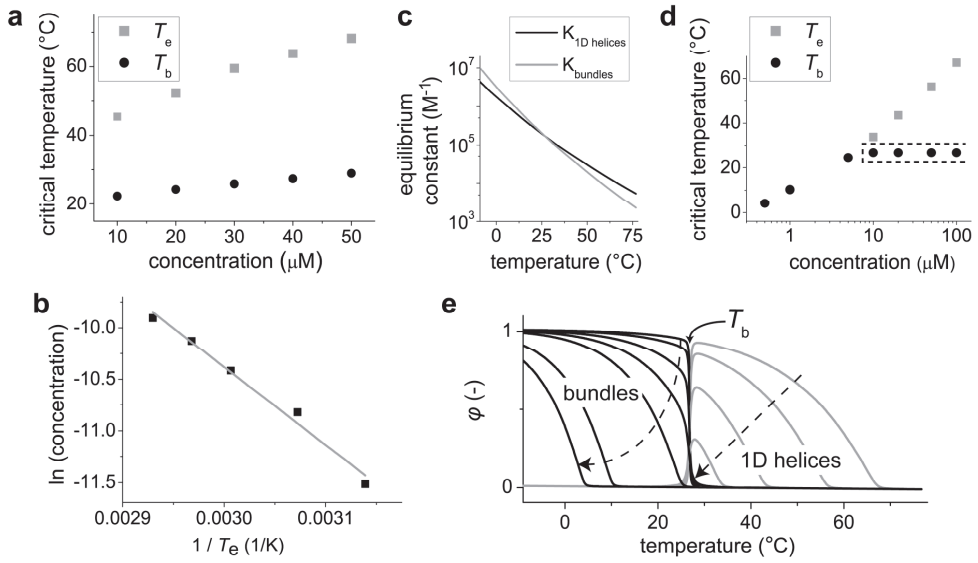

Figure 6.3 | Analysis of temperature-dependent aggregation of BTA-F8H. (a) The values of T_e and T_b as a function of concentration for BTA-F8H in MCH. (b) Van't Hoff plot based on the critical temperatures of elongation in UV (T_e). (c) Temperature-dependent equilibrium constants of elongation describing the stability of 1D helices (favoured in the high temperature regime) and bundles (favoured in the low temperature regime), respectively (paragraph 6.5). (d) Critical temperatures obtained with the temperature-dependent simulations, performed at multiple concentrations, for the appearance of 1D helices (T_e) and bundles (T_b). (e) Temperature-dependent degree of aggregation of monomers into 1D helices and bundles, simulated with the equilibrium model for multiple concentrations. The dashed arrows indicate a decrease in concentration.[7]

The simulated values of T_b however are concentration-independent, and equal to the temperature where the elongation constant for the bundles is defined to be equal to the elongation constant for 1D assembly (Fig 6.3de). The small temperature-dependence of T_b that is found experimentally can be related to the slow dynamics of the chiral structures. This phenomenon, further corroborated by kinetic experiments as shown below, hampers assessing the temperature-dependent assembly under equilibrium conditions.

The fact that CD active assemblies only appear when a hydrogen atom is present at the ω-position of the fluorinated tail of the BTA derivative indicates that the $–CF_2H$ group plays a critical role in the formation of the bundles. We hypothesize that the high polarization of the C–F bond causes polarization of the C–H bond at the ω-position of the fluorinated tail, thereby facilitating the formation of weak CF_2-*H*···*F*-CFH interactions between two or more BTA helices. Although the interaction between an electron-deficient hydrogen and a fluorine is weak[12, 13], the stabilizing effect of these type of interactions are demonstrated in several examples in supramolecular chemistry and crystal engineering.[14, 15] However, the weak

character of these fluorine-hydrogen interactions implies that a manifold of interactions is required to stabilize the bundling of BTA helices. Hence, we propose that prior to the bundling step, CF_2-*H*···*F*-CFH interactions among the fluorinated tails result in the formation of fluorine-enriched ribbons along the one-dimensional BTA helices, as shown in Fig 6.4a. Subsequently, these fluorine-enriched ribbons facilitate the hierarchical bundling, or surface-assisted nucleation of 1D helices into optically active fibres. Whereas these 1D helices are present in a racemic mixture, *i.e.* equal amounts of left- and right-handed helices, the chiral seed induces the formation of a non-racemic mixture of helices within these bundles.

Unravelling the bundling mechanism by kinetic experiments and theories. To further unravel the mechanism involved in the formation of these bundles, the aggregation kinetics of BTA-F_8H in solution are studied after a transfer from a good solvent (dichloroethane), in which the monomers are molecularly dissolved, into MCH, a poor solvent where they self-assemble. This injection is performed by using a stopped-flow setup and the formation of optically active bundles after injection is monitored via CD at 223 nm. To study the influence of concentration on the kinetics, injections are performed at 10 °C, leading to final concentrations of 20 μM, 30 μM, 40 μM, 48 μM and 50 μM, respectively, and 2 vol% dichloroethane in MCH (Fig 6.4b). Remarkably, in contrast to the kinetic studies on the assembly of SOPV, as shown in Chapter 2, the time at which the conversion equals 50% (*t*-50) does not show a concentration-dependence. However, the kinetic curves display a lag phase as expected for nucleated aggregation. In order to verify the nucleation mechanism from the lag phase, both functions $\varphi \sim t^2$ and $\varphi \sim 1 - \exp(-k \cdot t)$, corresponding to homogeneous and heterogeneous nucleation, respectively, are fitted to the initial phase of the growth process (up to 10% conversion, Fig 6.4c). Both fits describe the data well, meaning that the nucleation mechanism cannot unambiguously be identified based on the lag phase.

Next to the lag phase, also the relation between *t*-50 and concentration contains critical information about the growth mechanism. First we analyse if the aggregation of bundles can be described at least qualitatively via a homogeneous nucleation of free monomers, either in the absence (1) or presence (2) of 1D BTA helices. For different scenarios, we analyse if a concentration-independent rate (*i.e. t*-50), as is observed experimentally, can be expected.

(1) In case of homogeneously nucleated growth of the chiral aggregates, starting from a solution with only free monomers, the rate typically increases with concentration. Concentration-independent rates are only expected for very high (supersaturated) concentrations, as shown in Chapter 1. However, extrapolation of the CD values *vs.* concentration (Fig 6.4d) results in a critical aggregation concentration of ~10 μM. This indicates that the concentration-independent *t*-50 values are not acquired in the supersaturated regime, and hence homogeneous nucleation is not a likely mechanism for the formation of chiral bundles.

(2) If the homogeneous nucleation of chiral bundles is preceded by the fast formation of 1D helices, a critical free monomer concentration [M_{free}] that is independent of the total BTA concentration is available for the formation of the bundles (Fig 6.4e). The reaction rate of

homogeneous nucleation (in mol/L.s) is expected to be proportional to $[M_{free}]^2$ and hence independent on the total concentration. However, the amount of material that needs to be converted into bundles increases with the total concentration, resulting in an increasing *t*-50 with concentration. Thereby, also homogeneously nucleated formation of chiral bundles in temporarily coexistence of 1D helices is not a likely mechanism.

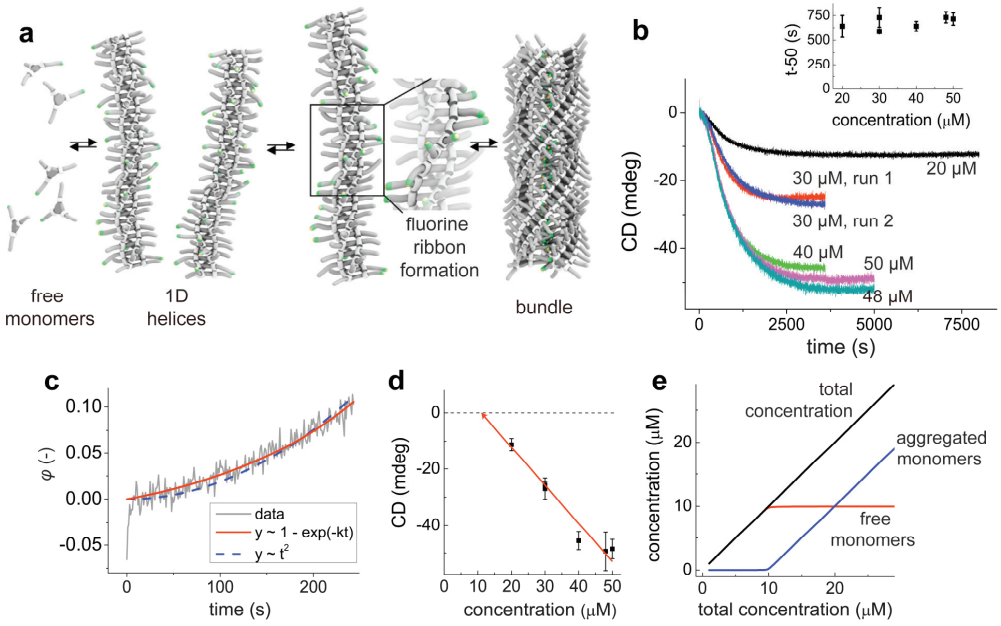

Figure 6.4 | Analysis of the kinetics of the aggregation of BTA-F8H. (a) Proposed aggregation mechanism involved the formation of chiral bundles: BTA assembles into 1D helices, the fluorinated chains form, via CF_2-*H*···*F*-CFH interactions, fluorine ribbons that induce the bundling of multiple helices. (b) Aggregation kinetics of BTA-F8H (stopped-flow, 223 nm). The inset shows *t*-50 *vs.* concentration. (c) Degree of aggregation *vs.* time, based on all CD data in (b), analysed with both functions $\varphi \sim t^2$ and $\varphi \sim 1 - \exp(-k \cdot t)$, corresponding to homogeneous and heterogeneous nucleation, respectively. (d) CD *vs.* concentration, derived from the steady state conditions in the kinetic experiments. Extrapolation of the data to CD = 0 mdeg suggests that a critical BTA-F8H concentration of ~10 μM is required to form chiral aggregates. (e) Concentration of free monomer and the concentration of aggregated monomers as a function of the total monomer concentration under equilibrium conditions.[7]

Next, we analyse, under the assumption that the formation of chiral bundles is preceded by the fast formation of 1D helices, several heterogeneous mechanisms to describe the kinetics of the bundling process.

(1) If the formation of fluor-enriched patches is the rate limiting step in the formation of the optically active bundles, the rate of this intrastack process (in mol/L.s) is proposed to be proportional to the initial concentration of monomers in one-dimensional stacks that can

convert into higher order aggregates, [M_{1D}^0]. If the final concentration of monomers in the bundles, [M_b^f], is close to [M_{1D}^0], *t*-50 is approximately concentration-independent.

(2) Alternatively, the concentration-independent rate of the formation of the optically active bundles can be rationalized by secondary nucleation of free monomers on the surface of (fluor-enriched) 1D helices as the rate limiting step. If this is the case, the fast nucleated formation of 1D helices results in a critical free monomer concentration that is independent of the total BTA concentration: [M_{free}]. The rate (in mol/L.s) of the subsequent secondary nucleation is proportional to the concentration of free monomers [M_{free}] times the initial concentration of monomers present in one-dimensional stacks [M_{1D}^0]. The normalized rate (reflected by *t*-50) is then proportional to [M_{free}]·[M_{1D}^0]/[M_b^f]. If [M_b^f] is close to [M_{1D}^0], *t*-50 is approximately concentration-independent.

(3) If the formation of the optically active bundles occurs via bundling of 1D helices with fluor-enriched patches, the reaction rate of bundling – a second order reaction between the surfaces of two helices – is expected to be proportional to the square of the available surface, *i.e.* the square of the initial monomer concentration in one-dimensional assemblies ([M_{1D}^0]^2). [M_{1D}^0] increases with the concentration and the amount of material that needs to be converted into bundles, [M_b^f], is approximately proportional to the total concentration. Therefore, the normalized rate will approximate [M_{1D}^0]^2 / [M_b^f]. Hence, *t*-50 decreases with total concentration and bundling of 1D helices as the rate limiting step is not a likely mechanism.

(4) Alternatively, the formation of the optically active bundles starts with a fast bundling of 1D helices, followed by a rate determining intra stack helix conversion from a racemic to a non-racemic distribution of left- and right-handed helices within the aggregates. As a result, the reaction rate (in mol/L.s) as well as the concentration of material that needs to be converted are proportional to the concentration of aggregated material. Hence, the resulting *t*-50 of this first order process is expected to be concentration-independent.

Concluding, the results indicate that the formation of the optically active fibres comprises two subsequent steps: 1) the nucleated assembly of BTA into equal amounts of left- and right-handed 1D helices, and 2) the formation of optically active bundles with a fluorinated core, in which either left- or right-handed helices dominate. Although an equal occurrence of positive and negative CD effects would be anticipated from a stochastic process, a strong preference for a negative CD effect is obtained. This phenomenon is ascribed to the involvement of chiral impurities that most likely are incorporated in the fluorinated core of the bundle and thereby induce the non-racemic distribution of BTA helices within these bundles. A homogeneous nucleation of these bundles can be excluded based on the kinetic results. However, it cannot be determined whether the rate limiting step is the formation of a fluorine ribbon along the periphery of the 1D helices, the conversion between left- and right-handed helices within the bundles or the surface-assisted secondary nucleation of free monomers along the fluorine ribbon of a BTA helix.

6.2.3 Competition between different pathways in multi-component assembly

The co-assembly of ROPV$_3$ and SOPV$_4$ has experimentally been investigated by dr. Christophe Grenier (Fig 6.5a). SOPV$_4$ assembles into left-handed helices as evidenced by the negative Cotton effect. ROPV$_3$ assembles into right-handed helices, resulting in a positive Cotton effect that is blue-shifted compared to the Cotton effect of SOPV$_4$ (Fig 6.5b). To investigate the co-assembly of both OPV derivatives, a "majority rules" experiment is conducted. Solutions of SOPV$_4$ and ROPV$_3$ in MCH (200 μM) are mixed in different ratios, and the co-assembly is assessed by analysing the CD spectra of the resulting assemblies. As shown in Figure 6.5b, mixing SOPV$_4$ and ROPV$_3$ in different ratios at room temperature yields CD spectra that are the weighted sum of the CD spectra of SOPV$_4$ and ROPV$_3$ aggregates, respectively. This is in agreement with the presence of homo-aggregates of SOPV$_4$ and ROPV$_3$ in solution. Similar to the co-assembly of SOPV$_4$ and ROPV$_4$ as demonstrated in Chapter 4, mixing the SOPV$_4$ and ROPV$_3$ assemblies at 20 °C does not result in notable monomer exchange. However, heating above the critical temperature of elongation (60 °C) and subsequently cooling with a rate of 1 °C/min results in disassembly of the homo-aggregates and formation of co-assemblies, as evidenced by the CD spectra obtained at 20 °C (Fig 6.5c).

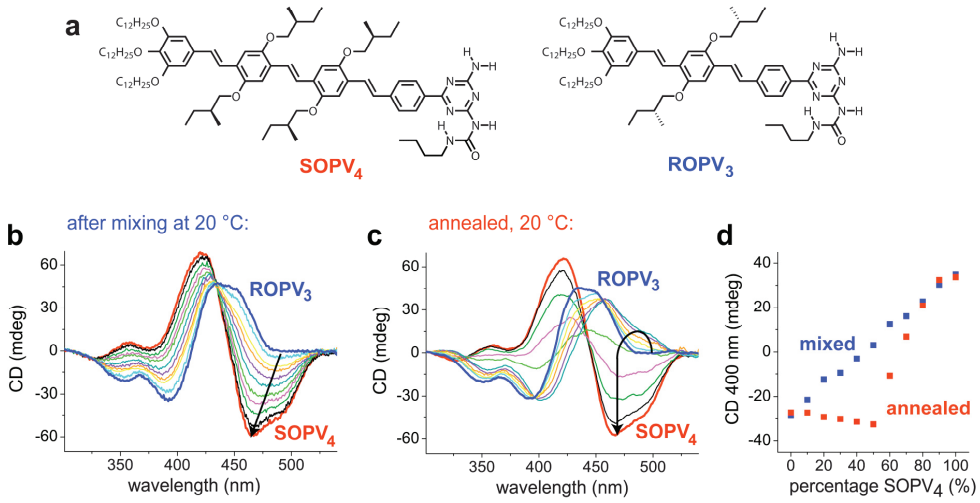

Figure 6.5 | Co-assembly of SOPV$_4$ and ROPV$_3$. (a) Molecular structure of SOPV$_4$ and ROPV$_3$. (b) CD spectra acquired after mixing SOPV$_4$ assemblies and ROPV$_3$ assemblies at 20 °C (200 μM, MCH). The arrow indicates the increasing SOPV$_4$ percentage, in steps of 10%. (c) CD spectra acquired after annealing at 60 °C and cooling, at 20 °C. (d) CD intensity at 400 nm for mixtures of SOPV$_4$ and ROPV$_3$ at 20 °C, acquired after mixing (blue) and after annealing (red).

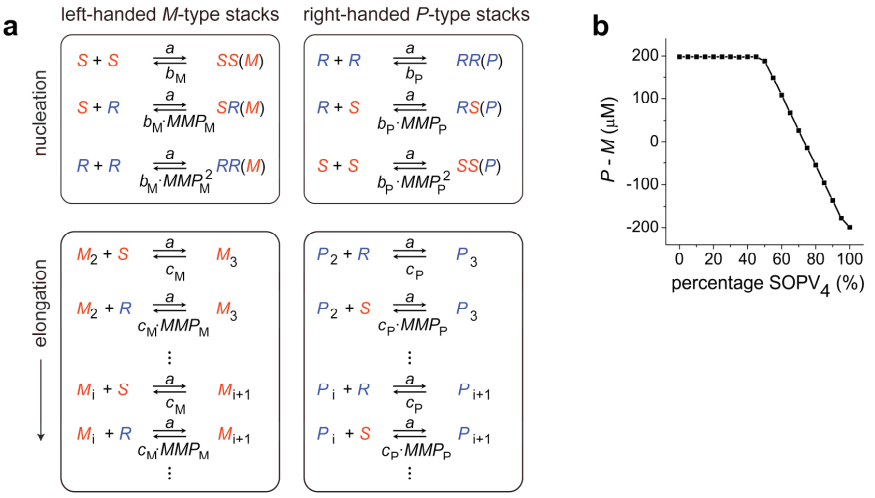

Figure 6.6 | Simulating the co-assembly of SOPV$_4$ and ROPV$_3$. (a) Schematic representation of kinetic model describing the nucleated co-assembly of ROPV$_3$ and SOPV$_4$ in *P*- and *M*-type helical stacks. (b) Difference between concentration of monomers assembled into *P*- and *M*-type helices under equilibrium conditions *vs*. percentage of SOPV$_4$, simulated with the kinetic co-assembly model. Parameters: MMP_M = 50; MMP_P = 1; (a/c_M) = 1.07·10^6 M^{-1}; $c_P = c_M/2$; $b_M = 10^4 \cdot c_M$; $b_P = 10^4 \cdot c_P$; c_{tot} = 200 μM.

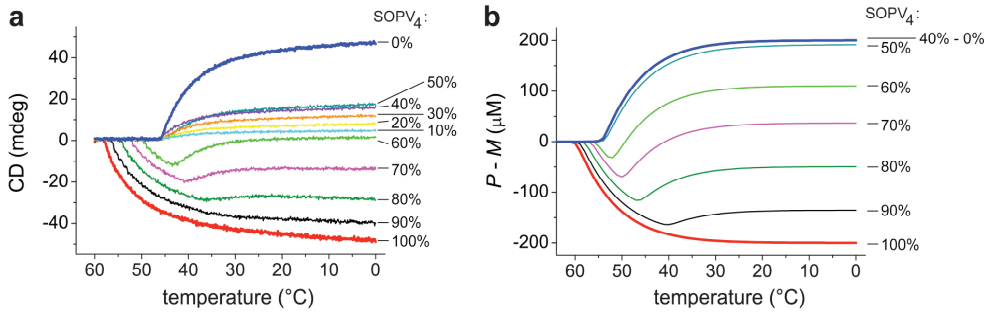

Figure 6.7 | Temperature-dependent co-assembly. (a) Temperature-dependent CD for SOPV$_4$/ROPV$_3$ mixtures (200 μM), probed at 490 nm upon cooling with a temperature ramp of 1 °C/min. The ROPV$_3$ solution is probed at 447 nm. (b) Temperature-dependent assembly of SOPV$_4$/ROPV$_3$ mixtures, simulated with the kinetic co-assembly model. Parameters: MMP_M = 50; MMP_P = 1; (a/c_M) = exp(–(ΔH^0 – $T \cdot \Delta S^0$)/RT) with ΔH^0 = –110 kJ/mol and ΔS^0 = –260 J/K.mol; $c_P = c_M/2$; $b_M = 10^4 \cdot c_M$; $b_P = 10^4 \cdot c_P$; c_{tot} = 200 μM.

To investigate which compound determines the net helicity of the co-assemblies obtained after annealing, we analyse the CD intensity at 400 nm. At this wavelength, pure ROPV$_3$ assemblies display a negative CD effect, and pure SOPV$_4$ assemblies a positive CD effect. As shown in Figure 6.5d, in mixtures that contain a majority of ROPV$_3$ the net helicity is identical to pure ROPV$_3$ solutions, indicating that ROPV$_3$ fully dominates the helicity of the formed co-assemblies. Only if the amount of SOPV$_4$ is larger than 50%, the net helicity deviates from pure

ROPV$_3$, and increases linearly towards the positive helicity of SOPV$_4$. These results suggest that ROPV$_3$ has a much stronger effect on the helicity of the system compared to SOPV$_4$. Hence, we hypothesize that this compound assembles only in its preferred *P*-type helicity, whereas SOPV$_4$ has not such a strong preference for its favourable helicity (*M*-type), and assembles in *P*-type helices as well.

The co-assembly model that is introduced in Chapter 4 allows verifying if the results can be rationalized by ROPV$_3$ having a high mismatch penalty for incorporation into *M*-type helices, whereas SOPV$_4$ has no preference for *M*- or *P*-type helices. Kinetic simulations are performed with the co-assembly model (Fig 6.6a). ROPV$_3$ assemblies are less stable than SOPV$_4$ assemblies, and therefore in the rate constant c_P, describing the rate of ROPV$_3$ monomer dissociation from *P*-type helices is defined to be equal to $2 \cdot c_M$, with c_M describing the rate of SOPV$_4$ monomer dissociation from *M*-type helices. The mismatch penalty factor for ROPV$_3$ in *M*-type assemblies (MMP_M) equals 50 and the mismatch penalty for SOPV$_4$ in *P*-type assemblies (MMP_P) equals 1. Since we are only interested in the equilibrium state, all forward reactions are described with the same rate constant *a*, and the concentrations of all species are analysed under equilibrium (*i.e.* steady state) conditions. As shown in Figure 6.6b, the simulations reveal that in between 100% and 50% ROPV$_3$, all monomers are assembled into *P*-type helices. Below 50% ROPV$_3$, *i.e.* above 50% SOPV$_4$, the inversion of the net helicity precedes linearly with the increasing percentage of SOPV$_4$, comparable to the experimental results.

Assessing co-assembly pathways by temperature-dependent experiments. Temperature-dependent studies provide a convenient approach to characterize the mechanisms involved in the assembly process, for instance by revealing nucleation events or different assembly pathways. Therefore, the co-assembly of ROPV$_3$ and SOPV$_4$ is assessed upon cooling from the molecularly dissolved state at 60 °C to 0 °C (Fig 6.7a). The temperature-dependent assembly is probed in CD at 490 nm, upon cooling with a temperature ramp of 1 °C/min. For pure SOPV$_4$, a negative CD effect appears at the critical temperature of elongation (T_e) of 58 °C, indicating the formation of *M*-type helices. For 90% SOPV$_4$, the T_e at which the negative CD effect emerges shifts to a lower temperature, and this trend continues for the samples with 80%, 70% and 60% SOPV$_4$. Moreover, for these samples a second transition can be observed in the CD cooling curves at lower temperatures. The rise in CD upon decreasing temperature suggests the formation of *P*-type helices below these temperatures. For samples having an ROPV$_3$ content of 50% or more, a positive CD effect appears at the T_e, indicating a direct formation of *P*-type helices. Moreover, in this regime the T_e is independent of the SOPV$_4$/ROPV$_3$ ratio.

The observed temperature-dependent co-assembly behaviour can be rationalized by the stabilities of SOPV$_4$ and ROPV$_3$ assemblies. The higher T_e for SOPV$_4$ indicates that SOPV$_4$ forms more stable assemblies than ROPV$_3$. Hence, cooling a mixture of SOPV$_4$ and ROPV$_3$ yields at high temperature the exclusive assembly of SOPV$_4$ into *M*-type helices. ROPV$_3$ is not included in these assemblies due to the high mismatch penalty of ROPV$_3$ molecules into *M*-type helices. Only at lower temperatures, the assembly of ROPV$_3$ is initiated and thereby the

CD effect increases again. Due to the low mismatch penalty of SOPV$_4$ into *P*-type helices, SOPV$_4$ can co-assemble with ROPV$_3$. As a result, in the presence of 50% ROPV$_3$ and beyond, *P*-type helices appear directly at T_e. As the total concentration of the building blocks available for these helices (*i.e.* ROPV$_3$ and SOPV$_4$) does not change with the composition of the system, in this regime the critical temperature is independent of the SOPV$_4$/ROPV$_3$ ratio.

To corroborate the role of the mismatch penalties experienced by ROPV$_3$ in *M*-type helices and SOPV$_4$ in *P*-type helices, temperature-dependent simulations are performed using the co-assembly model. Again, we are here only interested in the equilibrium state and therefore all forward reactions are described with the same temperature-independent rate constant *a*. Finally, the concentrations of all species are analysed under equilibrium (*i.e.* steady state) conditions. The temperature-dependent stability of SOPV$_4$ in *M*-type helices, *i.e.* the ratio of a/c_M, is defined via the Van't Hoff relation. The stability of ROPV$_3$ in *P*-type helices is defined accordingly via $a/c_P = 0.5 \cdot a/c_M$. The mismatch penalties are defined similar to the simulations performed at constant temperature: $MMP_M = 50$ and $MMP_P = 1$. As shown in Figure 6.7b, the temperature-dependent simulations performed with different ROPV$_3$/SOPV$_4$ ratios capture the experimental results and corroborate the premises that 1) SOPV$_4$ co-assembles into the assemblies preferred by ROPV$_3$ and 2) ROPV$_3$ does not co-assemble into the assemblies preferred by SOPV$_4$.

The temperature-dependent co-assembly reveals multiple pathways in the co-assembly of SOPV$_4$ and ROPV$_3$, and the analysis by simulation shows that the complex co-assembly behaviour can be rationalized by the asymmetric mutual mismatch penalties of both compounds. ROPV$_3$ experiences a high structural mismatch penalty when incorporated in *M*-type helices dominated by SOPV$_4$, which might be related to the shorter length of the π-conjugated part of ROPV$_3$ compared to SOPV$_4$. *Vice versa*, this mismatch is much lower when a long SOPV$_4$ molecule is incorporated in a helix dominated by short ROPV$_3$ molecules.

6.2.4 Aggregation of poly(diketopyrrolopyrrole-terthiophene) in chloroform prior to spin coating

Together with dr. Weiwei Li, the aggregation of poly(diketopyrrolopyrrole-terthiophene), PDPP3T, is investigated. PDPP3T (Fig 6.8a) is a promising donor material for bulk heterojunction solar cells.[16–18] It has been shown that this polymer, processed together with phenyl-C_{61}-butyric acid methyl ester (PCBM) as acceptor material, yields solar cells with efficiencies up to 7.1%.[18] The high performance of these solar cells has been ascribed to the aggregation of the PDPP3T into fibril structures that can be visualized with Transmission Electron Microscopy (TEM), and have dimensions of hundreds of nanometres in length and a few nanometres in width. These fibrils are expected to facilitate an efficient transport of the positive charge carrier to the respective electrode of the device. The importance of control over the formation of these fibrils is corroborated by solar cell efficiencies reported for PDPP3T polymers with different chain lengths. High molecular weight PDPP3T (M_n ~ 120 kg/mol) yields high efficiency solar cells with a fine dispersed fibril morphology, whereas less fine

dispersed fibrils and lower efficiencies are obtained with low molecular weight PDPP3T (M_n ~ 50 kg/mol).

To process PDPP3T/PCBM solar cells, typically PDPP3T and PCBM are spin coated together from a concentrated solution in chloroform, in which ortho-dichlorobenzene (ODCB) is added as a co-solvent to optimize the aggregation. To unravel the aggregation of PDPP3T into fibrils, we focus on the aggregation of PDPP3T prior to the spin coating process, *i.e.* in chloroform solution. A concentrated PDPP3T solution in chloroform (3 mg/mL) is prepared by heating a mixture of PDPP3T and chloroform in a closed sample vial to 100 °C for 1 hour. Subsequently, the solution is allowed to cool and spin coated on a glass slide. Whereas films spin coated from fresh prepared solutions that have been standing for only 5~10 minutes are completely homogeneous, solutions that have been standing for a couple of hours yield inhomogeneous films upon spin coating: a first indication that aggregation already occurs in the chloroform solution.

The aggregation process is further investigated by studying PDPP3T in chloroform solutions with UV/Vis spectroscopy. A 1 mg/mL stock solution of PDPP3T in chloroform is prepared. To allow analysis of the aggregation in this fresh stock solution by UV/Vis, a sample of this stock solution is diluted to 0.01 mg/mL (Fig 6.8b). Next, starting from the 1 mg/mL stock solution, a dilution series is prepared with concentrations of 0.5 mg/mL, 0.2 mg/mL, 0.1 mg/mL, 0.05 mg/mL, 0.02 mg/mL and 0.01 mg/mL. These solutions are all kept for one day at room temperature, subsequently diluted to 0.01 mg/mL and analysed by UV/Vis spectroscopy as well. Whereas the fresh solution has a maximum in UV/Vis at 810 nm, the solutions that are kept for one day display a shoulder at 866 nm. This shoulder becomes more dominant for solutions that have been standing at a higher concentration, and for the highest concentrations, 866 nm even corresponds to the maximum in UV/Vis absorption. The concentration-dependence of the appearance of the shoulder at 866 nm suggests that this phenomenon is related to intermolecular aggregation of the PDPP3T polymers.

To characterize whether the appearance of the shoulder in UV/Vis absorption at 866 nm can be ascribed to aggregation or degradation of the polymer in solution, a 0.1 mg/mL solution is studied with UV/Vis spectroscopy at 55 °C (Fig 6.8c). The shoulder at 866 nm disappears upon heating, and reappears at room temperature, albeit very slow. This indicates that the shoulder is not related to degradation of the polymer in chloroform but, most probably, to a (reversible) aggregates process.

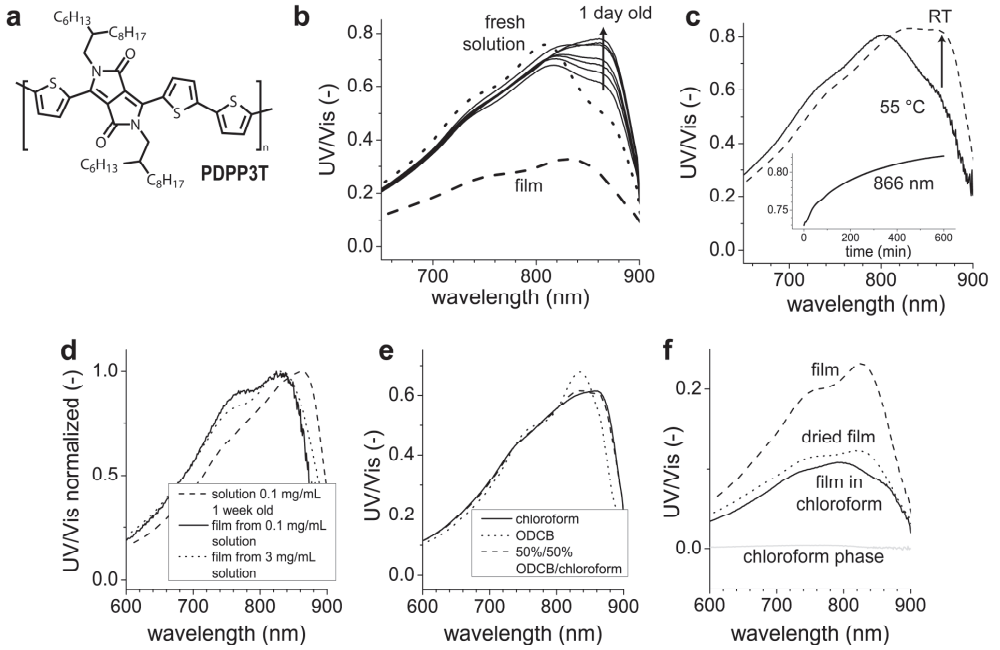

Figure 6.8 | Aggregation of PDPP3T in solution. (a) Molecular structure of poly(diketopyrollopyrrole-terthiophene), PDPP3T**.** (b) UV/Vis spectra of PDPP3T: 1) fresh solution in chloroform (0.01 mg/mL), 2) solutions that have been annealed in chloroform at room temperature for 1 day (arrow indicates increasing concentrations) and subsequently diluted to 0.01 mg/mL to measure UV/Vis, 3) spin coated film. (c) UV/Vis spectra of PDPP3T in chloroform at 55 °C and at room temperature (0.1 mg/mL). The inset shows the increase in UV/Vis at 866 nm after cooling to room temperature. (d) Normalized UV/Vis spectra of PDPP3T in solution and films: also spin coating a diluted solution does not yield the shoulder at 866 nm that is present in the spectrum of PDPP3T in chloroform. (e) UV/Vis spectra of PDPP3T in chloroform, ODCB and ODCB/chloroform mixture. (f) UV/Vis spectra of 1) the PDPP3T film, 2) the film while immersed in chloroform, 3) the dried film and 4) the chloroform phase in which the film has been immersed.

Remarkably, the shoulder in UV/Vis at 866 nm does not correspond to the aggregates that are present in spin coated films, since the UV/Vis spectrum of the film has a maximum at 834 nm and lacks a shoulder at 866 nm (Fig 6.8b). Annealing the film at high temperature (100 °C) or in the presence of chloroform vapour does not change the maximum of the UV/Vis spectrum. Furthermore, also films that are spin coated from PDPP3T solutions that have been standing for hours at room temperature yield similar UV/Vis spectra, *i.e.* without the shoulder at 866 nm.

Previously we have observed in our studies on the aggregation of SOPV that metastable aggregates can entrap monomers at high concentration. To investigate if the UV/Vis spectrum of the film that has been spin coated from a concentrated solution (3 mg/mL) corresponds to a metastable morphology, we spin coat a film from a less concentrated solution of 0.1 mg/mL. Due to the lower concentration, the presence of the shoulder at 866 nm in the UV/Vis spectrum

of the solution that is used to process the film can be verified directly. As shown in Figure 6.8d, the UV/Vis spectrum of the film processed from this diluted solution resembles the UV/Vis spectrum that is obtained upon spin coating the concentrated solution, and lacks the shoulder at 866 nm. Hence, we conclude that the UV/Vis spectrum with a maximum at 834 nm corresponds to an aggregated state that is in the film more stable compared to the aggregates that cause the shoulder (or maximum) at 866 nm in solution.

To analyse whether the shoulder in UV/Vis at 866 nm is related to chloroform, 1% of a PDPP3T solution in chloroform (1 mg/mL) is dispersed into 99% ODCB. Directly after preparing this solution, the UV/Vis spectrum displays a maximum at 834 nm, similar to the film, and the shoulder at 866 nm has disappeared (Fig 6.8e). Remarkably, addition of 50% chloroform results in a fast reappearance of the shoulder at 866 nm, much faster compared to the appearance of the shoulder in pure chloroform as shown in Figure 6.8c.

Finally, we analyse if the presence of chloroform affects the UV/Vis spectrum of the film. To this end, UV/Vis is measured on a film that is rinsed first with chloroform and then immersed into chloroform during the measurement. As shown in Figure 6.8f, the shoulder at 866 nm reappears for the immersed film. It should be mentioned that the UV/Vis absorption of the chloroform phase after removal of the film is negligible, meaning that the film has not been dissolved into chloroform during the measurement, and the shoulder at 866 nm disappears again after drying the film.

Combining these results, we hypothesize that PDPP3T slowly aggregates in chloroform, and chloroform intercalates within the PDPP3T fibrils that are formed, resulting in a shoulder in UV/Vis at 866 nm (Fig 6.9). Spin coating these fibrils from a chloroform solution results in an immediate removal of these chloroform molecules, and hence aggregates are obtained that have a maximum in UV/Vis at 834 nm. Also in excess of ODCB, chloroform is extracted from these fibrils. However, if the fibrils are present already, addition of chloroform, either to the aggregates in the film or to fibrils in ODCB, results in a fast re-intercalation of chloroform.

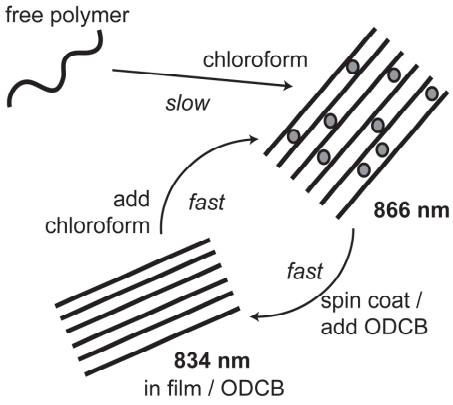

Figure 6.9 | Schematic representation of proposed aggregation mechanism of PDPP3T in solution and film.

Typically, addition of co-solvents like ODCB to the polymer solution is anticipated to speed up the aggregation of the polymer during spin coating, and thereby match the rate of this process to the concomitant aggregation of PCBM.[19, 20] Matching these aggregation rates is a prerequisite to obtain the optimum morphology: if the aggregation rate of PCBM exceeds that of the polymer, a large scale phase separation between donor and acceptor material is expected. This affects the morphology, and thereby the performance of the solar cell. The results presented here suggest that, in order to aggregate PDPP3T, the addition of ODCB is not required as this polymer aggregates in pure chloroform as well. This behaviour provides further opportunities to control the processing of PDPP3T solar cells. For instance, polymer fibrils can be pre-aggregated in chloroform, independent of the processing together with PCBM which can be further manipulated by the addition of ODCB.

6.3 Revisiting the kinetics of 1D assembly

The kinetic models that have been discussed in this thesis so far give a good, qualitative description of 1D assembly processes, and thereby provide new insights into the effect of competition between multiple pathways as well as the effect of solvent conditions on the dynamics. Nevertheless, describing the system with a simple numerical model requires assumptions that possibly affect the validity of the predicted behaviour. For instance, the model describing 1D assembly takes only monomer association and dissociation reactions into account, even though one can imagine that fragmentation (for instance splitting a 100-mer into an 80-mer and a 20-mer) and fusion (the reverse process) play a role in the dynamics of one-dimensional assemblies as well.[21, 22] Besides, the kinetic model describing the competition of on- and off-pathways is based on the assumption that both pathways compete for the monomer, even though one can imagine that larger species, for instance up to the nucleus, are shared between both pathways as well. In this paragraph, both the issue of fragmentation/fusion as well as the influence of the nucleation mechanism on the competition between multiple pathways are addressed.

6.3.1 The kinetics of fragmentation and fusion in 1D assembly

In this paragraph a simplified kinetic model is developed that includes fragmentation and fusion in the 1D assembly process. Similar to the model that involves only monomer association and dissociation, the model developed here is completely reversible. Reversibility is an indispensable feature, since disassembly and re-assembly play a dominant role in the analysis of on- and off-pathway systems and solvent-dependent kinetics.

The kinetic fragmentation model, as schematically depicted in Figure 6.10, considers four different terms: 1) the free monomer, 2) the dimer, 3) the total number of assemblies with size larger than two (*i.e.* stack number concentration), and 4) the total number of monomers assembled into these stacks (*i.e.* stack mass concentration). Six types of reactions are considered: 1) two monomers form a dimer, 2) a monomer and a dimer form a trimer (*i.e.* a

stack), 3) two dimers form a four-mer (*i.e.* a stack), 4) a monomer associates to a stack, 5) a dimer associates to a stack, 6) two stacks fuse. Analogous to the kinetic monomer association model that is introduced in paragraph 2.4 of Chapter 2, it is assumed that $[X_{i+1}] = \alpha[X_i]$ for $i > 2$. Due to this assumption, the concentration of every species with length i can be calculated based on the number and mass concentration of stacks, as shown in paragraph 6.5. The values of these concentrations are used to compute the contribution of fragmentation and fusion to the assembly kinetics.

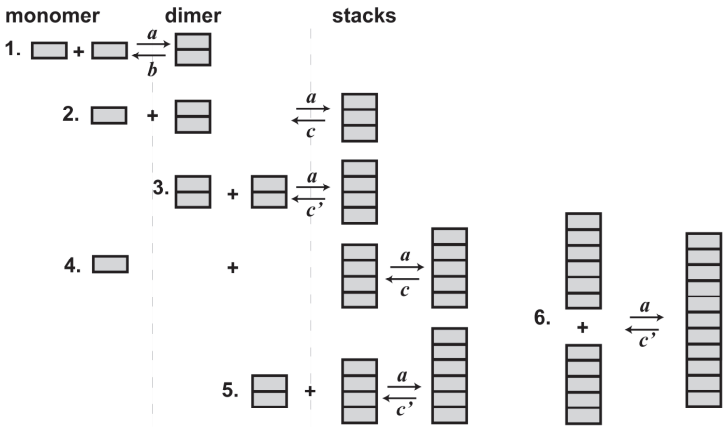

Figure 6.10 | Schematic representation of kinetic fragmentation model. Four different terms are taken into account: the monomer, the dimer, the number of stacks and the number of monomers assembled in these stacks. Via six types of reactions, the kinetics are simulated including fragmentation and fusion of long stacks.

The solvent-dependent assembly kinetics are simulated with the fragmentation model (Fig 6.11a-c), assuming the presence of different volume fractions of good solvent f. This good solvent destabilizes the assemblies upon increasing the rate constants of monomer dissociation and fragmentation, and decreasing the rate constants of monomer association and fusion. Analogous to the simulations shown in Chapter 3, that are based on monomer association and dissociation only, also with this model a minimum assembly rate is found close the critical solvent composition f_{crit}. However, significant differences are found between the rates predicted by the fragmentation model compared to the monomer association model. The fragmentation model predicts faster rates close to the critical solvent composition compared to the model using only monomer association and dissociation steps. The faster assembly rate close to f_{crit} can be rationalized by the fact that fragmentation allows to bypass the unfavourable nucleation step in the formation of new stacks. Besides, the slower assembly at lower values of f can be rationalized by fusion of stacks, which limits the number of chain ends

that are available for monomer association. If this effect dominates to process, slower rates are obtained compared to the simulations that only involve monomer association.

Simulations of the disassembly kinetics reveal, similar to the assembly kinetics, a minimum rate close to the critical solvent composition (Fig 6.11d-f). Here fragmentation yields faster kinetics for all values of *f*, indicating that bypassing the unfavourable nucleation step via fragmentation of aggregates dominates the process over the whole solvent composition regime. Hence, the contribution of fragmentation to the rate of the simulated disassembly process reduces the discrepancy between the kinetic simulations and experimental data as shown in Chapter 3.

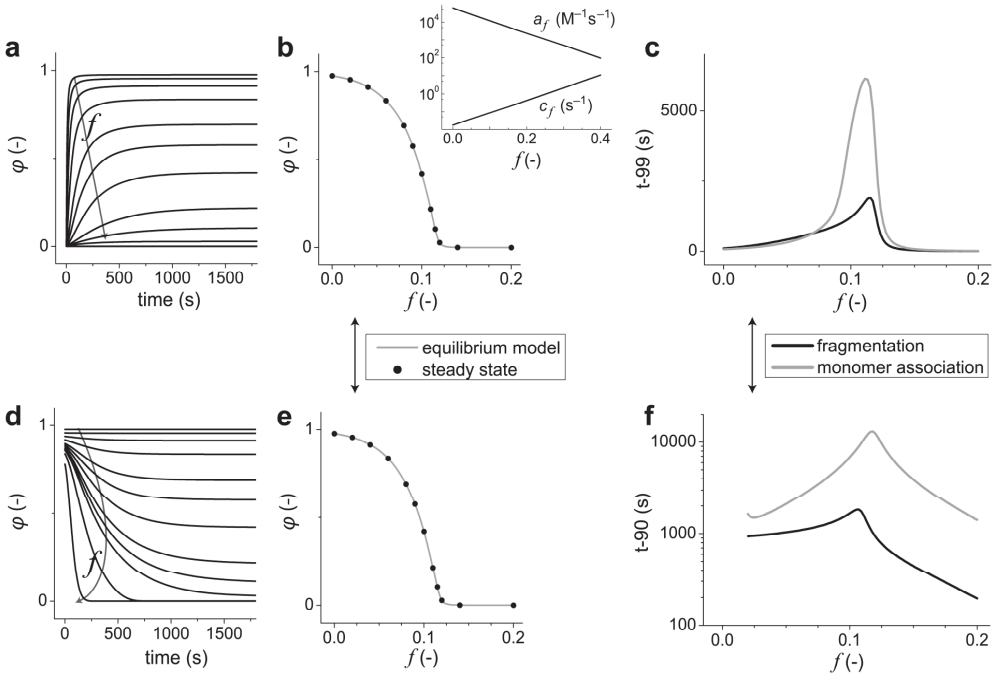

Figure 6.11 | Solvent-dependent assembly and disassembly kinetics, simulated with the fragmentation model. (a) Assembly kinetics simulated with increasing good solvent fraction *f*. The rate constants of monomer association and fusion decrease with *f*, and the rate constants of monomer dissociation and fragmentation increase with *f* as shown in the inset of pane b. (c) Similar to the monomer association model, also the fragmentation model predicts a minimum assembly rate close to f_{crit}. (d) Disassembly kinetics simulated with increasing good solvent fraction *f*. (f) Similar to the monomer association model, also the fragmentation model predicts a minimum disassembly rate close to f_{crit}, although the rate is much faster. (b,e) For both the assembly and disassembly kinetics, the steady state degree of aggregation φ predicted by the fragmentation model coincides with the denaturation curve calculated with the equilibrium model. In these simulations, the dependency of the association rate constant a_f and the dissociation rate constant c_f on the volume fraction of good solvent *f* is defined via $\log(a_f) = \log(a) - m_a \cdot f$ and $\log(c_f) = \log(c) + m_c \cdot f$, with $a = 6 \cdot 10^4$ $M^{-1}s^{-1}$, $m_a = 7$, $c = 0.0171$ s^{-1}, $m_c = 7$. Moreover, $c_{tot} = 12$ μM, $\sigma = 0.16^4$ and $n = 2$.

To verify the influence of fragmentation and fusion on the phenomenon of pathway complexity, an on-pathway (towards stable assemblies) and an off-pathway (towards metastable assemblies) are included in the fragmentation model. Both pathways are competing for the same free monomer. Similar to the kinetic simulations with the monomer association model, also here metastable assemblies appear in the initial stages of the assembly process, prior to the conversion into stable assemblies (Fig 6.12a). Furthermore, the simulated conversion from metastable to equilibrium assemblies is slower at higher concentrations due to the entrapment of monomers in the metastable pathway (Fig 6.12b).

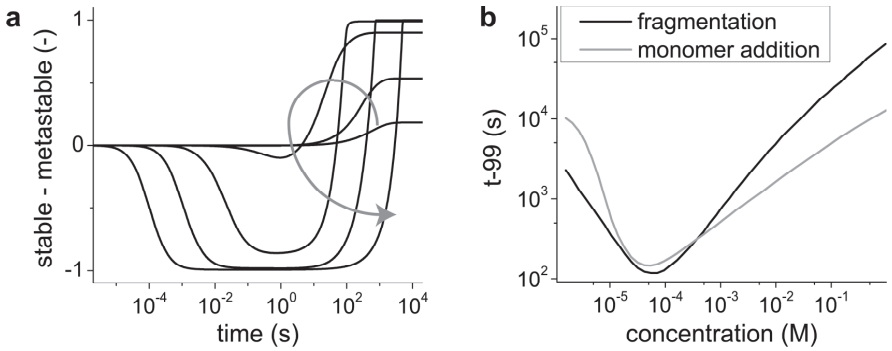

Figure 6.12 | Analysis of competition between two parallel assembly pathways with fragmentation model. (a) Concentration-dependent kinetics of assembly into metastable and stable assemblies, simulated with the fragmentation model: normalized difference between monomers present in stable and metastable assemblies *vs*. time. The arrow indicates increasing total concentration: 1 μM; 2 μM; 10 μM; 100 μM; 1 mM; 10 mM. (b) *t*-99 *vs*. concentration, simulated with both the fragmentation model and the monomer association model. Parameters: $a^* = 10^6\ M^{-1}s^{-1}$; $a = 10^4\ M^{-1}s^{-1}$; $K_e^* = 10^5\ M^{-1}$; $K_e = 10^6\ M^{-1}$; $\sigma^* = 0.01$; $\sigma = 0.01$; $n^* = 2$; $n = 2$.

6.3.2 A closer look to the nucleation regime of competing pathways

In Chapter 2 is has been demonstrated that entrapment of monomers in metastable assemblies slows down the assembly process along the equilibrium pathway. In the analyses performed so far on the competition between different assembly pathways, it is assumed that the nucleation pathway towards the equilibrium assemblies is different from the nucleation pathway towards the metastable structures (Fig 6.13a). This implies that the respective pathway is selected at the formation of a dimer. However, since all oligomers up to the nucleus are disordered structures, one could argue that both types of assemblies originate from the same type of nucleus, *i.e.* the nucleus results – upon monomer association – either a metastable or an equilibrium assembly. To investigate how this type of nucleation affects the predicted competition between both pathways, the kinetic model is modified by introducing a nucleation pathway, *i.e.* the formation of a nucleus, that is shared between both the metastable and stable pathway, as schematically depicted in Figure 6.13b.

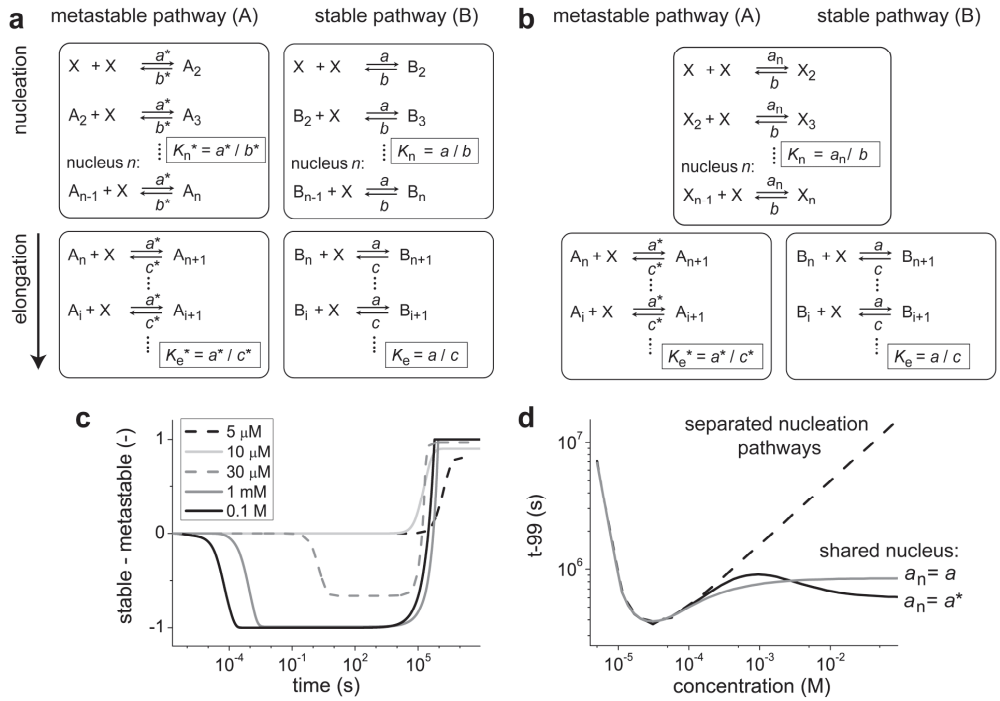

Figure 6.13 | The influence of separated *vs*. shared nucleation pathways on competition between metastable and stable assemblies. Schematic representation of the kinetic model, where metastable assemblies *A* and stable assemblies *B* originate from separated (a) and shared (b) nucleation pathways. (c) Concentration-dependent kinetics of assembly into metastable and stable assemblies, simulated with the kinetic model including a shared nucleation pathway (with $a_n = a^*$): normalized difference between monomers present in stable and metastable assemblies *vs*. time. (d) *t*-99 *vs*. concentration, simulated with both separated and shared nucleation pathways. Parameters: (separated nucleation pathways as in pane a) $a^* = 5{\cdot}10^7$ $M^{-1}s^{-1}$; $a = 10^4$ $M^{-1}s^{-1}$; $K_n^* = 10^3$ M^{-1}; $K_e^* = 10^5$ M^{-1}; $K_n = 10^3$ M^{-1}; $K_e = 10^6$ M^{-1}; $n^* = n = 5$; (shared nucleation pathway as in pane b) $a^* = 5{\cdot}10^7$ $M^{-1}s^{-1}$; $a = 10^4$ $M^{-1}s^{-1}$; $K_n^* = 10^3$ M^{-1}; $K_e^* = 10^5$ M^{-1}; $K_e = 10^6$ M^{-1}; $n = 5$.

Kinetic simulations with this modified model reveal in the low concentration regime a direct appearance of stable assemblies. Beyond the critical concentration of the metastable pathway, initially metastable assemblies appear, prior to the conversion towards the equilibrium assemblies (Fig 6.13c). Due to entrapment of monomers in these metastable assemblies, the rate of this conversion decreases with concentration. This is in agreement with the inverted concentration-rate relation predicted by the kinetic model in which the nucleation pathways of both types of assemblies are separated (Fig 6.13a).

In the high concentration regime however, notable differences are predicted by the model with separated (Fig 6.13a) and shared (Fig 6.13b) nucleation pathways, as demonstrated in Figure 6.13d, which displays the time at which 99% of the conversion towards stable

assemblies is completed (*t*-99) *vs*. concentration. The rate constant of monomer association in the nucleation phase (a_n, Fig 6.13b) plays a dominant role here: if a_n equals the monomer association rate constant of the stable pathway (*a*), *t*-99 levels off with concentration. However, if a_n equals the monomer association rate constant of the metastable pathway (*a**), *t*-99 decreases with concentration in the high concentration regime. However, also with fragmentation or a shared nucleation pathway included in the kinetic model, no exact description of the kinetic data is obtained (Fig 2.4d).

6.4 Towards a model-driven *modus operandi*

The aim of this thesis is to obtain control over aggregation pathways involved in assembly processes. To arrive at controlled assembly processes, understanding the mechanisms involved is a prerequisite. Here we recapitulate the lessons learned to reveal these mechanisms, unravel metastable pathways and understand the influence they exert on the overall assembly process. These insights provide an indispensable basis to arrive at a model-driven design of more complex and complicated supramolecular systems. Even though the main focus of this thesis is on π-conjugated materials, these insights are anticipated to be applicable to other types of supramolecular materials as well.

6.4.1 Analysing self-assembly mechanisms and pathways

In this chapter, multiple self-assembling systems are analysed, varying from the formation of small sized assemblies under diluted conditions to the aggregation of polymer fibrils in highly concentrated solutions. Obviously, it is impossible to define, based on these examples and the analyses described in previous chapters, *the* ideal approach to unravel self-assembly mechanisms. Nevertheless, some common elements can be identified. A starting point that often proves to be useful is modifying the driving force of the assembly process, for instance by changing temperature, concentration or the presence of a co-solvent. Starting from the free building blocks, e.g. at high temperature, and then gradually inducing the self-assembly process by cooling will – at least qualitatively – reveal characteristics of the mechanism like a nucleation event or a transition to a second type of assembly. Next, equilibrium models can be derived and analysed to verify whether they capture the experimentally observed behaviour.

Importantly, the conclusions drawn from temperature-, concentration- of co-solvent dependent data should be cross-checked via other experimental techniques, if possible. In this respect, the nucleated assembly of perylene bisimides into small objects serves as a warning that typical hallmarks of cooperative growth, in this instance a critical temperature of elongation, do not *per se* imply the formation of large objects, and additional experiments are required to clarify the growth mechanism involved in the supramolecular system of interest. Secondly, another important aspect is to verify that the data have been acquired under equilibrium conditions before analysing them with equilibrium models. A straight forward method to verify thermodynamic control is by comparing the assembly and disassembly process, for instance upon probing the assemblies upon cooling and subsequent heating. If the

cooling and heating curves coincide, it can be concluded that the data have been acquired under equilibrium conditions. The occurrence of hysteresis however indicates a failure of the system to reach equilibrium conditions. If this is the case, the system should get more time to reach equilibrium conditions during the analysis of the assembly process, for instance by applying a slower cooling rate or by annealing the system for a longer time prior to data acquisition.

Although slow dynamics complicate studying the assembly process under equilibrium conditions, the advantage is that it allows investigating the kinetics of the assembly process. As demonstrated by the studies on the bundling of fluorinated BTA helices, the combination of kinetic experiments and theories provides a powerful tool to identify the key steps in the assembly process. Moreover, via experiments under kinetic control, metastable assemblies can be identified and the pathways towards these non-equilibrium structures can be clarified. If entrapment of material in these metastable pathways hampers the formation of the thermodynamically stable aggregates, manipulating the relative stabilities – for instance by adding a destabilizing co-solvent – facilitates the selection of the equilibrium pathway. *Vice versa*, temporarily attachment of an auxiliary can direct the assembly process exclusively towards the metastable morphology.

6.4.2 Model-driven design of multi-component self-assembled systems

The co-assembly of different types of molecular building blocks (*i.e.* multi-component assembly) provides an interesting approach to construct functional nano-architectures. However, the outcome of a co-assembly process is hard to control, and in many cases even hard to predict. Imagine the one-dimensional co-assembly of A- and B-monomers in a block-type fashion (AAAABBBB). A manifold of alternative structures can be obtained, like random co-assemblies (AABABBBA), alternating co-assemblies (ABABABAB) and separated assemblies (AAAA, BBBB). An elegant approach to create functional co-assemblies with a block-type structure has been demonstrated by Aida and co-workers[23], following the seminal work of Manners and Winnik on crystallization induced self-assembly.[24, 25] Via the controlled co-assembly of two hexabenzocoronene (HBC) derivatives, supramolecular heterojunctions have been obtained, as shown in Figure 6.14. First, HBC **1** is assembled into tubular structures by vapour diffusion of methanol as a poor solvent into a solution of molecularly dissolved HBC **1** in tetrahydrofuran. Subsequently, the bipyridine (bpy) units that are attached to the triethylene glycol tails of HBC **1** allow to stabilize these assemblies in solution by forming $bpy_2{\cdot}Cu^{2+}$ complexes along the periphery of the HBC **1** blocks, upon the addition of a copper(II)salt. Next, these assemblies are treated with sonication in order to disperse them into short species that can serve as a seed to the assembly of the next molecular building block HBC **2**. Due to its molecular design, the interaction between HBC **2** and HBC **1** is stronger than the mutual interaction between two HBC **2** molecules. Hence, HBC **2** prefers to elongate on the HBC **1** blocks that are present as seeds in the solution, rather than forming *de novo* homo-assemblies. Due to the differences in electronic properties of HBC **1** and HBC **2**, these block-type assemblies behave like an organic heterojunction. This methodology does not yield di-

block HBC **1**–HBC **2** assemblies exclusively; HBC **2**–HBC **1**–HBC **2** assemblies have been observed as well. Nevertheless, this strategy of fixing the HBC **1** assemblies via the formation of $bpy_2{\cdot}Cu^{2+}$ complexes, which prevents the HBC **1** moieties from co-assembling in an alternating or random fashion with HBC **2**, demonstrates the key concept to obtain controlled multi-component assembly in a stepwise manner by manipulating the dynamics of intermediate structures formed.

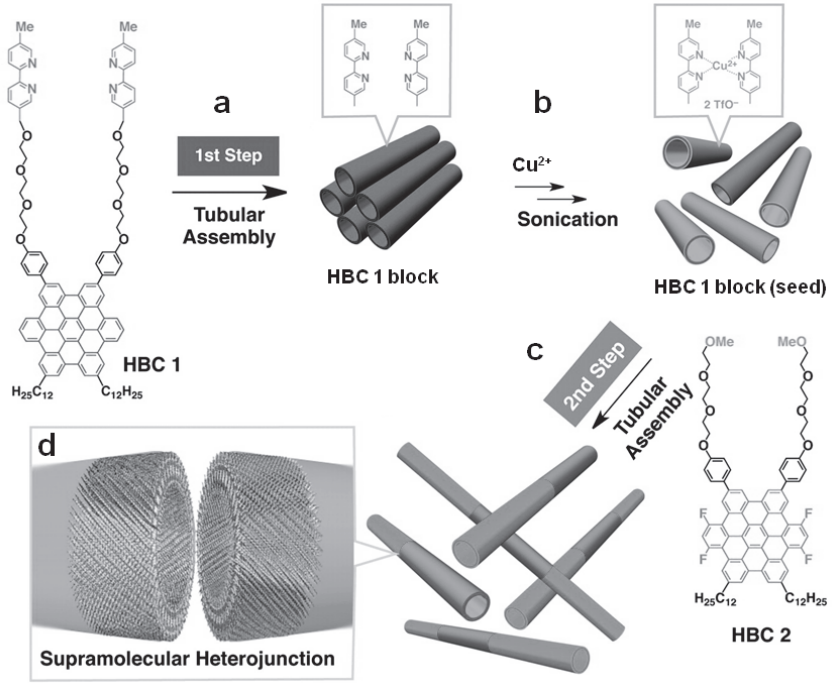

Figure 6.14 | Multi-step non-covalent synthesis of hexabenzocoronene (HBC) based heterojunctions. In the first step (a) HBC **1** nanotubes are assembled by methanol vapour diffusion into a solution of molecularly dissolved HBC **1** in tetrahydrofuran. In the next step (b) Cu^{2+} is added to stabilize the HBC **1** blocks via the formation of a bipyridine·Cu^{2+} complex. Upon sonication, small HBC **1** tubes are obtained which serve as seeds for the assembly of fluorinated HBC **2** (c), resulting into diblock (HBC **1**–HBC **2**) and triblock (HBC **2**–HBC **1**–HBC **2**) supramolecular heterojunction. Pane (d) displays a schematic illustration of an idealized cross section at the supramolecular heterojunction. Image from ref. 23.

Next to the controlled formation of multi-component assemblies by manipulating the dynamics during the process and kinetically trapping the desired morphology, multi-component systems can also be designed to master the dynamics of the system as an aim on itself. Inspired by the dynamic assembly and disassembly behaviour of microtubule in Nature, dr. Hirose and dr.ir. Helmich developed in our group a photo-regulated self-assembling system (Fig 6.15).[26] As a basic assembling unit, chiral porphyrin **1** is selected that bears a zinc atom in the core (Fig 6.15a) and assembles via a nucleated mechanism into long helices. To selectively switch on and off the assembly process, phenylazopyridine **2** is applied (Fig 6.15b).

Axial coordination of this pyridine ligand to the Zn atom of the porphyrin sterically blocks one side for assembly, and thereby inhibits the formation of elongated stacks. The association of **2** however is dependent of the conformation of the phenylazopyridine: whereas the *trans*-isomer can easily attach, association of the *cis*-isomer is hampered due to steric hindrance of the bulky mesityl group and results into a 4.4 fold reduction in binding strength. As a result, photoisomerization of *trans*-**2** into *cis*-**2** causes dissociation of the ligand from the porphyrin, and thereby initiates the assembly of the porphyrin.

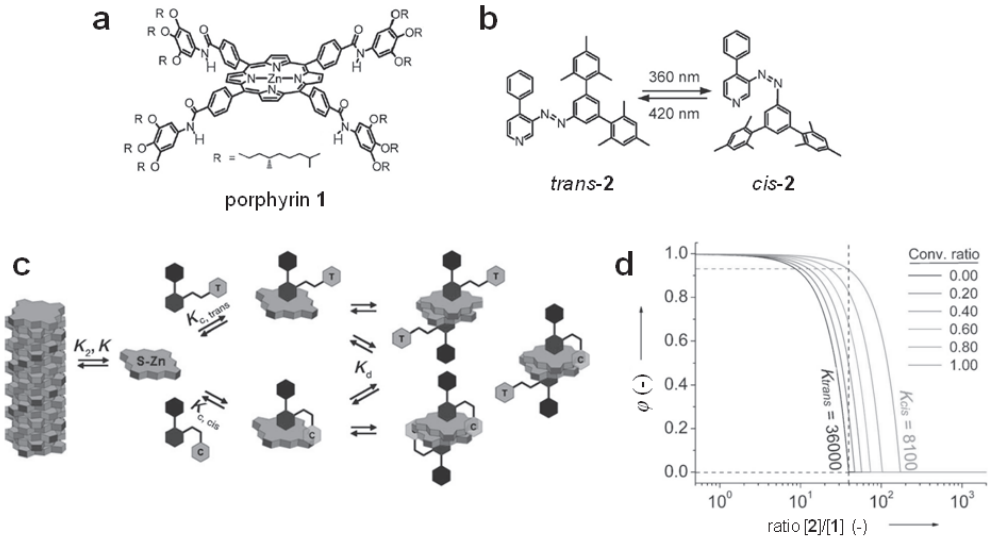

Figure 6.15 | Dynamic control over cooperative porphyrin self-assembly by photo switching phenylazopyridine ligands. The assembly of porphyrin **1** (a) into elongated stacks can be controlled by association of phenylazopyridine ligand **2** (b). The *cis*- and *trans*-isomer of **2** have different association constants to porphyrin **1**. As a result, the assembly of the porphyrin can be tuned by photo switching from *trans*-**2**, which has a high association constant, to *cis*-**2**, which has a lower association constant. As simulated with the multi-component equilibrium model (c), the degree of porphyrin aggregation φ depends on the ratio between the concentrations of ligand **2** and porphyrin **1**, as well as on the ratio between *cis*-**2** and *trans*-**2**. Hence, an optimum switch from disassembly (in the presence of *trans*-**2**) to assembly of porphyrin (in the presence of *cis*-**2**) can be obtained with a [**2**]/[**1**]-ratio of ~40. Image from ref. 26.

To optimize the switching from assembled to disassembled porphyrins by photo switching of the ligand, a multiple component equilibrium model is developed, which includes elongated porphyrin assemblies, free porphyrin monomers, monomers occupied with *cis*-**2** or *trans*-**2** and porphyrin dimers occupied with two ligands (Fig 6.15c). As shown in Figure 6.15d, the fraction of porphyrin monomers assembled into elongated stacks (φ) critically depends on the ratio between ligand and porphyrin. Furthermore, the ratio between *cis*-**2** and *trans*-**2** influences the equilibrium profile; due to the larger association constant of *trans*-**2**, a smaller

excess of this compound is required to induce complete disassembly of the porphyrin stacks. Hence, it can be derived from the equilibrium curves in Figure 6.15d that the maximum change in fraction of assembled porphyrins can be obtained by switching from *trans*-**2** to *cis*-**2** at the critical ligand/porphyrin ratio of *trans*-**2**: [*trans*-**2**]/[**1**] ~ 40. As the dashed vertical line in Figure 6.15d indicates, a switch from φ = 0% to φ = 92% is predicted. Moreover, analysis with the equilibrium model identifies the cooperativity as one of the key parameters facilitating these high-contrast switching properties, despite the small difference in the association constants of *trans*-**2** and *cis*-**2**. One can imagine that, compared to the sharp transitions displayed in Figure 6.15d, a less cooperative system would result in more gradual equilibrium curves, implying that a smaller optimum difference in the fraction of aggregated porphyrins can be obtained upon switching from *trans*-**2** to *cis*-**2**. Gratifyingly, due the cooperative nature of the porphyrin system, a photo switching of the assembly process between φ = 1% and φ = 81% is experimentally observed.

These examples make clear that the development of supramolecular systems cannot be solely based on the chemical design of the molecular components. Even though non-covalent interactions facilitated by supramolecular functional groups like hydrogen bonding moieties or solvophobic π-conjugated surfaces form the basis of the assembly process, the characteristics of the system are determined in a comparable extent by the dynamics of the system as a whole. Dynamic effects like entrapment of material into metastable aggregates or the association and dissociation rate of a ligand to the monomer should be considered, especially when they dominate the outcome of the assembly process. As a result, the only way in which the behaviour of every molecular element in the system can be orchestrated, is by deliberately designing a system in which all dynamic processes match. To this end, molecular modelling methodologies (*i.e.* density functional theory (DFT) or molecular dynamics) provide relevant insights into the strength and dynamics of individual non-covalent interactions. In a next step, kinetic models – that do not consider a detailed description of the molecules – can be helpful to understand the consequences of all these non-covalent interactions, and thereby predict the behaviour of the designed supramolecular system.

Designing such a system is not a trivial task. As illustrated by for instance the co-assembly of $ROPV_3$ and $SOPV_4$, in many cases we just have reached the stage where we can describe the assembly of multiple components into different pathways, and rationalize the influence of parameters by which the assembly behaviour can be tuned, in this instance temperature and $ROPV_3$/$SOPV_4$ ratio. Designing a system with this particular behaviour from scratch however is virtually impossible. Therefore, it remains to be seen whether the current *modus operandi* in supramolecular chemistry – synthesizing a molecule, analysing its self-assembly behaviour, trying to clarify the assembly mechanism, synthesizing a new molecule and starting the whole circle all over again – is sufficient to lift supramolecular chemistry to a level of sophistication that allows to design functional materials and systems.

Self-assembly, or self-organization, in Nature is often considered as a great source of inspiration for supramolecular synthesis.[27] Indeed, the complexity of a living cell, assembled

by a tremendous amount of different molecular building blocks is impressive. However, this does not mean that systems applied in Nature are *per se* the ideal candidates to copy in an artificial system. Although some plants like sugar cane reach peak efficiencies of 8% in their photosynthesis, most crops have an efficiency of only 0.5–2%[28]; a number that is outperformed by organic solar cells created with only a few different molecular components. On the other hand, the supramolecular organization of the chlorophyll chromophores in a photosynthetic system enables a very efficient transfer of photon energy into a long living charge separated state; an inspiring system to mimic in artificial supramolecular photo catalysis.[29]

A major problem faced when trying to develop a system inspired on natural self-assembly, like photo catalytic systems or microtubules that propel the cell by growing into one direction, is that natural systems do not easily reveal the pathways by which they have been assembled. For instance, mixing all elements of a photosynthetic system (proteins, chromophores, etc.) in a flask does not spontaneously lead to the chromophore-protein assemblies that are formed in the cell. Besides, observing a microtubule system, even with the best space-time resolution microscope, does not clarify *why* this system works, *i.e.* which molecular elements and supramolecular interactions are critical to the function of the system. This means that knowing the molecular elements of the natural system is not sufficient to mimic the system. Moreover, this implies that in order to arrive at artificial systems that oscillate, regenerate, catalyse their own formation, facilitate autonomous motion along a gradient or perform other functions comparable to natural systems, further understanding of assembly pathways and dynamics is a prerequisite. Hence control over the assembly pathways and supramolecular interactions, by manipulating their respective rates and stabilities, is of crucial importance to construct functional supramolecular materials, like to supramolecular heterojunction, or to develop dynamic systems, like the switching porphyrin system.

In the field of synthetic biology, the design of new systems in the cell is approached by applying the predictive power of modelling. Analysis of kinetic models that include all elements of the system as well as the interactions amongst them clarifies the behaviour of the system and – most importantly – reveal the parameter window in which the system will successfully display its function. In a similar way, this model-driven engineering approach seems an attractive route for the development of supramolecular systems. Instead of limiting the design of the system to the supramolecular interactions applied, the knowledge of mechanisms, dynamics and pathways involved in the self-assembly process should be combined to develop a kinetic model. Next, simulations allow identifying the parameters that are most critical to the functionality that is aimed for, e.g. oscillation between assembly and disassembly of one-dimensional aggregates. The qualitative relations amongst rate, stability, concentration, temperature and solvent conditions – demonstrated throughout this thesis – provide multiple possibilities to control the assembly process. Several parameters can be selectively manipulated via a methodology that is more convenient than to design and synthesize new molecules. Even though this model-driven strategy might require a more detailed mechanistic background, further elaborating this approach will open new

opportunities to control chemical self-assembly pathways and develop functional systems with unprecedented characteristics.

6.5 Details of simulations

Nucleation-elongation equilibrium model. The (normalized) degree of aggregation φ in Figure 6.1 is defined via φ = [UV/Vis(T) – UV/Vis(368 K)] / [UV/Vis(290 K) – UV/Vis(368 K)]. To analyse the data with the nucleation-elongation equilibrium model, φ is calculated via

$$\varphi = \frac{x_{\text{tot}} - x}{x_{\text{tot}}}, \tag{6.1}$$

analogous to the fitting procedure described in paragraph 3.7. A global nonlinear least-squares procedure is applied to find the parameters to describe the temperature-dependent UV/Vis data with the equilibrium model. The curve fit gives a very good description of the temperature-dependent degree of aggregation (Fig 6.1b), and based on the values of ΔH_n^0, ΔH_e^0, ΔS_n^0 and ΔS_e^0 that are obtained via curve fitting (ΔH_n^0 = –25.2 ± 0.2 kJ/mol; ΔH_e^0 = –52.22 ± 0.08 kJ/mol; $\Delta S_n^0 = \Delta S_e^0$ = –56.3 ± 0.2 J/K.mol, with n = 2) the weight-averaged degree of polymerization (DP_w) is calculated at 20 °C via:

$$DP_{\text{w}} = \frac{\sum_{\text{i=2}}^{\infty} i^2[\text{M}_\text{i}]}{\sum_{\text{i=2}}^{\infty} i[\text{M}_\text{i}]} = \frac{\dfrac{\sigma x^2\left(4-3x+x^2\right)}{\left(x-1\right)^3}}{x_{\text{tot}} - x}, \tag{6.2}$$

where x is found upon solving the dimensionless mass balance as given in eq. 2.3.

Attenuated equilibrium model. In the attenuated equilibrium model, the equilibrium constant of monomer association K_i depends on the length of the assembly i via $K_i = K/i$.

$$\begin{aligned}
&\text{X} + \text{X} \overset{K_2}{\rightleftarrows} \text{M}_2 && [\text{M}_2] = K_2[\text{X}]^2 = \sigma\frac{K}{2}[\text{X}]^2 \\
&\text{M}_2 + \text{X} \overset{K_3}{\rightleftarrows} \text{M}_3 && [\text{M}_3] = K_3[\text{M}_2][\text{X}] = K_3K_2[\text{X}]^3 = \sigma\frac{K}{3}\frac{K}{2}[\text{X}]^3 \\
&\text{M}_3 + \text{X} \overset{K_4}{\rightleftarrows} \text{M}_4 && [\text{M}_4] = K_4[\text{M}_3][\text{X}] = \sigma\frac{K}{4}\frac{K}{3}\frac{K}{2}[\text{X}]^4 \\
&\quad\vdots \\
&\text{M}_{\text{i}-1} + \text{X} \overset{K_\text{i}}{\rightleftarrows} \text{M}_\text{i} && [\text{M}_\text{i}] = K_\text{i}[\text{M}_{\text{i}-1}][\text{X}] = \sigma\frac{K}{i}\frac{K}{i-1}\cdots\frac{K}{3}\frac{K}{2}[\text{X}]^\text{i} = \sigma\frac{K^{\text{i}-1}}{i!}[\text{X}]^\text{i}. \\
&\quad\vdots
\end{aligned} \tag{6.3}$$

It should be noted that, in order to introduce a critical point at which the aggregation process starts, an energetically unfavourable nucleation is included by defining $K_2 = \sigma \cdot K/2$, with $\sigma < 1$. Next, the resulting mass balance is

$$c_{\text{tot}} = X + \sum_{i=2}^{\infty} i\sigma\frac{K^{i-1}}{i!}[X]^i, \tag{6.4}$$

analogously the dimensionless mass balance, with $x_{\text{tot}} = K \cdot c_{\text{tot}}$ and $x = K \cdot [X]$, is

$$x_{\text{tot}} = x + \sigma\sum_{i=2}^{\infty} i\frac{\text{x}^i}{i!}. \tag{6.5}$$

Expanding the sum in eq. 6.5 yields:

$$x_{\mathrm{tot}} = x + \sigma x\left(e^{x} - 1\right). \tag{6.6}$$

Upon numerically solving the mass balance, the dimensionless monomer concentration x can be found, and subsequently the weight averaged degree of polymerization DP_w, exclusive free monomer concentration, can be calculated:

$$DP_{\mathrm{w}} = \frac{\sum_{\mathrm{i}=2}^{\infty} i^2 P_{\mathrm{i}}}{\sum_{\mathrm{i}=2}^{\infty} i P_{\mathrm{i}}} = \frac{\sigma \sum_{\mathrm{i}=2}^{\infty} i^2 \frac{x^{\mathrm{i}}}{i!}}{x_{\mathrm{tot}} - x} = \sigma \frac{\mathrm{e}^{\mathrm{x}}\left(x + x^2\right) - x}{x_{\mathrm{tot}} - x}. \tag{6.7}$$

Attenuated growth preceded by unfavourable formation of a hydrogen-bonded dimer. To analyse if the critical temperature that is observed in the temperature-dependent assembly together with the formation of short assemblies can also be described by the attenuated assembly of hydrogen-bonded dimers, we modify the model that is introduced in the previous section. Initially, two monomers X combine to form a hydrogen-bonded dimer A, with equilibrium constant K_h. Subsequently, the hydrogen-bonded dimers assemble via stepwise association equilibria into assemblies P. The equilibrium constants involved in these association equilibria K_i again depend on the length of the assembly via $K_i = K/i$:

$$\begin{aligned}
&X + X \underset{\longleftarrow}{\xrightarrow{K_{\mathrm{h}}}} A && \left[A\right] = K_{\mathrm{h}}\left[X\right]^2 \\
&A + A \underset{\longleftarrow}{\xrightarrow{K_2}} P_2 && \left[P_2\right] = K_2\left[A\right]^2 = \frac{K}{2}K_{\mathrm{h}}^2\left[X\right]^4 \\
&P_2 + A \underset{\longleftarrow}{\xrightarrow{K_3}} P_3 && \left[P_3\right] = K_3\left[P_2\right]\left[A\right] = K_3K_2\left[A\right]^3 = \frac{K}{3}\frac{K}{2}K_{\mathrm{h}}^3\left[X\right]^6 \\
&P_3 + A \underset{\longleftarrow}{\xrightarrow{K_4}} P_4 && \left[P_4\right] = K_4\left[P_3\right]\left[A\right] = \frac{K}{4}\frac{K}{3}\frac{K}{2}K_{\mathrm{h}}^4\left[X\right]^8 \\
&\quad\vdots \\
&P_{\mathrm{i}-1} + A \underset{\longleftarrow}{\xrightarrow{K_{\mathrm{i}}}} P_{\mathrm{i}} && \left[P_{\mathrm{i}}\right] = K_{\mathrm{i}}\left[P_{\mathrm{i}-1}\right]\left[A\right] = \frac{K}{i}\frac{K}{i-1}\cdots\frac{K}{3}\frac{K}{2}\left[A\right]^{\mathrm{i}} = \frac{K^{\mathrm{i}-1}}{i!}K_{\mathrm{h}}^{\mathrm{i}}\left[X\right]^{2\mathrm{i}}. \\
&\quad\vdots
\end{aligned} \tag{6.8}$$

The resulting mass balance is

$$c_{\mathrm{tot}} = X + 2A + 2\sum_{i=2}^{\infty} iP_{\mathrm{i}} = X + 2K_{\mathrm{h}}\left[X\right]^2 + 2\sum_{i=2}^{\infty} i\frac{K^{\mathrm{i}-1}}{i!}K_{\mathrm{h}}^{\mathrm{i}}\left[X\right]^{2\mathrm{i}}, \tag{6.9}$$

analogously the dimensionless mass balance, with $\alpha = K_h / K$, $x_{tot} = K \cdot c_{tot}$ and $x = K \cdot [X]$:

$$x_{\mathrm{tot}} = x + 2\alpha x^2 + 2\sum_{i=2}^{\infty} i\frac{\left(\alpha x^2\right)^{\mathrm{i}}}{i!}. \tag{6.10}$$

Expanding the sum in eq. 6.10 yields:

$$x_{\mathrm{tot}} = x + 2\alpha x^2 + 2\alpha x^2\left(\mathrm{e}^{\alpha x^2} - 1\right) = x + 2\alpha x^2\mathrm{e}^{\alpha x^2}. \tag{6.11}$$

Upon numerically solving the mass balance, the dimensionless monomer concentration x can be found. Subsequently, DP_w, exclusive free monomers and hydrogen bonded dimers, is calculated, based on the material that is present in the assemblies P_i, with $i \geq 2$:

$$DP_{\mathrm{w}} = \frac{\sum_{\mathrm{i=2}}^{\infty} i^2 P_{\mathrm{i}}}{\sum_{\mathrm{i=2}}^{\infty} iP_{\mathrm{i}}} = \frac{\sum_{\mathrm{i=2}}^{\infty} (2i)^2 \frac{\left(\alpha x^2\right)^{\mathrm{i}}}{i!}}{x_{\mathrm{tot}} - x - 2\alpha x^2} = \frac{4\left(\mathrm{e}^{\alpha x^2}\left(\alpha x^2 + \alpha^2 x^4\right) - \alpha x^2\right)}{x_{\mathrm{tot}} - x - 2\alpha x^2}. \tag{6.12}$$

Equilibrium model to describe formation of 1D helices and bundles under equilibrium conditions. The assembly of fluorinated BTAs into a racemic mixture of left- and right-handed 1D helices, and the subsequent transition into bundles can be described by an equilibrium model that describes both the formation of helices (A) as well as bundles (B) via a sequence of monomer addition equilibria, starting with an unfavourable nucleation step and followed by more favourable elongation steps:

$$\begin{array}{ll} \mathrm{X} + \mathrm{X} \xrightleftharpoons{K_{\mathrm{n,A}}} \mathrm{A}_2 & \mathrm{X} + \mathrm{X} \xrightleftharpoons{K_{\mathrm{n,B}}} \mathrm{B}_2 \\ \mathrm{X} + \mathrm{A}_2 \xrightleftharpoons{K_{\mathrm{e,A}}} \mathrm{A}_3 & \mathrm{X} + \mathrm{B}_2 \xrightleftharpoons{K_{\mathrm{e,B}}} \mathrm{B}_3 \\ \vdots & \vdots \\ \mathrm{X} + \mathrm{A}_{\mathrm{i}} \xrightleftharpoons{K_{\mathrm{e,A}}} \mathrm{A}_{\mathrm{i+1}} & \mathrm{X} + \mathrm{B}_{\mathrm{i}} \xrightleftharpoons{K_{\mathrm{e,B}}} \mathrm{B}_{\mathrm{i+1}}, \\ \vdots & \vdots \end{array} \tag{6.13}$$

where X represents the free monomer, A_i an A-type assembly containing i monomers, B_i a B-type assembly containing i monomers, and K_n and K_e the equilibrium constants of nucleation and elongation involved in the formation of A- and B-type assemblies, respectively. The concentrations of A_i and B_i can be expressed via the equilibrium constants and monomer concentration [X]:

$$[\mathrm{A_i}] = {K_{\mathrm{e,A}}}^{i-2} K_{\mathrm{n,A}} [\mathrm{X}]^i; \qquad [\mathrm{B_i}] = {K_{\mathrm{e,B}}}^{i-2} K_{\mathrm{n,B}} [\mathrm{X}]^i. \tag{6.14}$$

The total concentration of monomers aggregated in A-type assemblies (A_{tot}) equals:

$$A_{\mathrm{tot}} = \sum_{2}^{\infty} i \cdot {K_{\mathrm{e,A}}}^{i-2} K_{\mathrm{n,A}} [\mathrm{X}]^i. \tag{6.15}$$

The total concentration of monomers aggregated in B-type assemblies (B_{tot}) equals:

$$B_{\mathrm{tot}} = \sum_{2}^{\infty} i \cdot {K_{\mathrm{e,B}}}^{i-2} K_{\mathrm{n,B}} [\mathrm{X}]^i. \tag{6.16}$$

Combining eq. 6.15 and 6.16 results in the mass balance:

$$c_{tot} = [\mathrm{X}] + \sum_{2}^{\infty} i \cdot {K_{\mathrm{e,A}}}^{i-2} K_{\mathrm{n,A}} [\mathrm{X}]^i + \sum_{2}^{\infty} i \cdot {K_{\mathrm{e,B}}}^{i-2} K_{\mathrm{n,B}} [\mathrm{X}]^i, \tag{6.17}$$

with c_{tot} the total monomer concentration. The dimensionless mass balance can be obtained with dimensionless total concentration $x_{tot} = K_{e,A} \cdot c_{tot}$, dimensionless free monomer concentration $x_M = K_{e,A} \cdot [X]$, $b = K_{e,B} / K_{e,A}$, $\sigma_A = K_{n,A} / K_{e,A}$ and $\sigma_B = K_{n,B} / K_{e,B}$.

$$x_{tot} = x_{\mathrm{M}} + \sigma_{\mathrm{A}} \sum_{2}^{\infty} i \cdot {x_{\mathrm{M}}}^i + \left(\frac{\sigma_{\mathrm{B}}}{b}\right) \sum_{2}^{\infty} i \cdot \left(b \cdot x_{\mathrm{M}}\right)^i. \tag{6.18}$$

The summation terms can be expressed in an algebraic equation, assuming $x_M < 1$ and $b \cdot x_M < 1$:

$$x_{tot} = x_M + \sigma_A \left(\frac{x_M}{(1 - x_M)^2} - x_M \right) + \sigma_B \left(\frac{x_M}{(1 - b \cdot x_M)^2} - x_M \right). \quad (6.19)$$

The temperature-dependent UV and CD data show that at elevated temperatures the 1D helices (A) have a higher stability compared to higher order aggregates (B), whereas below $T_{e,B}$ the higher order aggregates have a higher stability. Hence, at $T > T_{e,B}$, $K_{e,A} > K_{e,B}$ and at $T < T_{e,B}$, $K_{e,A} < K_{e,B}$. The temperature-dependency of each of the equilibrium constants of elongation is described via $K = \exp\left(-\frac{\Delta H^0 - T\Delta S^0}{RT} \right)$, as shown in Figure 6.3c, with $\Delta H_{e,A}^0 = -60$ kJ/mol; $\Delta S_{e,A}^0 = -100$ J/K.mol; $\Delta H_{e,B}^0 = -75$ kJ/mol; $\Delta S_{e,B}^0 = -150$ J/K.mol. The equilibrium constants of nucleation are described via $K_n = \sigma \cdot K_e$, with temperature-independent cooperativity σ. Simulations are performed assuming a high cooperativity for both A and B-type assemblies ($\sigma_A = 0.0001$ and $\sigma_B = 0.0001$). Via the temperature-dependent equilibrium constants, the fraction of monomers, A-type assemblies and B-type assemblies can be found upon solving the dimensionless mass balance equation using the Matlab *fsolve* solver function.

Kinetic model including fragmentation and fusion. The kinetic model considers four different species: 1) free monomer X, 2) dimer M_2, 3) the total number of stacks (assemblies with size larger than 2, F^M) and 4) the total number of monomers assembled in these stacks, Z^M. By assuming that for $i > 2$, $[M_{i+1}] = \alpha_M [M_i]$, it can be shown – analogous to eq. 2.13 and 2.14 – that:

$$\alpha_M = 1 - \frac{[F^M]}{[Z^M] - 2[F^M]}, \quad (6.20)$$

and

$$[M_3] = (1 - \alpha_M)[F^M], \quad (6.21)$$

respectively.

By combining reactions 1, 2 and 4 from Figure 6.10, the rate equation for the monomer becomes:

$$\frac{d[X]}{dt} = -2a[X]^2 + 2b[M_2] - 2a[X][M_2] + 2c[M_3] - 2a[F][X] + 2c([F] - [M_3]). \quad (6.22)$$

In this model, both monomer association and fusion of stacks are described with the same rate constant a. This means that the rate constants of monomer dissociation c and fragmentation c' cannot be defined independently. To define the relation between the c and c', we consider the equilibrium concentration of a species M_i that is either assembled via monomer association, or via fusion of M_{i-j} and M_j. When M_i, M_{i-j} and M_j are assembled via monomer association, their equilibrium concentrations equal $[M_i] = K_n K_e^{i-2} [X]^i$, $[M_{i-j}] = K_n K_e^{i-j-2} [X]^{i-j}$ and $[M_j] = K_n K_e^{j-2} [X]^j$. Since M_i can be formed via fusion of M_{i-j} and M_j as well, it can be shown that $[M_i] = K_e'[M_{i-j}][M_i] = K_e' K_n K_e^{i-j-2} [X]^{i-j} K_n K_e^{j-2} [X]^j$. Because of the principle of detailed balance, the equilibrium state should not be dependent on the path that has been followed. Hence, $[M_i] = K_n K_e^{i-2} [X]^i$ should equal $[M_i] = K_e' \cdot K_n K_e^{i-j-2} [X]^{i-j} \cdot K_n K_e^{j-2} [X]^j$. As a result, it can be shown that $K_e' = K_e^2 / K_n$, and $c' = c \cdot (K_n / K_e)$.

By combining reactions 1, 2, 3 and 5 from Figure 6.10, the rate equation for the dimer becomes:

$$\frac{d[M_2]}{dt} = a[X]^2 - b[M_2] - 2a[X][M_2] + 2c[M_3] - 2a[M_2]^2 + 2c\left(\frac{K_n}{K_e}\right)[M_4] - 2a[F][M_2] + 2c\left(\frac{K_n}{K_e}\right)([F] - [M_3] - [M_4]). \quad (6.23)$$

To describe the fragmentation of stacks, is should be considered that fragmentation of M_5 cannot yield another stack, M_6 can fragment in one way to yield another stack ($M_3 + M_3$), M_7 in two ways ($M_4 + M_3$; $M_3 + M_4$), M_8 in three ways ($M_5 + M_3$; $M_4 + M_4$; $M_3 + M_5$), and M_i in $i - 5$ ways. Hence, the term to describe the fragmentation rate becomes:

$$c'\sum_{i=6}^{\infty}(i-5)[M_i] = c'\sum_{i=6}^{\infty}(i-5)\cdot\alpha_M{}^{i-3}[M_3] = c'\frac{\alpha_M{}^3[M_3]}{(1-\alpha_M)^2}. \quad (6.24)$$

Next, the fusion of stacks can be described with the term $a\cdot[F]^2$. Combining reaction 2 and 3 from Figure 6.10 with eq. 6.24 yields for the rate equation of the number of stacks:

$$\frac{d[F]}{dt} = 2a[M_2][X] - 2c[M_3] + a[M_2]^2 - c\left(\frac{K_n}{K_e}\right)[M_4] + c\left(\frac{K_n}{K_e}\right)\frac{\alpha_M{}^3[M_3]}{(1-\alpha_M)^2} - a[F]^2. \quad (6.25)$$

Finally, combining reaction 2, 3, 4 and 5 from Figure 6.10 yields for the rate equation of the number of monomers in stacks:

$$\frac{d[Z]}{dt} = 3\cdot(2a[M_2][X] - 2c[M_3]) + 4\left(a[M_2]^2 - c\left(\frac{K_n}{K_e}\right)[M_4]\right) + 2a[F][X] - 2c([F] - [M_3]) + 2\left(2a[F][M_2] - 2c\left(\frac{K_n}{K_e}\right)([F] - [M_3] - [M_4])\right). \quad (6.26)$$

6.6 References

[1] Van der Weegen, R.; Korevaar, P. A.; Voudouris, P.; Voets, I. K.; De Greef, T. F. A.; Vekemans, J. A. J. M.; Meijer, E. W. *Chem. Commun.* **2013**, *49*, 5532.

[2] Chen, Z.; Stepanenko, V.; Dehm, V.; Prins, P.; Siebbeles, L. D. A.; Seibt, J.; Marquetand, P.; Engel, V.; Würthner, F. *Chem. Eur. J.* **2007**, *13*, 436.

[3] Stupp, S. I.; LeBonheur, V.; Walker, K.; Li, L. S.; Huggens, K. E.; Keser, M.; Amstutz, A. *Science* **1997**, *276*, 384.

[4] Li, X.; Sinks, L. E.; Rybtchinski, B.; Wasielewski, M. R. *J. Am. Chem. Soc.* **2004**, *126*, 10810.

[5] Arnoud, A.; Belleney, J.; Boué, F.; Bouteiller, L.; Carrot, G; Wintgens, V. *Angew. Chem. Int. Ed.* **2004**, *43*, 1718.

[6] Besenius, P.; Portale, G.; Bomans, P. H. H.; Janssen, H. M.; Palmans, A. R. A.; Meijer, E. W. *Proc. Natl. Acad. Sci. USA* **2010**, *107*, 17888.

[7] Stals, P. J. M.; Korevaar, P. A.; Gillissen, M. A. J.; De Greef, T. F. A.; Fitié, C. F. C.; Sijbesma, R. P.; Palmans, A. R. A.; Meijer, E. W. *Angew. Chem. Int. Ed.* **2012**, *51*, 11297.

[8] Lightfoot, M. P.; Mair, F. S.; Pritchard, R. G.; Warren, J. E. *Chem. Commun.* **1999**, *1945.*

[9] Filot, I. A. W.; Palmans, A. R. A.; Hilbers, P. A. J.; Van Santen, R. A.; Pidko, E. A.; De Greef, T. F. A. *J. Phys. Chem. B* **2010**, *114*, 13667.
[10] Smulders, M. M. J.; Schenning, A. P. H. J.; Meijer, E. W. *J. Am. Chem. Soc.* **2008**, *130*, 606.
[11] Nakano, Y.; Hirose, T.; Stals, P. J. M.; Meijer, E. W.; Palmans, A. R. A. *Chem. Sci.* **2012**, *3*, 148.
[12] Caminati, W.; Melandri, S.; Moreschini, P.; Favero, P. G. *Angew. Chem. Int. Ed.* **1999**, *38*, 2924.
[13] Caminati, W.; López, J. C.; Alonso, J. L.; Grabow, J.-U. *Angew. Chem. Int. Ed.* **2005**, *44*, 3840.
[14] Lee, H.; Knobler, C. B.; Hawthorne, M. F. *Chem. Commun.* **2000**, 2485.
[15] D'Oria, E.; Novoa, J. J. *CrystEngComm* **2008**, *10*, 423.
[16] Bijleveld, J. C.; Zoombelt, A. P.; Mathijssen, S. G. J.; Wienk, M. M.; Turbiez, M.; De Leeuw, D. M.; Janssen, R. A. J. *J. Am. Chem. Soc.* **2009**, *131*, 16616.
[17] Bijleveld, J. C.; Gevaerts, V. S.; Di Nuzzo, D.; Turbiez, M.; Mathijssen, S. G. J.; De Leeuw, D. M.; Wienk, M. M.; Janssen, R. A. J. *Adv. Mater.* **2010**, *22*, E242.
[18] Hendriks, K. H.; Heintges, G. H. L.; Gevaerts, V. S.; Wienk, M. M.; Janssen, R. A. J. *Angew. Chem. Int. Ed.* **2013**, *52*, 8341.
[19] Wienk, M. M.; Turbiez, M.; Gilot, J.; Janssen, R. A. J. *Adv. Mater.* **2008**, *20*, 2556.
[20] Shin, N.; Richter, L. J.; Herzing, A. A.; Kline, R. J.; DeLongchamp, D. M. *Adv. Energy Mater.* **2013**, *3*, 938.
[21] Knowles, T. P. J.; Waudby, C. A.; Devlin, G. L.; Cohen, S. I. A.; Aguzzi, A.; Vendruscolo, M.; Terentjev, E. M.; Welland, M. E.; Dobson, C. M. *Science* **2009**, *326*, 1533.
[22] Cohen, S. I. A.; Linse, S.; Luheshi, L. M.; Hellstrand, E.; White, D. A.; Rajah, L.; Otzen, D. E.; Vendruscolo, M.; Dobson, C. M.; Knowles, T. P. J. *Proc. Natl. Acad. Sci. USA* **2013**, *110*, 9758.
[23] Zhang, W.; Jin, W.; Fukushima, T.; Saeki, A.; Seki, S.; Aida, T. *Science* **2011**, *334*, 340.
[24] Wang, X.; Guerin, G.; Wang, H.; Wang, Y.; Manners, I.; Winnik, M. A. *Science* **2007**, *317*, 644.
[25] Gädt, T.; Ieong, N. S.; Cambridge, G.; Winnik, M. A.; Manners, I. *Nat. Mater.* **2009**, *8*, 144.
[26] Hirose, T.; Helmich, F.; Meijer, E. W. *Angew. Chem. Int. Ed.* **2013**, *52*, 304.
[27] Service, R. F. *Science* **2005**, *309*, 95.
[28] Olah, G. A.; Prakash, G. K. S.; Goeppert, A. *J. Am. Chem. Soc.* **2011**, *133*, 12881.
[29] Wasielewski, M. R. *J. Org. Chem.* **2006**, *71*, 5051.

Summary

Pathway complexity in π-conjugated materials

The three-dimensional positioning of π-conjugated, (semi)conducting molecules is one of the key parameters in the performance of organic electronic materials such as plastic solar cells, organic LEDs or field effect transistors. In many cases these materials are processed from free dissolved molecules (or polymers) in solution. During the processing molecules are induced to aggregate, for instance by changing the solvent conditions upon spin coating or by adding a co-solvent. The aggregation is facilitated by weak non-covalent interactions and as a result, the molecular building blocks can end up into different supramolecular structures. Directing the assembly process towards the optimized molecular morphology – the one that yields the best performance of the electronic material – requires many trial-and-error steps. The optimum morphology can either be formed under kinetic control, *i.e.* metastable, or under thermodynamic control. This thesis aims to develop experiments and models to unravel, understand and obtain control over chemical assembly pathways. The main focus of this thesis is on π-conjugated materials, however the results are anticipated to be applicable to other types of supramolecular materials as well.

In **Chapter 2**, the aggregation kinetics of a π-conjugated oligo(*p*-phenylene vinylene) derivative – as a molecular model system – are studied by a combination of stopped-flow techniques with circular dichroism (CD) spectroscopy. This approach allows us to probe the complete self-assembly process, starting from the individual monomers (building blocks) to the formation of one-dimensional helical assemblies in solution. Surprisingly, the kinetic experiments reveal metastable assemblies in the initial stages of the assembly process. By developing a numeric kinetic model, inspired on models applied in the field of protein aggregation, the phenomenon of pathway complexity is unravelled. Different assembly pathways are competing for the molecular building block. As a consequence, entrapment of monomers in the metastable pathway at high concentration hampers the formation of thermodynamically stable assemblies.

The assembly process of this model system is limited to the stacking of molecules into one-dimensional structures in diluted solutions, whereas processing of functional materials involves multiple aggregation steps beyond one-dimensional stacking. However, similar to the one-dimensional model system, metastable morphologies in these materials can be unravelled by experiments under kinetic control. Furthermore, the mutual interaction amongst the different aggregation pathways, *i.e.* pathway complexity, affects the nanostructures obtained.

In **Chapter 3**, the influence of solvent conditions on the stability and dynamics of the aggregates is investigated. The destabilizing effect of a good solvent, like chloroform for assemblies of π-conjugated molecules, can be described with a linear free-energy relationship. Moreover, addition of a good solvent to aggregates that are formed via a nucleated process results in a full disassembly at a critical ratio between good and poor solvent. Close to this critical solvent composition, a minimum equilibration rate is obtained in both the assembly

and disassembly of the aggregates. These effects, found by combining kinetic experiments and models, allow controlling assembly processes via solvent conditions.

In **Chapter 4**, the co-assembly of two different monomers is studied by experiments and developing a kinetic model. In the initial stages of the co-assembly process, metastable structures are formed that entrap free monomers and thereby slow down the formation of the thermodynamically favoured assemblies. The competition exerted by these metastable assemblies on the formation of equilibrium structures however is highly temperature-dependent. Therefore, the overall assembly rate of the equilibrium structures can be optimized upon tuning the temperature ramp by which the free dissolved monomers are cooled from elevated temperature.

Furthermore, the formation of equilibrium assemblies can be accelerated by taking advantage of the destabilizing effect of a good solvent, as demonstrated in Chapter 3. The presence of a certain amount of good solvent excludes assembly along the metastable pathway, whereas the equilibrium assemblies – that have a higher stability – can still be formed. By simulation we demonstrate that stepwise decreasing the content of good solvent results in a significant increase in the formation rate of equilibrium assemblies. In contrast, an assembly protocol in which no good solvent is applied yields entrapment of monomers into spurious, metastable assemblies. Guided by these theoretical insights, model-driven strategies can be developed that allow the controlled assembly of more complex systems.

In **Chapter 5**, the aggregation pathways of bio-active peptide-amphiphiles are investigated. Kinetic effects that are observed previously in the π-conjugated model system play a role here as well. Due to a large hysteresis, conditions temporarily encountered during the preparation of these assemblies exert their influence on the structures finally obtained. Thereby, the preparation protocol has a large influence on the assembly process.

In **Chapter 6**, self-assembly processes are analysed for molecular systems that cannot be described with regular one-dimensional assembly models under thermodynamic control. The investigated systems include the nucleated formation of small sized perylene bisimide assemblies, the bundling of one-dimensional fluorinated benzene-1,3,5-tricarboxamide helices, the co-assembly of different oligo(*p*-phenylene vinylene) derivatives and the pre-aggregation of poly(diketopyrrolopyrrole-terthiophene) in chloroform.

The outcome of self-assembly processes into functional materials is often hard to predict simply from the molecular design of the individual components. Hence, a model-driven approach is a pre-requisite to perform self-assembly at a more sophisticated level. In this chapter it is shown, illustrated with the above mentioned molecular systems, how models serve to understand self-assembly behaviour. If models can be expanded and improved to predict the self-assembly behaviour, this will allow us to go from *rationalized behaviour* to *rationalized design*. To this end, the last part of this chapter presents an outline how further insights into pathway complexity – based on kinetic experiments and models – pave the way towards model-driven engineering of functional supramolecular systems.

Samenvatting voor niet-chemici

Een van de grote uitdagingen in de chemie is het opbouwen van structuren uit moleculen. Net zoals de bekende lego-steentjes aan elkaar geklikt kunnen worden tot een huis, een auto of een trein, kunnen ook moleculen met elkaar verbonden worden tot een groter bouwwerk. Overigens is dit bouwen met moleculen nogal verschillend van het bouwen met lego-steentjes. Om te beginnen zijn moleculen 10 miljoen keer kleiner dan lego-steentjes, wat maakt dat je ze niet zomaar kunt plaatsen zoals je wilt. Tegelijk zorgen deze minuscule afmetingen van moleculen voor een andere eigenschap. Terwijl lego-steentjes gewoon blijven liggen als je er niets mee doet, zijn losse moleculen wanneer je ze oplost in bv. water continu in beweging en zweven ze rond in het oplosmiddel. Door nu deze moleculen speciale chemische eigenschappen te geven, kunnen ze – wanneer ze al rondzwevend door het oplosmiddel elkaar tegenkomen – spontaan aan elkaar blijven plakken. Dit verschijnsel, waarbij moleculen als lego-steentjes aan elkaar klitten heet *zelfassemblage*, en via dit principe kunnen allerlei grotere structuren, zoals bolletjes of lange fibers, gemaakt worden.

De meest spectaculaire voorbeelden van moleculen die georganiseerd worden in grotere structuren zijn te vinden in de natuur. Duizenden eiwitmoleculen aaneengeschakeld vormen actine fibers, staafjes die samen het skelet van een cel vormen. Vetmoleculen vormen de wand van een cel, waarin talrijke eiwitten zijn ingekapseld die fungeren als doorgeefluik voor bijvoorbeeld voedingsstoffen. Al met al is een cel een ongelofelijk complex systeem dat is opgebouwd uit miljarden moleculen, en allerlei functies kan uitoefenen zoals signalen van andere cellen herkennen, zich voortbewegen, zich vermenigvuldigen, etcetera.

Ook niet-natuurlijke materialen – hoewel een stuk minder ingewikkeld dan de cel – kunnen via zelfassemblage van moleculen gemaakt worden. Op deze manier worden moleculen die stroom geleiden opgebouwd tot elektronische materialen als een plastic zonnecel of een organische LED. Voor dit soort materialen is de precieze oriëntatie van elk molecuul ten opzichte van zijn buren enorm belangrijk: alleen als er goed contact is kan de stroom op de juiste manier doorgegeven kan worden. Hiervoor is het dus van belang om controle te krijgen over het zelfassemblage proces van deze moleculen.

En daar begint het probleem waar dit proefschrift zich op richt. Net zoals lego-steentjes op meerdere manieren aan elkaar geklikt kunnen worden, geldt ook voor moleculen dat er vaak meerdere opties zijn hoe ze zich aan elkaar kunnen hechten. Bij het maken van bv. plastic elektronische materialen komt het dan ook regelmatig voor dat er verschillende zelfgeassembleerde structuren gevonden worden. Aangezien de manier waarop de moleculen zijn geassembleerd invloed heeft op de eigenschappen, is het natuurlijk zaak om de juiste structuur te verkrijgen. Dit kan gedaan worden door te spelen met de omstandigheden, bv. temperatuur of oplosmiddel, waaronder de zelfassemblage plaats vindt. Echter, dit vergt een hoop proberen en om grip te krijgen achter alle processen die hierbij een rol spelen zijn meer fundamentele studies aan zelfassemblage belangrijk.

In dit onderzoek hebben we gebruik gemaakt van moleculen met een chemische structuur die vergelijkbaar is met materialen in plastic elektronica. Onze π-geconjugeerde oligo(*p*-fenyleenvinyleen) moleculen, afgekort OPV, stapelen wanneer ze zijn opgelost in olieachtige vloeistoffen op elkaar in schroefvormige draden zoals weergegeven in Figuur 2.1. Vanwege de asymmetrische vorm van de OPV moleculen hebben alle schroeven dezelfde draairichting, linksom. Om nu te begrijpen hoe het groeiproces van deze schroeven in zijn werk gaat, hebben we zogenaamde kinetische experimenten gedaan waarbij we de vorming van de schroeven volgen in de tijd. Hierbij lossen we OPV moleculen eerst op in chloroform, waarin ze niet zelfassembleren en dus vrij in het oplosmiddel rondzweven. Vervolgens voegen we methylcyclohexaan toe, een oplosmiddel dat zorgt voor zelfassemblage. Via een speciale spectroscopische techniek, circulair dichroisme, kunnen we dan de vorming van de schroeven volgen in de tijd.

Hierbij blijkt iets opmerkelijks te gebeuren. Terwijl OPV moleculen normaal in linksdraaiende schroeven assembleren, worden er in het begin van het groeiproces rechtsdraaiende schroeven gevormd, welke na verloop van tijd weer verdwijnen. Dit betekent dus dat OPV moleculen op verschillende manier kunnen assembleren: rechtsom of linksom. Kennelijk kan de rechtsdraaiende structuur het snelst gevormd worden. Echter, net als lego-steentjes zijn alle bindingen tussen OPV moleculen omkeerbaar: ze kunnen ook weer losraken. Na verloop van tijd vallen de rechtsdraaiende schroeven dus weer uit elkaar, waarna de resulterende OPV moleculen assembleren in linksdraaiende schroeven die weliswaar langzamer gevormd worden, maar een hogere stabiliteit hebben. Deze kinetische experimenten laten dus zien dat er, beginnende vanaf het losse molecuul, twee verschillende assemblageroutes gevolgd kunnen worden: één naar de metastabiele structuur en één naar de stabiele structuur.

Dit verschijnsel, waarbij moleculen assembleren in ofwel een structuur die snel gevormd wordt (metastabiel) of in een structuur die het meest stabiel is, heeft belangrijke consequenties. Aangezien beide structuren bestaan uit hetzelfde molecuul als bouwsteen, zijn ze elkaars concurrenten. Wanneer de moleculen terecht komen in zo'n snelgevormde metastabiele structuur en heel langzaam losraken, betekent dit dat de andere structuur, hoewel stabieler, slechts heel langzaam gevormd kan worden. Wanneer dit nu juist de gewenste structuur is, bv. vanwege de elektrische eigenschappen, is dat natuurlijk een probleem. Om beter te begrijpen hoe het zelfassemblage proces beïnvloed kan worden, hebben we simulatie modellen ontwikkeld waarmee we kunnen nagaan wanneer metastabiele structuren kunnen opduiken. Een combinatie van simulaties en tal van experimenten leert dat metastabiele structuren vooral een concurrent zijn voor de stabiele structuur bij hoge concentratie van de moleculaire bouwsteen. Daarnaast blijkt dat ook parameters als temperatuur en de samenstelling van het oplosmiddel gemanipuleerd kunnen worden om het hele assemblage proces te beïnvloeden en metastabiele structuren mis te lopen, of juist te isoleren indien gewenst.

De OPV moleculen zoals hier gebruikt zijn op zichzelf niet de meest voor de hand liggende keuze om elektronische materialen van te maken. Toch geeft het assemblage gedrag van deze

moleculen veel inzichten in de zelfassemblage van elektronische materialen, dankzij de vorming van rechts- en linksdraaiende schroeven die experimenteel gemakkelijk te volgen zijn. Echter, zelfassemblage beperkt zich niet tot elektronische materialen. Daarom hebben we gekeken of alle nieuwe inzichten ook van nut zijn voor het begrip van andere zelfassemblerende systemen. Voor materialen die kunnen worden ingezet voor biomedische toepassingen speelt zelfassemblage van moleculen eveneens een belangrijke rol. Zo is in samenwerking met de onderzoeksgroep van prof.dr. Samuel Stupp in Evanston (VS) de assemblage van fibers uit zogenaamde peptide moleculen bestudeerd. Deze peptiden blijken behoorlijk vast aan elkaar te binden, wat ervoor zorgt dat fibers die eenmaal gevormd zijn niet zomaar meer uit elkaar vallen, en de geassembleerde structuur dus "in één keer goed" moet zijn. Daarom zijn ook hier de condities tijdens het assemblage proces zeer belangrijk. Deze kennis biedt nieuwe aanknopingspunten om het maken van de fibers te optimaliseren.

Het hele idee van zelfassemblage is dat de moleculen simpelweg doen wat de wetten van de chemie en fysica hun voorschrijven, en het hele proces dus vanzelf gaat. Echter, voor de zelfassemblage van één molecuul hebben we gezien dat er al meerdere structuren gevormd kunnen worden. Het is te verwachten dat voor het maken van meer ingewikkelde structuren die uit verschillende soorten moleculen bestaan, het aantal opties alleen maar groter wordt. Om toch voor elkaar te krijgen dat de moleculen op de juiste manier assembleren, moeten gedurende het assemblage proces de condities zo worden gekozen dat de ongewenste structuren niet gevormd worden. Dit vereist inzicht in de relatie tussen allerlei parameters (temperatuur, concentratie, oplosmiddel) en de snelheid en stabiliteit waarmee de verschillende structuren ontstaan. Kinetische experimenten en modellen, waarmee in dit proefschrift een begin is gemaakt, zijn hierbij onmisbaar en kunnen de volgende stap in moleculaire zelfassemblage mogelijk maken.

Curriculum Vitae

Peter Korevaar werd geboren op 1 augustus 1986 te Graafstroom (Goudriaan, Zuid-Holland). Na het behalen van zijn gymnasium diploma aan de Christelijke Scholen Gemeenschap Oude Hoven te Gorinchem begon hij in 2004 aan de studie Scheikundige Technologie aan de Technische Universiteit Eindhoven. Tijdens zijn studie heeft hij stages uitgevoerd aan de University of California Santa Barbara (VS) in de onderzoeksgroep van prof.dr. S. Han, en aan het IBM Almaden Research Center (San Jose, VS) in de onderzoeksgroep van dr. J.L. Hedrick. Het afstudeerwerk werd uitgevoerd in de groep van prof.dr. E.W. Meijer, onder begeleiding van dr.ir. T.F.A. de Greef en dr.ir. M.M.J. Smulders. Dit onderzoek aan de kinetiek en thermodynamica van supramoleculaire polymerisaties werd in 2010 bekroond met de KNCV Golden Master Award en een Unilever Research Prize. Na het *cum laude* afronden van zijn studie startte hij in februari 2010 met een promotieonderzoek in het Instituut voor Complexe Moleculaire Systemen (ICMS) en in de capaciteitsgroep Macromoleculaire en Organische Chemie aan de Technische Universiteit Eindhoven, onder begeleiding van prof.dr. E.W. Meijer en dr.ir. T.F.A. de Greef. De belangrijkste resultaten van dit promotieonderzoek staan beschreven in dit proefschrift.

Peter Korevaar was born on August 1st, 1986 in Graafstroom (the Netherlands). After finishing secondary school at the "Christelijke Scholen Gemeenschap Oude Hoven" in Gorinchem (The Netherlands), he started in 2004 studying Chemical Engineering at the Eindhoven University of Technology (The Netherlands). During his study, he conducted interships at the University of California Santa Barbara (USA) in the research group of prof.dr. S. Han, and at the IBM Almaden Research Center (San Jose, USA) in the research group of dr. J.L. Hedrick. His master thesis project was formed in the research group of prof.dr. E.W. Meijer, under supervision of dr.ir. T.F.A. de Greef and dr.ir. M.M.J. Smulders. This research into the kinetics and thermodynamics of supramolecular polymerizations has been awarded in 2010 with the Golden Master Award of the Royal Netherlands Chemical Society and a Unilever Research Prize. After finishing his study *cum laude* he started in February 2010 with a PhD project in the Institute for Complex Molecular Systems (ICMS) and in the laboratory of Macromolecular and Organic Chemistry, at the Eindhoven University of Technology, under supervision of prof.dr. E.W. Meijer and dr.ir. T.F.A. de Greef. The most important results of this research are described in this thesis.

List of publications

'Model-driven optimization of multi-component self-assembly processes'
P. A. Korevaar, C. Grenier, A. J. Markvoort, A. P. H. J. Schenning, T. F. A. de Greef & E. W. Meijer, *Proc. Natl. Acad. Sci. USA* **2013**, *110*, 17205–17210.

'Pathway complexity in π-conjugated materials'
P. A. Korevaar, T. F. A. de Greef & E. W. Meijer, *Chem. Mater.* **2013**, DOI: 10.1021/cm4021172.

'The influence of π-conjugated moieties on the thermodynamics of cooperatively self-assembling tricarboxamides'
F. García, P. A. Korevaar, A. Verlee, E. W. Meijer, A. R. A. Palmans & L. Sánchez, *Chem. Commun.* **2013**, *49*, 8674–8676.

'Small sized perylene-bisimide assemblies controlled by both cooperative and anti-cooperative assembly processes'
R. van der Weegen, P. A. Korevaar, P. Voudouris, I. K. Voets, T. F. A. de Greef, J. A. J. M. Vekemans & E. W. Meijer, *Chem. Commun.* **2013**, *49*, 5532–5534.

'Pathway complexity in supramolecular polymerization'
P. A. Korevaar, S. J. George, A. J. Markvoort, M. M. J. Smulders, P. A. J. Hilbers, A. P. H. J. Schenning, T. F. A. de Greef & E. W. Meijer, *Nature* **2012**, *481*, 492–496.

'Controlling chemical self-assembly by solvent-dependent dynamics'
P. A. Korevaar, C. Schaefer, T. F. A. de Greef & E. W. Meijer, *J. Am. Chem. Soc.* **2012**, *134*, 13482–13491.

'Symmetry breaking in the self-assembly of partially fluorinated benzene-1,3,5-tricarboxamides'
P. J. M. Stals, P. A. Korevaar, M. A. J. Gillissen, T. F. A. de Greef, C. F. C. Fitié, R. P. Sijbesma, A. R. A. Palmans & E. W. Meijer, *Angew. Chem. Int. Ed.* **2012**, 51, 11297–11301.

'Consequences of cooperativity in racemizing supramolecular systems'
S. Cantekin, H. M. M. ten Eikelder, A. J. Markvoort, M. A. J. Veld, P. A. Korevaar, M. M. Green, A. R. A. Palmans & E. W. Meijer, *Angew. Chem. Int. Ed.* **2012**, *51*, 6426–6431.

'Broad-spectrum antimicrobial supramolecular assemblies with distinctive size and shape'
K. Fukushima, J. P. K. Tan, P. A. Korevaar, Y. Y. Yang, J. Pitera, A. Nelson, H. Maune, D. J. Coady, J. E. Frommer, A. C. Engler, Y. Huang, K. Xu, Z. Ji, Y. Qiao, W. Fan, L. Li, N. Wiradharma, E. W. Meijer & J. L. Hedrick, *ACS Nano* **2012**, *6*, 9191–9199.

'Local water dynamics in coacervated polyelectrolytes monitored through dynamic nuclear polarization-enhanced ^{1}H-NMR'
R. Kausik, A. Srivastava, P. A. Korevaar, G. Stucky, J. H. Waite & S. Han, *Macromolecules* **2009**, *42*, 7404–7412.

'Iterative tandem catalysis of racemic AB monomers'
Ü. Kanca, J. van Buijtenen, B. A. C. van As, P. A. Korevaar, J. A. J. M. Vekemans, A. R. A. Palmans & E. W. Meijer, *J. Polym. Sci. Part A: Polym. Chem.* **2008**, *46*, 2721–2733.

'The role of heterogeneous nucleation in the self-assembly of oligothiophenes'
M. Wolffs, P. A. Korevaar, P. Jonkheijm, O. Henze, W. J. Feast, A. P. H. J. Schenning & E. W. Meijer, *Chem. Commun.* **2008**, 4613–4615.

Dankwoord / Acknowledgements

Nu is dan het moment daar dat ik kan beginnen aan het meest gelezen onderdeel van mijn proefschrift. Waar sommigen een dankwoord zien als een onderwerp van grondige studie op zichzelf, betekenen deze 4 bladzijden voor mij vooral een gelegenheid om terug te kijken op een fantastische periode van 7 ½ jaar waarin ik achtereenvolgens als Spinoza-student, afstudeerder en promovendus deel heb mogen uitmaken van de SMO familie.

Allereerst wil ik graag mijn promotor Bert Meijer bedanken voor alle mogelijkheden die er zijn om binnen deze fantastische groep onderzoek te doen. Bert, jouw persoonlijke stijl van begeleiden heb ik altijd als bijzonder prettig ervaren. Altijd als ik je kantoor binnenliep had je wel tijd om me van een kort maar waardevol advies te voorzien. Ook kijk ik met zeer veel plezier terug op alle langere discussies – gepland of spontaan – over de wetenschap of zaken daarbuiten. De stimulerende manier waarop jij in staat bent om resultaten te interpreteren, nieuwe ideeën van opbouwende kritiek te voorzien en al het werk in een breder perspectief te plaatsen heeft mij enorm vooruit geholpen. Verder lopen onder jouw leiding zowel de groep als het instituut als een trein, wat ervoor zorgt dat het hier naast de uitstekende sfeer ook qua faciliteiten goed toeven is. Tot slot wil ik je graag bedanken voor alle hulp en adviezen aangaande het vinden van een postdocplaats.

Ook copromotor Tom de Greef is onmisbaar geweest voor de totstandkoming van dit proefschrift. Tom, jouw tip tijdens mijn afstuderen om "eens een keer naar die kinetiek te kijken" heeft zeker niet verkeerd uitgepakt. Aangespoord door de positieve resultaten van wat ooit als een vrijdagmiddag experiment begon raakten we verzeild in een oerwoud aan modelletjes, pagina's lange afleidingen en Matlab scriptjes. Ik heb altijd erg genoten van je directe manier van communiceren, je enthousiasme en natuurlijk wat misschien wel je handelsmerk is: het altijd en overal bijhouden van de gehele wetenschappelijke literatuur. Aan die laatste eigenschap hebben we maar mooi het begrip "pathway complexity" te danken. Ik denk dat ook mijn onderzoek enorm heeft geprofiteerd van het feit dat jij uitstekend in staat bent om verbanden te leggen naar verschijnselen die optreden in andere wetenschapsgebieden en om op zoek te gaan naar "selling points" voor het maken van een goed verhaal. Dank verder voor alle hulp met het schrijven van artikelen en heel veel succes met het in elkaar zetten van je DNA netwerkjes!

I am really honoured that prof.dr. Frank Würthner, prof.dr. Daan Frenkel and dr. Subi George are taking part in my PhD committee, and I would like to thank them for making the journey all the way to Eindhoven to attend my defence. Daarnaast zou ik graag dr.ir. Pascal Jonkheijm en prof.dr.ir. René Janssen willen bedanken voor hun deelname aan mijn promotiecommissie.

Het aan elkaar knopen van twee verschillende assemblage pathways in een kinetisch model was iets dat aan het begin van mijn promotie alleen mogelijk bleek dankzij het mathematische vernuft van Bart Markvoort. Bart, ik ben nog steeds onder de indruk van jouw vermogen om meteen in te zien hoe wiskundige vergelijkingen en modellen zich gaan gedragen en, als het niet werkt, waar de fout zit. Tegelijk ben je in staat om ook de koppeling met supramoleculaire systemen te maken. Ik denk dat dit een bijzondere combinatie is: in ieder geval heeft het mij enorm vooruit geholpen. Verder dank voor het kritisch volgen van al mijn modellen en bijbehorende Matlab capriolen.

I would like to thank Subi George also for his work on the isolation of metastable OPV helices via tartaric acid. This work turned out to be indispensable to give our joint Nature paper the impact that it has in its current form. Subi, thanks for your hospitality when we visited Bangalore in December 2011. Next, I would like to thank dr. Christophe Grenier for all his work on the co-assembly of different OPV

enantiomers, which forms the experimental basis for the work described in Chapter 4 and paragraph 6.2.3.

I really enjoyed the collaboration with prof.dr. Samuel Stupp and Christina Newcomb on the assembly of peptide amphiphiles. Christina, many thanks for providing me with quite some PAs to study with CD, and for all the discussions we had on their assembly behaviour. Hopefully the manuscript will get published soon. I would like to thank the Stupp group for their hospitality when I visited Chicago in July 2012. Furthermore, I would like to thank Patricia Dankers and Job Boekhoven for stimulating discussions.

Daar ik niet bepaald bekend sta als een groot syntheticus heb ik dankbaar gebruik gemaakt van moleculen die door anderen in elkaar zijn gezet. Het belangrijkste molecuul – in ieder geval in dit proefschrift – is natuurlijk de OPV. Graag bedank ik Albert Schenning, Pascal Jonkheijm, Freek Hoeben, Christophe Grenier, Željko Tomović, Martin Wolffs, Maarten Poederooijen, Subi George, Robin de Bruijn en alle anderen die zich met OPV hebben bezig gehouden voor hun werk waarop ik in dit proefschrift verder heb kunnen bouwen. Verder dank aan Anja Palmans voor de BiPy ster, Floris Helmich voor de peryleen, en Tristan Mes voor de thioBTA (en natuurlijk alle gezamenlijke dineersessies!).

Ook Maarten Smulders en Martin Wolffs wil ik graag bedanken voor alle hulp met het opzetten en aan de praat krijgen van onze stopped-flow setup.

Gedurende mijn promotie heb ik het genoegen gehad om meerdere studenten te begeleiden, al dan niet in samenwerking met anderen. Met Tim Paffen heb ik met zeer veel plezier gewerkt aan het begrijpen van de vouwing van polymeren nanodeeltjes. Tim, helaas heeft dit onderwerp de eindmontage van dit proefschrift niet overleefd, maar dat neemt niet weg dat ik nog steeds onder de indruk ben van je capaciteiten om nieuwe modellen te doorgronden en te simuleren. Daarnaast wist je in korte tijd ook nog eens flink wat synthesewerk te doen. Heel veel succes met je promotie binnen SMO! Bram Teunissen heb ik mogen begeleiden met de zelfassemblage van porphyrines. Bram, die enorme dierentuin van porphyrines die jij wist te synthetiseren – uiteraard niet onder mijn begeleiding maar samen met Rob van der Weegen – is nog steeds indrukwekkend. Met alle inzichten die je hieruit wist te destilleren moet een hele mooie publicatie te maken zijn. Ook jij bent gelukkig bij SMO aan de slag gegaan als promovendus, heel veel succes hiermee! Bij het fitten van de denaturatie datasets ben ik geholpen door Charley Schaefer, de man die sneller programmeert dan zijn eigen schaduw. Charley, ikzelf en anderen maken nog steeds met veel plezier gebruik van alle Matlab scripts die jij in elkaar gesleuteld hebt, enorm bedankt hiervoor! Het is mooi dat je je met al die programmeer skills nu volledig uit kunt leven op een promotie aan het Holst Centre. Ook jij heel veel succes hiermee! Gerben van Straaten wil ik graag bedanken voor alle stopped-flow metingen en kinetiek simulaties die hij als bachelor student heeft uitgevoerd.

Naast de projecten waarin ikzelf een leidende rol had, ben ik ook verzeild geraakt in behoorlijk wat samenwerkingen. Met wisselend succes, maar desalniettemin altijd met veel plezier. Om te beginnen het werk aan de fluor-BTAs die een CD effect lieten zien terwijl dat helemaal niet mocht, waarvoor dank aan Patrick Stals. Rob van der Weegen wil ik bedanken voor de samenwerking aangaande de coöperatieve groei van korte peryleen stacks. I would like to thank Weiwei Li, Martijn Wienk and René Janssen for the collaboration on the aggregation behaviour of DPP polymers. Seda Cantekin, Bart Markvoort, Huub ten Eikelder en Anja Palmans dank ik graag voor alle discussies over de mechanismen in racemiserende BTAs. Daan van der Zwaag wil ik graag bedanken voor de plezierige samenwerking met het uitzoeken van de parallelle vs. sequentiële aggregatie. Next, I would like to

thank Chidambar Kulkarni and Subi George for the collaboration on the stereomutation of coronene derivates; Julia Guilleme and David González-Rodríguez for the collaboration on the self-assembly of subphthalocyanines, and Fatima García and prof. Luis Sánchez for the collaboration on the self-assembly of tricarboxamides. I certainly enjoyed the interactions and learned a lot from all these collaborations.

Misschien wel de meest merkwaardige samenwerking waaraan ik een bescheiden bijdrage heb mogen leveren is het in elkaar zetten van de filmpjes voor onze jaarlijkse uitjes met de vakgroep. Zelden werden het reilen en zeilen van de vakgroep op zulk een treffende en waarachtige wijze in perspectief geplaatst en van duiding voorzien als in dit fenomenale beeldmateriaal. Ter relativering voor de minder geïnformeerde lezer is het misschien goed te vermelden dat het altijd weer spannend was of we a) het filmpje af zouden krijgen voordat de bus vertrok en b) na het vertonen ervan nog in Eindhoven konden blijven wonen. Gelukkig kwam het elk jaar goed, en uiteraard dank ik mijn collegae in dezen: Patrick Stals, Janus Leenders, Martijn Gillissen, Bob Jakobs en Marcel Koenigs. Maar minstens net zo belangrijk waren natuurlijk onze grootste bronnen van inspiratie AP, EWM, RJ, LB, RS, JV, BdW, MvG, TdG, PD, JS, SM, MW, IdF & RvdW; allen dank.

Groot was het genoegen om deel uit te maken van alle groepsbijeenkomsten en subgroepbijeenkomsten. De naamswijzigingen en herindelingen hebben elkaar te snel opgevolgd om alles en iedereen hier te noemen, maar dank aan alle leden van de groep voor de talrijke positieve discussies en het vele wat ik daarvan heb geleerd. Björne Mollet wil ik bedanken voor de prettige samenwerking met de organisatie van de (inmiddels weer opgeheven) Academisch Genootschap Meetings.

Na eerst 2 ½ jaar op vloer 4 in Helix te hebben geresideerd was het tijd om te verhuizen naar Ceres, het nieuwe en om architectonische redenen alom bejubelde ICMS gebouw. Graag bedank ik al mijn (oud)kantoorgenoten in Helix en Ceres: Michel, Maarten, Floris, Marko, Marta, Yoko, Bram T., Anneloes, Daan, Bram P. en Martijn. Bedankt voor de gezelligheid, alle zinnige en minder zinnige discussies, raak geformuleerde analyses van de dagelijkse beslommeringen en natuurlijk het gedogen van mijn expansiedrift. Het mooie aan Ceres is dat alles er van glas is: ik kreeg er ineens een heleboel buren bij. Voor de gezelligheid die dit met zich meebrengt bedank ik graag Ceres-stamgasten Tom, Ilja, Marta, Bas, Rik, Lenny, Koen (ook bedankt voor de prachtige OPV plaatjes!), Gijs, Tim, Bert, Nora, Janna, Cindy, Carla, Patricia, Lorenzo, Isja, Andreas en Sagitta. Sagitta Peters wil ik tevens bedanken voor alle inspanningen waardoor het instituut nu terecht is gekomen in dit prachtige gebouw, en natuurlijk voor de nodige hulp bij het oplossen van probleempjes en problemen die onvermijdelijk zijn bij het in gebruik nemen van een gloednieuw lab. Sagitta, het is geweldig wat je allemaal doet voor het instituut en je voornemen om een glijbaan aan te leggen tussen vloer 4 van Helix en vloer 1 van Ceres steun ik van harte.

Al het tot nog toe beschrevene zou een stuk ingewikkelder zijn geweest zonder de hulp van zij die ervoor zorgen dat SMO en het ICMS als goed gesmeerde machines draaien. Graag dank ik Hans Damen voor alle hulp bij het bestellen van chemicaliën, oplosmiddelen en lampen voor spectrometers. Ook woorden van dank aan Henk Eding voor de koffie, het verzenden van pakketjes en allerhande klusjes in het Helix gebouw, en aan Xianwen Lou, Joost van Dongen en Ralf Bovee voor alles op het analytische lab. Verder natuurlijk onze (oud)secretaresses Nora van den Berg, Patricia Arentsen, Joke Rediker, Jolanda Mensen, Martina Jiricka, Janna Verkaik, Cindy Plompen en Carla Bouwman: bedankt voor alle goede zorgen.

Paranimf op de links positie Daan van der Zwaag, vanaf het moment dat je in Eindhoven kwam hebben we veel met elkaar gewerkt vanwege onze gedeelde interesse in het modelleren van zelf-assemblage processen. Naast dat je heel veel weet van de chemie en ook dit onderwerp heel snel hebt opgepakt, ben je daarnaast heel gemakkelijk in de omgang. Ik kijk dan ook met veel plezier terug op ons gezamenlijke conferentie bezoek in Washington plus het vermaak daaromheen. Heel veel succes met de rest van je promotie, en dank dat je mijn paranimf wilt zijn. Ook paranimf op rechts Bram Pape wil ik graag bedanken. Nadat ik verhuisde naar Ceres, waar jij het mooiste bureau met uitzicht op de schoorsteen al had geclaimd, heb ik ook aan jou een heel plezierige kantoorgenoot gehad. Dank daarvoor, een ook jij heel veel succes met de rest van je promotie!

Met dik 7 ½ jaar SMO, MST en ICMS op de teller begint de groep collega's waarmee je in allerlei wisselende verbanden te maken hebt gehad indrukwekkende vormen aan te nemen. Ik ga me dan ook niet wagen aan een opsomming. Maar natuurlijk is het aan velen te danken dat ik het ongelofelijk naar mijn zin heb gehad gedurende mijn promotie. Therefore, I would like to thank many colleagues that contribute(d) to the great atmosphere in the lab as well as during all kinds of organized or spontaneous activities outside the lab.

Uiteraard wil ik ook graag mijn vrienden bedanken voor al hun belangstelling en goedbedoelde interpretaties van mijn wetenschappelijke vorderingen. Ook al liep ik weleens, en met name de laatste tijd, met een emmer over mijn kop, dankzij jullie bleef ik op de hoogte van wat er in de rest van de wereld gebeurde.

Tot slot een woord van welgemeende dank aan mijn ouders. Terugkijkend ben ik enorm dankbaar dat jullie mij altijd hebben gesteund en gestimuleerd om te studeren. Ook wil ik hierbij graag mijn broertjes en zusjes (met aanhang) Anita & Aldwin, Aart, Marien, Renske en Arjen betrekken. Hoewel alles een beetje begint uit te waaieren nu en de Korevaren naast het hoofdkantoor in Goudriaan nu ook vestigingen hebben in Leiden, Dordrecht, Enschede en wie weet straks overzee, vormen jullie toch wat ik beschouw als een permanente thuisbasis.

Bedankt allemaal!

Peter.